Colloidal Dispersions in Fluid Media: Electric, Magnetic and Light Control

Sergi Hernández Navarro

Doctoral Program: Ciència i Tecnologia de Materials

Colloidal Dispersions in Fluid Media: Electric, Magnetic and Light Control

Author:

Sergi Hernández Navarro

Supervisors:

Dr. Jordi Ignés-Mullol
Departament de Química Física,
Universitat de Barcelona

Dr. Pietro Tierno
Departament d'Estructura i Constituents de la Matèria
Universitat de Barcelona

Als meus iaios:

Pepe, Neus, Teodoro i Paquita

Agraïments

En primer lloc agraeixo als meus directors Jordi Ignés i Pietro Tierno, així com també a en Francesc Sagués, a qui merescudament considero també com a director, tots els esforços i temps que m'han dedicat, ja sigui amb temes experimentals, teòrics o burocràtics, sense els quals aquesta tesi no hagués estat possible. Evidentment també vull donar mil gràcies als membres *juniors* amb els qui he compartit més estones al laboratori durant aquest darrers anys: Mª Àngels, Patricia, Núria i Alba, i més recentment, en Pau. És de justícia fer una menció especial per l'Alba, la que m'ha hagut de suportar més temps, i amb la que he compartit matins i tardes amb inacabables anades d'olla, exercitant la memòria amb poesies infantils, fent accents de tota mena, o component cançons que algun dia seran un èxit mundial: lady Coflow, sens dubte tu t'endús el premi OTB!! ;).

Per descomptat, no m'oblido dels altres membres de la banda més "forajida" al oeste de la Diagonal: Oriol *Guey* Fargo, Fransis the Kid, Anna Canyon, Trapoteitor, Vela Starr i Calamity Maria, fent que cada dinar fos una aventura on llençar la dinamita era un risc que no tothom estava disposat a acceptar...Dinamita Hernàndez us saluda, sense vosaltres no hauria arribat tan lluny sense esclatar ;)!

També vull fer constar que un milió de gràcies són poques per agrair el suport incondicional que tota la meva família m'ha brindat, i que m'ha permès arribar on sóc, en especial als meus pares i al meu germà (sí, tu també Lluís ;p).

Per acabar, us dono les gràcies també a totes i tots els que m'heu anat acompanyant i recolzant durant d'aquests últims anys i que no puc escriure amb noms i cognoms perquè acabaria amb tots els arbres de l'Amazones, i és l'últim que necessita el planeta. Bromes a part: moltes gràcies a tots!!

ᓭᐱᒋ ᑊᐧ ᔑᒣᒐᓗᐧ ᐯᐧ ᐧᑎᒣᐦᐃᓭᐱᒋ!

INDEX

CHAPTER 1

INTRODUCTION

1.1 Motivation of the Work

Mankind has observed and made use of colloidal systems since the earliest days of civilization: from prehistorical paintings or medical unguents, to cosmetics, sauces or modern pharmaceutical preparations. However, it was not until the early XIXth century when scientists, like Thomas Graham[1] or Michael Faraday,[2] started to focus in their study. Since then, the Physics and Chemistry of colloids have been broadly studied and described both theoretically and experimentally.[3] Nevertheless, characterization and preparation of new colloidal suspensions is still a widely explored field of research, with potential application in nano- and micro-technology,[4,5] and biological[6] or medical science.[7]

Perhaps one of the most common medium to disperse colloidal particles and study their properties is water. However, the interest to combine both colloids and complex fluids has increased enormously during the past decades. As an example, dispersions of colloids in liquid crystals constitute nowadays a type of mixture which can be used to unveil new fundamental concepts or to explore original applications.[8–11] The capability of the host elastic matrix of the liquid crystal to mediate interactions between suspended colloids was already discovered nearly two decades ago[12–15] and has been profusely invoked since then.[16–19] One of the most intriguing characteristics of liquid crystals is that their interaction with colloidal inclusions leads to the proliferation of topological point and line defects. This feature can be used to develop colloid-based self-assembling materials[20–25] or as a positioning mechanism for embedded colloids.[26]

In this thesis, I have studied colloidal dispersions composed of micrometer-sized particles of different nature, dispersed in water as well as in a nematic liquid crystal (NLC). In the next sections I will first review some basic concepts about colloidal dispersions. Secondly I will focus on the fundamentals of liquid crystals, as well as their behavior under external fields or their structure around embedded inclusions. Finally, I will comment on the essentials

of nonlinear electrophoresis, used to transport particles employing alternate current electric fields in water based solvents as well as in a liquid crystal media.

1.2 Colloidal Dispersions

A colloidal system is composed by a dispersed phase of micro- or nano-scale particulate matter, and a continuous phase, which is the suspension medium. Colloidal dispersions are important for industrial applications, and a huge variety of examples can be found in everyday life: from milk, jelly, hand cream or inks, to smoke or fog.[27] Due to their large surface to volume ratio, colloidal dispersions are thermodynamically unstable and tend to spontaneously aggregate with time. For many industrial applications, the stability of a colloidal dispersion is an important issue. This tendency to aggregate can be overcome by finely adjusting the attractive and repulsive interactions between colloidal particles.

In colloidal dispersions there are attractive and repulsive forces acting between the particles, and attractive interactions results mainly from Van der Waals forces. These forces emerge from the interaction of the ensembles of molecules composing the particles, interacting via their electric dipoles. These dipoles can be permanent (due to their molecular structure) or not. In the latter case, they can be formed by spontaneous fluctuations of charge densities in the molecule, or induced by the neighboring molecules.[28]

Repulsive interactions between colloidal particles can be induced in two ways: either by using the *double layer* repulsion or via steric interaction due to a polymer coating. Focusing on the first case, when a charged particle is submerged in an electrolyte solution, ions in the dispersing medium reorganize around the inclusion in order to counteract the particle charge, creating an electric *double layer*. As depicted in figure 1.1a, the charged particle will attract ions of opposite sign, which will form a first layer of immobile charges known as the *Stern* layer. Beyond this layer, mobile ions create a gradient in the concentration of charges close to the particle surface. This leads to an exponential decay of the potential from the Stern layer until reaching the bulk of the solution (figure 1.1b). This decay in the potential of the surface of the particle can be described by the Poisson-Boltzmann equation:[29]

$$\nabla^2\psi = \frac{-1}{\varepsilon_0\varepsilon_r}\sum_i n_i^0 z_i e \cdot \exp\left(\frac{-z_i e\psi}{k_B T}\right) \qquad \text{eqn (1.1)}$$

where ψ is the potential, ε_0 and ε_r are, respectively, the vacuum permittivity and the relative dielectric permittivity of the medium, n_i^0 is the bulk concentration of ions of type i (number of ions per cubic meter), z_i is their valence (positive or negative), e is the charge of an electron, k_B is the Boltzmann constant and T is the absolute temperature.

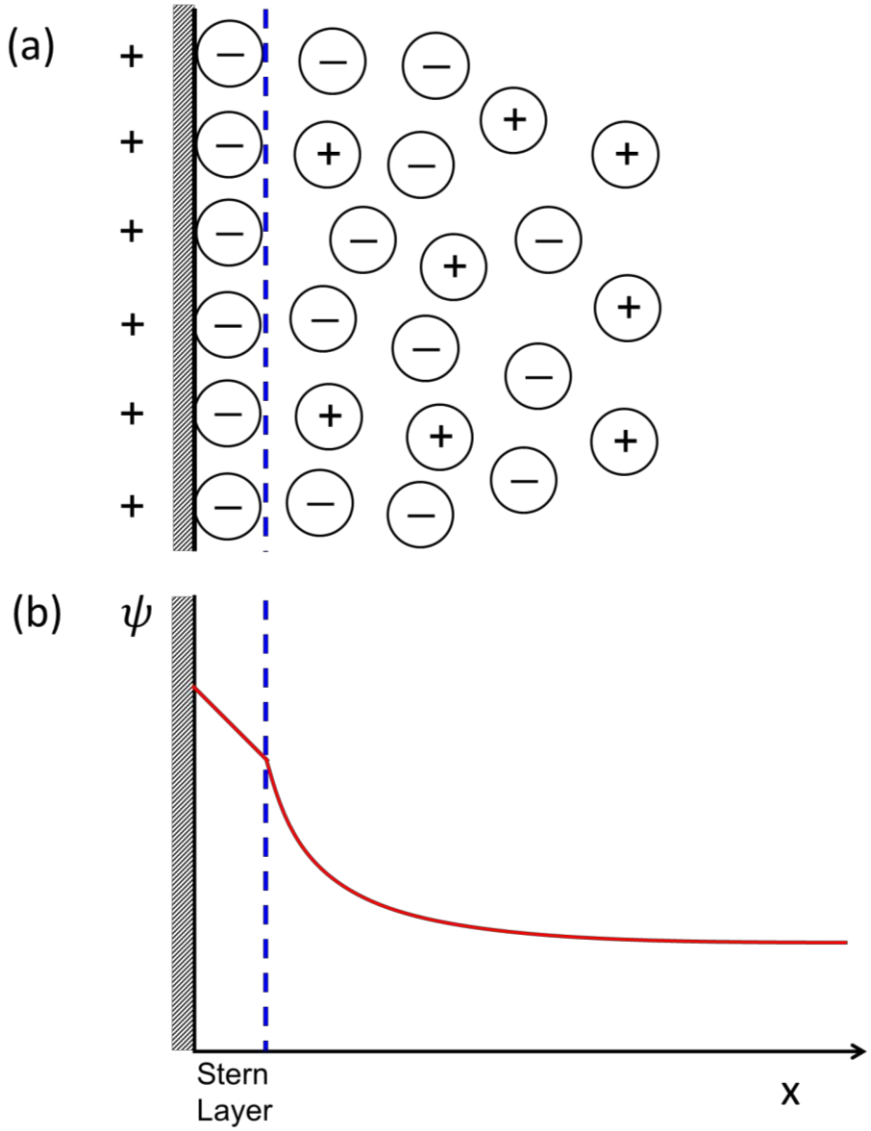

Figure 1.1: (a) Schematic of the double layer formed when a charged surface is placed in contact with an electrolyte solution. (b) Representation of the potential ψ near a charged surface as a function of the distance. The potential inside the Stern layer decays linearly, while it drops exponentially until reaching the bulk of the solution.

By applying the Debye-Hückel approximation, valid for thin double layers, i.e. if the electrostatic energy is small compared to thermal energy ($|z_i e\psi| < k_B T$), eqn (1.1) can be simplified to:

$$\nabla^2\psi = \left[\frac{\sum z_i^2 e^2 n_i^0}{\varepsilon_0 \varepsilon_r k_B T}\right]\psi = \kappa^2\psi \qquad \text{eqn (1.2)}$$

The solution of eqn (1.2) is given by a potential which decays exponentially with the distance from the surface $\psi = \text{const.}\exp(-\kappa x)$. The extent of the double layer is quantified by the *Debye screening length* λ_D, which is defined as $\lambda_D = 1/\kappa = \sqrt{\left[\frac{\varepsilon_0 \varepsilon_r k_B T}{e^2 \sum z_i^2 n_i^0}\right]}$. The Debye screening length can be understood as the "effective thickness" of this double layer, and it depends only on the temperature and the bulk electrolyte concentration.[30,31]

When two colloidal particles approach each other, their double layers start to overlap and a repulsion force arises. This repulsion can be explained by considering the osmotic pressure which is built up when the two ion clouds approach each other. As the particles come close, the concentration of ions between them increases in order to maintain the electrical neutrality of the medium. This implies a large osmotic pressure which can be calculated as the difference between the osmotic pressure of the particles and the bulk solution. It is possible to show[29] that the repulsive interaction per unit area between two approaching double layers is given by:

$$V_R = \frac{64\, k_B T\, n^0}{\kappa}\; e^{-\kappa d} \qquad \text{eqn (1.3)}$$

being *d* the distance between the particle surfaces. Thus, as the concentration of ions increases, the electrostatic repulsion of particles decreases.

1.3 Liquid Crystals

1.3.1 Fundamental Concepts

Liquid crystals are anisotropic fluids (either pure substances, mixtures or solutions) that share properties of both liquid and crystalline solid phases at the same time.[28,32] The building units (i.e. molecules, aggregates or clusters) of a liquid crystal can move easily with respect to one another, just like an ordinary liquid does. However, these building units tend to have orientational order or even a certain degree of translational order, similarly to solid crystalline phases. There are four basic types of liquid crystals, classified according to the dimensionality of the translational correlations of the building units: *nematic* (no translational order, long range orientational order, see figure 1.2), *smectic* (1D correlations, ordered in layers), *columnar* (2D correlations) and various 3D-correlated structures, such as *cubic* phases.[32]

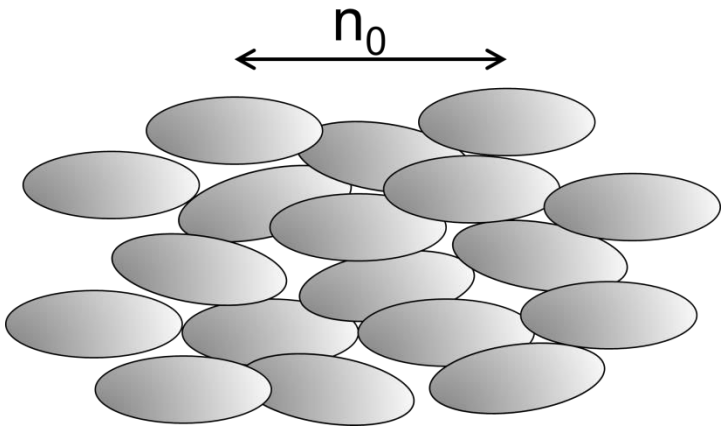

Figure 1.2: Schematic representation of a nematic liquid crystal (NLC). The mean orientation of the molecules (grey ellipses) is indicated by the director field $\boldsymbol{n_0}$.

Another classification is possible regarding the chemical composition of the liquid crystals. In particular, if the building blocks are composed of organic molecules, either pure or mixed, which reach the liquid crystal phase through a temperature change, they are called *thermotropics*. On the other hand, when the

building blocks are self-assembled units dispersed in a solvent within a certain concentration range, they are called *lyotropics*. In contrast to lyotropics, thermotropic liquid crystals do not need a solvent to exhibit a liquid crystal phase within a suitable temperature region.

In this thesis, I use thermotropic nematic liquid crystals (NLC). The long-range mean orientation of NLC molecules is described by the unit vector $\vec{n}$ (also noted $\boldsymbol{n_0}$) called the *director field*, as shown in figure 1.2. Even if the constituting molecules are polar, molecular flip-flops and head-to-head overlapping establish a centrosymmetric arrangement in the nematic bulk, thus making the directors $\boldsymbol{n_0}$ and $-\boldsymbol{n_0}$ equivalent.[28] The director field orientation can be established by the boundary conditions where the nematic sample is confined. These conditions can be controlled by a proper functionalization of the bounding plates (further details on functionalization processes and related anchoring conditions are found in chapter 2 section 2.1).

1.3.2 Frank-Oseen Free Energy: Defects in a NLC

In absence of external constrains, the lowest free energy for a NLC corresponds to homogeneous alignment of the director field $\vec{n}$. However, in many scenarios this ideal case is not satisfied, such as near the bounding cell plates, around immersed inclusions or in the presence of external fields. The free energy costs of such distortions are typically modeled by the Frank-Oseen free energy functional f, which can be written as:[32]

$$f = \frac{1}{2}K_1(\nabla \cdot \vec{n})^2 + \frac{1}{2}K_2(\vec{n} \cdot \nabla \times \vec{n})^2 + \frac{1}{2}K_3(\vec{n} \times \nabla \times \vec{n})^2$$

$$+ \frac{1}{2}K_4\,\nabla \cdot (\vec{n}\,\nabla \cdot \vec{n} + \vec{n} \times \nabla \times \vec{n}) + K_{13}\,\nabla \cdot (\vec{n}\,\nabla \cdot \vec{n}) \quad \text{eqn (1.3)}$$

where K_i are distortion constants related with different deformations of the NLC. If one assumes that there are strong surface anchoring conditions, K_4 and K_{13} can be neglected and the expression can be written in the simplified Frank form:

$$f = \frac{1}{2}K_1(\nabla \cdot \vec{n})^2 + \frac{1}{2}K_2(\vec{n} \cdot \nabla \times \vec{n})^2 + \frac{1}{2}K_3(\vec{n} \times \nabla \times \vec{n})^2 \quad \text{eqn (1.4)}$$

where K_1, K_2 and K_3 are, respectively, the *splay, twist* and *bend* constants, which account for the three basic NLC distortions and are of the order of 10^{-12}N. The splay and bend distortions are 2D deformations of the director, and are represented in figure 1.3a and 1.3c, respectively. The twist distortion is a 3D deformation showed in figure 1.3b.

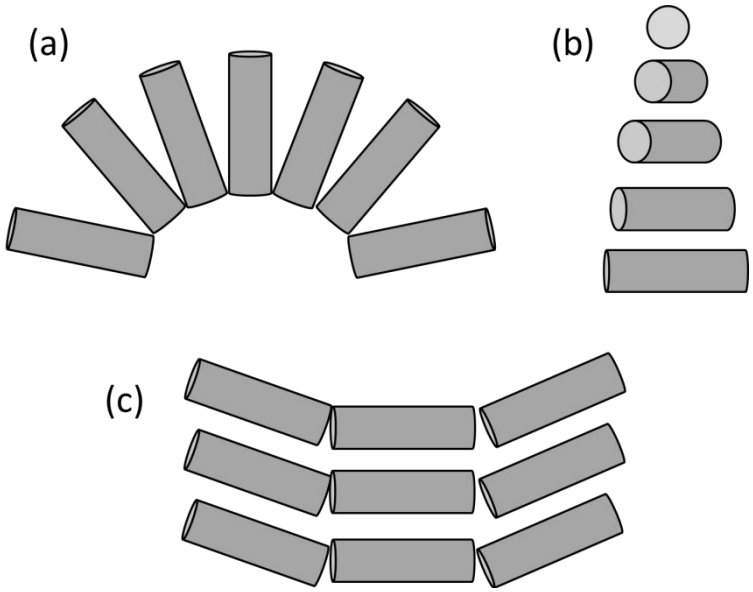

Figure 1.3: Schematics of the splay (a), twist (b), and bend (c) distortions. The local NLC director is represented by grey cylinders.

In the NLC cells studied in this thesis, the most common distortions encountered are 2D splay and bend. Topological incompatibilities in the

boundary conditions lead to singularities in the form of point or line defects. These defects are further classified by a number m termed the *topological rank*, also called the *topological charge*. Examples of different 2D distortions and their topological charges can be seen in figure 1.4.

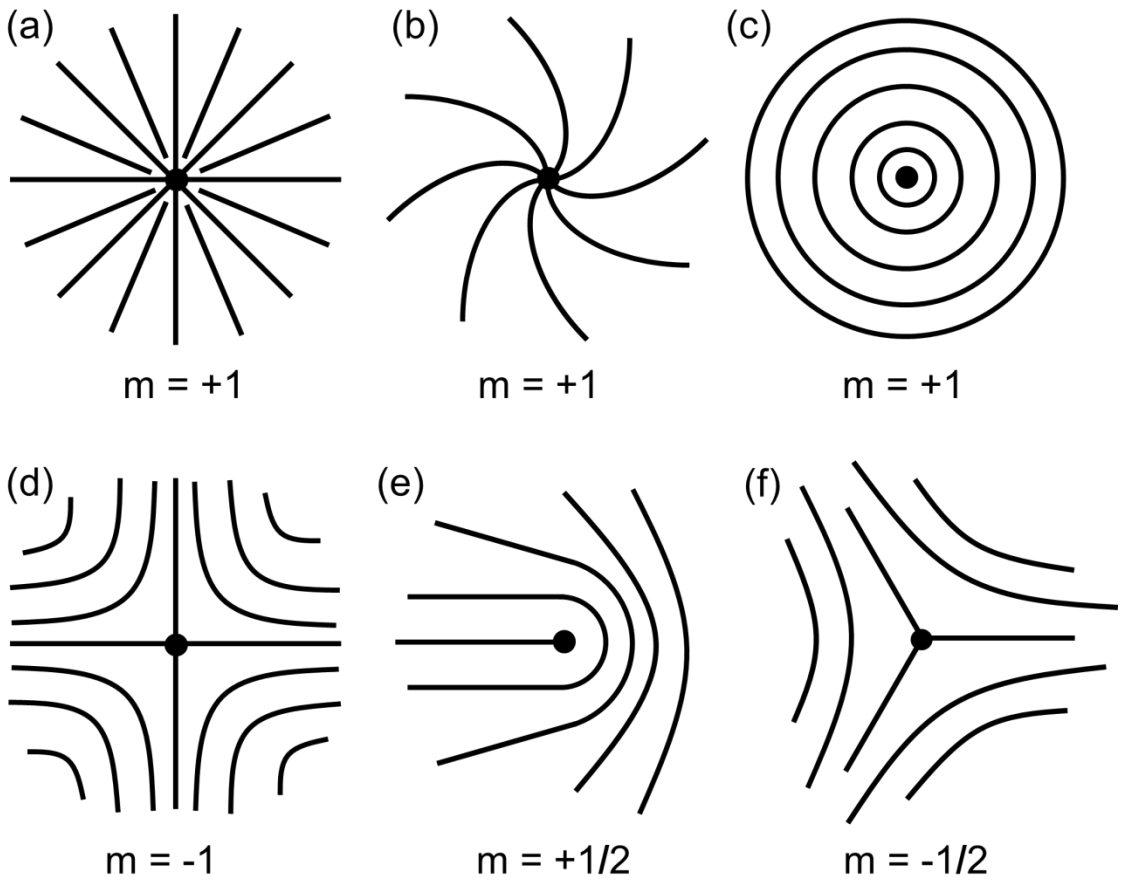

Figure 1.4: Examples of 2D distortions found in NLC cells, and their corresponding topological charge m. Distortion (a) is a pure splay, and distortion (c) is a pure bend, while (b) is a mixture of splay and bend distortions. Each of the distortions (a-c) has the same topological charge.

As shown in figure 1.5, the topological charge of a defect can be determined by first considering a closed loop, called the *Burgers* circuit γ, which encircles the defect and defines a sense of rotation. Starting from an arbitrary point of the Burgers circuit, one can draw each director $\vec{n}$ encountered when following the circuit γ. After a complete rotation, $\vec{n}$ will have turned by an angle

Ω, which is positive if the rotation sense is the same as the Burgers circuit, or negative if it is in the opposite sense. Considering this angle, the topological rank is defined as $m = \Omega/2\pi$. In figure 1.5 an example of a Burgers circuit is depicted for a $m = -1/2$ defect.

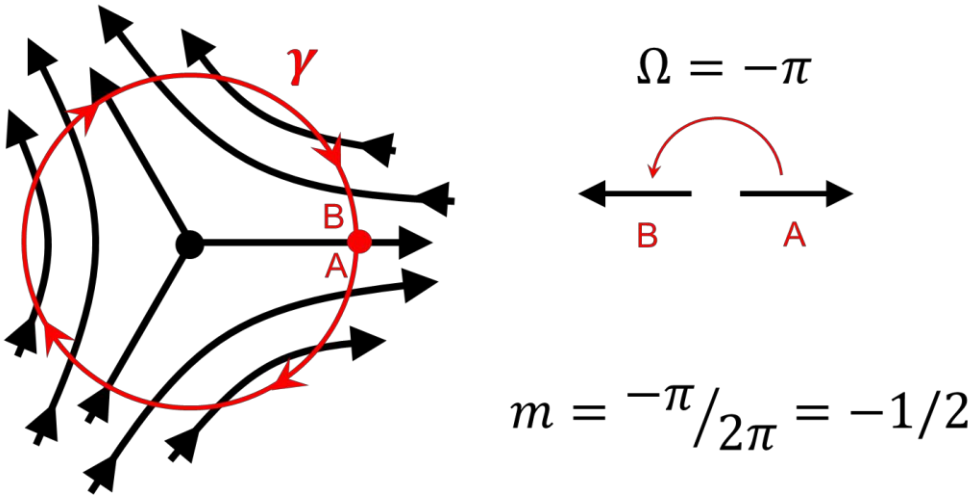

Figure 1.5: Example of the determination of the topological charge of a defect. The Burgers circuit γ is represented by a red circle enclosing the defect. The circuit starts (A) and finishes (B) at the same point after a clockwise rotation. The director $\vec{n}$ features a counter-clockwise half-turn rotation while traveling the circuit, which results in a topological charge of $m = -1/2$.

1.3.3 Electric and Magnetic Frederiks transition

When a nematic liquid crystal (NLC) is subjected to an external electric or magnetic field, NLC molecules tend to reorient parallel or perpendicular to the field, depending on the NLC molecular structures.[32] For example, in the case of an external applied electric field, if each molecule carries a permanent dipole moment parallel (perpendicular) to its long axis, the NLC director tends to orient parallel (perpendicular) with the field when the parallel dielectric permittivity is higher than the perpendicular one $\varepsilon_{\parallel} > \varepsilon_{\perp}$ (lower, $\varepsilon_{\parallel} < \varepsilon_{\perp}$). The difference between both dielectric permittivities is the *dielectric anisotropy* of the liquid crystal $\Delta\varepsilon = \varepsilon_{\parallel} - \varepsilon_{\perp}$. For an external applied magnetic field the reorientation phenomenon also occurs. In this case the difference between parallel and perpendicular magnetic susceptibilities $\Delta\chi = \chi_{\parallel} - \chi_{\perp}$ is what defines the reorientation behavior of the NLC, which for nematics is usually positive $\Delta\chi > 0$.[33]

For small field amplitudes (either electric or magnetic) the director keeps the alignment set by the boundary conditions. When the field strength reaches a threshold value, NLC molecules start to deviate from their initial orientation. This phenomenon is known as the *Frederiks transition*. By balancing elastic and field-induced torques, one can find the expression for the threshold field, which in the case of a magnetic field is:

$$B_C = \frac{\pi}{d}\sqrt{\frac{\mu_0 K}{|\Delta\chi|}} \qquad \text{eqn (1.5)}$$

where B_C is the threshold magnetic field, d is the thickness of the sample, μ_0 is the vacuum magnetic permeability, $|\Delta\chi|$ is the difference between parallel and perpendicular NLC magnetic susceptibilities, and K is the relevant Frank elastic constant.[32] Substitution of these parameters for their typical values in liquid crystals leads to a threshold magnetic field on the order of hundreds of milliTesla (Earth magnetic field is on the order of $5 \cdot 10^{-2}$mT).

The threshold field E_C for the Frederiks transition induced by the electric field is given by:

$$E_C = \frac{\pi}{d}\sqrt{\frac{K}{|\Delta\varepsilon| \cdot \varepsilon_0}} \qquad \text{eqn (1.6)}$$

where ε_0 is the vacuum dielectric permittivity, $\Delta\varepsilon$ is the dielectric anisotropy of the NLC, and K is the relevant Frank elastic constant. For an experimental cell composed by two electrodes separated by a distance d, the threshold electric field is equal to the threshold voltage V_C divided by the sample thickness d, $E_C = V_C/d$. This implies that the threshold voltage V_C does not depend on sample thickness. For the NLC mixture employed through this thesis, MLC-7029, the dielectric anisotropy is $\Delta\varepsilon = -3.6$ and the average elastic constant can be approximated to $K = 15{,}6\text{pN}$. Using these values, the resulting threshold voltage is $V_C = 2.2\text{V}$.

1.3.4 Colloidal Inclusions in Liquid Crystals

When a microscale inclusion is dispersed in a NLC medium, the distortion of the director field caused by the particle leads to the formation of defects around the inclusion. These defects will mainly depend on the anchoring conditions at the particle surface, the elasticity of the liquid crystal and the particle radius.[34,35] The orientation of a NLC close to a surface can be *homeotropic* or *planar*. In the first case, the molecules orient perpendicular to the surface, while in the other case they orient parallel to it. The effect of these

distortions in a NLC with unidirectional alignment is limited to the inclusion surroundings, since the addition of all the topological charges generated by the inclusion is zero.

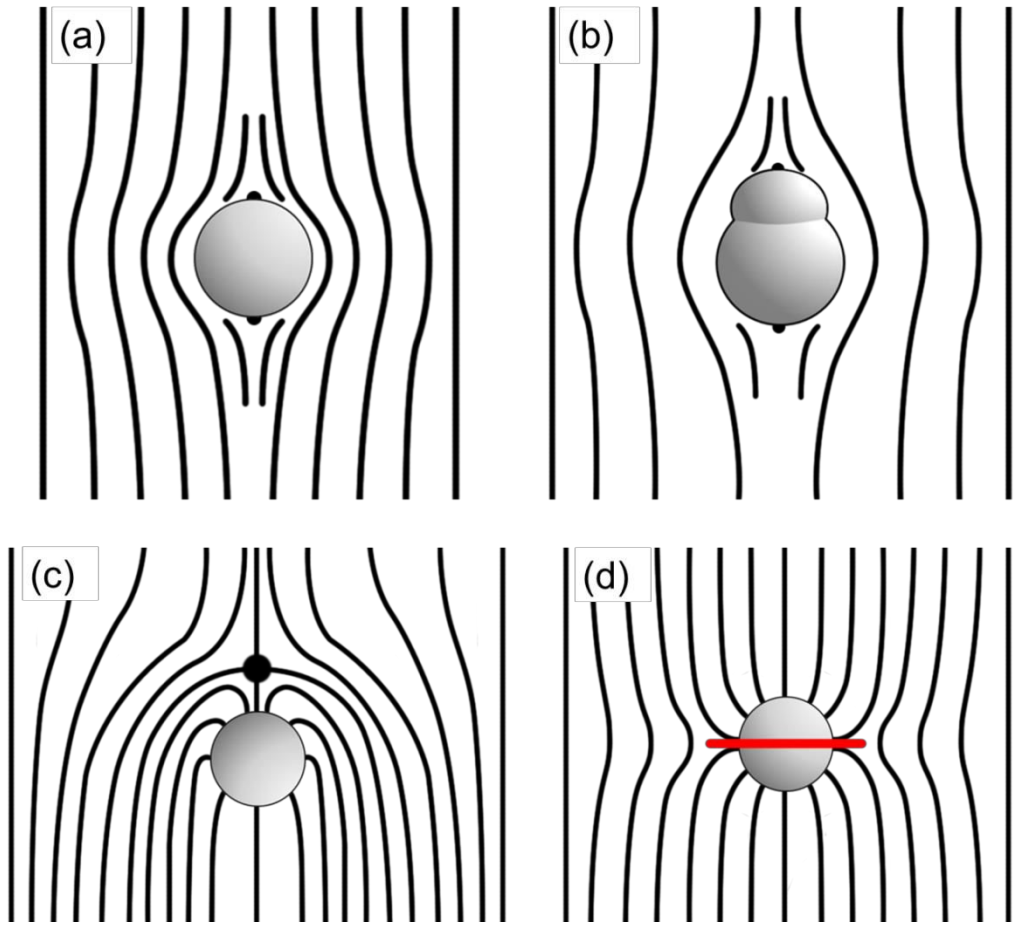

Figure 1.6: Schematics of the distortions generated by particles with different shape and anchoring conditions suspended in a NLC with unidirectional vertical alignment. Spherical (a) and pear-shaped (b) planar (tangential anchoring) inclusions immersed in a NLC present two defects at the particles' poles that are called double Boojum. Particles with homeotropic anchoring (perpendicular alignment) in NLC can exhibit a hedgehog (c) or a Saturn ring (d) defect. The hedgehog presents a $m = -1$ point defect at one of the particle poles (black spot), while the Saturn ring features a $m = -1/2$ disclination loop (line defect) around the particle equator (red line). Each panel has axial symmetry.

I will start by first describing the defects encountered when dispersing inclusions with tangential (planar) boundary conditions at their surface in a unidirectionally aligned NLC. In figure 1.6a and 1.6b two examples of planar

inclusions used during this thesis are shown: spherical inclusions and *pear*-shaped particles. Both types of particles present two point defects at their poles. Each point defect has a topological charge $m = -1/2$ (see figure 1.4f), which are compensated by a virtual $m = +1$ defect in the center of the inclusion (not drawn, see figure 1.4c), giving a null global topological charge. Nevertheless, while the spherical particle has quadrupolar symmetry (it has three orthogonal symmetry planes), for the pear-shaped particle this symmetry is not present.

In the case of inclusions with homeotropic (perpendicular) anchoring conditions at their surface, two types of arrangements for the NLC director field are possible: dipolar hedgehog[14] or quadrupolar Saturn ring,[36,37] as shown in figure 1.6c and 1.6d, respectively. The dipolar hedgehog defect is characterized by a point defect located at one of the poles of the homeotropic particle. This point defect has a topological charge $m = -1$, compensated by a $m = +1$ virtual point defect at the center of the sphere (see figure 1.4d and 1.4a respectively). In contrast, the quadrupolar Saturn ring is characterized by a disclination loop (*line* defect) with a topological charge $m = -1/2$ situated around the equator of the sphere, which is also compensated by the $m = +1$ virtual point defect located at the center of the sphere.

1.4 Nonlinear Electrophoresis

1.4.1 Fundamentals of the Induced-Charge Electrophoresis

First of all, it is worth remarking that the term "electro-osmosis" is used when speaking of the electrokinetic flow around stationary surfaces (such as electrodes), while "electrophoresis" is reserved specifically to the electrokinetic motion of freely suspended particles. After this clarification, I will start by first describing the classical linear fixed-charge electrophoresis (FCEP). This phenomenon is based on the electro-osmotic flow that appears when a uniform electric field is applied to a charged particle suspended in an electrolyte (typically water). In FCEP the surface charge of the particle is fixed, and the electro-osmotic flow around it is *linear* with the applied electric field. The charged particle then moves towards the electrode of opposite sign. In the thin-double-layer limit (i.e. small Debye screening length) the electrophoretic velocity U_{FCEP} is given by Smoluchowski's formula:[38]

$$U_{FCEP} = \frac{\varepsilon_s \zeta}{\eta} E_0 \qquad \text{eqn (1.8)}$$

where ε_s is the dielectric permittivity of the solvent, ζ is the particle *zeta-potential* (it is the potential of the first ionic mobile layer around the particle, and it is related to the particle surface charge density),[29,31] η is the viscosity of the solvent, and E_0 is the externally applied electric field. In this case, there is only effective motion if the applied electric field is DC (direct current), because for AC (alternate current) fields the particle only oscillates, showing no net displacement.

In contrast to the linear case, if the suspended particle is polarizable, the applied external electric field can induce surface charges on the particle, and the nonlinear phenomenon of *induced-charge electro-osmosis* (ICEO) takes place. In ICEO, the dependence of the velocity is quadratic with the electric field $U_{ICEO} \propto {E_0}^2$, thus allowing the use of AC and not only DC fields to generate constant electro-osmotic flows. Bazant and Squires[38] modeled the general

phenomenon of ICEO with DC and AC electro-osmotic flows at electrodes. The model describes the flows resulting from the action of an applied electric field on the field-induced diffuse charge near a polarizable surface. They also predicted how broken symmetries (for example dipolar, but not quadrupolar symmetries) could cause polarizable particles to move in electric fields by nonlinear *induced-charge electrophoresis* (ICEP).

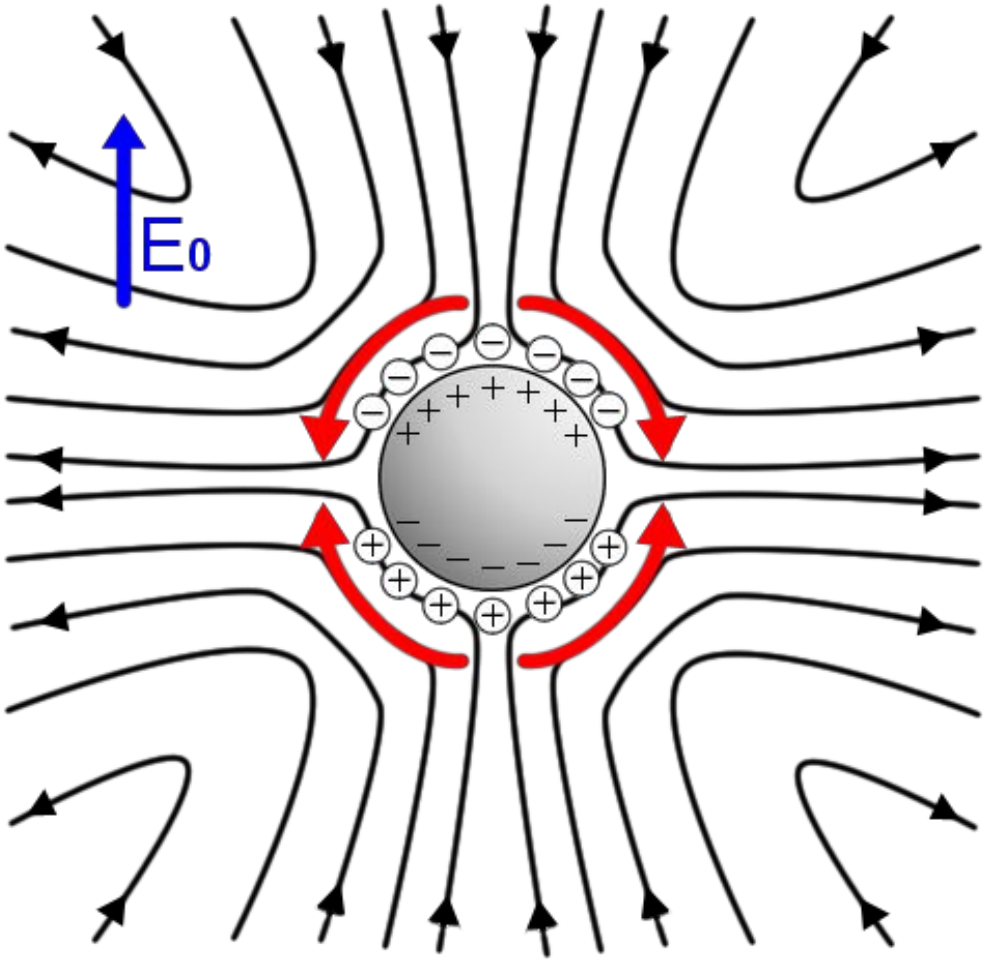

Figure 1.7: Representation of the induced-charge electro-osmotic flow around a particle with zero net charge. Black lines indicate the direction of the quadrupolar fluid flow, and red thick arrows show the flow next to the particle, from its poles to its equator. Notice that reversing the electric field results in identical flow lines.

If we have a spherical polarizable inclusion immersed in a liquid electrolyte and subjected to an external electric field, a quadrupolar electro-

osmotic flow is formed around the inclusion, from its poles to its equator, as shown in figure 1.7. The electric field first induces a charge separation in the particle, which in turn attracts ions of opposite sign from the solvent in order to screen the electrostatic charges present on the particle surface, thus generating the corresponding screening cloud in the solvent. In this case, the particle's zeta-potential is non-uniform [$\zeta(\vec{r})$] and its magnitude now depends linearly on the applied external electric field $\zeta \propto E_0$. After inducing the charge separation, the field drives the resulting electro-osmotic flow in the same way as the FCEP, but now the velocity of the flow U_{ICEO} depends on the square of the electric field as:

$$U_{ICEO} = \frac{\varepsilon_s \zeta}{\eta} E_0 \rightarrow U_{ICEO} \propto {E_0}^2 \qquad \text{eqn (1.9)}$$

That is, one power of E_0 sets up the induced-charge screening cloud, and the second drives the resultant electro-osmotic flow. Both AC and DC fields drive identical flows, since in figure 1.7 an oppositely directed field would induce an oppositely charged screening cloud, giving the same net flow from the particle poles to its equator. When using AC fields, it must be noted that electro-osmotic flows will only take place if the frequency of the field is low enough to let the induced-charge screening cloud form, but high enough to avoid screening of the electric field by the diffuse-layer charging at the electrodes.

In isotropic fluids like water, either for AC or DC electric fields, this quadrupolar electro-osmotic flow around non-charged spherical inclusions is symmetric, thus it does not lead to effective propulsion, as shown in figure 1.7. To generate particle motion by ICEP, the quadrupolar symmetry of the flow must be broken,[39] and this can be achieved by using for example *Janus* particles (i.e. microparticles with one dielectric and one metal-coated hemisphere),[40] nonspherical inclusions,[41] or using as a dispersing medium an anisotropic fluid such as a NLC, as explained in the following section.

1.4.2 Liquid Crystal-Enabled Electrophoresis (LCEEP)

A recent breakthrough in electric field transport of colloidal microspheres showed that colloidal particles with point defects can be transported in a NLC by using AC electric fields.[10,42–44] The Liquid Crystal-Enabled Electrophoresis (LCEEP) is based on the electrophoretic motion of spherical particles enabled by the anisotropy of the dispersing medium. As explained in section 1.3.4, when a homeotropic spherical particle is suspended in NLC, it can generate two different defect configurations of the neighboring NLC. The dipolar hedgehog defect, in contrast to the quadrupolar symmetric Saturn ring, can break the spatial symmetry, unbalancing the ionic flows created by the AC field around the particle, as it is schematized in figure 1.8a,b respectively. The spatial symmetry can also be broken by using non-spherical particles with planar anchoring, as shown in figure 1.8c. In both cases, the quadrupolar symmetry of the electro-osmotic flow is broken, thus generating propulsion, and giving rise to the so called LCEEP. It is worth mentioning that in the geometry depicted in figure 1.8, which is the one used in this thesis, the classical lineal electrophoresis is decoupled from the LCEEP, as they present orthogonal directions.

The main advantage of this technique, compared to the standard electrophoresis methods based on the use of a direct current electric field, is the absence of ion migration, avoiding electrochemical processes and screening phenomena,[45] thus making it suitable to transport also liquid[46] rather than solid inclusions.[44] It is worth remarking that for LCEEP to occur, the basic requirement is that the system must feature broken symmetries. As commented in the previous section, nonlinear electrophoresis has been also reported for Janus particles in aqueous solution, where the contrast between metallic and dielectric hemispheres results in unbalanced ionic flow and in particle motion under AC fields.[40] In this respect, the use of NLC provides a more versatile strategy, compatible with solid particles as well as droplets of any nature, since

it does not require the introduction of structural anisotropies, specifically in liquid droplets, which is a technically challenging process.[47]

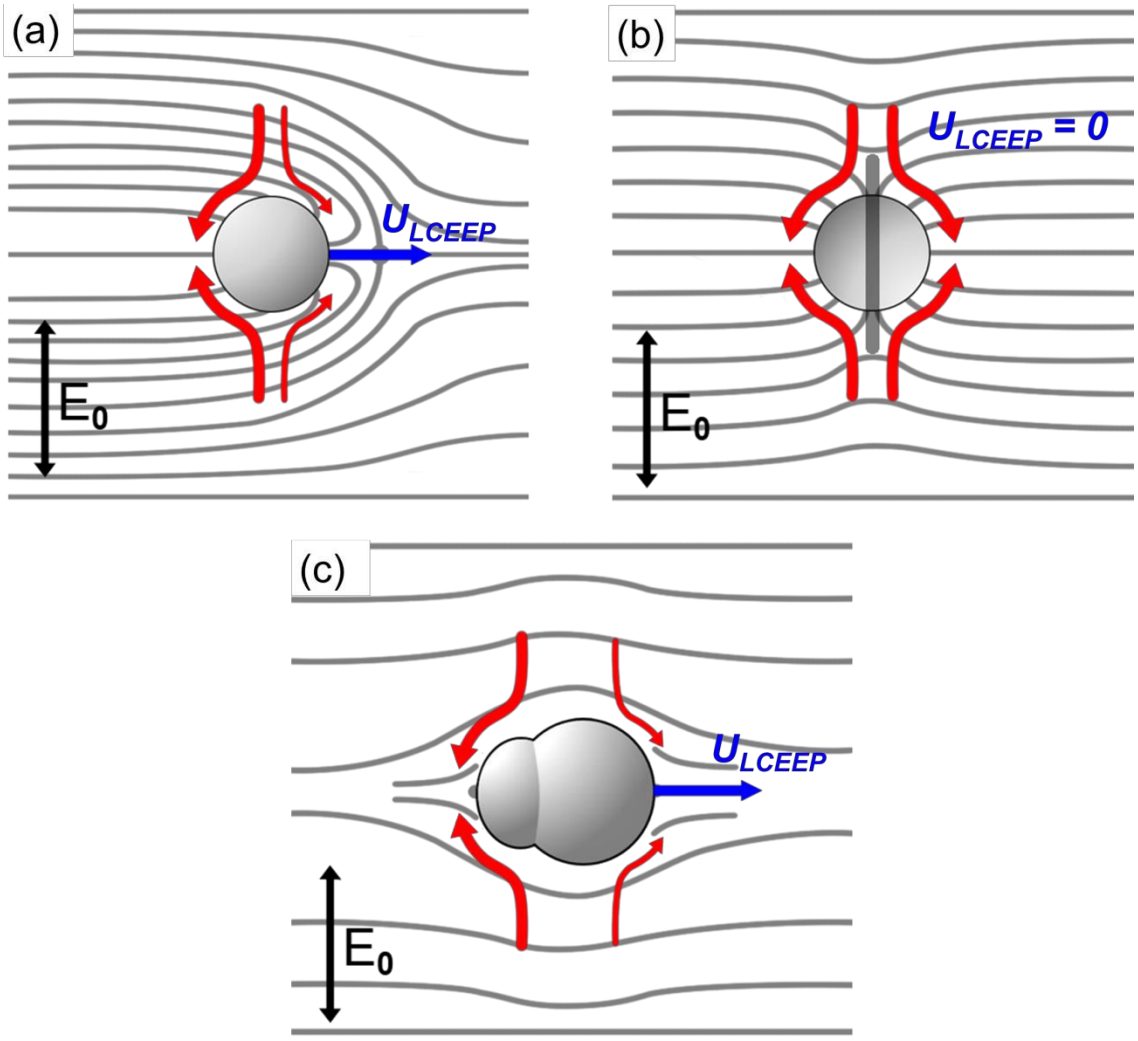

Figure 1.8: Schematics of the LCEEP mechanism around a dipolar hedgehog particle (a), a quadrupolar Saturn ring particle (b), and a planar pear-shaped particle (c). Red arrows indicate the electro-osmotic flow, while the NLC director field lines are shown in the background. There is motion only in (a) and (c), where the quadrupolar electro-osmotic flow is distorted by the surrounding NLC. The direction of motion depends on the liquid crystal used and the geometry of the experimental cell. Here it is depicted as it is found in the experiments reported in this thesis.

1.5 Aims and Objectives

The objectives of the present thesis are the following:

1. Study of the assembly and structural properties of colloidal particles under external alternate current electric fields. Compare the behavior and dynamics of spherical and non-spherical particles. Use externally driven magnetic particles to probe the structural properties of the colloids assemblies.

2. Control the orientation of a nematic liquid crystal using anisometric paramagnetic inclusions externally actuated by means of weak magnetic fields.

3. Validate the use of the Liquid Crystal-Enabled Electrophoresis (LCEEP) for aqueous microdroplets or photosensitive particles. Use these droplets to develop novel strategies for the transport of different microscopic cargoes, such as solid particles or chemical reactants. Control the LCEEP activation or deactivation of particles featuring photosensitive surfaces.

4. Control the direction of motion of anisometric particles propelled via LCEEP, by using photosensitive cell plates. Study the collective motion of particles and explore new possibilities for lab-on-a-chip applications.

1.6 References

(1) Thomas Graham. *Encyclopaedia Britannica*, 2014.

(2) Michael Faraday. *Encyclopaedia Britannica*, 2014.

(3) Hauser, E. A. The History of Colloid Science. *J. Chem. Educ.* **1955**, *32*, 2.

(4) Bumb, A.; Sarkar, S. K.; Billington, N.; Brechbiel, M. W.; Neuman, K. C. Silica Encapsulation of Fluorescent Nanodiamonds for Colloidal Stability and Facile Surface Functionalization. *J. Am. Chem. Soc.* **2013**, *135*, 7815–7818.

(5) Sacanna, S.; Irvine, W. T. M.; Chaikin, P. M.; Pine, D. J. Lock and Key Colloids. *Nature* **2010**, *464*, 575–578.

(6) Park, S. Y.; Lytton-Jean, A. K. R.; Lee, B.; Weigand, S.; Schatz, G. C.; Mirkin, C. A. DNA-Programmable Nanoparticle Crystallization. *Nature* **2008**, *451*, 553–556.

(7) Monti, D. M.; Guarnieri, D.; Napolitano, G.; Piccoli, R.; Netti, P.; Fusco, S.; Arciello, A. Biocompatibility, Uptake and Endocytosis Pathways of Polystyrene Nanoparticles in Primary Human Renal Epithelial Cells. *J. Biotechnol.* **2015**, *193*, 3–10.

(8) Koenig, G. M.; Lin, I.-H.; Abbott, N. L. Chemoresponsive Assemblies of Microparticles at Liquid Crystalline Interfaces. *Proc. Natl. Acad. Sci.* **2010**, *107*, 3998–4003.

(9) Lintuvuori, J. S.; Stratford, K.; Cates, M. E.; Marenduzzo, D. Colloids in Cholesterics: Size-Dependent Defects and Non-Stokesian Microrheology. *Phys. Rev. Lett.* **2010**, *105*, 178302.

(10) Lavrentovich, O. D.; Lazo, I.; Pishnyak, O. P. Nonlinear Electrophoresis of Dielectric and Metal Spheres in a Nematic Liquid Crystal. *Nature* **2010**, *467*, 947–950.

(11) Pishnyak, O. P.; Tang, S.; Kelly, J. R.; Shiyanovskii, S.; Lavrentovich, O. D. Levitation, Lift, and Bidirectional Motion of Colloidal Particles in an Electrically Driven Nematic Liquid Crystal. *Phys. Rev. Lett.* **2007**, *99*, 127802.

(12) Ramaswamy, S.; Nityananda, R.; Raghunathan, V. A.; Prost, J. Power-Law Forces between Particles in a Nematic. *Mol. Cryst. Liq. Cryst.* **1996**, *288*, 175–180.

(13) Poulin, P.; Stark, H.; Lubensky, T. C.; Weitz, D. A. Novel Colloidal Interactions in Anisotropic Fluids. *Science* **1997**, *275*, 1770–1773.

(14) Poulin, P.; Weitz, D. A. Inverted and Multiple Nematic Emulsions. *Phys. Rev. E* **1998**, *57*, 626–637.

(15) Lubensky, T. C.; Pettey, D.; Currier, N.; Stark, H. Topological Defects and Interactions in Nematic Emulsions. *Phys. Rev. E* **1998**, *57*, 610–625.

(16) Loudet, J.-C.; Barois, P.; Poulin, P. Colloidal Ordering from Phase Separation in a Liquid-Crystalline Continuous Phase. *Nature* **2000**, *407*, 611–613.

(17) Yamamoto, J.; Tanaka, H. Transparent Nematic Phase in a Liquid-Crystal-Based Microemulsion. *Nature* **2001**, *409*, 321–325.

(18) Yada, M.; Yamamoto, J.; Yokoyama, H. Direct Observation of Anisotropic Interparticle Forces in Nematic Colloids with Optical Tweezers. *Phys. Rev. Lett.* **2004**, *92*, 185501.

(19) Yamamoto, T.; Yokoyama, H.; Tabe, Y. Light-Induced Transformation of Defect Structures in Photochromic Liquid-Crystal Emulsions. *Mol. Cryst. Liq. Cryst.* **2007**, *478*, 211–219.

(20) Nazarenko, V. G.; Nych, A. B.; Lev, B. I. Crystal Structure in Nematic Emulsion. *Phys. Rev. Lett.* **2001**, *87*, 075504.

(21) Smalyukh, I. I.; Chernyshuk, S.; Lev, B. I.; Nych, A. B.; Ognysta, U.; Nazarenko, V. G.; Lavrentovich, O. D. Ordered Droplet Structures at the Liquid Crystal Surface and Elastic-Capillary Colloidal Interactions. *Phys. Rev. Lett.* **2004**, *93*, 117801.

(22) Musevic, I.; Skarabot, M.; Tkalec, U.; Ravnik, M.; Zumer, S. Two-Dimensional Nematic Colloidal Crystals Self-Assembled by Topological Defects. *Science* **2006**, *313*, 954–958.

(23) Ravnik, M.; Skarabot, M.; Zumer, S.; Tkalec, U.; Poberaj, I.; Babič, D.; Osterman, N.; Musevic, I. Entangled Nematic Colloidal Dimers and Wires. *Phys. Rev. Lett.* **2007**, *99*, 247801.

(24) Ognysta, U.; Nych, A.; Nazarenko, V.; Musevic, I.; Skarabot, M.; Ravnik, M.; Zumer, S.; Poberaj, I.; Babič, D. 2D Interactions and Binary Crystals of Dipolar and Quadrupolar Nematic Colloids. *Phys. Rev. Lett.* **2008**, *100*, 217803.

(25) Wood, T. A.; Lintuvuori, J. S.; Schofield, A. B.; Marenduzzo, D.; Poon, W. C. K. A Self-Quenched Defect Glass in a Colloid-Nematic Liquid Crystal Composite. *Science* **2011**, *334*, 79–83.

(26) Martinez, A.; Mireles, H. C.; Smalyukh, I. I. Large-Area Optoelastic Manipulation of Colloidal Particles in Liquid Crystals Using Photoresponsive Molecular Surface Monolayers. *Proc. Natl. Acad. Sci.* **2011**, *108*, 20891–20896.

(27) Petrucci, R. H.; Herring, F. G.; Madura, J. D.; Bissonnette, C. *General Chemistry: Principles & Modern Applications*; 10th editi.; Pearson Canada: Toronto, 2011.

(28) Kleman, M.; Lavrentovich, O. D. *Soft Matter Physics - An Introduction*; Springer, 2003.

(29) Hunter, R. J. *Foundations of Colloid Science*; Oxford University Press: New York, 2001.

(30) Robinson, R. A.; Stokes, R. H. *Electrolyte Solutions*; Dover Publications: Mineola, NY, 2002; p. 76.

(31) Hiemenz, P. C.; Rajagopalan, R. *Principles of Colloid and Surface Chemistry*; Marcel Dekker: New York, 1997.

(32) Oswald, P.; Pieranski, P. *Nematic and Cholesteric Liquid Crystals: Concepts and Physical Properties Illustrated by Experiments*; Taylor& Francis: Boca Raton, 2005.

(33) De Gennes, P. G.; Prost, J. *The Physics of Liquid Crystals*; Oxford University Press, 1993.

(34) Burylov, S. V; Raikher, Y. L. Orientation of A Solid Particle Embedded In A Monodomain Nematic Liquid-Crystal. *Phys. Rev. E* **1994**, *50*, 358–367.

(35) Stark, H. Physics of Colloidal Dispersions in Nematic Liquid Crystals. *Phys. Rep.* **2001**, *351*, 387–474.

(36) Terentjev, E. M. Disclination Loops, Standing Alone and Around Solid Particles, In Nematic Liquid-Crystals. *Phys. Rev. E* **1995**, *51*, 1330–1337.

(37) Gu, Y.; Abbott, N. L. Observation of Saturn-Ring Defects around Solid Microspheres in Nematic Liquid Crystals. *Phys. Rev. Lett.* **2000**, *85*, 4719–4722.

(38) Squires, T. M.; Bazant, M. Z. Induced-Charge Electro-Osmosis. *J. Fluid Mech.* **2004**, *509*, 217–252.

(39) Squires, T. M.; Bazant, M. Z. Breaking Symmetries in Induced-Charge Electro-Osmosis and Electrophoresis. *J. Fluid Mech.* **2006**, *560*, 65–101.

(40) Gangwal, S.; Cayre, O.; Bazant, M.; Velev, O. D. Induced-Charge Electrophoresis of Metallodielectric Particles. *Phys. Rev. Lett.* **2008**, *100*, 58302.

(41) Yariv, E. Induced-Charge Electrophoresis of Nonspherical Particles. *Phys. Fluids* **2005**, *17*, 051702.

(42) Lavrentovich, O. D. Transport of Particles in Liquid Crystals. *Soft Matter* **2014**, *10*, 1264–1283.

(43) Lazo, I.; Peng, C.; Xiang, J.; Shiyanovskii, S. V; Lavrentovich, O. D. Liquid Crystal-Enabled Electro-Osmosis through Spatial Charge Separation in Distorted Regions as a Novel Mechanism of Electrokinetics. *Nat. Commun.* **2014**, *5*, 5033.

(44) Lazo, I.; Lavrentovich, O. D. Liquid-Crystal-Enabled Electrophoresis of Spheres in a Nematic Medium with Negative Dielectric Anisotropy. *Philos. Trans. R. Soc. A-mathematical Phys. Eng. Sci.* **2013**, *371*, 20120255.

(45) Dukhin, A. S.; Dukhin, S. S. Aperiodic Capillary Electrophoresis Method Using an Alternating Current Electric Field for Separation of Macromolecules. *Electrophoresis* **2005**, *26*, 2149–2153.

(46) Hernàndez-Navarro, S.; Tierno, P.; Ignés-Mullol, J.; Sagués, F. AC Electrophoresis of Microdroplets in Anisotropic Liquids: Transport, Assembling and Reaction. *Soft Matter* **2013**, *9*, 7999–8004.

(47) Guzowski, J.; Korczyk, P. M.; Jakiela, S.; Garstecki, P. The Structure and Stability of Multiple Micro-Droplets. *Soft Matter* **2012**, *8*, 7269–7278.

CHAPTER 2

EXPERIMENTAL SETUPS AND PROTOCOLS

2.1 Experimental Cells

2.1.1 Basic Components and Construction

The experimental cells used in this thesis to study colloidal dispersions are basically composed of two glass plates separated by thin spacers and glued together. The glass plates can be functionalized with different molecules or materials, depending on the type of experiments performed. I use plate separations ranging from 13µm up to 70µm, which correspond to the thickness of the Mylar spacers placed between the glass plates. The cells are prepared

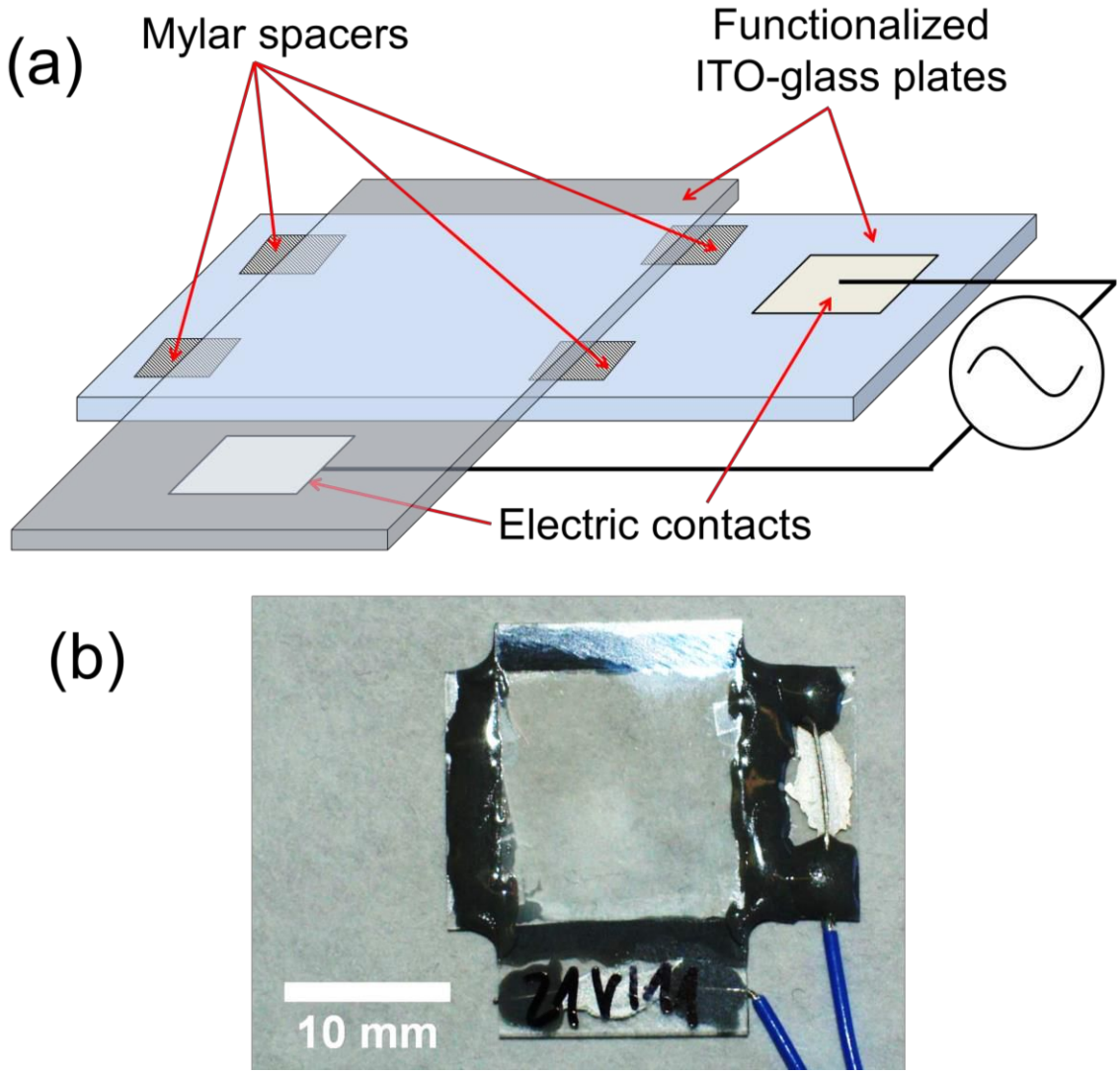

Figure 2.1: (a) Schematic showing the basic parts of the typical experimental cell used in this thesis. (b) Photograph of an experimental cell.

using 0.7mm thick microscope slides of dimensions 15x25mm^2, coated with a thin layer of indium-tin oxide (ITO) with a surface resistivity of 100Ω/sq (VisionTek Systems). The ITO coating is a transparent electrode used to apply an external electric field inside the experimental cells. To assemble the plates, a two-component epoxy glue (3450 Loctite) is employed. When water is used as dispersing medium for the colloidal particles, the cells are sealed by applying petroleum jelly (vaseline) at their borders before gluing, in order to avoid contamination and water evaporation. Colloidal silver is used to make the electric contacts between the wires and the ITO layer. Schematic of the typical cells used during the experiments is showed in figure 2.1.

2.1.2 Surface Functionalization via Self-Assembled Monolayer

Perhaps the simplest way to functionalize the glass plates of the experimental cells, widely used in applications involving colloidal dispersions in water as well as in liquid crystals, is to deposit a self-assembled monolayer (SAM) on the surface of the plates. Self-assembled monolayers are ordered molecular assemblies formed by the binding of active surfactant molecules on a solid surface. [1,2]

As shown in figure 2.2, the procedure basically involves dipping the substrate plates in a solution containing the designated molecule for a certain amount of time, from seconds to hours depending on the molecules and the

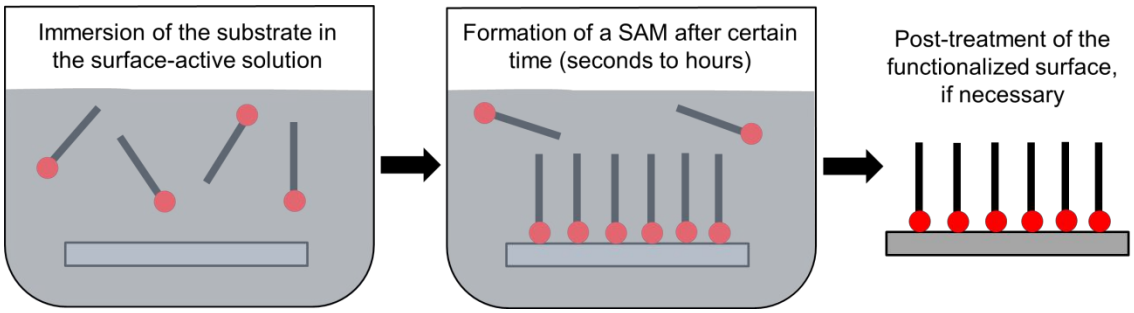

Figure 2.2: Scheme of the procedure for the formation of a SAM on a substrate.

substrates. To functionalize the plates, two chemical compounds are used in this thesis:

a) Poly(sodium 4-styrenesulfonate)

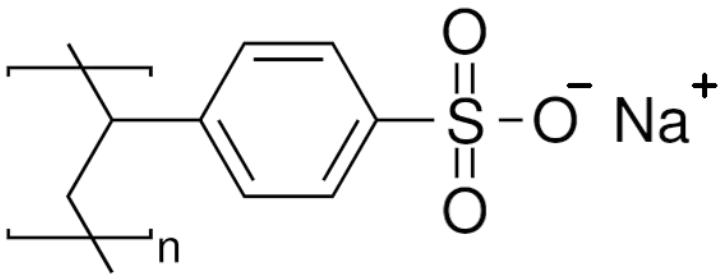

Figure 2.3: Chemical formula for Poly(sodium 4-styrenesulfonate).

This poly-electrolyte is a negatively-charged polymer which is used in the experiments presented in chapter 3 to avoid irreversible sticking of the particles to the ITO layer. To obtain a self-assembled monolayer of this molecule, the plates are previously cleaned by sonication with a 1% Micro-90 surfactant solution (Sigma-Aldrich). Then the slides are submerged for 20 minutes in an aqueous solution composed of 5mg/mL of poly(sodium 4-styrenesulfonate) (Sigma-Aldrich) in 0.5M NaCl. Afterwards the plates are rinsed with Milli-Q water (18.2MΩ · cm, Millipore Gradient A-10) and dried

under a stream of nitrogen.[3,4] Functionalized plates are stored in a desiccator until used (typically within a few days).

b) Dimethyloctadecyl[3-(Trimethoxysilyl)propyl]ammonium chloride

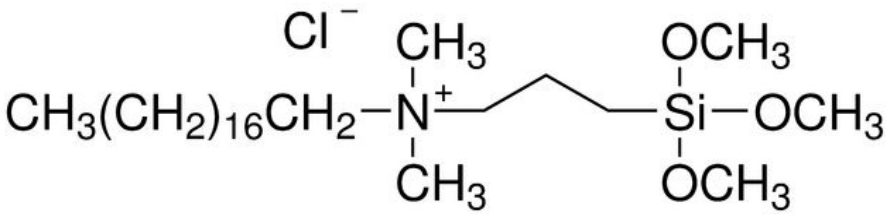

Figure 2.4: Chemical formula for DMOAP.

This molecule, also known as DMOAP, is used to obtain homeotropic (perpendicular) anchoring conditions at the surface of the cells filled with the nematic liquid crystal (NLC cells). The protocol to create a SAM of this compound is the following:[5] first, the ITO-glass plates are cleaned with a 1% Micro-90 solution (Sigma-Aldrich). Then these plates are immersed in a Milli-Q water solution containing 0.5%(v/v) of DMOAP (72%, Aldrich Chemistry) for 20 minutes. Afterwards, the slides are gently rinsed with running water, since strong washing can lead to molecular desorption. Next they are dried under a stream of nitrogen and subsequently baked at 130ºC for 90 minutes, to chemically bind the silane group onto the ITO surface. Finally, they are stored in a desiccator until used (typically within a week).

2.1.3 Spin-coating

Spin-coating is a process used to deposit thin uniform films containing resins or polymers on flat substrates. The basic operation consists on first depositing a spin-coating solution on the substrate (figure 2.5a), and then the substrate is rotated at high speed in order to spread the solution homogeneously by the centrifugal force, while the excess of fluid is ejected (figure 2.5b). This results in a thin film, its thickness depending on the velocity and time of the spinning (figure 2.5c). Afterwards, the substrate is baked to evaporate the solvent as well as to anneal the resin or polymer onto the surface (figure 2.5d). In the experiments described in this thesis, the used spinner is a Chemat Technologies Spin-Coater KW-4A.

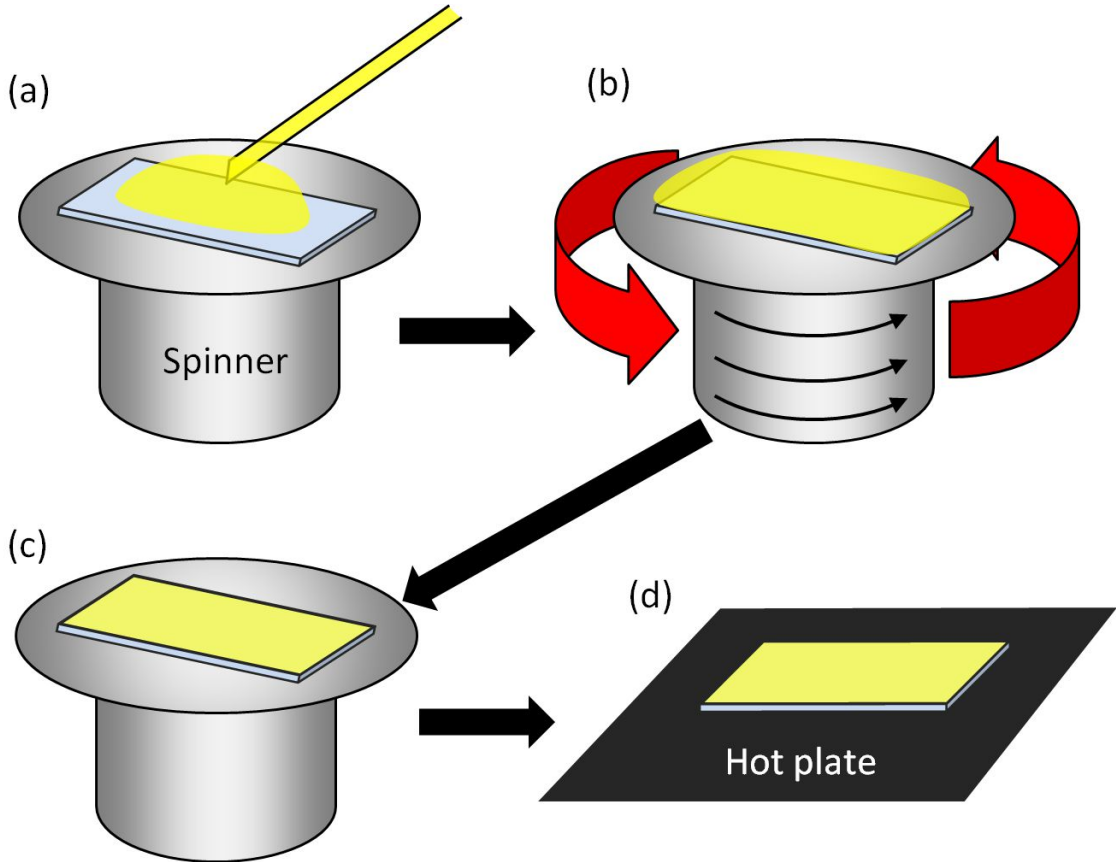

Figure 2.5: Scheme of the spin-coating process. (a) Deposition of the resin or polymer solution onto the surface. (b) Rotation at high velocity to create a thin film (c). (d) Baking to evaporate the solvent and anneal the resin or polymer onto the surface.

Next, I explain how to obtain planar directional or homeotropic anchoring of the NLC by using this technique.

Planar Directional Alignment

This type of alignment is obtained by first spin-coating the solution onto the ITO-glass surface, and afterwards rubbing this surface with a velvet cloth. In this thesis, two different solutions were used: Polyimide PI-2555 resin (HD-Microsystems), or an aqueous solution (5%w/v) of polyvinyl alcohol (PVA, 88% hydrolyzed, MW 88000, Acros Organics). The ITO-glass plates are first cleaned by sonication with a 1% Micro-90 solution (Sigma-Aldrich), and are subsequently dried at 120ºC for 20min.

For the polyimide resin, the protocol consists in first depositing a thin film via spin-coating at 750rpm for 3s, and then at 2000rpm for 60s. Afterwards the plates are pre-baked at 100ºC for 1min to evaporate the solvent, and then baked at 300ºC for 2 hours. On the other hand, for the PVA solution the plates are spinned at 750rpm for 3s, and then at 2000rpm for 30s. The plates are subsequently baked at 150ºC for 1 hour. In both cases, after the thermal treatment, the coated plates are rubbed with a velvet cloth 5-10 times along the same direction. While the chemical nature of these coatings induces planar anchoring of the NLC, the rubbing creates microgrooves that define a preferred in-plane direction for alignment.

Homeotropic alignment

To induce homeotropic alignment I use a solution containing the resin Nissan 0626 dispersed at 5%(w/w) in solvent 26 (both from Nissan Chemical Industries). In this case, the ITO-glass plates are first made hydrophilic in order to be completely wetted by the resin. The cleaning process is performed by submerging the plates for 1 hour at 70ºC in an alkaline piranha solution

composed by 5:1:1 $H_2O+H_2O_2(30\%)+NH_3(25\%)$.[6] Afterwards, they are rinsed with running Milli-Q water (18.2MΩ · cm, Millipore Gradient A-10) and dried at 120ºC for 20min. After this process, the resin is spin-coated at 2000rpm for 9s, and later the plates are pre-baked at 100ºC for 1min, and finally baked at 170ºC for 45min.

2.1.4 Realization of Photosensitive Plates

Photosensitive ITO-glass plates are prepared in a two-step process that results in the formation of an azosilane monolayer, as shown in figure 2.6. The first step is to coat the plates with a self-assembled monolayer of (3-aminopropyl)triethoxysilane (APTES, Sigma-Aldrich):[7] The plates are first cleaned by sonication in a 1% aqueous solution of Micro-90 (Sigma-Aldrich) for 2 minutes, rinsed with Milli-Q water (18.2MΩ · cm, Millipore Gradient A-10), and dried at 120ºC for 20 minutes. Afterwards they are immersed in a 10%(v/v) solution of APTES in toluene (> 99.9%, Scharlau) at 60ºC for 100 minutes, and subsequently rinsed with toluene, methanol (99.9%, Scharlau) and Milli-Q water. The plates are then stored in a desiccator for 2h before further use. This first step renders the ITO surface both hydrophilic and chemically reactive for the subsequent functionalization step.

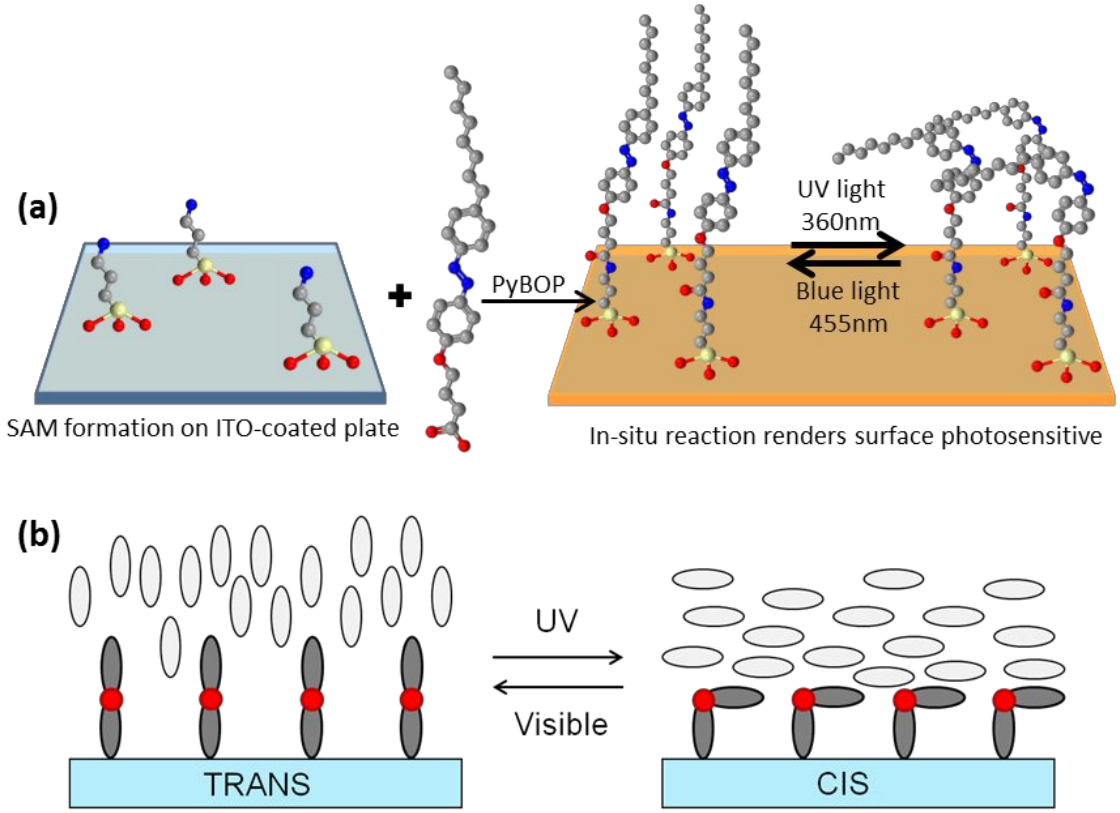

Figure 2.6: (a) Two-step functionalization method to prepare photo-sensitive glass substrates using APTES and 8Az3COOH. (b) *trans-cis* isomerization induced via UV-visible irradiation, and its effect on the anchoring of the nematic liquid crystal (NLC), where white ellipses represent NLC molecules.

The second step consists on the formation of the amide bond between the amino terminal group of APTES and the azobenzene compound 4-octyl-4'-(carboxy-3-propyloxy)azobenzene (8Az3COOH). The latter was supplied by Prof. Joan-Antoni Farrera's group, Organic Chemistry Department, University of Barcelona.[8] The synthesis of the azosilane usually consists in dissolving 0.6mg of 8Az3COOH, and 1.0mg of the coupling agent pyBOP (>97%, Fluka) each in 1mL of dimethylformamide (DMF, peptide synthesis grade, Scharlau).[9] The functionalized APTES-ITO-glass plates are then rinsed in DMF and submerged in a petri-dish with DMF under stirring. Afterwards, the solutions of 8Az3COOH and pyBOP are successively added into the petri-dish, and finally 6µL of N-ethyldiisopropylamine (DIPEA, >98%, Fluka) are added to

obtain the necessary alkaline environment. The petri-dish is then kept in the dark and under stirring overnight. When the reaction is over, the plates are rinsed first with DMF and then slightly with Milli-Q water, and afterwards dried with a stream of N_2. Overexposure to water must be avoided because it degrades the synthesized azosilane. Finally, the functionalized plates are stored in the dark under Argon atmosphere until used (typically within a week).

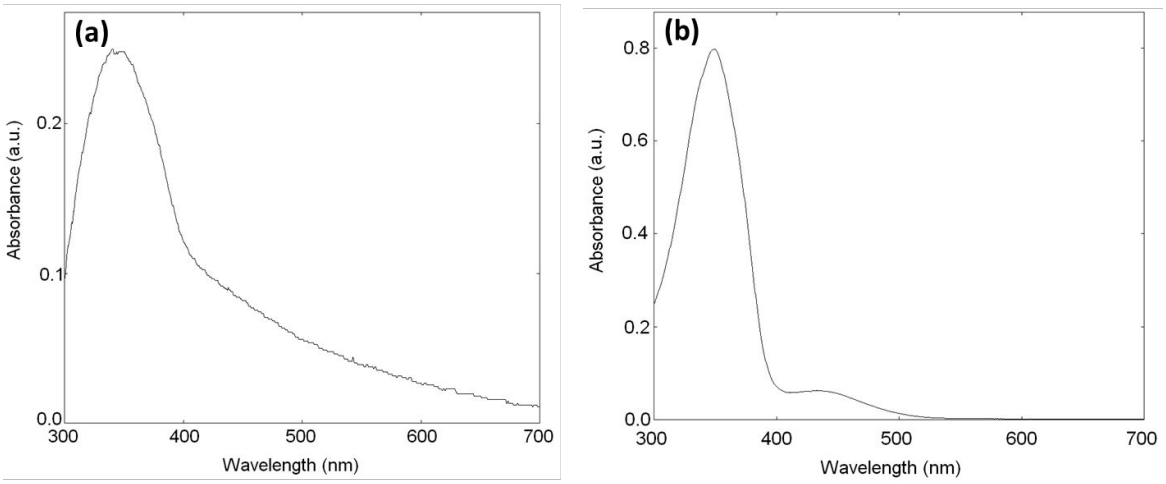

Figure 2.7: UV-visible spectrum of the azosilane-coated plate (a) and of an ethanolic solution of 8Az3COOH (b).

A UV-Visible spectrophotometer (Shimadzu UV-1603) is used in order to verify the photosensitivity of the azosilane monolayer (figure 2.7a). As a reference, I also measure the spectrum of a solution of the azobenzene derivative in ethanol (figure 2.7b). In the latter case, the spectrum displays a peak located at λ = 350nm, corresponding to the transition from *trans* to *cis* isomer. The small peak at λ = 430nm matches with the reverse transition from the less abundant *cis* to *trans* isomers. Both spectra present similar features: the spectrum of the azosilane monolayer exhibits a peak at λ = 350nm, while the small peak is hidden under the tail of the largest peak. These results demonstrate the presence of the azosilane on the surface of the plate.

In order to measure the relaxation time for the *cis* to *trans* isomerization of the azosilane film, I have monitored a NLC cell transmittance under crossed polarizers. The typical half-life time for this relaxation is obtained by measuring the decreasing transmittance of red light (it does not affect the *cis* to *trans* relaxation) following irradiation with UV light. Immediately after the irradiation, the amount of transmitted light is maximum, since the NLC director has planar configuration while in contact with the *cis* azosilane molecules. As shown in figure 2.8, the transmitted light decreases gradually until extinction. That is, when all *cis* azosilane molecules assume the *trans* configuration, the NLC molecules become perpendicular to the cell plates. In this situation, the light is not transmitted through the sample.

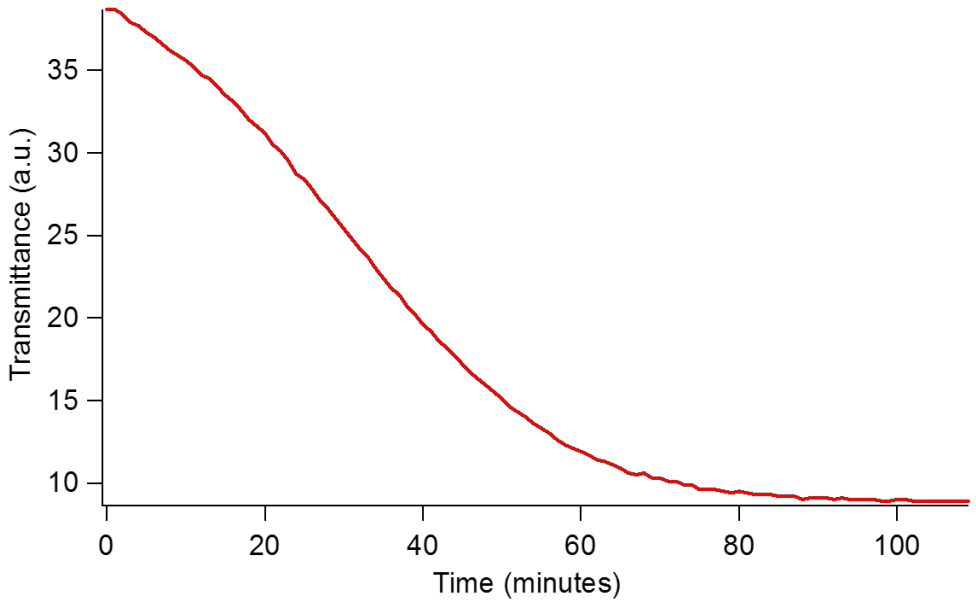

Figure 2.8: Relaxation of an irradiated *cis*-azosilane spot. This measurement is performed in the dark at 25ºC. The estimated half-life is 33min.

2.1.5 Cell Thickness Measurements

The accurate thickness of an empty cell can be measured using a UV-Vis spectrophotometer. Once inserted in the spectrophotometer, the internal surfaces of the cell partially reflect the trespassing light and generate a pattern of fringes due to constructive and destructive interferences, as seen in figure 2.9. The separation of the two plates can be extracted from the interference spectrum using the equation:[10]

$$d = \frac{M}{2n} \cdot \frac{\lambda_1 \cdot \lambda_2}{|\lambda_1 - \lambda_2|}$$

Where d is the cell thickness, n is the index of refraction of the medium between the plates (for an empty cell this is the index of refraction of air, $n \approx 1$), and M is the number of peaks in the interference pattern between the wavelengths λ_1 and λ_2. This technique is only useful for cell thicknesses thinner than 30µm, as the interference pattern for thicker cells cannot be resolved.

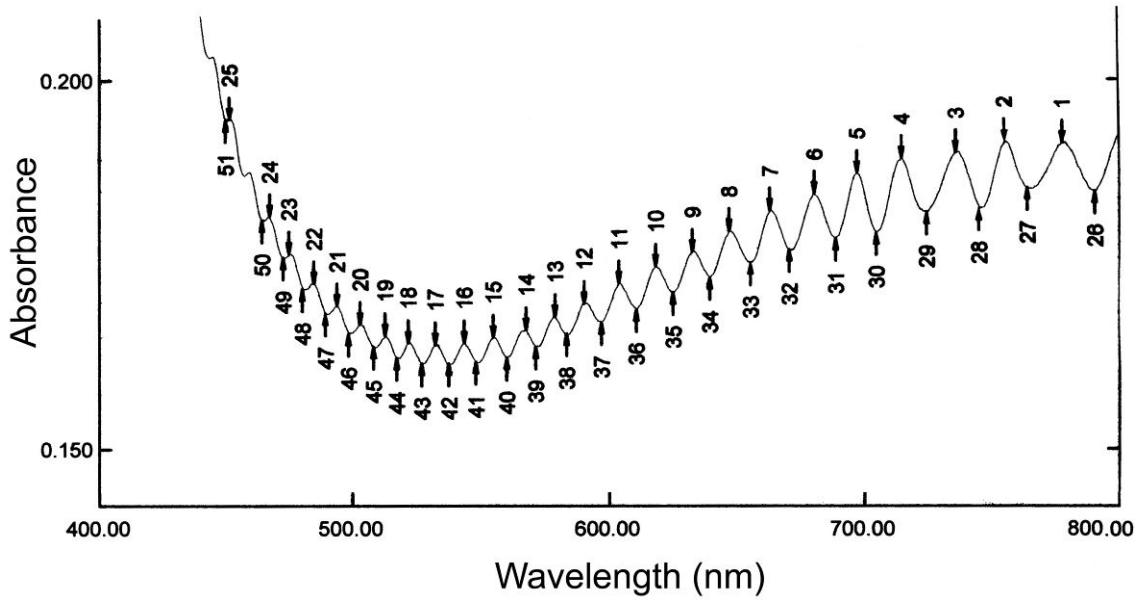

Figure 2.9: Example of an interference pattern spectrum for a 13µm-thick experimental cell.

2.2 Particle Dispersions

2.2.1 Cleaning Procedure

In most of the experiments presented in this thesis, commercial colloidal particles are cleaned by redispersing them in different fluid media. The cleaning process ensures the elimination of surfactants or other chemicals present in the original stock solution, as well as the suspension of the particles in the different media needed for further treatments.

This cleaning process is performed by first centrifuging the aqueous particle dispersion, so the particles, which have higher density than water, sediment at the bottom of the flask. The centrifugation time is usually between 5-20 minutes at 2500rpm, but it highly depends on the centrifugation speed and the difference of densities between the particles and the solvent. Once the particles are all settled down, a syringe is used to extract the supernatant liquid. Then the flask is refilled with Milli-Q water, and is ultrasonicated for 20 minutes. This process is repeated at least 3 times to ensure complete cleaning of the particles.

Once the particles are cleaned and dispersed in water, they are ready to be used, or they can be then functionalized or re-shaped, as explained in the following section.

2.2.2 Functionalization and Elongation of Colloidal Particles

Photosensitive particles

In chapter 5 the photosensitive particles are prepared from commercial amino-functionalized silica particles. The process is similar to that explained in section 2.1.4 for ITO-glass plates. The acid groups of the azoderivative molecules (8Az3COOH) are bound by an amide bond formation, to the amino terminal groups grafted at the surface of the particles.

First the amino silica particles, previously cleaned and suspended in Milli-Q water, are re-dispersed in dimethylformamide (DMF), the solvent medium where the chemical reaction takes place. The centrifugation and redispersion process is repeated 7 times, in order to eliminate any residual water in the solvent, as it would inhibit the chemical reaction. Once the particles are cleaned and suspended in DMF, the reaction is performed following the second step of the procedure explained in section 2.1.4, adding the 8Az3COOH solution, the PyBOP solution and the DIPEA. Afterwards, particles are cleaned with pure DMF by centrifugation and redispersion. The cleaning process is repeated 3 times, and in the last step the solvent is extracted and the remaining DMF is evaporated in a desiccator. Finally the photosensitive particles are stored at 1-5ºC under Argon atmosphere until used.

Homeotropic particles

Homeotropic alignment on the surface of silica particles is obtained by bounding DMOAP molecules onto their surface, by means of a self-assembled monolayer, as explained in section 2.1.2 for ITO-glass plates.

Plain silica particles are first cleaned and then suspended in a 0.5%(v/v) of DMOAP (72%, Aldrich Chemistry) solution for 30 minutes, under ultrasonication. Afterwards, the suspension is cleaned 3 times with Milli-Q water. The solvent is subsequently extracted and the particles are heated at

130ºC for 90 minutes. Finally the dry particles are stored at 1-5ºC under Argon atmosphere until used (typically within a month).

Ellipsoidal paramagnetic particles

Paramagnetic ellipsoids are obtained by mechanically stretching a thin film seeded with the original paramagnetic polystyrene spherical particles.[11]

First of all, a commercial dispersion of spherical uncrosslinked (i.e. susceptible to be dissolved in apolar solvents) polystyrene paramagnetic particles (Compel, Bangs Laboratories, 12μm in diameter) is dispersed in a solution containing 7%(w/w) polyvinyl alcohol (PVA, 88% hydrolyzed, MW 88000, Acros Organics) and 2%(w/w) of glycerol (99.5%, Sigma-Aldrich) in Milli-Q water. Afterwards, the mixture is let to dry for 2-3 days in a flat container to obtain a particle-seeded PVA film. Once the film is completely dry, an area of ~5x10cm^2 is cut and mounted in a custom-built stretching support, which is later submerged for 3 hours in toluene (99.9% Scharlau), in order to liquate the polystyrene paramagnetic particles without dissolving the PVA film. At this point, the film is stretched slowly (1cm/10min) while immersed in toluene, until approximately doubling its length. In this way, the liquated particles adopt the ellipsoidal shape of the stretched hollows. Afterwards, the stretched film is immersed in isopropyl alcohol (99.5% Sigma-Aldrich) for 12 hours in order to re-solidify the polystyrene particles in their new ellipsoidal shape. The PVA film, now containing ellipsoidal paramagnetic particles, is dissolved in a mixture of isopropyl alcohol-water 30:70. Subsequent sedimentations (instead of centrifugation, the use of a magnet facilitates a quick sedimentation of the paramagnetic particles) and redispersions permit to have the ellipsoidal paramagnetic particles dispersed in water, ready to use.

2.2.3 Colloidal Dispersions in Liquid Crystal

The nematic liquid crystal (NLC) used as suspending medium during this thesis is the commercial mixture MLC-7029 (Merk) which features nematic phase from below room temperature to 95ºC. It has a dielectric anisotropy $\Delta\varepsilon(\text{at 1kHz}) = \varepsilon_{\parallel} - \varepsilon_{\perp} = 3.6 - 7.2 = -3.6$, and its splay and bend constants are K_1 = 16.1pN and K_3 = 15.0pN, respectively. In the experimental cells used in this thesis, the electric Frederiks transition occurs at a threshold voltage of 2.2V, as calculated in chapter 1 section 1.3.3. The NLC cells are filled by capillary action with freshly prepared dispersions in the nematic phase (at room temperature) to avoid particle degradation. There are different ways to disperse microscopic particles in liquid crystals, each method having different advantages and disadvantages.

One technique to disperse microparticles is to initially re-suspend the particles in methanol by centrifugation and redispersion until reaching a final solid content of 0.5-1%, without any residual water. Then a small amount (5-20μL) of the ultrasonicated methanol dispersion is carefully deposited on top of a small volume (7-15μL) of the NLC, and the methanol is let to evaporate in a desiccator. Afterwards, the NLC dispersion is agitated in a vortex and finally ultrasonicated for 5-10 minutes. This technique is very useful for stable particles, i.e. particles non-soluble in neither methanol nor NLC, and is used in chapter 6 to disperse pear-shape polystyrene particles.

In an alternative method, a small amount of the solid particle in the form of a dry powder (less than a milligram) is placed on top of a glass slide. Then the NLC (7-15μL) is deposited onto the particles with a micropipette, and subsequently the mixture is gently stirred with the same micropipette. This technique is used in chapter 4 with polystyrene spherical and ellipsoidal paramagnetic particles, since these particles are uncrosslinked and thus soluble in apolar solvents, and the ultrasonication step can induce their dissolution in NLC. This method is also useful with functionalized silica particles to avoid degradation of the grafted molecules when in contact with methanol. In this

latter case the NLC dispersion can be ultrasonicated without degradation of the grafted molecules.

2.3 Experimental Setups

2.3.1 Optical Polarization Microscope

In this thesis, experimental cells are observed through an optical polarization microscope Eclipse 50iPol (Nikon). As shown in figure 2.10, two polarizers are placed in the optical path, before and after the sample (they are called polarizer and analyzer, respectively). To observe liquid crystals, these polarizers are normally crossed, i.e. their polarization orientation is rotated 90º from one to the other.

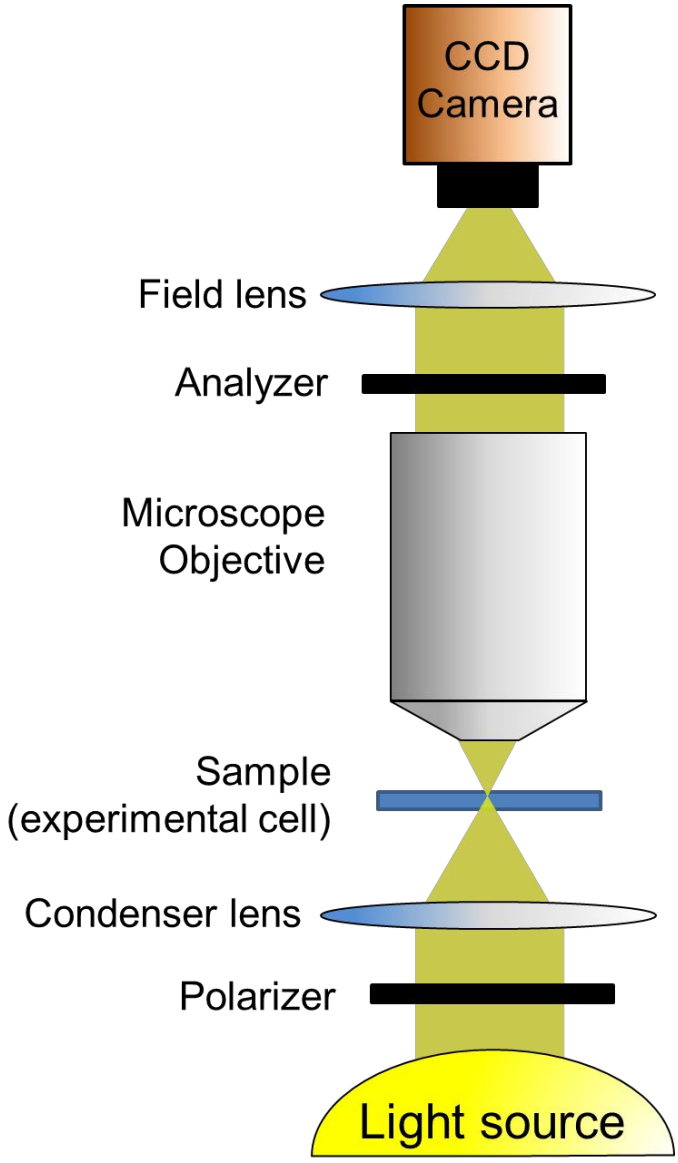

Figure 2.10: Schematics of an optical polarization microscope.

2.3.2 Helmholtz Coils

The Helmholtz coils consist in a couple of solenoids placed at a distance equal to their inner radius in order to generate uniform magnetic fields in the zone between the two coils, as shown in figure 2.11a.[12] When current passes through the wires, a magnetic field is induced parallel to the coiling axis, and its magnitude depends on the intensity of the current, the number of loops, the radius and the separation of the coils.

In order to apply uniform magnetic fields onto the experimental cells, a Helmholtz coils-like setup is mounted on the stage of the optical polarization microscope in a custom-made arrangement, as shown in figure 2.11c. In this setup the separation of the two coils is larger than their inner radius, due to geometrical constrains. This arrangement allows rotating the aluminum stage where the coils stand, which in turn rotates the magnetic field in-plane orientation with respect to the fixed cell. The generated magnetic field is calibrated in terms of the intensity of the applied current, and the coil separation.

To enhance the magnetic field applied onto the cells, a custom-shaped Permendur bar (Goodfellow) can be inserted along the coils axes. Permendur is a cobalt/iron alloy that focuses the magnetic field generated by the Helmholtz coils-like setup. In this way one can apply a stronger though more localized uniform magnetic field onto the experimental cells, without increasing the intensity of current, thus avoiding coil overheating by Joule effect.[13] As shown in figure 2.11b, this permendur bar is also employed with a single coil to generate strong and localized magnetic field gradients that can be used to translate paramagnetic particles, as shown in chapter 3, section 3.3.2.

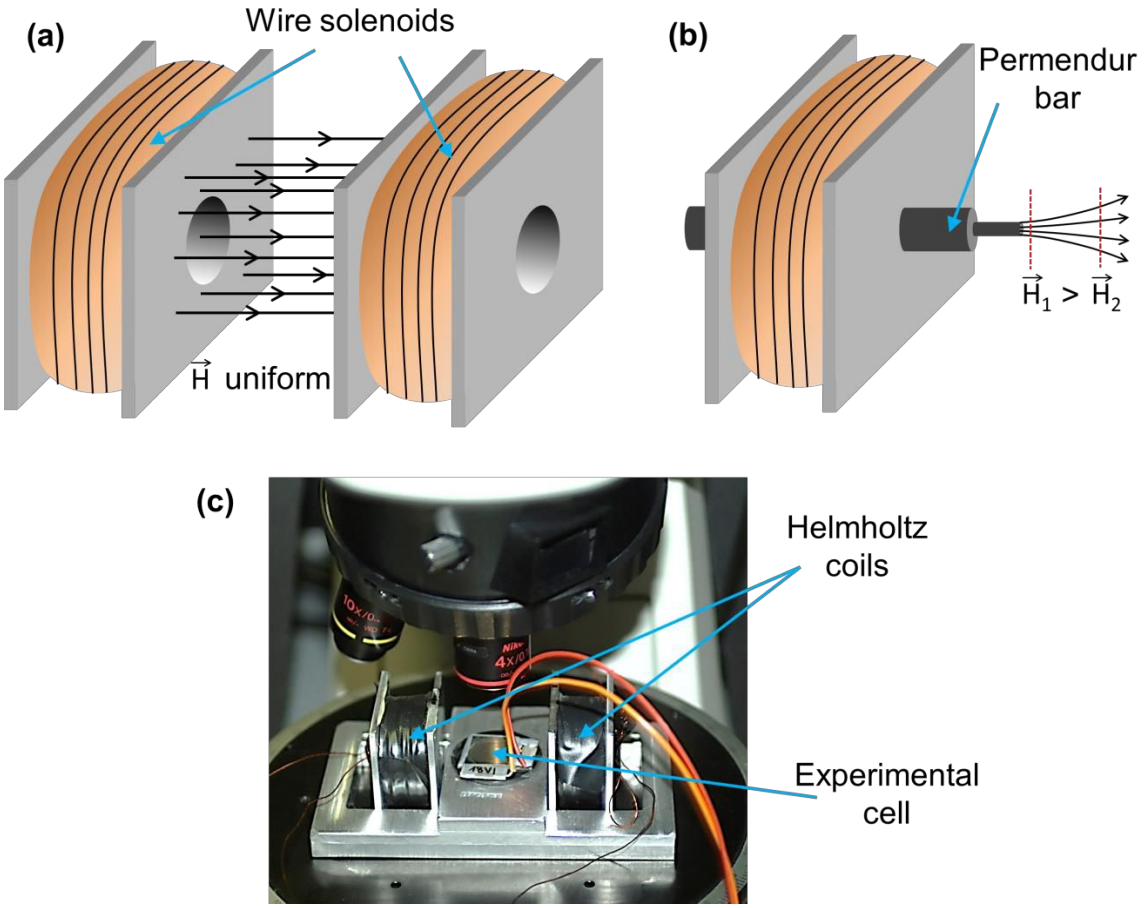

Figure 2.11: (a) Schematics of the Helmholtz coils, where a uniform magnetic field, represented by black arrows, is generated between the coils. (b) Schematics of a single coil with the Permendur bar inserted along its main axis. The magnetic field lines are focused at the tip of the Permendur bar. (c) Photograph of the Helmholtz coil setup mounted on the optical polarization microscope.

2.3.3 Irradiation Setup

Irradiation of the samples at wavelengths of 365nm and 455nm is performed by means of a custom-built LED epi-illumination setup (Thorlabs, Inc.) integrated in the optical polarization microscope, as shown in figure 2.12. Irradiation is performed by using the optical components of the microscope, such as its objectives. A red filter placed in front of the light source (645nm ± 50nm) is used in all observations and measurements to avoid perturbation of the azosilane coating. Optionally, the standard polarizer and analyzer of the microscope can be used to obtain images between crossed polarizers, as they do

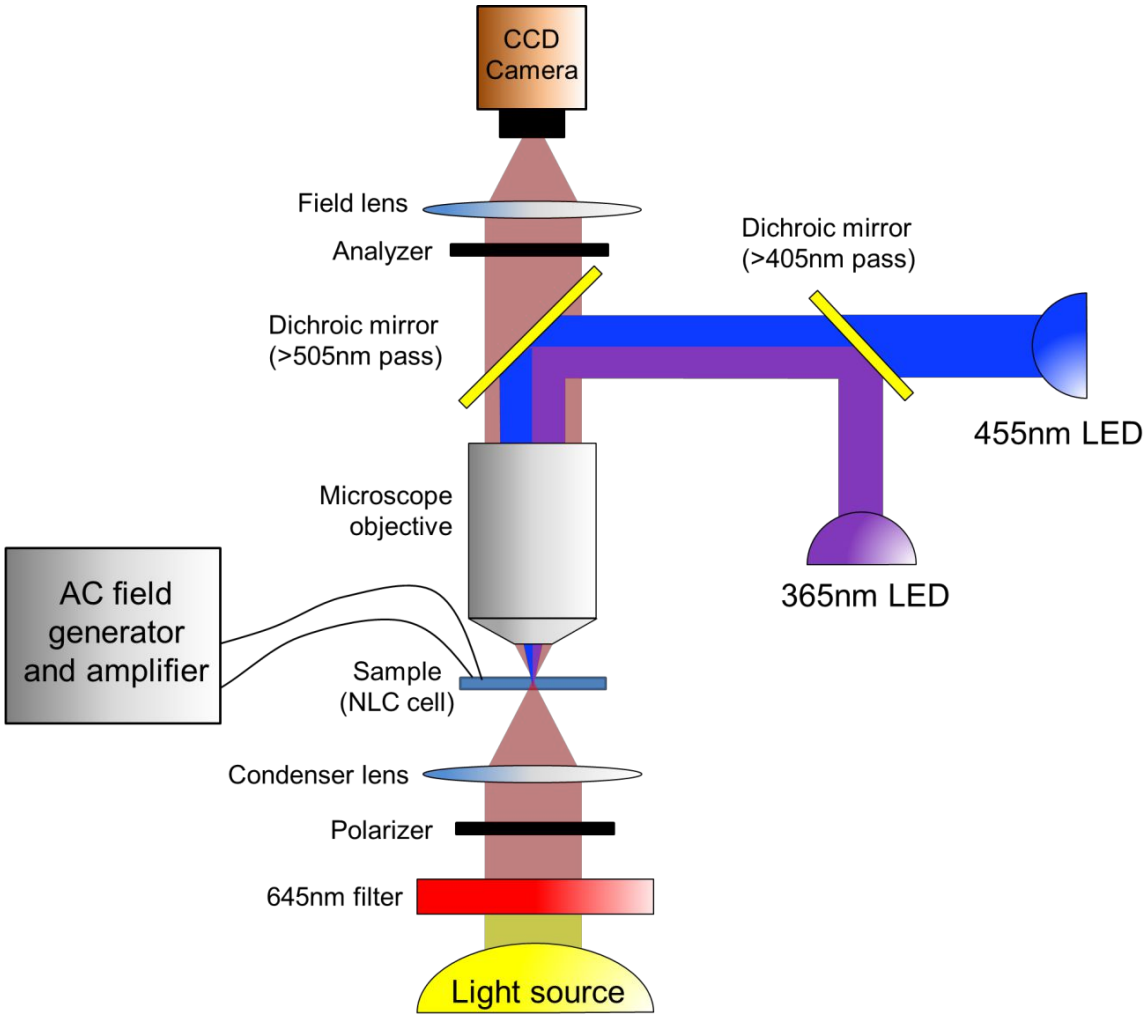

Figure 2.12: Schematics of the custom-built LED irradiation setup mounted on the optical polarization microscope.

not interfere with the irradiation path. A long-pass dichroic mirror (cutoff wavelength 405nm) is used to combine the blue (455nm) and the UV (365nm) light along the same optical path. A second long-pass dichroic mirror (cutoff wavelength 505nm) prevents excitation light from reaching the camera. The microscope objective is used to focus the irradiation light onto the experimental cell, where the azoderivative molecules grafted onto particles or glass plates photo-isomerize. For the photosensitive cells studied in chapter 6, tracks are imprinted on the NLC cells by simply moving the sample stage while the UV irradiation light is on.

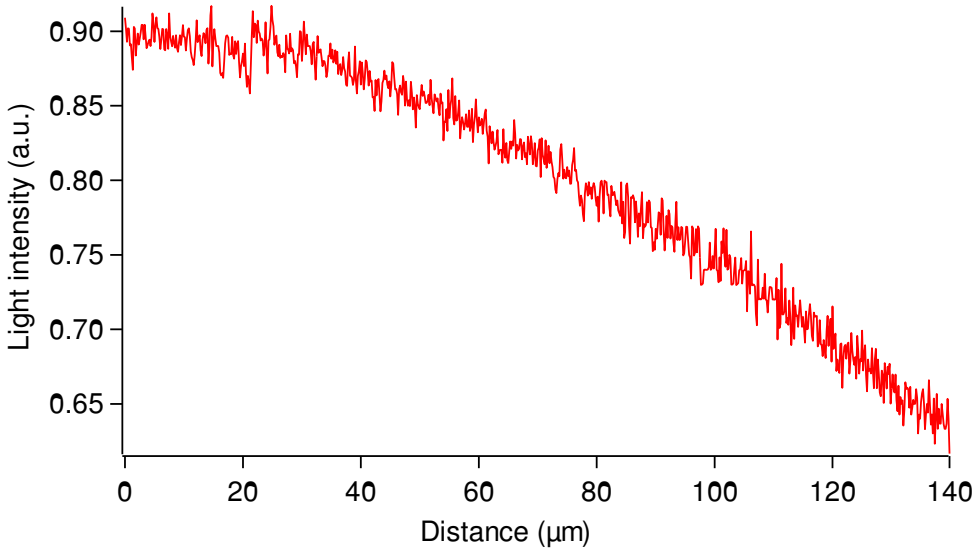

Figure 2.13: Intensity profile of the irradiation as a function of the distance from the center of the spot.

The light power density is measured using an optical power meter S120A Optical Power Meter System (Thorlabs Inc.). The power density supplied by the blue light LED at wavelength 455nm is measured at the output of the objective, i.e. after the light has passed all the microscope lenses and dichroic mirrors, just before reaching the experimental cell. The typical light power density used in experiments is ~1W/cm^2. Using the previous measurement and the LEDs characteristics provided by the manufacturer, the power density supplied by

the 365nm LED can be estimated as ~0.1W/cm^2. The illuminated spot size is in the sub-millimeter range, and the irradiation is not uniform. The light intensity profile has rotational symmetry and it decreases with the distance to the center of the spot, as shown in figure 2.13. As a consequence, *trans* to *cis* isomerization starts at the spot center and propagates outwards, which originates the reported radial orientation of the planar NLC anchoring (see chapter 6, section 6.3.1).

2.4 References

(1) Ulman, A. *An Introduction to Ultrathin Organic Films*; Academic Press: Boston, 1991.

(2) Ulman, A. Formation and Structure of Self-Assembled Monolayers. *Chem. Rev.* **1996**, *96*, 1533–1554.

(3) Tierno, P.; Reddy, S. V; Johansen, T. H.; Fischer, T. M. Rupture and Healing of One-Dimensional Chains in a Parametric Magnetic Ratchet Potential. *Phys. Rev. E* **2007**, *75*, 41404.

(4) Helseth, L. E.; Wen, H. Z.; Fischer, T. M.; Johansen, T. H. Adsorption and Diffusion in a One-Dimensional Potential Well. *Phys. Rev. E* **2003**, *68*, 11402.

(5) Lelidis, I.; Oedman, C. Influence of Substrate Nature and Growth Conditions on the Morphology of Thin DMOAP Films. *Liq. Cryst.* **2003**, *30*, 643–649.

(6) Markovich, I.; Mandler, D. Preparation and Characterization of Octadecylsilane Monolayers on Indium–tin Oxide (ITO) Surfaces. *J. Electroanal. Chem.* **2001**, *500*, 453–460.

(7) Howarter, J. A.; Youngblood, J. P. Optimization of Silica Silanization by 3-Aminopropyltriethoxysilane. *Langmuir* **2006**, *22*, 11142–11147.

(8) Crusats, J.; Albalat, R.; Claret, J.; Ignés-Mullol, J.; Sagués, F. Influence of Temperature and Composition on the Mesoscopic Textures of Azobenzene Langmuir Monolayers. *Langmuir* **2004**, *20*, 8668–8674.

(9) Albericio, F.; Bofill, J. M.; El-Faham, A.; Kates, S. A. Use of Onium Salt-Based Coupling Reagents in Peptide Synthesis1. *J. Org. Chem.* **1998**, *63*, 9678–9683.

(10) Miller, D. S.; Carlton, R. J.; Mushenheim, P. C.; Abbott, N. L. Introduction to Optical Methods for Characterizing Liquid Crystals at Interfaces. *Langmuir* **2013**, *29*, 3154–3169.

(11) Tierno, P.; Albalat, R.; Sagués, F. Autonomously Moving Catalytic Microellipsoids Dynamically Guided by External Magnetic Fields. *SMALL* **2010**, *6*, 1749–1752.

(12) http://physicsx.pr.erau.edu/HelmholtzCoils/.

(13) Halliday, D.; Resnick, R. *Physics (part 2)*; John Wiley & Sons, Inc., 1960; p. 695.

CHAPTER 3

STUDY OF ELECTRODYNAMICALLY INDUCED COLLOIDAL AGGREGATES

3.1 Introduction

The often encountered tendency of dispersed colloidal particles to spontaneously aggregate can be tailored for certain applications. In particular, the controlled assembly of colloidal particles under external fields, like electric, magnetic or optic, has the potential towards the fast realization of field reversible structures characterized by the regular arrangement of individual components via tunable interactions. Such structures can find use in several applications ranging from the construction of photonic band gap materials,[1] to diffraction gratings,[2] biosensors,[3] or even microchip reactors.[4] From a fundamental point of view, studying the ordering of colloidal building blocks in presence of external fields can improve our understanding of more general phenomena occurring in dissipative non-equilibrium systems with thermal noise.[5] In particular, a vast although still under continuous development field of research regards the use of electric fields to aggregate colloidal particles into compact structures like clusters,[6] crystals,[7] or more complex dynamic phases, including stripes,[8] worm-like chains,[9] vortex rings[10] and traveling waves.[11]

After the pioneering work by Richetti et al.,[12] it is well established that latex spheres dispersed in water and confined between two electrodes are capable to form ordered aggregates when subjected to an alternating (AC) electric field. Since then, the organization of isotropic colloids under AC or DC fields has been the subject of several experimental and theoretical studies prompted mainly by the richness of encountered phenomena and the wide range of parameters which can be tuned to control the particle ordering.[13–17] For example, beside the applied field (strength, frequency) and the material used (particle size, density, dispersing medium), an important role is also played by geometrical factors like proximity of the particles to the electrodes, or distance between the electrodes and their geometries.[18] While isotropic particles have been the main focus of such investigations, only few and recent works have focused on the use of anisotropic colloids and how the particle shape could

affect the aggregation process. These works include the use of ellipsoids,[19] rod-like particles,[20] and dumbbells[21] under AC fields.

Shape anisotropy plays an important role in many systems at the microscale. For example, it can increase the random packing of hard spheres,[22] or be used to assemble novel photonic band gap materials.[23] Shape anisotropy is also important in dipolar systems such as paramagnetic ellipsoids,[24] since in the presence of an applied magnetic field it gives a preferred direction for the induced moment and thus opens up the possibility to apply torques[25,26] and measure viscosities in biological films.[27] Moreover, it has been shown that under planar AC fields, i.e. *parallel* to the plane of the particles, ellipsoids assemble into chains at an angle with respect to the applied field,[28] or can be used to prepare thin films with peculiar mechanical properties.[19]

In this chapter I studied the assembly behavior of confined isotropic particles and also anisometric pear-shaped particles (from now on, "pears") when subjected to external AC electric fields, in order to unveil the role of anisotropy in the ordering process. In contrast to previous studies reported in literature, in this study both types of particles are subjected to external AC fields applied *perpendicular* to the particle plane. For the range of amplitudes used and at low frequencies (f < 2.5kHz), the external field generates an electrohydrodynamic flow which brings together the Brownian particles giving rise to an effective attractive interaction which nucleates compact clusters. In contrast, at higher frequencies, repulsive dipolar interactions dominate, and the particles stay dispersed into a liquid–like phase. While both types of behaviors are observed for the isotropic and anisometric colloids, the latter tend to form much smaller clusters with elongated shape, and show faster kinetics in the aggregation process.

In the second part of this chapter I also covered the interaction of aggregates of isotropic particles with magnetic inclusions in order to measure the cohesion force between the particles that form the clusters. This is first attempted by using two repelling magnetic probe beads embedded in a cluster,

which are expected to break the cluster due to repulsive dipolar interaction above a threshold magnetic field. As an alternative approach, I also studied the possibility to dismantle clusters by making individual paramagnetic beads and longer aggregates collide against these clusters.

3.2 Experimental Procedures

The experimental cell is schematically depicted in figure 3.1(a), and is prepared as explained in chapter 2, section 2.1.2. For this setup the cells have a cell gap thickness of 14.6±1.0μm. They are also completely sealed with grease and epoxy glue in order to avoid evaporation of water.

As colloidal particles, polystyrene spherical particles (Invitrogen) with diameter 2.8μm (figure 3.1b), and anisometric polystyrene particles (Magsphere) with pear shape (that is, composed of two connected spherical lobes with different size) and having 3x2μm^2 (figure 3.1c) are used. Paramagnetic polystyrene beads of different size (Compel, Bangs Laboratories, 6μm in diameter; and Dynabeads, Invitrogen, 2.8μm in diameter), are also used during the measurement of the cohesion force of the clusters. All particles are cleaned as explained in chapter 2, section 2.2.1 to eliminate traces of surfactants present in the original commercial solutions, and used in concentrations ranging from 1-7% (w/w).

Sinusoidal AC electric fields are applied to the experimental cells by using a function generator (ISO-TECH IFA 730) monitored by an oscilloscope (Agilent Technologies DSO-X 2002A). The range of amplitudes used vary from 2.8V to 11.2V peak to peak which correspond, respectively, to 0.19V/μm and 0.77V/μm, while the applied range of frequencies go from 1kHz up to 20kHz. The colloids are observed with an optical microscope (Nikon Eclipse 50iPol). A custom-built Helmholtz coils setup mounted in the microscope is used in order to apply the magnetic field gradients which control the paramagnetic probe beads. A more detailed explanation of the experimental system can be found in chapter 2, section 2.3.2. Images are captured with an AVT Marlin F-131C CMOS camera controlled with the software AVT SmartView 1.10.2, and are then treated and analyzed using the software packages ImageJ, IgorPro and Matlab. A Field Emission Scanning Electron Microscope S.E.M. (HITACHI model 4100) is used to observe the particle morphology.

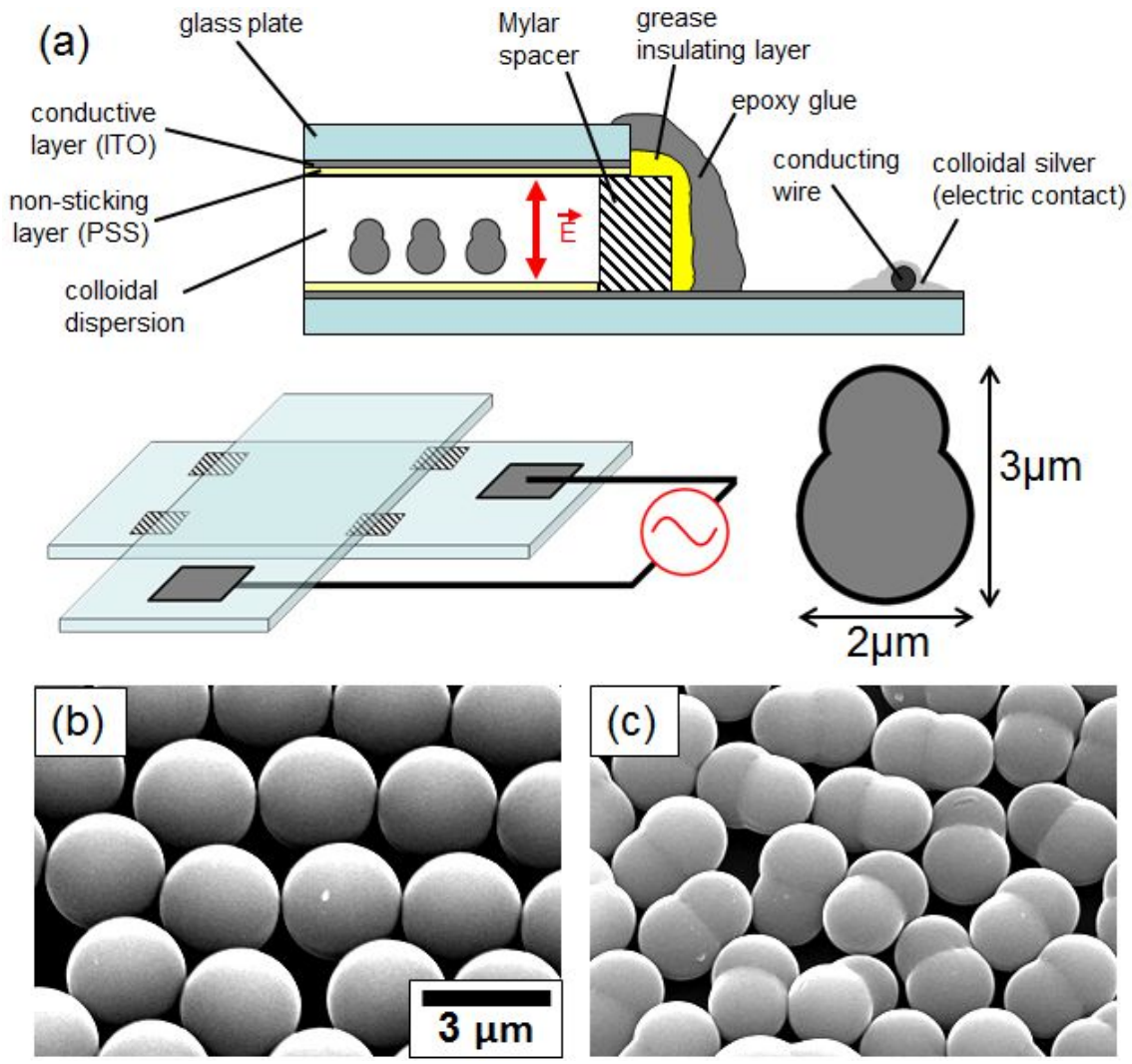

Figure 3.1: (a) Schematics showing the experimental setup used to apply the AC electric fields to the colloidal suspensions. (b) Scanning electron microscopy images of the spherical particles with diameter 2.8µm, and (c) of the pear particles with axial lengths 3x2µm^2.

3.3 Results and Discussion

3.3.1 Assembly of Non-magnetic colloids

In this study, I have decided to test and compare colloids made of the same type of material (polystyrene), and thus the same polarizability, and within the same size range to exclude other effects related to different density, electric susceptibility or chemical compositions of the employed particles. The behavior of the spherical particles is described in the voltage/frequency plane, where these particles form various structures after the application of the external electric field, as shown in the phase diagrams in figures 3.2 and 3.3. The isotropic particles assemble into compact clusters at low frequencies, i.e. from 1kHz to 2.5kHz (*clusters* region), while they stay separated at higher frequencies, i.e. from 2.5kHz up to 8kHz (*repulsive* region). To avoid unwanted effects related with electrolysis of water, the applied frequency is not decreased below 1kHz. At frequencies higher than 8kHz, one observes that some particles assemble into repulsive vertical columns (oriented parallel to the field), containing two-three colloids (*columns* region). In all experiments the system is let to reach stationary assemblies (waiting for more than 5 min), characterized by the formation of static arrangements which did not change with time, even after several hours of continuous exposure to the field. Moreover, all the reported structures are reversible, since switching off the field releases the particles from their positions due to thermal motion.

The collective behavior of particles in the presence of the AC field can be understood by considering the competition between attractive and repulsive interactions generated, respectively, by convective electrohydrodynamic (EHD) flows in the surrounding fluids, and induced electric dipoles in the particles. As explained in the seminal work by Trau et al.,[29] and by Sides,[30,31] the attractive interactions are of hydrodynamic nature and result from the distortion by the particles of the density of charges (ions) accumulated near the electrodes (see chapter 1 section 1.4.1). These works have been later extended by the same and other authors[32–36] to include concepts from electrochemistry and colloidal

science to explain this phenomenon.[37] The EHD flow decreases at higher frequencies since, as previously reported,[38] the free charge density near the electrodes reduces with increasing frequency. Repulsive interactions on the other hand are of dipolar nature, since the applied electric field polarizes the particles and their double layer, inducing in each particle an electric dipole pointing along the field direction (see chapter 1 section 1.2.2). In the geometry of figure 3.1a, the induced dipoles are repulsive, since they are perpendicular to the particle separation distance. At high frequencies, the EHD effect decreases, and repulsive interactions become dominant. At even higher frequencies, where EHD flow vanishes, dipolar interactions tend to assemble nearby particles into columns in order to further increase their lateral separation.

The general features observed for the isotropic particles (figure 3.2), that is, formation of clusters at low frequencies and repulsive liquid-like phases at higher frequencies, are also evidenced for the pears (figure 3.3). However, the corresponding phase diagram is richer, since the particle anisotropy introduces a further degree of complexity in the ordering process. In particular, at parity of electric field strength and frequency, one can observe that the pears aggregate into clusters with typical size smaller than in the case of spheres and characterized by a more elongated shape, as shown in the bottom images of figure 3.3. Inside the clusters, pears are parallel to the supporting plane, and their orientation within the packed structures is clearly visible via optical microscopy. Increasing the frequency, the repulsive interactions start to dominate, and the pears tend to align standing up with the field, while some of them remain parallel to the plane. Both situations are distinguished in the phase diagram of figure 3.3 by denoting them RV (i.e., repulsive particles aligning vertically) and RP (i.e., repulsive particles aligning parallel to the plane), while RP/RV denotes situations with an equal probability to find both types of alignments.

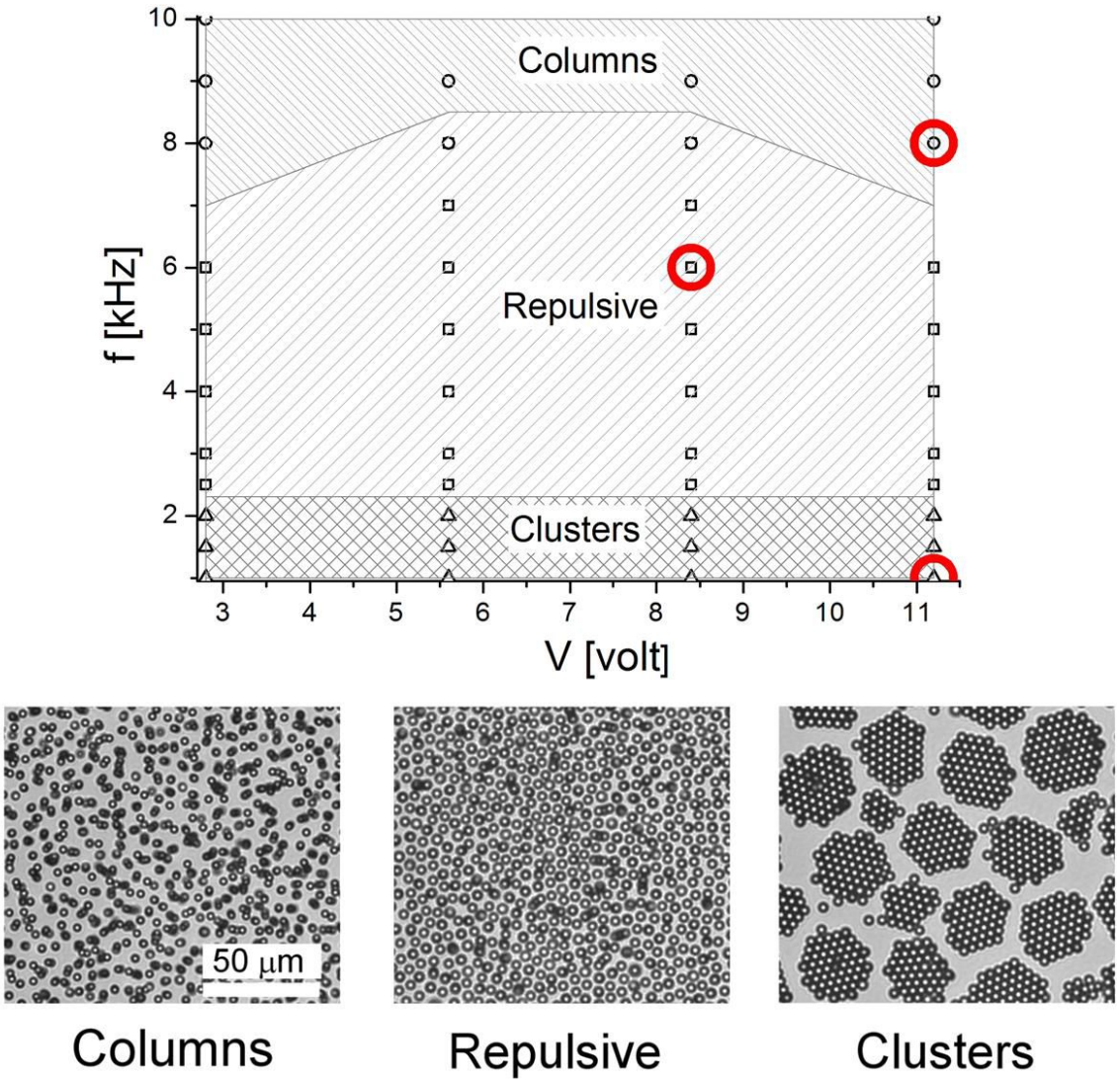

Figure 3.2: Phase diagram in the (frequency/voltage) plane showing the various assemblies observed for the spherical particles. Representative images are shown in the underlying row (8kHz - 11.2V, 6kHz - 8.4V, 1kHz - 11.2V, respectively). Video 3.1 in the Additional Multimedia Content shows the clustering of spherical particles.

It is worth mentioning that if one decreases the thickness of the experimental cell to be in the order of the diameter of the particles, the EHD flow cannot be formed, and so there does not appear a cluster phase. On the contrary, at this thin cell thickness the repulsive phase expands at the all studied electric field conditions.

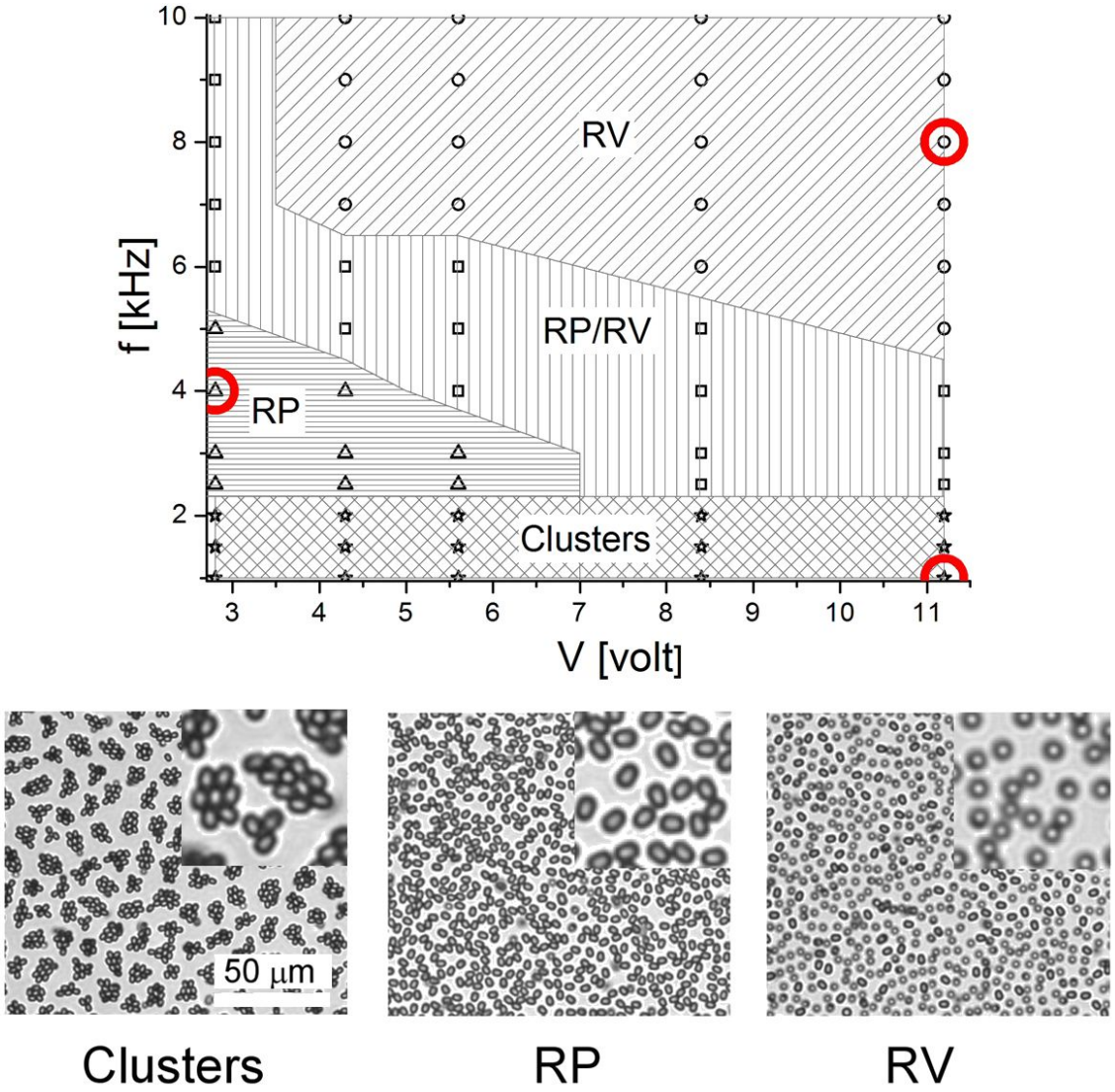

Figure 3.3: Phase diagram in the (frequency/voltage) plane showing the various assemblies observed for the pears. Representative images are shown in the underlying row (1kH - 11.2V, 4kHz - 2.8V, 8kHz - 11.2V, respectively). The insets show an enlargement in order to distinguish between particle orientations. Video 3.2 in the Additional Multimedia Content shows the clustering of pear particles.

In order to quantify the effect of particle anisotropy in the observed structures, one can extract the position of the particles (r_i) via standard particle tracking[39] and measure the pair correlation function $g(r)$ (see Appendix A.3 for a definition), which quantifies the static translational order of the aggregates. Figure 3.4a shows $g(r)$ in two different locations of the phase diagram, namely, in the *repulsive* region (bottom) and in the *clusters* region (top) of the two

diagrams of figures 3.2 and 3.3. In the *repulsive* region, $g(r)$ shows a fast decay (exponential-like) which reflects the poor translational order of the structures, and both types of particles form a liquid-like phase with average mean distance given by the location of the first peak in $g(r)$, that is, 4μm for the spherical and 4.8μm for the pears. Compared to other dipolar systems[40] where repulsive colloids assembled into crystalline phases, the absence of such an order in this case is due to the lack of a lateral confinement of the particles and the resulting lower density of the system. In contrast, in the cluster phase, the spherical particles show much better positional order, and the corresponding $g(r)$ is characterized by a slower decay (power law-like). This type of order is absent in the pears, since they tend to form more fragmented clusters, with anisometric shape and composed of fewer particles. This tendency is mainly due to the particle shape, which frustrates the growth of large clusters during the nucleation process.

The compactness of the clusters can be quantified by measuring the radius of gyration R_g of the clusters versus the number of particles they contain. Figure 3.4b shows R_g (see Appendix A.2 for a definition) for anisometric colloids assembled into clusters under the application of a field of frequency 1kHz and amplitude 11.2V. The radius of gyration is directly connected to the local fractal dimension d_f as $R_g \sim N^{1/d_f}$ and from the power law fit of figure 3.4b we obtain the value $d_f = 1.7 \pm 0.1$, which is smaller than the value obtained for the spherical particles (maximum compactness), $d_f = 2.0 \pm 0.1$, consistently with the non-compact morphology of clusters of anisometric particles.[41]

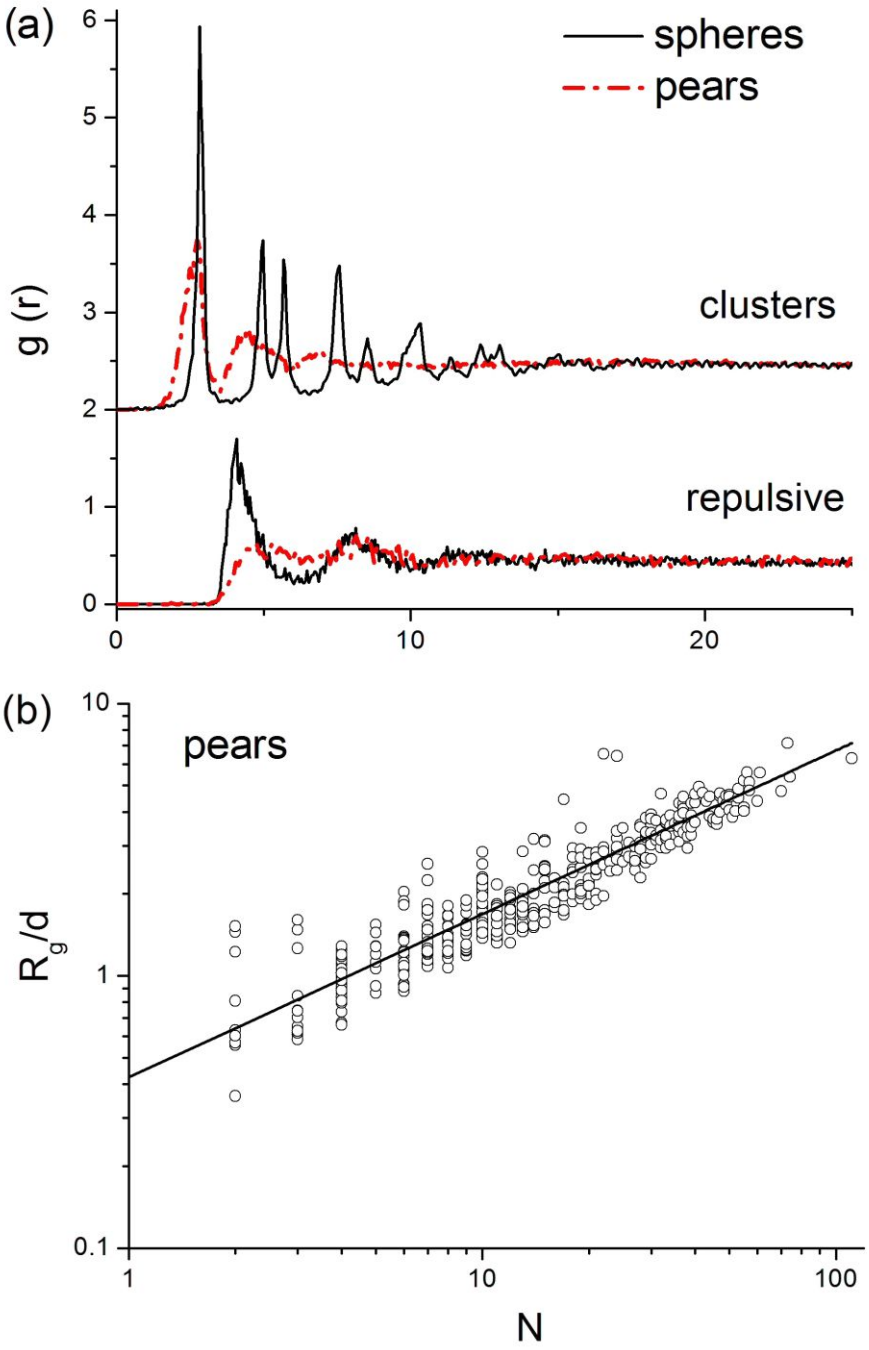

Figure 3.4: (a) Radial distribution functions *g(r)* (a.u.) for spherical particles (continuous black lines) and pears (dotted red lines) in the *repulsive* region (bottom) and in the *cluster* region (top). For clarity, the *g(r)* data in the cluster phases are shifted by 2 units. In the *repulsive* region spherical particles are made repulsive by applying an AC field with frequency 2.5kHz and amplitude 11.2V, and pears are made repulsive by applying 5kHz at 2.8V, while in the *cluster* region the applied field had frequency 1 kHz and amplitude 11.2V for both types of particles. In (b) it is shown the normalized radius of gyration R_g/d versus the number of particles in the clusters *N*, for pears assembled in the cluster phase. Continuous line is a power law fit to extract the fractal dimension $d_f = 1.7 \pm 0.1$.

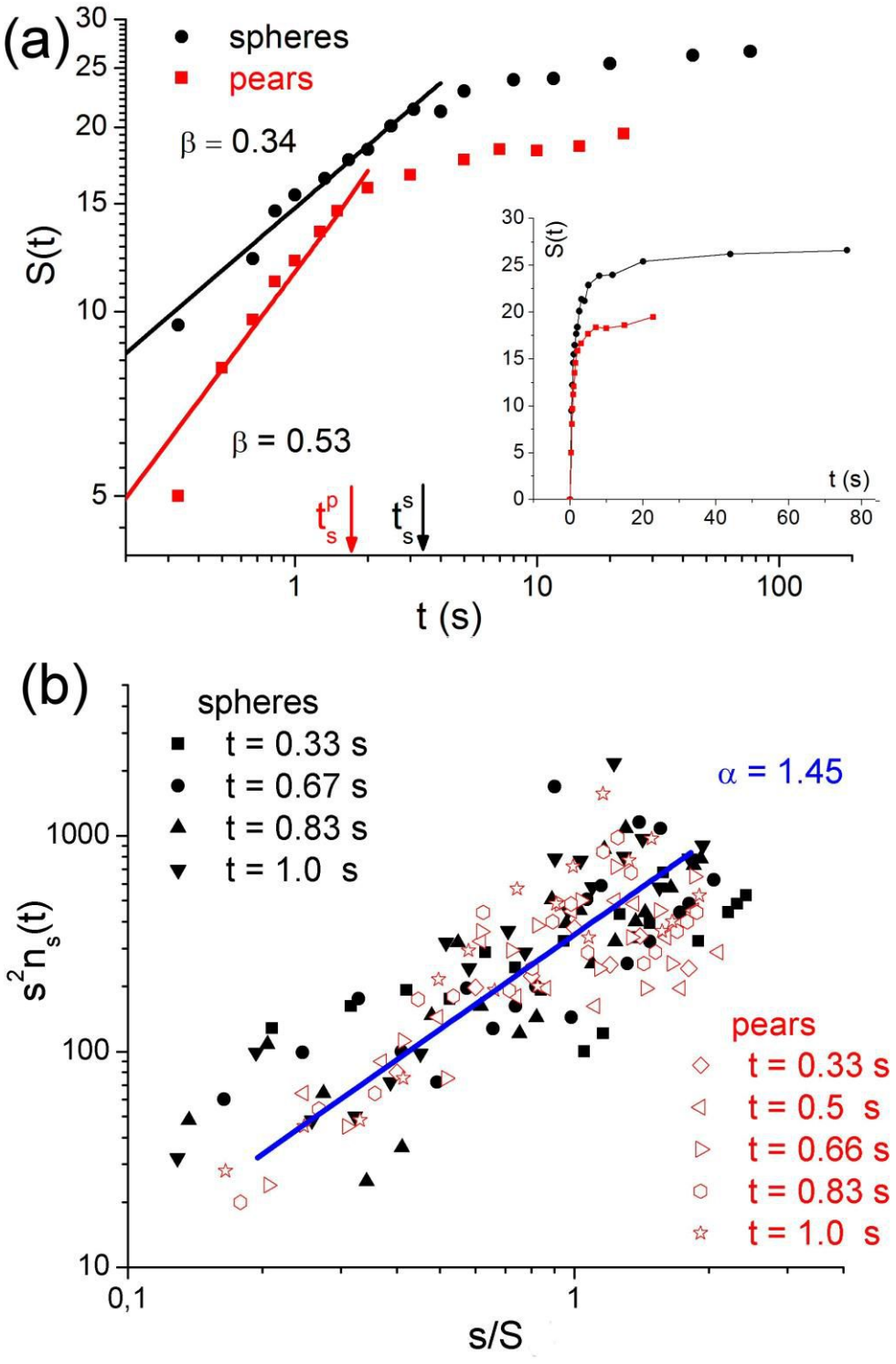

Figure 3.5: (a) Mean cluster size *S(t)* versus time *t* for spheres (black circles) and pears (red squares) subjected to an AC field with frequency 1kHz and amplitude 11.2V. Continuous lines denote power law fits with exponents β = 0.34 for spheres and β = 0.53 for pears calculated before the saturation time $t_s^s = 3.4s$ for spheres and $t_s^p = 1.7s$ for pears. Small inset shows the full data range of *S(t)*. (b) Scaling function $s^2 n_s(t)$ for spherical particles (black solid symbols) and pears (red empty symbols) versus the normalized cluster size *s/S* at different time intervals fitted with a power law with exponent α = 1.45.

The reversible nature of the ordering process enables studying the particle aggregation dynamics in real time by performing experiments where clusters are continuously grown under application of the field, and then disintegrated by switching off the field. In particular, one can monitor the variation of the mean cluster size *S(t)* as a function of time *t*, as shown in figure 3.5a for a suspension of spherical particles (black circles) and pears (red squares) subjected to an AC field with frequency 1kHz and amplitude 11.2V. *S(t)* is calculated using the expression:[42]

$$S(t) = \frac{\sum n_s(t)s^2}{\sum n_s(t)s}$$

where $n_s(t)$ denotes the number of clusters composed of *s* particles. As one can see in figure 3.5a, for both types of particles *S(t)* initially increases until reaching a constant (saturation) value, where individual clusters do not grow further at the expense of their neighbors (there is no coarsening). In both cases, the initial growth of the clusters can be interpreted by using the dynamic scaling approach developed by Vicsek and Family,[42–44] to model diffusion-limited aggregation (DLA), in which the rate of diffusional transport of a particle to another particle or aggregate is slow relative to adhesion on contact. This approach seems to be capable to describe cluster formation by non-equilibrium processes in different contexts[45,46] and, as shown here, it is also suitable to this system. In particular, one can observe a power law behavior for the mean cluster size $S(t) \sim t^{\beta}$, and this expression can be used to fit the experimental points before the onset of saturation, which is reached at times t_s^s for spheres and t_s^p for pears, as shown in figure 3.5a. It is worth noticing that, in contrast to the work of Vicsek and Family,[42] the size of the clusters studied here did not diverge with time, due to the absence of coarsening in this system. The difference between the exponents of the spheres (β = 0.34) and of the pears (β = 0.53) reflects the fact that the aggregation process of the anisometric colloids is faster. Surprisingly, by comparing the diffusion coefficients of the individual particles, $D_s = 0.08 \pm 0.02\,\mu m^2/s$ for spheres and $D_p = 0.14 \pm 0.02\,\mu m^2/s$ for

pears (independently measured via mean square displacements, see Appendix A.1), it emerges that thermal forces are stronger for anisometric colloids, and thus the energy barrier to overcome in order to initiate the clustering process is higher, which is apparently in contrast to the experimental observations. It is possible, however, to explain the fast aggregation behavior of the pears by arguing that, since the pears, when parallel to the plane, have a larger contact area compared to the spherical particles, the distortion of the charge density near the electrode is larger, and so must be the lateral attractive force between the particles. As a consequence, the anisometric shape increases the kinetics of the aggregation process. Nevertheless, the system shows some characteristic behavior independent of the particle shape. Indeed, in the context of the dynamic scaling theory, one can extract the exponent α by taking into account that[47] $s^2 n_s(t) \sim (s/S(t))^{\alpha}$, and the same value for both the spheres and the pears is found, as shown in figure 3.5b, indicating that both type of particles have the same aggregation mechanism.

Another interesting feature of the anisometric colloids is related to their orientation with respect to the applied external field. As mentioned when discussing figure 3.3, the anisometric colloids can align either parallel or perpendicular to the electrode, depending on the field parameters. Parallel alignment has been observed during clustering process, since in this way the area covered by the particles above the electrode is maximized, while perpendicular alignment without clustering has been observed at high frequencies, when dipolar interactions dominate. In figure 3.6 the orientation dynamics of an ensemble of pears is followed by counting the number of particles parallel to the electrode N_p, with respect to the total number of particles N_T. In particular, these particles are first aligned perpendicular to the plane (*repulsive* region) with a high frequency external field (20kHz, 11.2V), and then secondly the field is decreased to 1kHz keeping constant the amplitude (*clusters* region). The transition from one orientation to the other is quite fast (~1s), as compared to the pears self-diffusion time $t_p = R^2/D_p \sim 64s$, the latter measured with respect to the particle long axis. From the behavior of N_p/N_T, it

is clear that this transition is rather smooth: initially few pears orient planar to the plane, and other pears keep attaching to them and getting also planar oriented, until all pears are planar oriented in compact clusters, as shown in video 3.3 in the Additional Multimedia Content. This fast switching of orientation, which is solely controlled by the external field, opens up further possibilities to use the anisometric colloidal assemblies into fast devices and switches.

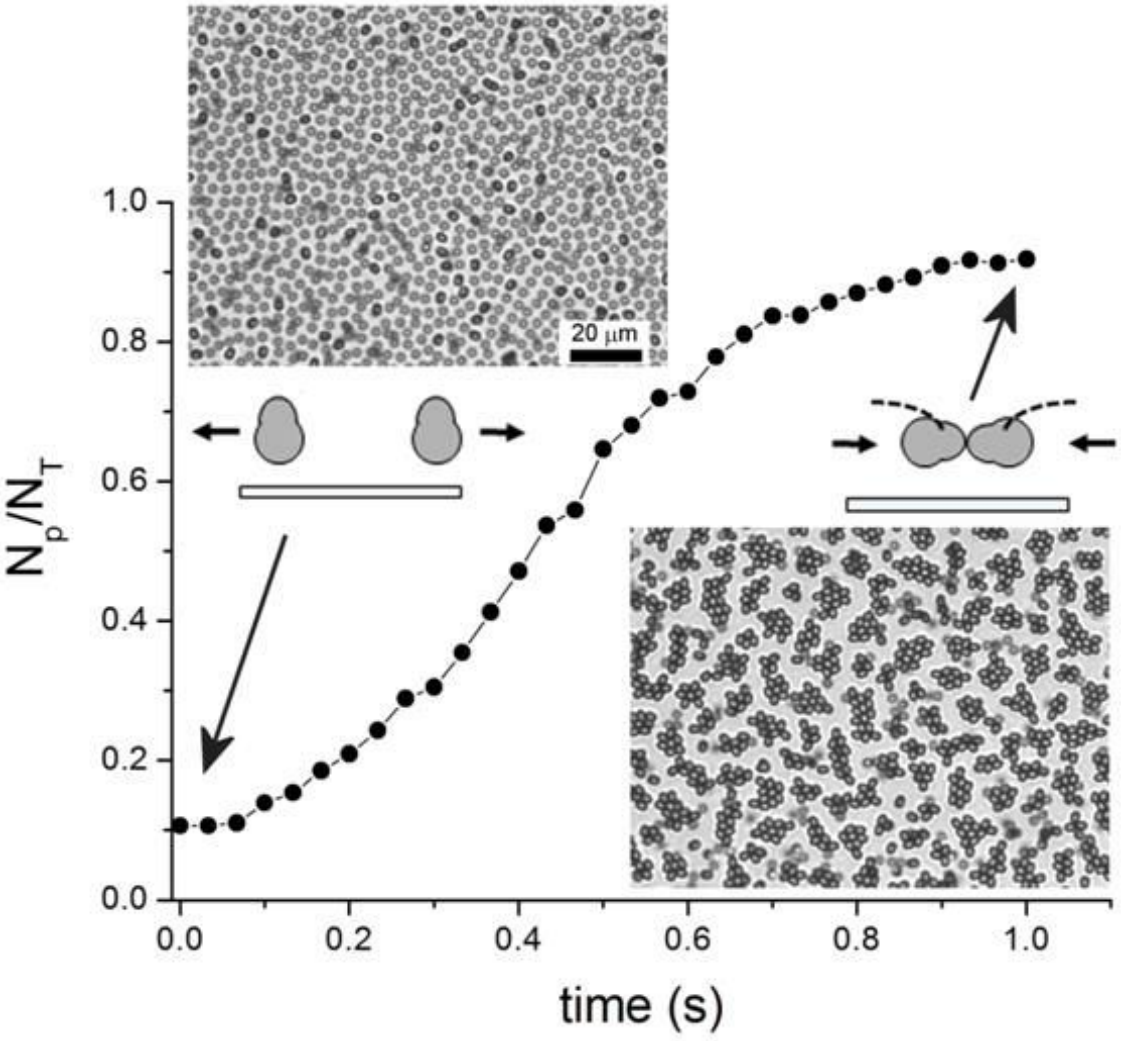

Figure 3.6: Variation of the normalized number of particles parallel to the plane versus time for an ensemble of pears initially aligned normal to the plane by an electric field with amplitude 11.2V and frequency 20KHz that is then switched to 1kHz. Insets show microscope images of the particles in the initial and final state.

3.3.2 Magnetic Colloidal Probes in EHD clusters

In order to measure the cohesion force of the clusters created by convective electrohydrodynamic (EHD) flows, I first tried to study the dismantlement of a cluster of spherical particles by tuning the repulsive interaction between pairs of paramagnetic particles embedded in the clusters.

Paramagnetic colloids can be made attractive or repulsive depending on the orientation of the external applied magnetic field. When a paramagnetic particle is subjected to an external magnetic field ($\vec{H}$), the field induces a magnetic dipolar moment in the particle $\vec{m} = V\chi\vec{H}$ (V is the volume of the particle and χ its magnetic susceptibility) along the same direction. If we consider two similar spherical paramagnetic particles separated by a distance $\vec{r}$ under an external magnetic field, one particle will interact with the other through their induced magnetic dipolar moments. For similar particles, $\overrightarrow{m_1} = \overrightarrow{m_2} = \vec{m}$, and the interaction ($U_d$) between the two particles with a center to center distance *r* is given by:[48]

$$U_d = -\frac{\mu_m m^2}{4\pi r^3}(3(\cos\theta)^2 - 1)$$

where μ_m is the magnetic permeability of the dispersing medium, and θ the angle between the dipoles $\vec{m}$ and the line of separation of particles $\vec{r}$. When θ < 54.7° (called "magic" angle), U_d < 0 and the dipoles attract each other, as shown in figure 3.7a,b where θ = 0°. On the contrary, when θ > 54.7°, U_d > 0 and the particles repel each other, as depicted in figure 3.7c, where θ = 90°.

Taking advantage of these tunable interactions, figure 3.7 proposes a procedure to measure the attractive force between the particles in a cluster due to EHD flows.

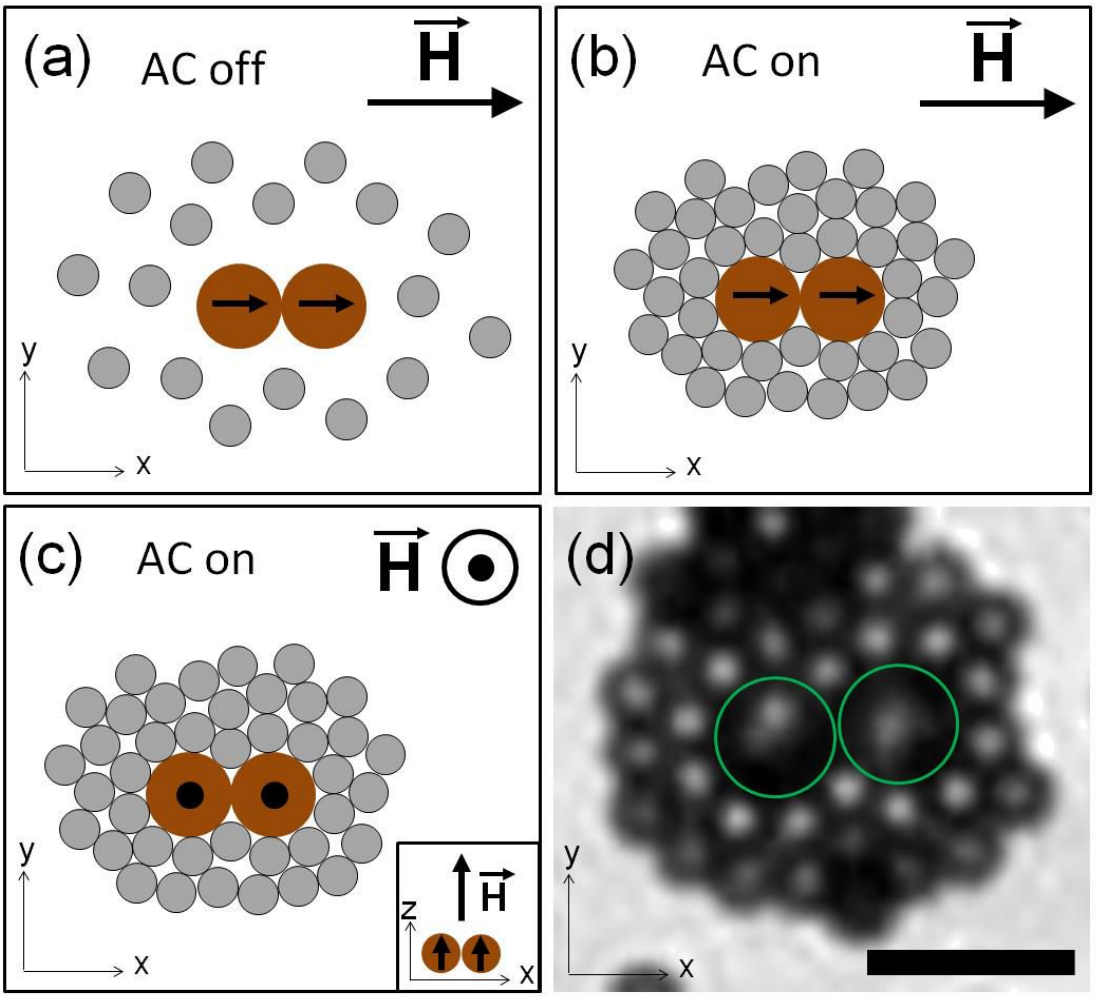

Figure 3.7: (a-c) Scheme of the proposed procedure to measure the strength of a 2D cluster by employing two paramagnetic beads (brown circles) surrounded by polystyrene particles (grey circles). Black arrows in the paramagnetic beads indicate their magnetically induced dipoles (in the *x* axis in (a,b) and in the *z* axis in (c)). Inset in the bottom right corner of panel (c) shows the induced magnetic dipoles in the *z* axis. (d) Shows an experimental image of two paramagnetic beads (5.8µm in diameter, marked by green circles) in the middle of a cluster of smaller polystyrene particles (2.8µm in diameter). Scale bar marks 10µm.

The procedure consists on first mixing a few paramagnetic beads with the spherical polystyrene particles, and filling the experimental cell with this mixture. With a magnetic field applied *parallel* to the plates (in the *x*-*y* plane, for example by placing a magnet lying on top of the cell), one induces dipolar *attractive* interactions between paramagnetic particles which assemble into a doublet (figure 3.7a). Then an electric field (in the *Clusters* region of figure 3.2) is

applied and 2D clusters form around these doublets of paramagnetic colloids (figure 3.7b). Once the clusters are formed, if a magnetic field along the *z* axis is applied, dipolar *repulsive* interactions appear between the two neighboring paramagnetic beads. The strength of the repulsive interaction between the paramagnetic colloids can be increased by increasing the magnitude of the magnetic field (figure 3.7c). When this repulsion reaches a critical value, the cluster should finally break and, through a proper calibration, one should be able to measure the attractive interaction resulting from the EHD flow. Unfortunately, the experimental system in this configuration is only able to apply perpendicular magnetic fields up to ten milliTesla, which are not strong enough to overcome the EHD cohesive force.

As an alternative strategy to measure the cohesion strength of clusters grown by EHD flow, I studied collisions of magnetic particles against 2D clusters. By applying a controlled magnetic field gradient by using Helmholtz coils (see chapter 2, section 2.3.2), one can make individual particles as well as chains or aggregates of paramagnetic beads move at a given speed due to the magnetic gradient $\nabla\vec{H}$ (velocity $\sim \nabla\vec{H}$). It was found that in order to be able to break and go across clusters, the system must meet two basic requirements.

The first requirement is that the electric field applied must be in the cluster region near the transition to a repulsive state (as a way to diminish the cohesive force of the clusters). For these conditions, what it is found is that individual paramagnetic particles cannot pass through clusters, even when the highest possible magnetic gradient is applied. An example can be seen in figure 3.8, where a paramagnetic bead collides with two different small clusters but is unable to cross them. There is only a slight rearrangement of the external particles of the clusters, or the introduction of some defects in the lattice. This leads to the second requirement: to break a cluster it is required to use aggregates instead of individual paramagnetic beads due to the higher force these aggregates can exert. The latter can be formed by incrementing the ratio of paramagnetic beads in the colloidal suspension. At a higher ratio, induced

magnetic dipole interaction assembles particles into chains or elongated aggregates.

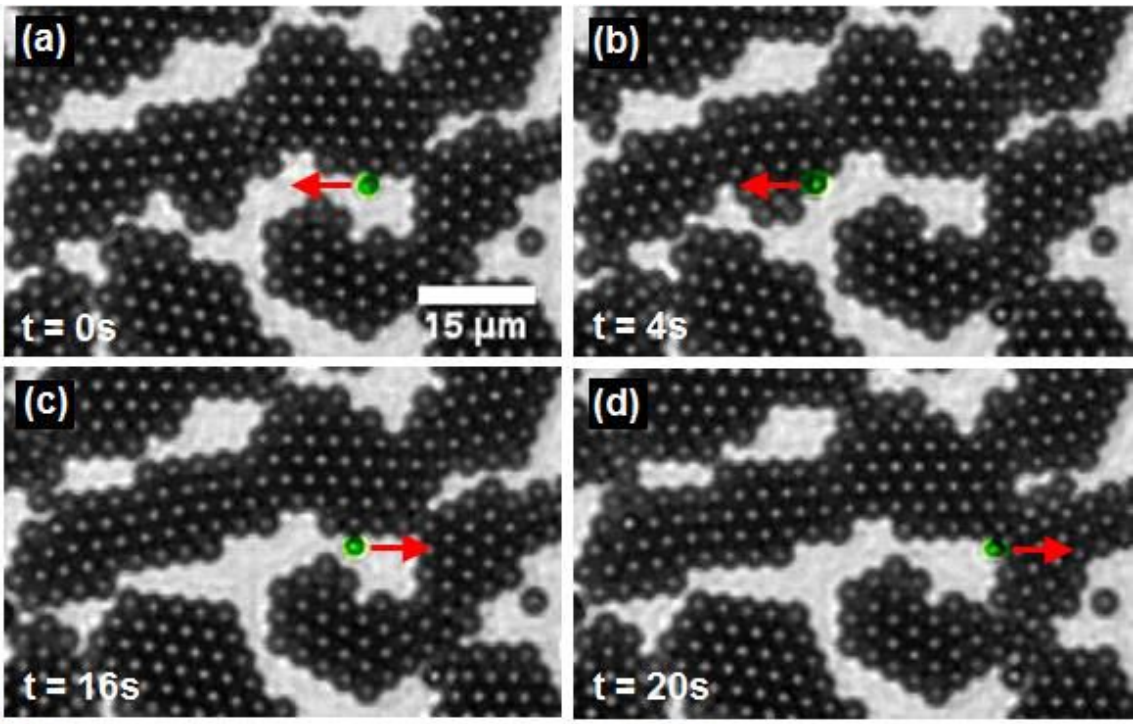

Figure 3.8: Image sequence of a paramagnetic bead (2.8µm in diameter, artificially colored for clarity) moving to the left (a,b) and then to the right (c,d) trying to pass through clusters of spherical non-magnetic particles. Magnetic pulling is indicated by red arrows. The bead is unable to go across the surrounding clusters. Applied electric field is 10V at 2400Hz, in the cluster region near the repulsive phase, as explained in the text. Magnetic field gradient applied is 16mT/mm. This sequence corresponds to video 3.4 in Additional Multimedia Content.

If these two requirements are accomplished, even the thicker clusters can be traversed. In figure 3.9 it is shown how a paramagnetic elongated aggregate travels across a 30-particle-long straight trajectory to pass through a big cluster. This magnetic aggregate is big enough to split the non-magnetic cluster into two smaller ones, which do not coalesce again under constant applied AC electric field. In the same way, chains of paramagnetic particles can cross any-sized clusters, provided the chain is long enough. As an example, in figure 3.10

it is demonstrated that a three-particle chain cannot traverse a thick cluster (figure 3.10a) until another chain attaches to it to form a long enough chain able to pass through the cluster (figure 3.10b-d).

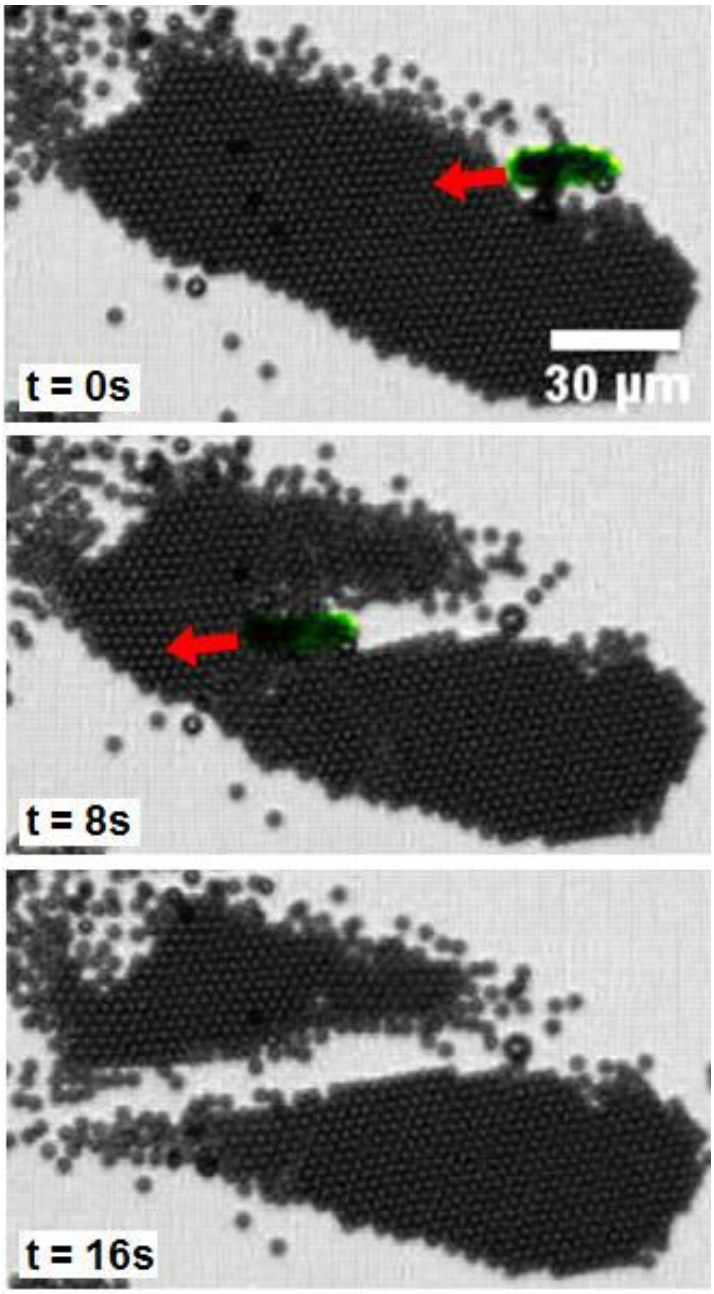

Figure 3.9: Image sequence of a paramagnetic aggregate (22x9µm², artificially colored for clarity) traversing a cluster of spherical non-magnetic particles. Magnetic pulling is indicated by a red arrow. The aggregate goes across the cluster and breaks it into two pieces. Applied electric field is 10V at 2400Hz, and magnetic field gradient is 16mT/mm. This sequence corresponds to video 3.5 in Additional Multimedia Content.

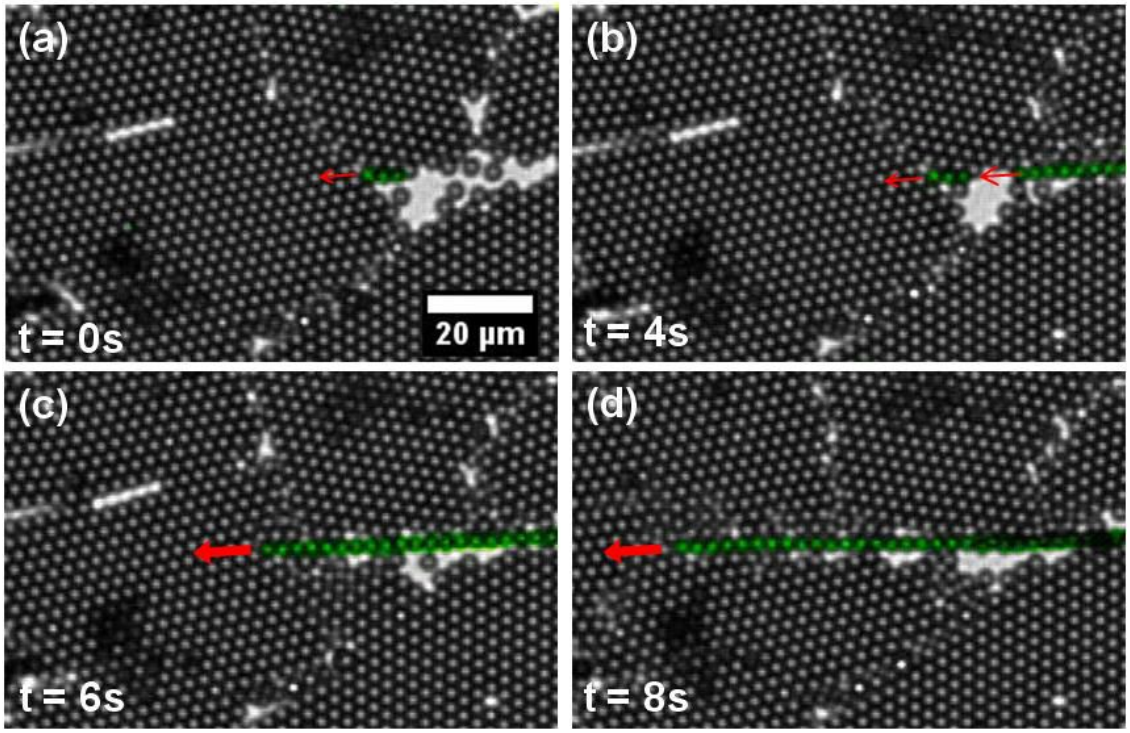

Figure 3.10: Image sequence of a paramagnetic chain (artificially colored for clarity) passing through a cluster of spherical non-magnetic particles. Magnetic pulling is indicated by red arrows. The initial 3-particle chain in (a) is not able to go across the cluster, but when a longer chain is attached to it, the chain (now composed of more than 30 particles in a row) can go across the cluster. Applied electric field is 10V at 2400Hz, and magnetic field gradient is 16mT/mm. This sequence corresponds to video 3.6 in Additional Multimedia Content.

The main drawbacks of these strategies using paramagnetic colloids and aggregates are the limitation of the experimental system used in terms of generation of strong enough magnetic fields, as well as the poor control one has of the number of paramagnetic particles in a chain or aggregate, as they are spontaneously formed, and keep growing as long as the magnetic field is applied. Up to now, this precludes quantitative measurements of cluster cohesion forces.

3.4 Conclusions

- Anisometric pear-shaped particles, when subjected to AC electric fields perpendicular to the electrodes, present richer morphologies compared to isotropic spherical particles.

- The anisometric shape alters the aggregation process to make it faster although less ordered when compared to spherical colloids. Nonetheless, the aggregation mechanism seems to be of the same nature for both types of particles.

- Different strategies have been tested to measure the cohesion of the spherical clusters. While qualitative results can be easily drawn, further experimental tests will be required in order to obtain quantitative data.

3.5 Additional Multimedia Content

Six video files can be found in the following web page:

http://tinyurl.com/phd-shn-chapter3

- Video 3.1 (speed x0.5) shows the formation of clusters of spherical particles starting from a complete Brownian disordered state by applying a field of 1kHz - 11.2V.

- Video 3.2 (speed x0.5) shows the formation of clusters of pear-shaped particles from a complete Brownian disordered state by applying a field of 1kHz - 11.2V.

- Video 3.3 (speed x0.33) correspond to figure 3.6, showing the formation of clusters of pears starting from a repulsive configuration (20kHz - 11.2V) to a clustered state (1kHz - 11.2V).

- Video 3.4 shows a single paramagnetic particle (2.8µm in diameter, slightly darker) trying to pass through two different clusters of spherical non-magnetic particles (2.8µm in diameter). Applied electric field is 10V at 2400Hz, and magnetic field gradient is 16mT/mm.

- Video 3.5 shows an aggregate ($22x9\mu m^2$) of paramagnetic spherical beads (2.8µm in diameter) passing through a cluster of spherical non-magnetic particles (2.8µm in diameter). Applied electric field is 10V at 2400Hz, and magnetic field gradient is 16mT/mm.

- Video 3.6 shows a chain (initially composed of 3 particles, and afterwards more than 30) of paramagnetic spherical beads (2.8µm in diameter) going across a cluster of spherical non-magnetic particles (2.8µm in diameter). Applied electric field is 10V at 2400Hz, and magnetic field gradient is 16mT/mm.

3.6 References

(1) Lin, S. Y.; Chow, E.; Hietala, V.; Villeneuve, P. R.; Joannopoulos, J. D. Experimental Demonstration of Guiding and Bending of Electromagnetic Waves in a Photonic Crystal. *Science* **1998**, *282*, 274–276.

(2) Blanco, A.; Chomski, E.; Grabtchak, S.; Ibisate, M.; John, S.; Leonard, S. W.; Lopez, C.; Meseguer, F.; Miguez, H.; Mondia, J. P.; et al. Large-Scale Synthesis of a Silicon Photonic Crystal with a Complete Three-Dimensional Bandgap near 1.5 Micrometres. *Nature* **2000**, *405*, 437–440.

(3) Velev, O. D.; Kaler, E. W. In Situ Assembly of Colloidal Particles into Miniaturized Biosensors. *Langmuir* **1999**, *15*, 3693–3698.

(4) Gau, H.; Herminghaus, S.; Lenz, P.; Lipowsky, R. Liquid Morphologies on Structured Surfaces: From Microchannels to Microchips. *Science* **1999**, *283*, 46–49.

(5) Tierno, P.; Muruganathan, R.; Fischer, T. M. Viscoelasticity of Dynamically Self-Assembled Paramagnetic Colloidal Clusters. *Phys. Rev. Lett.* **2007**, *98*, 28301.

(6) Yeh, S.-R.; Seul, M.; Shraiman, B. I. Assembly of Ordered Colloidal Aggregates by Electric-Field-Induced Fluid Flow. *Nature* **1997**, *386*, 57–59.

(7) Zhang, K.-Q.; Liu, X. Two Scenarios for Colloidal Phase Transitions. *Phys. Rev. Lett.* **2006**, *96*, 105701.

(8) Hu, Y.; Glass, J.; Griffith, A.; Fraden, S. Observation and Simulation of Electrohydrodynamic Instabilities in Aqueous Colloidal Suspensions. *J. Chem. Phys.* **1994**, *100*, 4674–4682.

(9) Fraden, S.; Hurd, A. J.; Meyer, R. B. Electric-Field-Induced Association of Colloidal Particles. *Phys. Rev. Lett.* **1989**, *63*, 2373–2376.

(10) Han, Y.; Grier, D. G. Fluid Dynamics: Vortex Rings in a Constant Electric Field. *Nature* **2003**, *424*, 267–268.

(11) Pérez, C. L.; Posner, J. D. Electrokinetic Vortices and Traveling Waves in Nondilute Colloidal Dispersions. *Langmuir* **2010**, *26*, 9261–9268.

(12) Richetti, P.; Prost, J.; Barois, P. Two-Dimensional Aggregation and Crystallization of A Colloidal Suspension of Latex Spheres. *J. Phys. Lettres* **1984**, *45*, 1137–1143.

(13) Wei, Q.; Zhou, C.; Ming, N. Crossover from Flocculation to Gelation in Two-Dimensional Aggregation Induced by an Alternating Electrical Field. *Phys. Rev. E* **1995**, *52*, 1877–1881.

(14) Trau, M.; Saville, D. A.; Aksay, I. A. Field-Induced Layering of Colloidal Crystals. *Science* **1996**, *272*, 706–709.

(15) Hayward, R. C.; Saville, D. A.; Aksay, I. A. Electrophoretic Assembly of Colloidal Crystals with Optically Tunable Micropatterns. *Nature* **2000**, *404*, 56–59.

(16) Zhang, K.-Q.; Liu, X. In Situ Observation of Colloidal Monolayer Nucleation Driven by an Alternating Electric Field. *Nature* **2004**, *429*, 739–743.

(17) Velev, O. D.; Bhatt, K. H. On-Chip Micromanipulation and Assembly of Colloidal Particles by Electric Fields. *Soft Matter* **2006**, *2*, 738–750.

(18) Gong, T.; Wu, D. T.; Marr, D. W. M. Two-Dimensional Electrohydrodynamically Induced Colloidal Phases. *Langmuir* **2002**, *18*, 10064–10067.

(19) Mittal, M.; Furst, E. M. Electric Field-Directed Convective Assembly of Ellipsoidal Colloidal Particles to Create Optically and Mechanically Anisotropic Thin Films. *Adv. Funct. Mater.* **2009**, *19*, 3271–3278.

(20) Mantegazza, F.; Caggioni, M.; Jimenez, M. L.; Bellini, T. Anomalous Field-Induced Particle Orientation in Dilute Mixtures of Charged Rod-like and Spherical Colloids. *Nat. Phys.* **2005**, *1*, 103–106.

(21) Demirors, A. F.; Johnson, P. M.; van Kats, C. M.; van Blaaderen, A.; Imhof, A. Directed Self-Assembly of Colloidal Dumbbells with an Electric Field. *Langmuir* **2010**, *26*, 14466–14471.

(22) Donev, A.; Cisse, I.; Sachs, D.; Variano, E.; Stillinger, F. H.; Connelly, R.; Torquato, S.; Chaikin, P. M. Improving the Density of Jammed Disordered Packings Using Ellipsoids. *Science* **2004**, *303*, 990–993.

(23) Hosein, I. D.; Lee, S. H.; Liddell, C. M. Dimer-Based Three-Dimensional Photonic Crystals. *Adv. Funct. Mater.* **2010**, *20*, 3085–3091.

(24) Tierno, P.; Claret, J.; Sagués, F.; Cebers, A. Overdamped Dynamics of Paramagnetic Ellipsoids in a Precessing Magnetic Field. *Phys. Rev. E* **2009**, *79*, 21501.

(25) Güell, O.; Sagués, F.; Tierno, P. Magnetically Driven Janus Micro-Ellipsoids Realized via Asymmetric Gathering of the Magnetic Charge. *Adv. Mater.* **2011**, *23*, 3674–3679.

(26) Tierno, P.; Albalat, R.; Sagués, F. Autonomously Moving Catalytic Microellipsoids Dynamically Guided by External Magnetic Fields. *SMALL* **2010**, *6*, 1749–1752.

(27) Dhar, P.; Cao, Y.; Fischer, T. M.; Zasadzinski, J. A. Active Interfacial Shear Microrheology of Aging Protein Films. *Phys. Rev. Lett.* **2010**, *104*, 16001.

(28) Singh, J. P.; Lele, P. P.; Nettesheim, F.; Wagner, N. J.; Furst, E. M. One- and Two-Dimensional Assembly of Colloidal Ellipsoids in Ac Electric Fields. *Phys. Rev. E* **2009**, *79*, 50401.

(29) Trau, M.; Saville, D. A.; Aksay, I. A. Assembly of Colloidal Crystals at Electrode Interfaces. *Langmuir* **1997**, *13*, 6375–6381.

(30) Sides, P. J. Electrohydrodynamic Particle Aggregation on an Electrode Driven by an Alternating Electric Field Normal to It. *Langmuir* **2001**, *17*, 5791–5800.

(31) Sides, P. J. Calculation of Electrohydrodynamic Flow around a Single Particle on an Electrode. *Langmuir* **2003**, *19*, 2745–2751.

(32) Ristenpart, W. D.; Aksay, I. A.; Saville, D. A. Assembly of Colloidal Aggregates by Electrohydrodynamic Flow: Kinetic Experiments and Scaling Analysis. *Phys. Rev. E* **2004**, *69*, 021405.

(33) Fagan, J. A.; Sides, P. J.; Prieve, D. C. Vertical Motion of a Charged Colloidal Particle near an AC Polarized Electrode with a Nonuniform Potential Distribution: Theory and Experimental Evidence. *Langmuir* **2004**, *20*, 4823–4834.

(34) Hoggard, J. D.; Sides, P. J.; Prieve, D. C. Electrolyte-Dependent Multiparticle Motion near Electrodes in Oscillating Electric Fields. *Langmuir* **2008**, *24*, 2977–2982.

(35) Fagan, J. a; Sides, P. J.; Prieve, D. C. Mechanism of Rectified Lateral Motion of Particles near Electrodes in Alternating Electric Fields below 1 kHz. *Langmuir* **2006**, *22*, 9846–9852.

(36) Fagan, J. a; Sides, P. J.; Prieve, D. C. Evidence of Multiple Electrohydrodynamic Forces Acting on a Colloidal Particle near an Electrode due to an Alternating Current Electric Field. *Langmuir* **2005**, *21*, 1784–1794.

(37) Prieve, D. C.; Sides, P. J.; Wirth, C. L. 2-D Assembly of Colloidal Particles on a Planar Electrode. *Curr. Opin. Colloid Interface Sci.* **2010**, *15*, 160–174.

(38) Ristenpart, W. D.; Aksay, I. A.; Saville, D. A. Electrically Guided Assembly of Planar Superlattices in Binary Colloidal Suspensions. *Phys. Rev. Lett.* **2003**, *90*, 128303.

(39) Sbalzarini, I. F.; Koumoutsakos, P. Feature Point Tracking and Trajectory Analysis for Video Imaging in Cell Biology. *J. Struct. Biol.* **2005**, *151*, 182–195.

(40) Murray, C.; Van Winkle, D. H. Experimental Observation of Two-Stage Melting in a Classical Two-Dimensional Screened Coulomb System. *Phys. Rev. Lett.* **1987**, *58*, 1200–1203.

(41) Mach, J.; Mas, F.; Sagués, F. Two Representations in Multifractal Analysis. *J. Phys. A. Math. Gen.* **1995**, *28*, 5607–5622.

(42) Vicsek, T.; Family, F. Dynamic Scaling for Aggregation of Clusters. *Phys. Rev. Lett.* **1984**, *52*, 1669–1672.

(43) Hoshen, J. Percolation and Cluster Structure Parameters: The Radius of Gyration. *J. Phys. A-mathematical Gen.* **1997**, *30*, 8459–8469.

(44) Sciortino, F.; Tartaglia, P.; Zaccarelli, E. One-Dimensional Cluster Growth and Branching Gels in Colloidal Systems with Short-Range Depletion Attraction and Screened Electrostatic Repulsion. *J. Phys. Chem. B* **2005**, *109*, 21942–21953.

(45) Cernak, J.; Helgesen, G. Aggregation of Magnetic Holes in a Rotating Magnetic Field. *Phys. Rev. E* **2008**, *78*, 61401.

(46) Erb, R. M.; Krebs, M. D.; Alsberg, E.; Samanta, B.; Rotello, V. M.; Yellen, B. B. Beyond Diffusion-Limited Aggregation Kinetics in Microparticle Suspensions. *Phys. Rev. E* **2009**, *80*, 51402.

(47) Domínguez-García, P.; Melle, S.; Pastor, J.; Rubio, M. Scaling in the Aggregation Dynamics of a Magnetorheological Fluid. *Phys. Rev. E* **2007**, *76*, 051403.

(48) Tierno, P. Recent Advances in Anisotropic Magnetic Colloids: Realization, Assembly and Applications. *Phys. Chem. Chem. Phys.* **2014**.

CHAPTER 4

BREAKING THE DEGENERACY OF NEMATIC LIQUID CRYSTALS BY MEANS OF ACTUATED ANISOMETRIC PARAMAGNETIC COLLOIDS

4.1 Introduction

In contrast to research on liquid crystal dispersions of sub-micron or nano-scale particles,[1,2] the study presented in this chapter is centered on inclusions at the micrometer scale, which enable a local control of the medium. Commonly, the dispersed phase in such a self-assembled medium consists of ensembles of spherical particles.[3] More recently the field has been extended to incorporate anisometric, either actuated[4,5] or non-actuated,[6,7] inclusions. Tailoring particle shape opens new possibilities regarding the manipulation and assembling of the dispersed entities.[8,9]

In spite of the extensive research reported in literature, there is still a non-explored perspective which consists in using non-spherical paramagnetic inclusions to control the orientation of a liquid crystal. This approach is contrary to the usually adopted one, since here externally actuated particles are acting on their host rather than passively adapting to the constraints imposed by the liquid crystal medium where they reside.

As a proof of concept, here I demonstrate that anisometric aggregates of paramagnetic spherical particles or isolated paramagnetic micro-ellipsoids, oriented by weak magnetic fields, break the orientational degeneracy of a thin nematic sample which is transited to a planar configuration from a uniform homeotropic alignment. In particular, a combination of an electric (acting over the medium) and a magnetic field (acting on the inclusions) is used to orient a nematic liquid crystal over localized areas around the dispersed colloids. In this system, the strength of the orienting magnetic field (a few milliTesla) is well below (*c.a* two orders of magnitude) the magnetic Frederiks threshold of the homeotropic to planar transition (see chapter 1 section 1.3.3), as the initial dismantling of the homeotropic alignment is fully reserved to the action of the AC electric field. Moreover, with this method it is possible to generate and control textures of different symmetries, either target-like or displaying spiral forms, which can be easily obtained and manipulated through the magnetic field-actuated ellipsoids.

4.2 Experimental Procedures

Nematic liquid crystal (NLC) cells with induced planar degenerate alignment are prepared by first coating the glass-ITO plates with a homeotropic self-assembled monolayer, as explained in chapter 2 section 2.1.2, and then the plates are glued together separated by a Mylar spacer with 23μm of nominal thickness (actual cell thicknesses are measured as described in chapter 2 section 2.1.5). By filling these cells with dispersions based on a negative dielectric anisotropy NLC, and applying a strong enough AC electric field between the glass-ITO plates, it is possible to induce a planar alignment with azimuth degeneration,[10] that is, the NLC molecules orient parallel to the plates but with no preferred orientation.

The inclusions used in the experiments are paramagnetic spherical particles (Compel, Bangs Laboratories, 6 or 12μm in diameter), used either as received or changing their shape to ellipsoidal by using a stretching technique (see chapter 2 section 2.2.2).[11] Typical long axis of the ellipsoids ranges from 24 to 29μm. These particles are gently dispersed in the NLC (see chapter 2 section 2.2.3) and finally the cell is filled with the dispersion by capillarity. According to preliminary observations, the liquid crystal adopts a tangential (parallel) anchoring at the contact surface with the inclusions.

To observe and control the cells I use a polarizing microscope (Nikon Eclipse 50iPol) equipped with a Helmholtz coil configuration in a custom-built assembly, which enables application of a magnetic field in the desired in-plane direction and also the rotation of the field in this plane (see chapter 2 section 2.3.2). The potential difference is applied to cells (up to 9V at 1kHz) by a NI-DAQ board (NI PCI-6221 37-pin) computer-controlled with a LabView custom-made program. The magnetic field necessary to orient the particles is about 3mT and it is generated using the Helmholtz coils. Images are captured with an AVT Marlin F-131C CMOS camera controlled with the software AVT SmartView 1.10.2 and they are then treated and analyzed using the software packages ImageJ and IgorPro.

4.3 Results and Discussion

4.3.1 Magnetic Alignment using Paramagnetic Colloidal Inclusions

First of all, to better illustrate the reported phenomenon, I prepared a homeotropically aligned nematic sample free of paramagnetic inclusions (figure 4.1a). To this cell I first applied a ramped AC electric field perpendicular to the glass plates without applying the magnetic field. The material, having a negative dielectric anisotropy, globally reorients and, above the (electric) Frederiks threshold (see chapter 1 section 1.3.3), progressively bends towards the center of the cell, adopting a planar configuration at its mid plane (figure 4.1b). The ramp is applied slowly ($2mV \cdot s^{-1}$) to avoid the formation of point defects and Schlieren textures.[12] Although the panel reproduces a small area with a quite uniform reflectivity, larger observed regions display different gray levels, featuring degenerated in-plane molecular orientations. Introduction of the in-plane magnetic field has no appreciable effect in this non-doped sample as demonstrated in figure 4.1c.

The experiment is repeated when the cell is filled with NLC containing paramagnetic spherical particles. The latter, once dispersed in the NLC, organize into separated clusters due to attractive long-range interactions of elastic nature.[13] One can observe that once formed, these clusters, which contain up to 10 particles and have anisometric shape, remain dispersed in the medium over time. In absence of external fields, the clusters align so as to minimize the distortion caused in the host matrix (figure 4.1d). When applying the electric field there is no significant difference (figure 4.1e) with the sample free of particles, since the orientation of the magnetic inclusions is dictated by the degenerated orientation of the NLC. The active role of the inclusions is revealed only after the application of the additional magnetic field on the particle-laden planar sample. Paramagnetic clusters align along the direction imposed by the magnetic field, which results in a neat and contrasted reflectivity change in areas around the dispersed clusters, as can be seen in figure 4.1f. This clearly shows that the inclusions, when oriented by the magnetic field, are capable of

aligning the NLC director in their neighborhood. Notice that to be able to transmit a mechanical torque through coupling with the magnetic field, the paramagnetic objects must be anisometric; isolated spherical particles are not affected by the magnetic reorientation forcing.

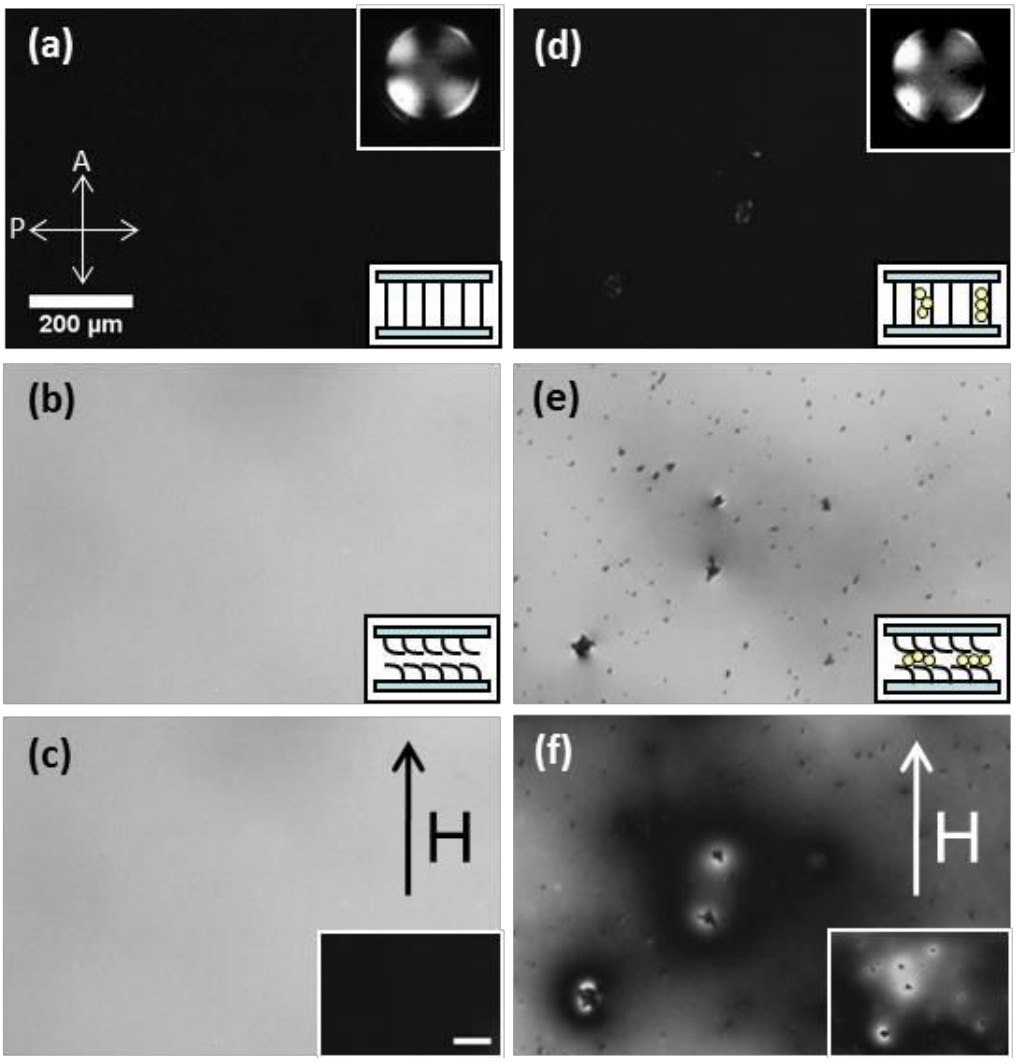

Figure 4.1: Polarizing microscope images showing the effect of the paramagnetic inclusions on the NLC orientation. (a-c) are images of a NLC cell without particles, and (d-f) are images of a NLC cell doped with the spherical particles. In the absence of external fields, (a) and (d), the cells are homeotropic (conoscopy image in the inset, the Malt-cross pattern indicates homeotropic anchoring). An electric field perpendicular to the cell plates is applied in (b) and (e), and an additional in-plane magnetic field (6mT) is applied in (c) and (f). The inset in the latter frames corresponds to the samples rotated 30° counter clock-wise (CCW) to see the reflectivity change. Schemes drawn at the right bottom part of images (a), (b), (d) and (e) are representations of a cross section of the cells. In both cases cell thickness is 30±2µm.

In order to better characterize the particle-induced director reorientation, the effect of an isolated paramagnetic ellipsoidal particle embedded in the NLC has been analyzed (figure 4.2). The direction of the magnetic field is adjusted so that the reference orientation is given by the local (in-plane) azimuth of the NLC. Modest reorientations induced by slowly rotating the magnetic field result in a dark halo that grows away from the torqued ellipsoid. The maximal effect is realized for a particle reorientation near 90º (figure 4.2b). Beyond that value, a white halo starts to grow (figure 4.2c) and further rotating the magnetic field leads to a target-like structure (figure 4.2d). Notice that the distortion in the nematic field has rotational symmetry despite being generated by anisometric inclusions. The effect is reversible and the whole structure is relaxed after turning off the magnetic field: the inner rings collapse successively towards the central magnetic inclusion as the particle turns back to its original orientation (see video 4.1 in Additional Multimedia Content).

The director field lines in the target patterns are spirals that wind according to the handedness of the magnetic field rotation (see theoretical model in the following section 4.3.2).[14] Nevertheless, textures generated by clock-wise (CW) or counter clock-wise (CCW) rotation have rotational symmetry, and are indistinguishable under the polarizing microscope as a result of the planar configuration of the nematic director. However, the latter can be forced to escape into the third dimension by tuning the voltage applied across the sample, bringing its amplitude closer to the electric Frederiks threshold. A few tenths of volts before the particle-induced pattern fades, a helical texture can be observed (figure 4.3a,b). Its handedness correlates with the rotation of the magnetic field used to create the target pattern, as shown in figure 4.3c,d, where the NLC configuration around the rotated ellipsoids is schematically represented by green lines. The rotational symmetry present in the textures around isolated ellipsoids is now broken, and the anisometric nature of the inclusions is now playing a relevant role. In this respect it is worth emphasizing that with this technique one can resolve through such 3D constructions the hidden chirality of the pure in-plane target-like structures.

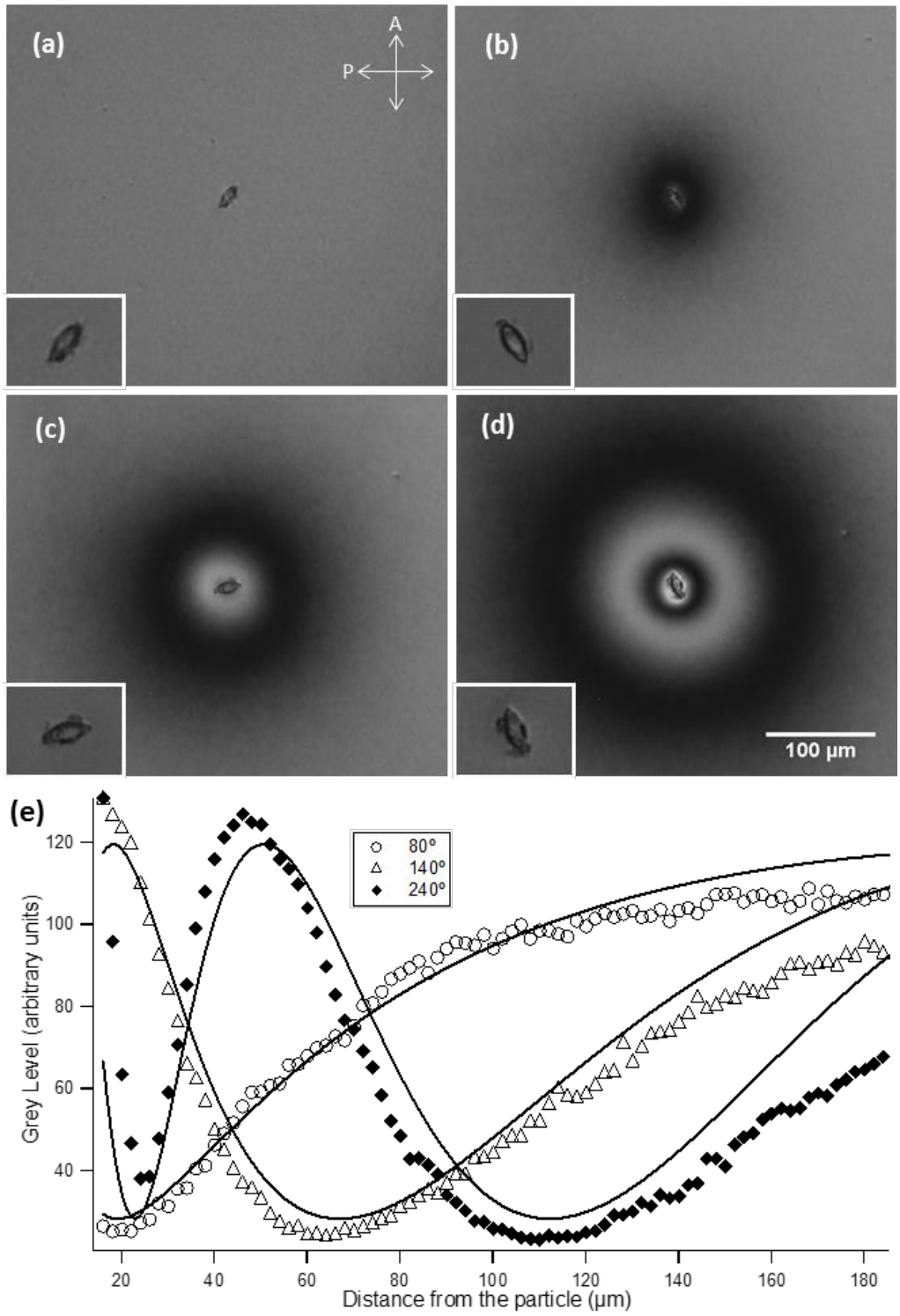

Figure 4.2: Distortion generated by a 25µm long, 10µm wide ellipsoid rotated CCW inside a 30±2µm thick cell. The four insets are enlargements (factor 1.8) of the central ellipsoid. Initial (field-free) orientation is taken as 0° (a). The magnetic field (3 mT) is applied in (a), and then the particle rotates, following the magnetic field, by an angle of 80° (b), 140° (c), and 240° (d). Grey level vs. distance from the particle for different rotation angles are shown in (e). Solid lines are fits to eqn (4.5), yielding to $r_0 = 2.8 \pm 0.1\mu m$, and $R = 251 \pm 2\mu m$.

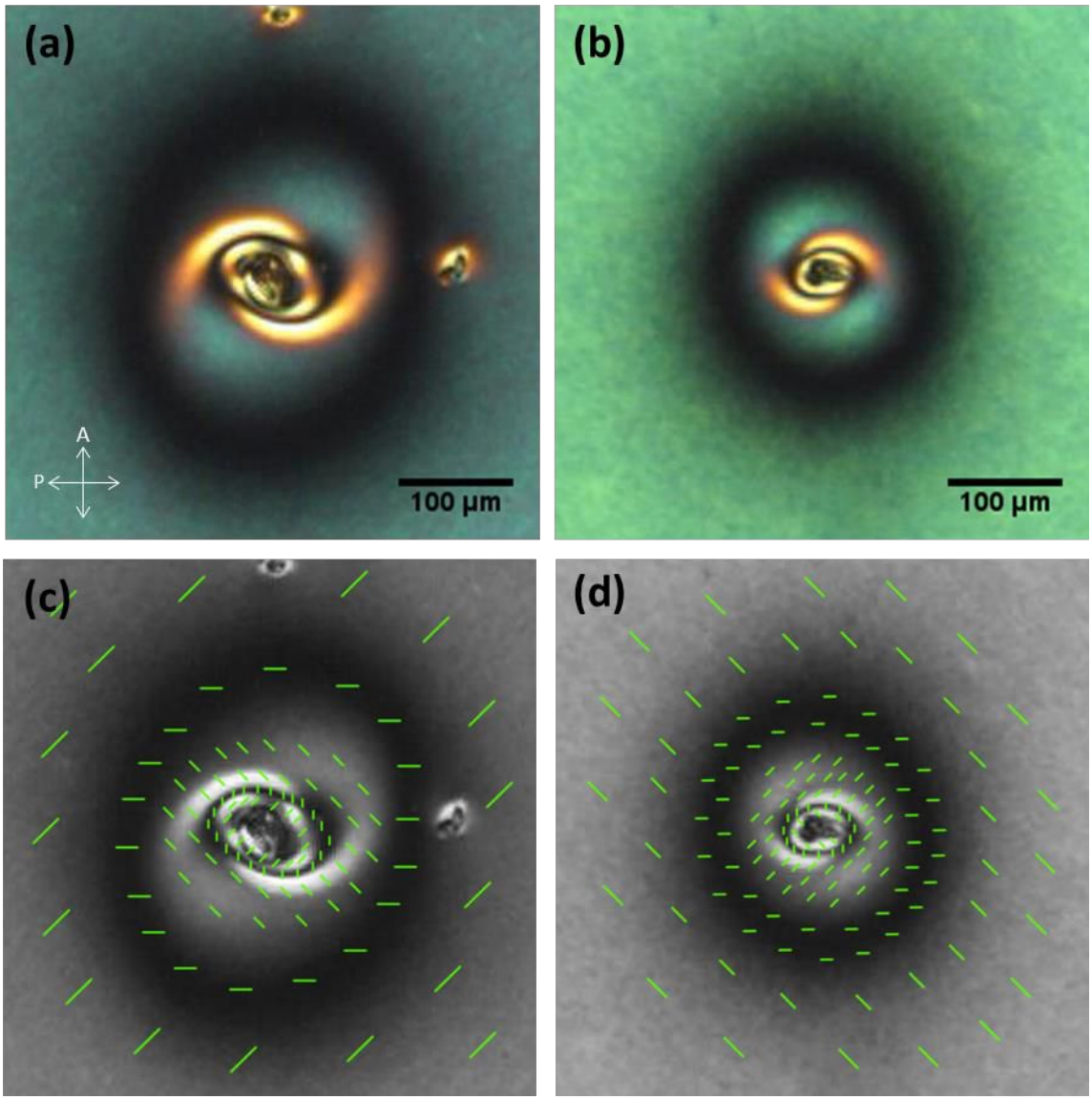

Figure 4.3: Polarizing microscope images of double-armed helical patterns under crossed polarizers. These chiral structures appear when the electric field is decreased until 2.5V from 9V. It is possible to distinguish whether the inclusion has been rotated CW (a) or CCW (b). In panels (c) and (d) the orientation of NLC molecules are represented by green lines, showing the CW and CCW configuration, respectively. Corresponding videos can be found in the Additional Multimedia Content.

4.3.2 Theoretical Model

A simple model is proposed to account quantitatively for the observed reflectivity pattern around an isolated ellipsoid. Similar modeling approaches have been applied to forced free-standing Smectic-C films.[15–17] A two-dimensional approach for the director field configuration is here justified for symmetry reasons, and this permits to describe the director field as $\vec{n} = (\cos\phi, \sin\phi)$. Also, K_2 (*twist* constant in the Frank-Oseen elastic free energy density, see chapter 1 section 1.3.2) is mainly a three-dimensional deformation of the liquid crystal, so its term of the elastic free energy density expression can be neglected. Taking these into account, and using the usual one constant approximation (K_1 (*splay*) ~ K_3 (*bend*) ~ K), the elastic free energy can be expressed in terms of the azimuthal angle $\phi(\vec{r})$:[18]

$$F_{el} = \frac{1}{2} K \int (\nabla\phi)^2 d\vec{r} \qquad \text{eqn (4.1)}$$

Minimizing eqn (4.1) under steady state conditions leads to the well-known Laplacian equation for in-plane distortions,

$$\nabla^2\phi = \frac{1}{r}\frac{\partial\phi}{\partial r} + \frac{\partial^2\phi}{\partial r^2} = 0 \qquad \text{eqn (4.2)}$$

This harmonic approximation is easily solved[19] in terms of close- and far-field boundary conditions: $\phi(r = r_0) = \phi_p$; $\phi(r = R) = \phi_b$. The first condition refers to the distance to the ring center at which the director field has rotated the same angle as the ellipsoid (ϕ_p). It must be understood as an effective distance that should scale with the ellipsoid size. The second prescription refers to the spontaneous azimuth alignment that spans submillimeter regions in the planar NLC configuration. This phenomenon is attributed to the unavoidable presence of orientational quenched disorder on the confining surfaces[20] and, even though it results in weak bulk forces that are easily overcome by the applied magnetic torques, it nevertheless provides a fixed boundary condition far from the colloidal inclusions. One can take into account such effect assuming that at some cut-off distance R from the center of the analyzed

particle, the orientation of the liquid crystal is unaffected by the presence of the ellipsoid and it keeps its original local value ϕ_b. The latter is taken equal to zero according to the initial condition of the experiment as previously mentioned. The closed solution of eqn (4.2) then reads:

$$\phi(r) = \frac{\phi_p \ln\left(\frac{r}{R}\right)}{\ln\left(\frac{r_0}{R}\right)} \qquad \text{eqn (4.3)}$$

Here, ϕ_p is taken as the orientation of the long axis of the ellipsoid, while the parameters R and r_0 are fitted to the data. Bearing in mind that the transmittance T in a liquid crystal cell is equivalent to the grey level measured in the captured images, and that it follows the expression[21]

$$T(\phi) = A + B \cdot sin^2(2\phi - D) \qquad \text{eqn (4.4)}$$

One can combine both eqn (4.3) and (4.4) to obtain the expression used in the data analysis:

$$T(\phi) = A + B \cdot sin^2\left(\frac{2\phi_p \ln\left(\frac{r}{R}\right)}{\ln\left(\frac{r_0}{R}\right)} - D\right) \qquad \text{eqn (4.5)}$$

where A is the minimum grey value, B is the difference between the maximum and minimum grey value, and D is a phase parameter related with ϕ_b, which in our case is equal to 0. The adjustment parameters r_0 and R are characteristic of the studied system (figure 4.2e).

For r_0, values smaller than the width of ellipsoids are obtained. This result means that there is not a completely tangential anchoring of the liquid crystal on the surface of ellipsoids, there is a shift in the anchoring angle (that is, the liquid crystal "cannot follow" the particle orientation) due to the torque exerted. The obtained values for R, as explained before, indicate the distance at which the liquid crystal remains unaffected despite the presence of the ellipsoid.

4.4 Conclusions

- Paramagnetic colloidal inclusions in a nematic liquid crystal can play an active role in the control of the bulk configuration of the LC director field.

- The use of anisometric aggregates or anisometric paramagnetic particles makes possible to apply a local torque by means of weak magnetic fields, provided the nematic director is not bound by strong anchoring conditions at the cell plates.

- By using the described techniques it is possible to create stable complex patterns such as targets or chiral textures.

- The reported phenomena can be well described by a simple theoretical model based on the Frank-Oseen elastic free energy for a liquid crystal.

4.5 Additional Multimedia Content

Three video files can be found in the following web page:

http://tinyurl.com/phd-shn-chapter4

- Video 4.1 (speed x10) shows the formation of a target pattern upon a CCW rotation of a 3mT magnetic field, and its subsequent relaxation (unscrewing) when the magnetic field is turned off. Image sequence was taken between crossed polarizers, and applied electric field was 9V at 1kHz.

- Video 4.2 shows (between crossed polarizers) the generation of a helix pattern with a clock-wise (CW) orientation. The AC (1kHz) electric field applied across the cell periodically changes between 2.5V and 6V with a period of 1 second. The electric field variations correspond to reversible changes from the target pattern (6V) to the CW helix (2.5V) and back. The CW orientation of the helix is due to the CW rotation of the applied magnetic field (3mT) which generates the target.

- Video 4.3 shows (between crossed polarizers) the generation of a helix pattern with a counter clock-wise (CCW) orientation. The electric field applied across the cell periodically changes between 2.4V and 6V with a period of 3.5 seconds. The electric field variations correspond to reversible changes from the target pattern (6V) to the CCW helix (2.4V) and back. The CCW orientation of the helix is due to the CCW rotation of the applied magnetic field (3mT) which generates the target.

4.6 References

(1) Qi, H.; Kinkead, B.; Hegmann, T. Unprecedented Dual Alignment Mode and Freedericksz Transition in Planar Nematic Liquid Crystal Cells Doped with Gold Nanoclusters. *Adv. Funct. Mater.* **2008**, *18*, 212–221.

(2) Acharya, S.; Kundu, S.; Hill, J. P.; Richards, G. J.; Ariga, K. Nanorod-Driven Orientational Control of Liquid Crystal for Polarization-Tailored Electro-Optic Devices. *Adv. Mater.* **2009**, *21*, 989+.

(3) Musevic, I.; Skarabot, M. Self-Assembly of Nematic Colloids. *Soft Matter* **2008**, *4*, 195–199.

(4) Lapointe, C. P.; Hultgren, A.; Silevitch, D. M.; Felton, E. J.; Reich, D. H.; Leheny, R. L. Elastic Torque and the Levitation of Metal Wires by a Nematic Liquid Crystal. *Science* **2004**, *303*, 652–655.

(5) Rovner, J. B.; Lapointe, C. P.; Reich, D. H.; Leheny, R. L. Anisotropic Stokes Drag and Dynamic Lift on Cylindrical Colloids in a Nematic Liquid Crystal. *Phys. Rev. Lett.* **2010**, *105*, 228301.

(6) Tkalec, U.; Škarabot, M.; Muševič, I. Interactions of Micro-Rods in a Thin Layer of a Nematic Liquid Crystal. *Soft Matter* **2008**, *4*, 2402–2409.

(7) Mondiot, F.; Chandran, S. P.; Mondain-Monval, O.; Loudet, J.-C. Shape-Induced Dispersion of Colloids in Anisotropic Fluids. *Phys. Rev. Lett.* **2009**, *103*, 238303.

(8) Lapointe, C. P.; Mason, T. G.; Smalyukh, I. I. Shape-Controlled Colloidal Interactions in Nematic Liquid Crystals. *Science* **2009**, *326*, 1083–1086.

(9) Lapointe, C. P.; Hopkins, S.; Mason, T. G.; Smalyukh, I. I. Electrically Driven Multiaxis Rotational Dynamics of Colloidal Platelets in Nematic Liquid Crystals. *Phys. Rev. Lett.* **2010**, *105*, 178301.

(10) Oswald, P.; Ignes-Mullol, J. Backflow-Induced Asymmetric Collapse of Disclination Lines in Liquid Crystals. *Phys. Rev. Lett.* **2005**, *95*.

(11) Tierno, P.; Albalat, R.; Sagués, F. Autonomously Moving Catalytic Microellipsoids Dynamically Guided by External Magnetic Fields. *SMALL* **2010**, *6*, 1749–1752.

(12) De Gennes, P. G.; Prost, J. *The Physics of Liquid Crystals*; Oxford University Press, 1993.

(13) Poulin, P.; Stark, H.; Lubensky, T. C.; Weitz, D. A. Novel Colloidal Interactions in Anisotropic Fluids. *Science* **1997**, *275*, 1770–1773.

(14) Kojima, M.; Yamamoto, J.; Sadakane, K.; Yoshikawa, K. Generation of Multiple Circular Walls on a Thin Film of Nematic Liquid Crystal by Laser Scanning. *Chem. Phys. Lett.* **2008**, *457*, 130–133.

(15) Cladis, P. E.; Couder, Y.; Brand, H. R. Phase Winding and Flow Alignment in Freely Suspended Films of Smectic-C Liquid Crystals. *Phys. Rev. Lett.* **1985**, *55*, 2945–2948.

(16) Eremin, A.; Bohley, C.; Stannarius, R. C-Director Relaxation around a Vortex of Strength +1 in Free-Standing Smectic c Films. *Eur. Phys. J. E* **2006**, *21*, 57–67.

(17) Stannarius, R.; Bohley, C.; Eremin, A. Vortex Flow in Free Standing Smectic Films Driven by Elastic Relaxation of the c-Director. *Phys. Rev. Lett.* **2006**, *97*, 097802.

(18) Kleman, M.; Lavrentovich, O. D. *Soft Matter Physics - An Introduction*; Springer, 2003.

(19) Spiegel, M. R.; Liu, J.; Abellanas, L. *Fórmulas Y Tablas de Matemática Aplicada*; McGraw-Hill: Madrid, 2005; p. 105.

(20) Nespoulous, M.; Blanc, C.; Nobili, M. Orientational Quenched Disorder of a Nematic Liquid Crystal. *Phys. Rev. Lett.* **2010**, *104*, 097801.

(21) Oswald, P.; Pieranski, P. *Nematic and Cholesteric Liquid Crystals: Concepts and Physical Properties Illustrated by Experiments*; Taylor& Francis: Boca Raton, 2005.

CHAPTER 5

NONLINEAR ELECTROPHORESIS OF MICRODROPLETS AND PHOTOSENSITIVE PARTICLES

5.1 Introduction

Water based microemulsions in oil phases are of fundamental importance in chemical and analytical sciences, due to the possibility to encapsulate and deliver chemical or biological entities otherwise immiscible in the dispersion medium. The controlled transport of these microdroplets is of crucial importance for many applications related with lab-on-a-chip,[1–4] drug delivery,[5] or the realization of remotely addressable micromotors.[6–10] In contrast to simple oils as dispersion media, anisotropic fluids like liquid crystals offer the advantage of showing a variety of phases and structures which can be easily controlled and changed via temperature or external fields (see chapter 1 section 1.3). These features, in turn, could be used to manipulate the physical or chemical properties of the dispersed droplets.[11–16]

When a microscale inclusion is dispersed in a nematic liquid crystal (NLC), it causes a distortion in the nematic director field that leads to the formation of defects around the inclusion. These defects will mainly depend on the anchoring conditions at the surface of the inclusion.[17,18] As explained in chapter 1 section 1.4.2, if the defects surrounding the inclusions are of dipolar nature (hedgehog type), particles can be transported in a NLC by using alternating current (AC) electric fields through the mechanism known as Liquid Crystal-Enabled Electrophoresis (LCEEP). On the contrary, if the defects have quadrupolar symmetry (Saturn ring, or double Boojum), there is no net propulsion with LCEEP.

In the first part of this chapter, I demonstrate the controlled motion of water microdroplets dispersed in a NLC and propelled via AC electric fields. Once dispersed in the NLC, the microdroplets acquire a dipolar point defect, which enables controlled motion of these inclusions in the direction of the defect. Here is employed a NLC with negative dielectric anisotropy (see chapter 1 section 1.3.3), which induces motion of the inclusions perpendicular to the AC electric field, thus completely decoupling linear from nonlinear electrophoresis (i.e. parallel and perpendicular to the electric field, respectively). I also

characterize the velocity of the microdroplets in terms of their size, frequency and strength of the applied field, and show that these droplets can be used as microreactors to transport, in the nematic medium, microscale particles or to mix femtoliter volumes of chemicals.

In the second part of this chapter I focus on the nonlinear electrophoresis of custom-prepared photosensitive particles. It has already been reported in the literature that the anchoring conditions of a NLC can be regulated by functionalizing the surfaces with photosensitive molecules.[19–22] In this study I demonstrate how the anchoring conditions of photosensitive particles can be reversibly tuned from a dipolar configuration, where they are propelled by LCEEP, to a quadrupolar configuration, where LCEEP is not effective, by suitable irradiation with blue or UV light, respectively. Thus, one should be able to control the nonlinear electrophoresis of individual photosensitive particles, without affecting the neighboring inclusions, via irradiation of a localized portion of the sample.

5.2 Experimental Procedures

The electrophoretic NLC cells are composed of two ITO-glass plates presenting unidirectional planar alignment as result of a rubbed polyimide coating (for a more detailed explanation see chapter 2 section 2.1.3). The two plates are separated by a polyethylene terephthalate spacer (Goodfellow, nominal thickness 23µm) and glued together along two sides with the ITO layers facing inwards.

Dispersions of aqueous microdroplets are created by adding 1µL of water-based aqueous solution to 10µL of a negative dielectric anisotropy nematic liquid crystal (MLC-7029, Merck) followed by vortex agitation (IKA MS3 basic) for 3 minutes. Some tests are also performed with the nematic liquid crystals MLC-2037 (Merk, $\Delta\varepsilon$ = -3.1 at 1kHz) and MBBA (Synthon Chemicals, $\Delta\varepsilon$ = -0.5 at 1kHz). The emulsions are stabilized using 0.01-0.05M Sodium Dodecylsulphate (SDS, Sigma-Aldrich) which, in turn, induces homeotropic (perpendicular) alignment of the nematic molecules at the LC/water interface. The experimental cells are then filled by capillarity with freshly prepared dispersions and sealed with glue. With this protocol one can obtain suspensions of polydispersed water droplets with sizes ranging from 1 to 20µm in diameter and a distribution peaked at a diameter of 3µm (figure 5.1e).

Photosensitive particles are obtained from commercial amino functionalized silica particles (diameter 4.63µm, Bangs Laboratories) by chemically bonding a previously synthesized azoderivative 8Az3COOH[23] (supplied by Prof. Joan-Antoni Farrera's group, Organic Chemistry Department, University of Barcelona). More extended details of the synthesis process and dispersion in NLC can be found in chapter 2 section 2.2.2.

Sinusoidal electric fields are applied to the experimental cells by using a function generator (ISO-TECH IFA 730) feeding a voltage amplifier (TREK model PZD700). The voltages are monitored by a multimeter (HP 34401A) and are in the range 0 to 30 Volts peak to peak, while the applied range of

frequencies varies from 0 to 100Hz. Experimental observations are performed with an optical microscope (Nikon Eclipse 50iPol). Irradiation of the samples with blue (455nm) and UV (365nm) light is performed with the custom-built LED setup described in chapter 2 section 2.3.3. Images and videos are captured with an AVT Marlin F-131C CMOS camera controlled with the software AVT SmartView 1.10.2. They are then treated and analyzed using the software packages ImageJ and IgorPro.

5.3 Results and Discussion

5.3.1 LCEEP of Microdroplets

Figures 5.1a,c show optical micrographs of droplets featuring hedgehog (a) or Saturn-ring (b) defect types. As it can be seen in the corresponding schematics (figure 5.1b,d), the hedgehog defect appears as a dark circular spot on one side of the microdroplet, and oriented along the nematic director. As a result, the symmetry of the nematic director resembles that of an electric dipole. In contrast, the Saturn-ring defect displays a circular ring surrounding the microdroplet and features quadrupolar symmetry. In most of the experimental cells used in this work, it was found that the distribution of defects around the microdroplets was predominantly of the hedgehog type, while only a small fraction of inclusions (<1%) feature Saturn-ring defects. For the studies reported below, analyses are restricted to droplets of diameter less than 7μm. This includes the majority of the microdroplets, as shown in the size distribution plot in figure 5.1e, and these smaller inclusions are also less prone to be subjected to buoyancy effects. This effect tends to pin larger droplets, which are more difficult to displace under the AC field.

In figure 5.2a the geometry of the studied experimental system is shown. Water microdroplets are stabilized in the NLC matrix with sodium dodecyl sulphate (SDS). This surfactant provides strong homeotropic anchoring at the water/NLC interface, that is, the NLC molecules tend to orient perpendicular to the surface of the inclusions. The suspensions of SDS-stabilized aqueous microdroplets are enclosed between two transparent electrodes. The cell spacing (23μm) is chosen as a compromise to minimize the interactions of the inclusions with the cell substrates and to guarantee that most of the droplets where in the same observation plane.

In order to completely decouple the AC electrophoresis from any residual linear (DC) electrophoretic contribution, I used a NLC characterized by a negative dielectric anisotropy, i.e. the nematic director orients perpendicular

to the direction of the applied field. With this strategy, one can transport the inclusions always perpendicularly to the direction of the oscillating field.[24,25]

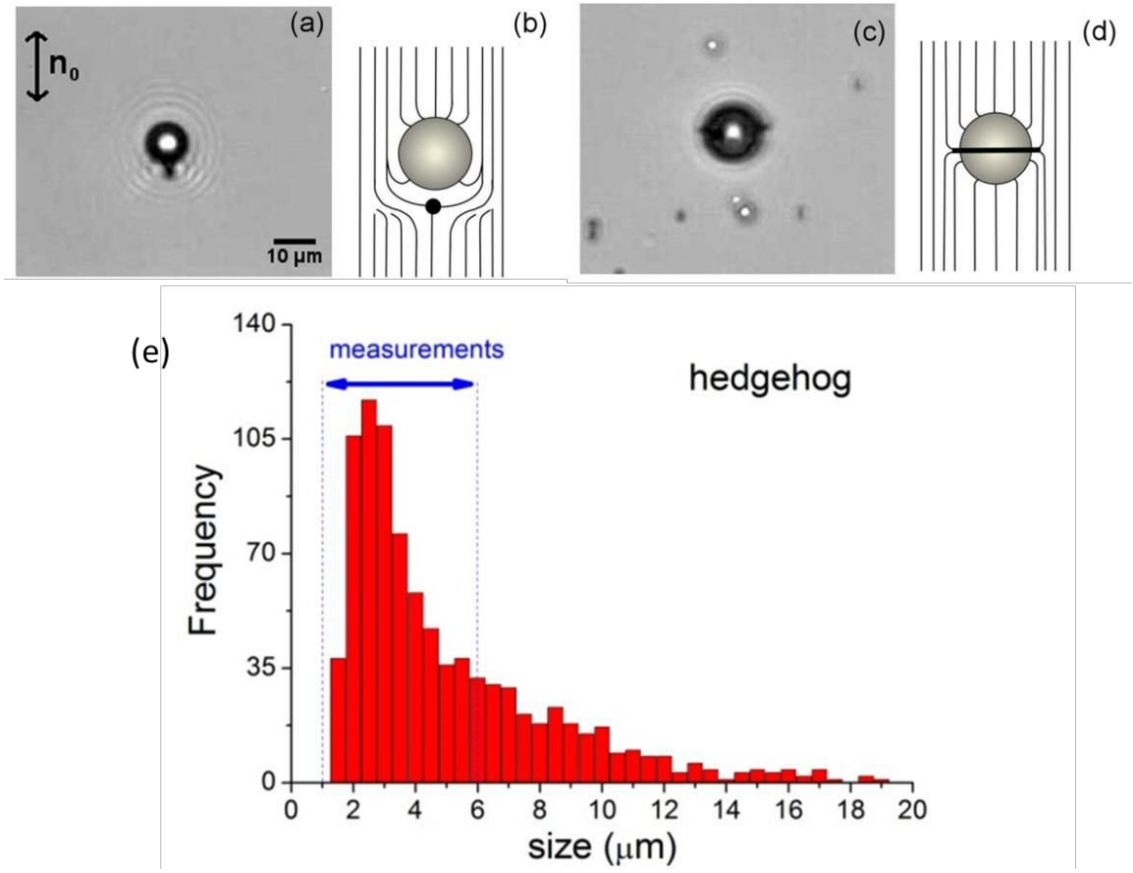

Figure 5.1: (a,c) Optical microscope images showing water microdroplets characterized by a dipolar hedgehog defect (a), and a quadrupolar Saturn-ring defect (c). In (a) the double arrow indicates the orientation of the director field n_0. (b) and (d) show schematics of the corresponding configurations of the nematic liquid crystal around the water droplets. (e) Histogram showing the typical population of particles with hedgehog defects in an experimental cell. The fraction of observed particles featuring a Saturn-ring was below 1%. Subsequent measurements were performed for droplet sizes between 1-6µm, as indicated in the image.

In this system, application of an external AC electric field between both electrodes sets the droplets in motion always with the point defect ahead, as shown in figure 5.2a. As it was reported by Lavrentovich and co-workers,[26] depending on the LC used the motion can be with the point defect ahead or

behind for the same particles and under the same conditions of applied field. After testing different liquid crystals, it is found that the motion of the microdroplets is with the point defect ahead for MLC-7029 or MLC-2037, and with the point defect behind for MBBA.

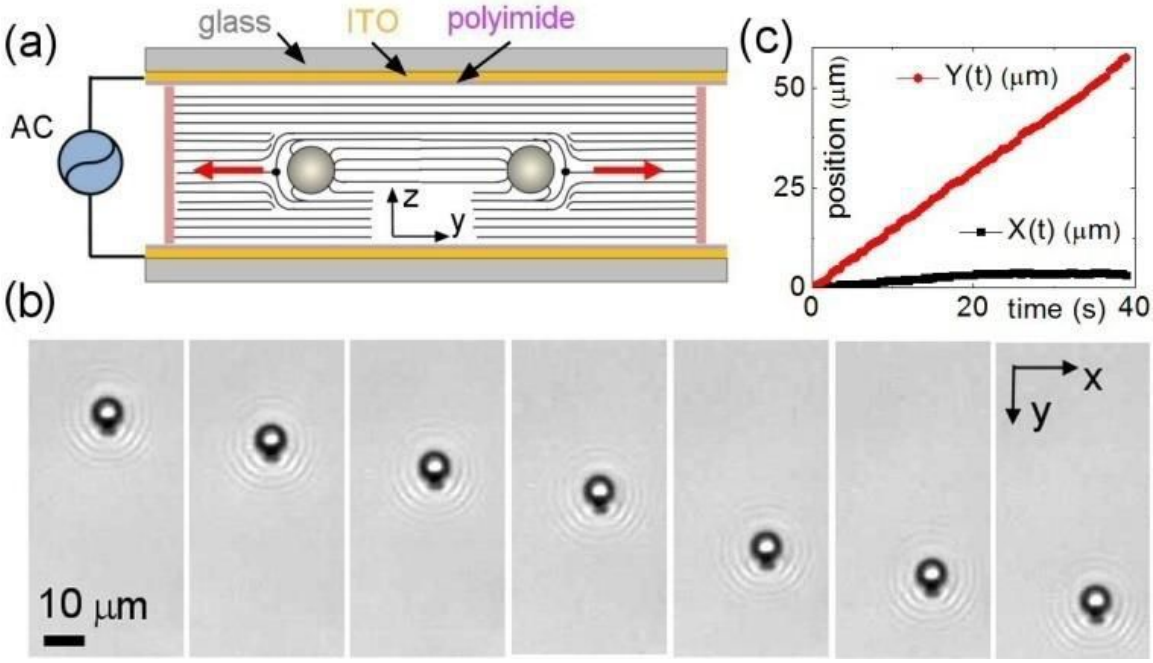

Figure 5.2: (a) Schematic of the experimental cell composed of water microdroplets dispersed in a nematic liquid crystal and enclosed between two transparent glass electrodes treated to induce surface planar anchoring. The water droplets are propelled by application of an AC electric field between the electrodes. (b) Optical micrographs taken every 4.5s of a water droplet having 6.5μm of diameter and propelled at a speed of 1.7μm/s by an AC field with amplitude E = 0.7V/μm and frequency f = 10 Hz. The corresponding video (video 5.1) can be found in the Additional Multimedia Content. (c) Positions (x,y) versus time of the droplet shown in panel (b).

One can characterize the transport properties of the microdroplets by measuring their average speed as a function of the strength E (figure 5.3a) and frequency f (figure 5.3b) of the applied field, and as a function of the droplet diameter ϕ for a fixed value of E and f (figure 5.3c). In the first case, one can

observe that the droplets start to move above a threshold field $E_0 \sim 0.5\,V/\mu m$ and that their speed increases quadratically with the field, $v \sim (E - E_0)^2$. This electrophoretic behavior in a nematic medium is in agreement with previous works,[24,26] where it was found that the first nonlinear term in the speed was quadratic, rather than cubic like in isotropic fluids.

A quadratic term allows using a symmetric AC field to move the particles in the medium, since changing the field polarity does not affect the particle speed. This quadratic behavior is further confirmed by fitting the experimental values shown in figure 5.3a to $v = \beta(E - E_0)^2$, which leads to the threshold field strength $E_0 = 0.49\,V/\mu m$. Also, it is found that the dependence of the droplets' velocity on the frequency of the applied AC field can be well described by invoking the Liquid Crystal-Enabled Electrophoresis (LCEEP) model, which was originally developed for isotropic fluids with the name of induced-charge electro-osmosis (ICEO) (see chapter 1 section 1.4.1). Following the model developed by Squires and Bazant,[27] the dependence of the velocity of the electrodynamically induced flow with the driving frequency can be described by the following equation:

$$v(\omega) = v_0 \frac{\omega^2 \tau_e^2}{(1 + \omega^2 \tau_c^2)(1 + \omega^2 \tau_e^2)} \qquad \text{eqn (5.1)}$$

being $\omega = 2\pi f$. As proposed by Lavrentovich *et al*,[26] this equation can also be used to describe the velocity of a particle in LCEEP, where v_0 contains a quadratic dependence with the amplitude of the applied electric field, consistently with the data trend shown in figure 5.3a. In eqn (5.1), $\tau_c = \lambda_D \phi / 2D$ is the droplet charging time and $\tau_e = \lambda_D L / 2D$ is the electrode charging time, due to the applied electric field. Here the diameter of the droplet is $\phi = 5\mu m$, and the distance between the electrodes is $L = 23\mu m$, which gives the ratio $\tau_e / \tau_c = L/\phi = 4.6$. Unknown parameters are λ_D, which is the Debye screening length of the droplet in the NLC, and D the diffusion coefficient of the ions. From the nonlinear fit of the experimental data, it is found that $v_0 = 11.5\mu m \cdot s^{-1}$, $\tau_e \sim 0.09s$, and $\tau_c \sim 0.02s$, which gives a ratio $\lambda_D / D = 0.008 s/\mu m$.

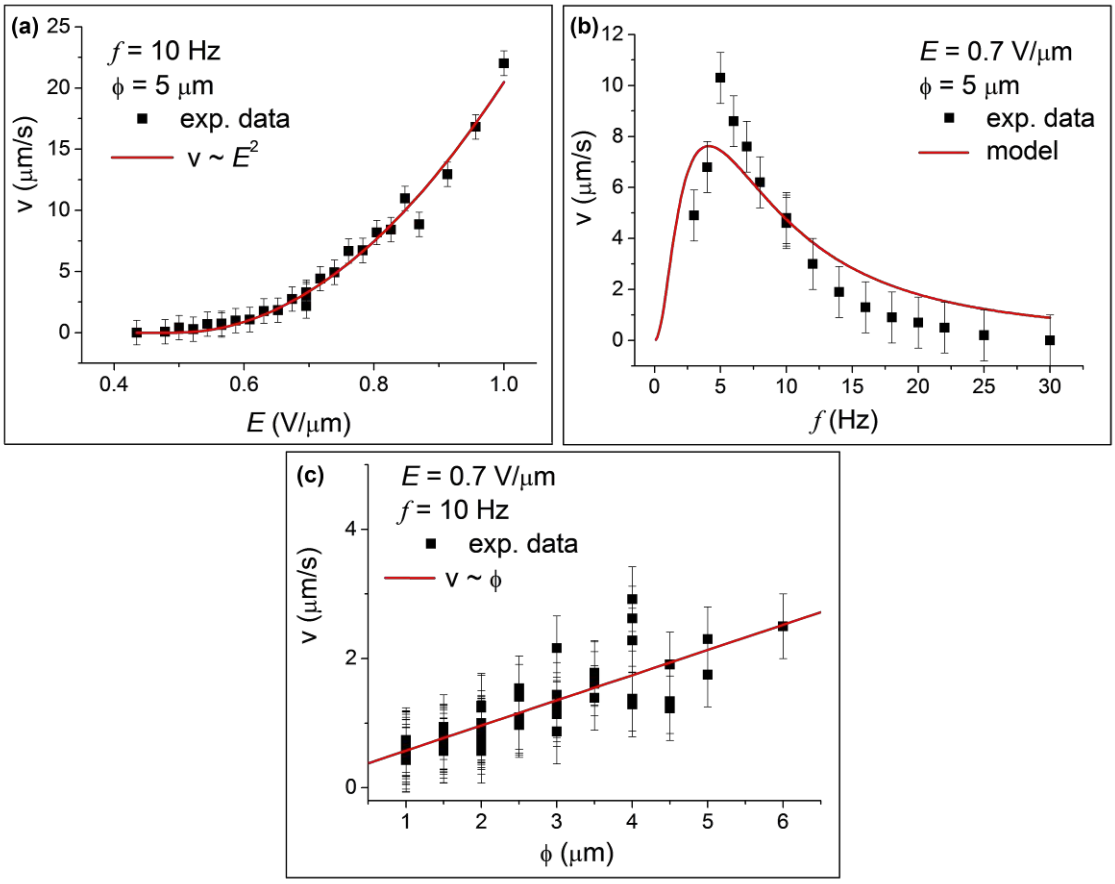

Figure 5.3: (a) Mean velocity v versus field strength E of an applied AC field with frequency f = 10Hz for a microdroplet with diameter $\phi = 5\mu m$. (b) v versus frequency f of a $\phi = 5\mu m$ water droplet subjected to an applied AC field with strength E = 0.7V/μm. (c) v versus size ϕ for microdroplets driven by an applied field of f = 10 Hz and E = 0.7V/μm. For images (a) and (b), the continuous red lines denote fits following the equations described in the text, while in (c) it denotes a linear relationship between speed and size.

Considering that only symmetric monovalent ions are present in the NLC, one can estimate the Debye screening length λ_D of the system by using the following equation (see chapter 1 section 1.2.2):[28,29]

$$\lambda_D = \sqrt{\frac{\varepsilon_r \varepsilon_0 k_B T}{n^0 e^2}} \qquad \text{eqn (5.2)}$$

where $k_B = 1.38 \cdot 10^{-23} J/K$ is the Boltzmann constant and $e = 1.60 \cdot 10^{-19} C$ is the charge of an electron. For the NLC media, $\varepsilon_r = (\varepsilon_{r\parallel} + \varepsilon_{r\perp})/2 = 5.4$, T = 298K, and the number of monovalent ions per cubic meter in the NLC is in the

range of $n^0 = [10^{19} - 10^{20}]m^{-3}$,[30] which leads to $\lambda_D \sim [0.3 - 0.9]\mu m$. The fitted value λ_D/D is consistent with the previous range of values of λ_D, giving typical values of D in the range of $[10^{-10} - 10^{-11}]m^2 s^{-1}$.[31]

Larger droplets induce stronger distortions of the nematic director, thus enabling higher electrophoretic speed. However, it is also true that larger microdroplets would present higher friction, so their speed should decrease with their size. This reflects the complexity of the phenomenon. Nevertheless, it is experimentally demonstrated, as shown in figure 5.3c, that an increase of the size of the microdroplets, leads to a linear increase of their velocity, for a fixed strength and frequency of the applied field. Consequently, it seems that the stronger distortion effect is predominant over the higher friction.

I next demonstrate that these liquid droplets can be effectively used as microcarriers to transport, mix or disperse solid particles or femtoliter volumes of aqueous solutions. First, one can observe that microdroplets with Saturn ring defects, although immobile, distort the motion of neighboring droplets with point defects. The attraction between dipolar and quadrupolar droplets is long range and mediated by the elastic distortion of the nematic medium.[32,33] This property can be used to realize a localized cargo release operation, as shown in figure 5.4a. In particular, one microdroplet is previously loaded with polystyrene particles having 1.7μm diameter, and driven by an AC field towards a larger droplet characterized by a Saturn ring defect. The large droplet attracts the small one, and they coalesce releasing the colloidal cargo into a larger volume of fluid.

Droplets with point defects feature highly anisotropic interactions**.** In particular, a microdroplet with a point defect can be considered as a dipole, with one charge located on the point defect and the other, of opposite sign, located inside the droplet. In general, two approaching inclusions in the NLC will thus try to assemble with the defects in opposite sides.[34] In the case studied here, it is found that when driven towards each other, the microdroplets deviate from their collision trajectory. After crossing, their dipolar defects are in

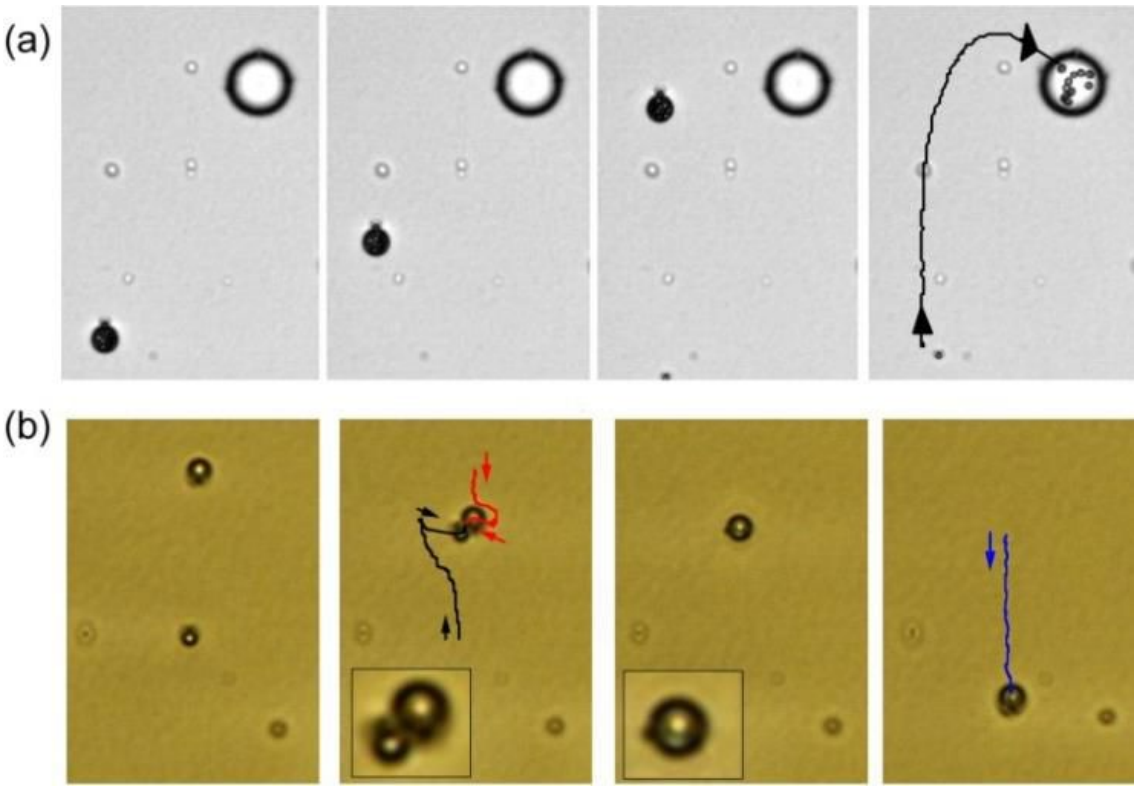

Figure 5.4: (a) Sequence of images showing the absorption of a microdroplet ($\phi = 7.3\mu m$), filled with 11 polystyrene particles (diameter 1.7µm), by a larger droplet ($\phi = 18\mu m$) with a Saturn ring defect (E = 0.7V/µm, f = 10Hz). Time interval between images is 17.2s. (b) Microscope images showing two water microdroplets ($\phi = 2.7\mu m$ and $3.7\mu m$) driven in opposite directions by an AC field (E = 0.7V/µm, f = 10Hz) and containing the separated reactants, potassium hexacyanoferrate(II) (0.2M) and iron(III) chloride solution (0.3 M). The droplets approach and coalesce in a larger one ($\phi = 4.3\mu m$), forming Prussian blue [Iron(III) hexacyanoferrate(II)] as a precipitate. The AC field then drives the resulting droplet away from the reaction zone. Total elapsed time is 46s. The corresponding videos (video 5.2 and video 5.3) can be found in the Additional Multimedia Content.

antiparallel configuration, and the two droplets attract and coalesce into a larger one. In figure 5.4b this feature is used to realize a chemical reaction by coalescing two water droplets doped with aqueous solutions of the reactants, potassium hexacyanoferrate(II) in one droplet and iron(III) chloride in the other, in order to obtain Prussian blue [Iron(III) hexacyanoferrate(II)],

$$4FeCl_{3\,(aq)} + 3K_4[Fe(CN)_6]_{(aq)} \rightarrow Fe_4[Fe(CN)_6]_3 \downarrow + 12KCl_{(aq)}$$

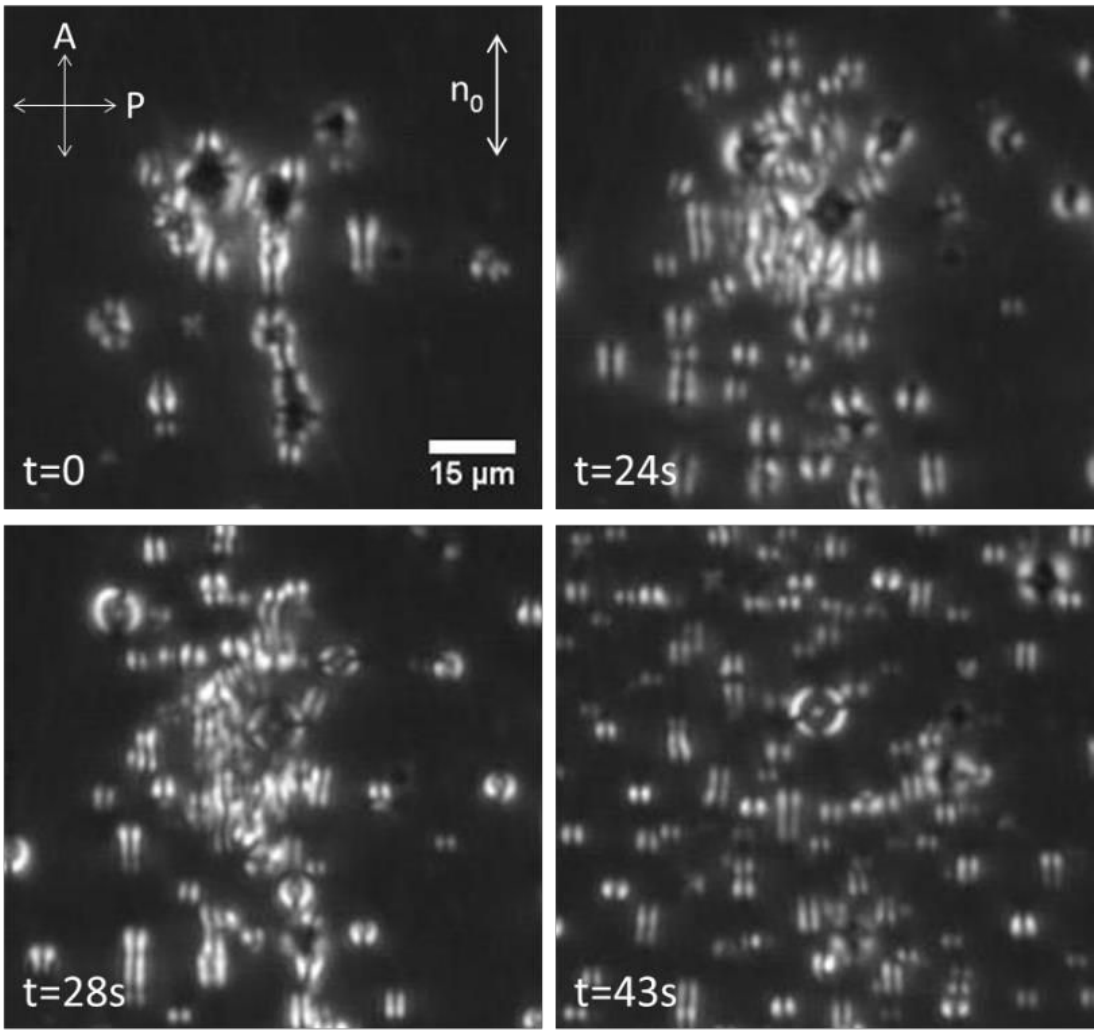

Figure 5.5: Images between crossed polarizers of small droplets (~1µm) accumulated around bigger Saturn ring droplets (~15µm) by a sinusoidal electric field of 0.65V/µm and 20Hz. Small droplets are expelled when the electric field is switched from 20Hz to 3Hz (t=0). The direction of the director field n_0 and the analyser A and polarizer P are indicated in the top left panel. The corresponding video (video 5.4) can be found in the Additional Multimedia Content.

The resulting droplet shows the typical dark-blue precipitate of Iron(III) hexacyanoferrate(II) (slightly blue shadow at the bottom of the droplet), and after defect rearrangement, it quickly transforms back into a hedgehog defect, allowing to drive the reaction product to a desired location of the experimental platform. The process shown in figure 5.4b is only an example of localized microreactions which can be performed with this technique.

This system also allows exploring different self-assembly scenarios under AC fields. In particular, upon modification of the experimental protocol by introducing an ultrasonication step on the NLC emulsion formation, one is able to further reduce the size of the microdroplets. It is then found that smaller water droplets, with diameters below 1μm, are less prone to coalesce. As shown in figure 5.5 (and in video 5.4 in the Additional Multimedia Content), application of the AC field is able to accumulate smaller droplets around bigger Saturn ring ones without coalescence. By decreasing the frequency, the droplets are released in the nematic medium, and they expand through a large area.

All these results open up new perspectives in the transport of water-miscible chemicals or drugs, and also an alternative approach to microreactors based in soft matter science.

5.3.2 LCEEP of Photosensitive Particles

The LCEEP efficiency is mainly conditioned by the nature of the defects of the NLC surrounding the inclusions. By tuning the anchoring conditions at the particle surface, one can control the generated defects, which in turn induce the LCEEP on the particles. In this section, the anchoring conditions are light-controlled by means of an azoderivative molecule grafted on the surface of the dispersed silica particles. As shown in figure 5.6, this azoderivative has two isomers, *trans* and *cis*, that can be interconverted by irradiation of blue (455nm) or UV (365nm) light respectively. The used azoderivative induces homeotropic (perpendicular) alignment in its *trans* form, and planar alignment in its *cis* form, as it is also found in the literature for similar azoderivatives.[20,21]

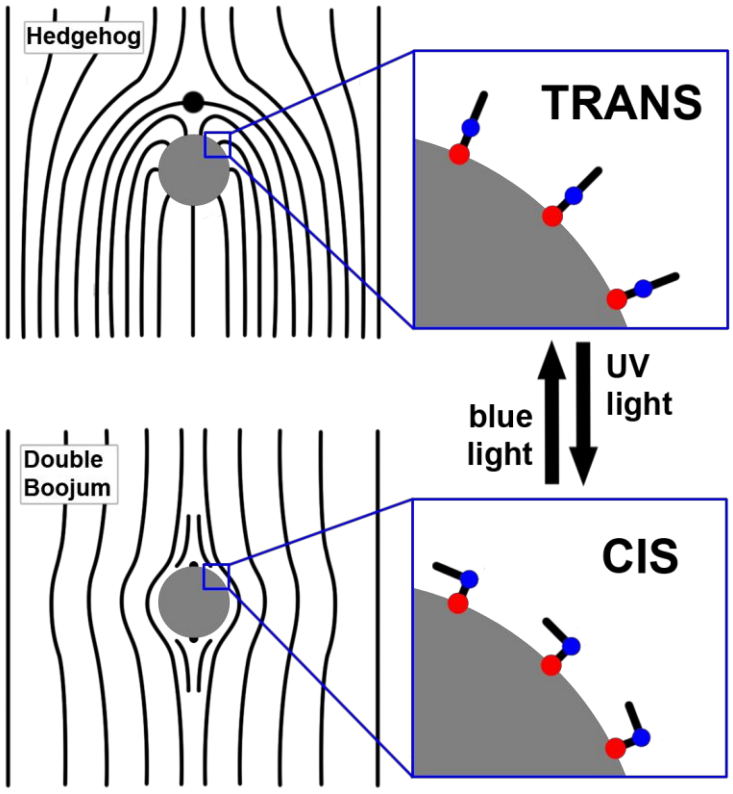

Figure 5.6: Schematics showing the two different alignments corresponding to the *trans* (up) and *cis* (bottom) isomers of the photoswitchable azoderivative bound at the surface of the particles. Black lines stand for NLC director field around the inclusions (represented by grey circles), while in the enlargements, the azoderivative molecules are represented by straight and bent sticks.

First I studied the response of the photosensitive particles immersed in the NLC to the blue and UV irradiation. Initially, under no illumination, the particles present homeotropic anchoring with a hedgehog defect (dipolar, asymmetric defect) as shown in figures 5.7a,b. When these particles are irradiated with UV light (365nm) for 1-3 seconds, their defect configuration changes to a double Boojum (quadrupolar, symmetric defect), a configuration typically found in colloidal particles characterized by a planar anchoring (figure 5.7c,d). It is worth noticing that there is no need of continuous irradiation, as the double Boojum configuration is stable for tens of minutes once formed. If the particles are then exposed with blue light (455nm), the hedgehog configuration reappears.

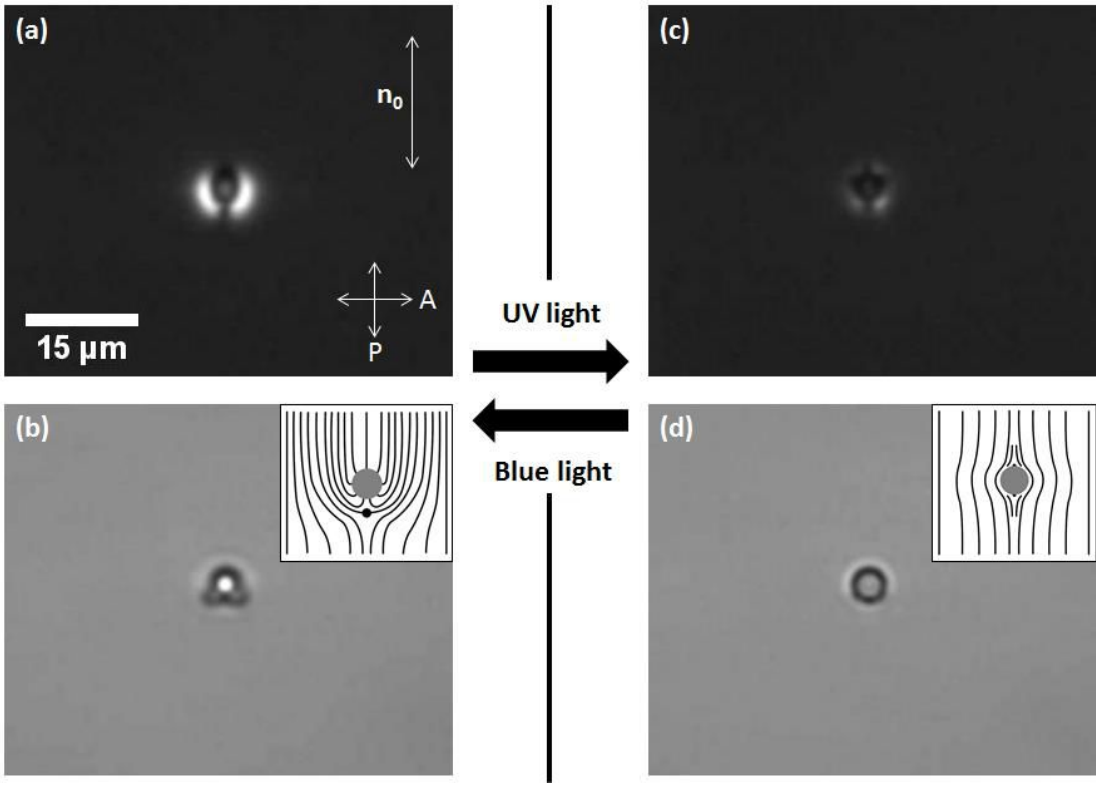

Figure 5.7: Images between crossed polarizers (a,c) and under bright field (b,d) of the two different defects around photosensitive particles. Hedgehog defect (a,b) is formed under irradiation of blue (455nm) light or under room light conditions, while double Boojum defect (c,d) is formed under UV (365nm) light. In panel (a) is indicated the crossed orientation of the polarizers P,A and the orientation of the NLC director field n_0. Insets in panels (b,d) show schemes of hedgehog and double Boojum defects, respectively.

When returning to the hedgehog configuration, one would expect that the dipolar defect should form indistinctly at either side of the particles with equal probability. Nevertheless, if the particles are subjected to cyclic *cis-trans* isomerizations, it is observed that the hedgehog defect always forms at the same side for each particle (see video 5.5 in the Additional Multimedia Content). This could be due to two different reasons. One possibility may be the incomplete *cis* isomerization. Some residual azoderivative molecules in the particle surface do not isomerize to the *cis* form under UV irradiation, probably owing to unequal illumination of the particle surface. The other possibility is that the anchoring angle of the NLC molecules on the *cis* molecules at the particle surface is not fully planar. In either case, this results in maintaining a memory of the location of the previous dipolar defect. When the *cis* molecules are isomerized back to the *trans* form, this memory effect determines the position of the hedgehog defect.

Being able to change the director field configuration on the photosensitive particles immersed in the NLC, the next step is to try LCEEP on these particles. Indeed, when an AC field is applied to the cell, these particles start to move, as long as they present a dipolar hedgehog configuration (i.e. the azoderivative is in its *trans* isomer, in blue light conditions). When the electrophoretic NLC cell is locally irradiated a few seconds with UV light, the illuminated particles change the nature of their defect from dipolar to quadrupolar, and become arrested under the AC field. If these particles are irradiated with blue light, they recover the dipolar hedgehog defect form and the particles start to propel again. An example of this phenomenon can be found in figure 5.8 and also in video 5.6 in the Additional Multimedia Content.

Due to the previously mentioned memory effect, it was not possible to change the side of the hedgehog defect around a particle. This drawback avoids changing the direction of motion of these particles under LCEEP, limiting their dynamics towards one direction. More studies with different types of

azoderivatives may be interesting in order to get full control and better performance of the photosensitive inclusions during LCEEP.

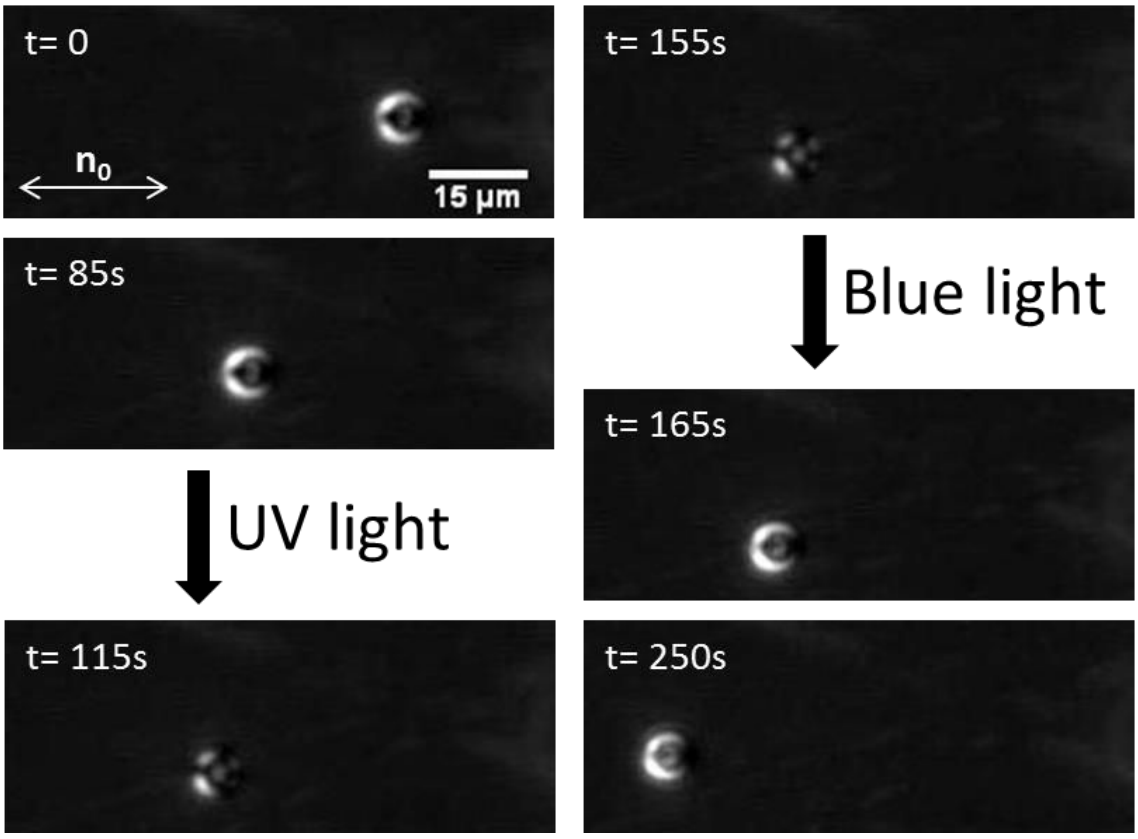

Figure 5.8: Image sequence between crossed polarizers of a photosensitive particle translating in an electrophoretic NLC cell. An AC field of E= 0.7V/µm and f=25Hz is applied between the cell plates for the entire duration of the experiment. The particle, which initially has a dipolar hedgehog configuration, starts to move. At t=115s it is irradiated with UV light (365nm) and the defect configuration changes to a quadrupolar double Boojum, and thus the particle stops moving. At t=165s it is transformed back into a dipolar hedgehog configuration with blue light (455nm), and motion is restored. In the initial image, n_0 marks the orientation of the NLC director field. Corresponding video (video 5.6) can be found in the Additional Multimedia Content.

5.4 Conclusions

- I have demonstrated several strategies to transport, react and assemble microdroplets of aqueous solutions driven by AC electric fields in a nematic liquid crystal medium, opening up new perspectives for controlled transport of water miscible chemicals or drugs.

- This process can be described by the model of Liquid Crystal-Enabled Electrophoresis, although the actual mechanism that drives the liquid inclusions has still some pending questions, such as how the nature of the NLC determines the direction of motion of the dipolar droplets with respect to the position of the hedgehog defect.

- It is possible to locally control the NLC director field around photosensitive particles by means of irradiation with blue or UV light. This light control of the defect configuration enables activation or inhibition of LCEEP on these particles by reversibly changing from a dipolar (moving) to a quadrupolar (arrested) configuration of the defects around the inclusions.

5.5 Additional Multimedia Content

Four video files can be found in the following web page:

http://tinyurl.com/phd-shn-chapter5

- Video 5.1 shows a water droplet with 6.5μm of diameter propelled at a speed of 1.7μm/s by an AC field with amplitude E = 0.7V/μm and frequency f = 10Hz, corresponding to figure 5.2b.

- Video 5.2 shows the absorption of a microdroplet (ϕ = 7.3μm), filled with 11 polystyrene particles (1.7μm diameter), by a larger droplet (ϕ = 18μm) with a Saturn ring defect (E = 0.7V/μm, f = 10Hz), corresponding to figure 5.4a.

- Video 5.3 shows the reaction between two water microdroplets (ϕ = 2.7μm and 3.7μm) driven in opposite directions by an AC field (E = 0.7V/μm, f = 10Hz). The droplets approach and coalesce in a larger one (ϕ = 4.3μm), forming Prussian blue [Iron(III) hexacyanoferrate(II)] as a precipitate (slightly blue shadow at the bottom-left inside of the resulting droplet). In this particular example, the field is momentarily switched off to facilitate the assembly of the droplets. The AC field is then used to prompt coalescence and to drive the resulting droplet away from the reaction zone. This video corresponds to figure 5.4b.

- Video 5.4 shows several small microdroplets (ϕ ~ 1μm) which are accumulated around larger ones (ϕ ~ 15μm) with a Saturn ring defect via application of an AC field with strength E = 0.65V/μm and frequency f = 20Hz (duration 45s), and later are dispersed with no coalescence (duration 40s) by decreasing the frequency of the field to f = 3Hz. To better visualize the small droplets, the video was recorded with crossed polarizers. This video corresponds to figure 5.5.

- Video 5.5 (speed x10) shows 11 cycles of the *trans-cis-trans* isomerization of two photosensitive particles (diameter 5μm) dispersed in the nematic liquid crystal MLC-7029. *Trans-cis* and *cis-trans* isomerization are achieved by a few seconds irradiation with blue (455nm) or UV (365nm) light, respectively (power density 0,1W/cm^2). This video was recorded with crossed polarizers.

- Video 5.6 (speed x25) shows the control of LCEEP in a photosensitive particle by means of light. Initially the particle moves, presenting a dipolar hedgehog configuration. When UV (365nm) light is irradiated, the defect configuration changes to a quadrupolar double Boojum and the particle stops. Irradiation with blue (455nm) light makes the particle adopt a dipolar hedgehog once more, so it starts to move again. An AC sinusoidal electric field of strength E = 0.7V/μm and frequency f = 25Hz is applied during all the experiment. This video was recorded with crossed polarizers.

5.6 References

(1) Stone, H. A.; Stroock, A. D.; Ajdari, A. Engineering Flows in Small Devices: Microfluidics toward a Lab-on-a-Chip. *Annu. Rev. Fluid Mech.* **2004**, *36*, 381–411.

(2) Squires, T. M.; Quake, S. R. Microfluidics: Fluid Physics at the Nanoliter Scale. *Rev. Mod. Phys.* **2005**, *77*, 977–1026.

(3) Song, H.; Chen, D. L.; Ismagilov, R. F. Reactions in Droplets in Microflulidic Channels. *Angew. Chemie-international Ed.* **2006**, *45*, 7336–7356.

(4) Shim, J.; Cristobal, G.; Link, D. R.; Thorsen, T.; Jia, Y.; Piattelli, K.; Fraden, S. Control and Measurement of the Phase Behavior of Aqueous Solutions Using Microfluidics. *J. Am. Chem. Soc.* **2007**, *129*, 8825–8835.

(5) Buhr, D. L.; Acca, F. E.; Holland, E. G.; Johnson, K.; Maksymiuk, G. M.; Vaill, A.; Kay, B. K.; Weitz, D. A.; Weiner, M. P.; Kiss, M. M. Use of Micro-Emulsion Technology for the Directed Evolution of Antibodies. *Methods* **2012**, *58*, 28–33.

(6) Paxton, W. F.; Kistler, K. C.; Olmeda, C. C.; Sen, A.; St. Angelo, S. K.; Cao, Y.; Mallouk, T. E.; Lammert, P. E.; Crespi, V. H. Catalytic Nanomotors: Autonomous Movement of Striped Nanorods. *J. Am. Chem. Soc.* **2004**, *126*, 13424–13431.

(7) Fournier-Bidoz, S.; Arsenault, A. C.; Manners, I.; Ozin, G. A. Synthetic Self-Propelled Nanorotors. *Chem. Commun.* **2005**, 441–443.

(8) Sanchez, S.; Solovev, A. A.; Mei, Y.; Schmidt, O. G. Dynamics of Biocatalytic Microengines Mediated by Variable Friction Control. *J. Am. Chem. Soc.* **2010**, *132*, 13144–13145.

(9) Howse, J. R.; Jones, R. A. L.; Ryan, A. J.; Gough, T.; Vafabakhsh, R.; Golestanian, R. Self-Motile Colloidal Particles: From Directed Propulsion to Random Walk. *Phys. Rev. Lett.* **2007**, *99*, 48102.

(10) Gao, W.; Pei, A.; Wang, J. Water-Driven Micromotors. *ACS Nano* **2012**, *6*, 8432–8438.

(11) Poulin, P.; Stark, H.; Lubensky, T. C.; Weitz, D. A. Novel Colloidal Interactions in Anisotropic Fluids. *Science* **1997**, *275*, 1770–1773.

(12) Loudet, J. C.; Barois, P.; Poulin, P. Colloidal Ordering from Phase Separation in a Liquid-Crystalline Continuous Phase. *Nature* **2000**, *407*, 611–613.

(13) Musevic, I.; Skarabot, M.; Tkalec, U.; Ravnik, M.; Zumer, S. Two-Dimensional Nematic Colloidal Crystals Self-Assembled by Topological Defects. *Science* **2006**, *313*, 954–958.

(14) Lapointe, C. P.; Mason, T. G.; Smalyukh, I. I. Shape-Controlled Colloidal Interactions in Nematic Liquid Crystals. *Science* **2009**, *326*, 1083–1086.

(15) Koenig, G. M.; Lin, I.-H.; Abbott, N. L. Chemoresponsive Assemblies of Microparticles at Liquid Crystalline Interfaces. *Proc. Natl. Acad. Sci.* **2010**, *107*, 3998–4003.

(16) Wood, T. A.; Lintuvuori, J. S.; Schofield, A. B.; Marenduzzo, D.; Poon, W. C. K. A Self-Quenched Defect Glass in a Colloid-Nematic Liquid Crystal Composite. *Science* **2011**, *334*, 79–83.

(17) Burylov, S. V; Raikher, Y. L. Orientation of A Solid Particle Embedded In A Monodomain Nematic Liquid-Crystal. *Phys. Rev. E* **1994**, *50*, 358–367.

(18) Stark, H. Physics of Colloidal Dispersions in Nematic Liquid Crystals. *Phys. Rep.* **2001**, *351*, 387–474.

(19) Martinez, A.; Mireles, H. C.; Smalyukh, I. I. Large-Area Optoelastic Manipulation of Colloidal Particles in Liquid Crystals Using Photoresponsive Molecular Surface Monolayers. *Proc. Natl. Acad. Sci.* **2011**, *108*, 20891–20896.

(20) Ichimura, K.; Suzuki, Y.; Seki, T.; Hosoki, A.; Aoki, K. Reversible Change in Alignment Mode of Nematic Liquid Crystals Regulated Photochemically by "Command Surfaces" Modified with an Azobenzene Monolayer. *Langmuir* **1988**, *4*, 1214–1216.

(21) Aoki, K.; Tamaki, T.; Seki, T.; Kawanishi, Y.; Ichimura, K. Regulation of Alignment of Cyanobiphenyl Liquid Crystals by Azobenzene Molecular Films. *Langmuir* **1992**, *8*, 1014–1017.

(22) Yamamoto, T.; Tabe, Y.; Yokoyama, H. Photochemical Transformation of Topological Defects Formed around Colloidal Droplets Dispersed in Azobenzene-Containing Liquid Crystals. *Colloids Surfaces A Physicochem. Eng. Asp.* **2009**, *334*, 155–159.

(23) Crusats, J.; Albalat, R.; Claret, J.; Ignés-Mullol, J.; Sagués, F. Influence of Temperature and Composition on the Mesoscopic Textures of Azobenzene Langmuir Monolayers. *Langmuir* **2004**, *20*, 8668–8674.

(24) Lazo, I.; Lavrentovich, O. D. Liquid-Crystal-Enabled Electrophoresis of Spheres in a Nematic Medium with Negative Dielectric Anisotropy. *Philos. Trans. R. Soc. A-mathematical Phys. Eng. Sci.* **2013**, *371*, 20120255.

(25) Hernàndez-Navarro, S.; Tierno, P.; Ignés-Mullol, J.; Sagués, F. Breaking the Degeneracy of Nematic Liquid Crystals by Means of Actuated Anisometric Paramagnetic Colloids. *Soft Matter* **2011**, *7*, 5109–5112.

(26) Lavrentovich, O. D.; Lazo, I.; Pishnyak, O. P. Nonlinear Electrophoresis of Dielectric and Metal Spheres in a Nematic Liquid Crystal. *Nature* **2010**, *467*, 947–950.

(27) Squires, T. M.; Bazant, M. Z. Induced-Charge Electro-Osmosis. *J. Fluid Mech.* **2004**, *509*, 217–252.

(28) Robinson, R.; Stokes, R. *Electrolyte Solutions*; Dover Publications: Mineola, NY, 2002; p. 76.

(29) Hiemenz, P. C.; Rajagopalan, R. *Principles of Colloid and Surface Chemistry*; Marcel Dekker: New York, 1997.

(30) Naito, H.; Yoshida, K.; Okuda, M.; Sugimura, A. Transient Current Study of Ultraviolet-Light-Soaked States In N-Pentyl-P-N-Cyanobiphenyl. *Jpn. J. Appl. Phys.* **1994**, *33*, 5890–5891.

(31) Dunmur, D. A.; Fukuda, A.; Luckhurst, G. R. *Physical Properties of Liquid Crystals: Nematics*; INSPEC, Ed.; 2001; pp. 460–461.

(32) Ognysta, U.; Nych, A.; Nazarenko, V.; Skarabot, M.; Musevic, I. Design of 2D Binary Colloidal Crystals in a Nematic Liquid Crystal. *Langmuir* **2009**, *25*, 12092–12100.

(33) Eskandari, Z.; Silvestre, N. M.; Tasinkevych, M.; Telo da Gama, M. M. Interactions of Distinct Quadrupolar Nematic Colloids. *Soft Matter* **2012**, *8*, 10100–10106.

(34) Yada, M.; Yamamoto, J.; Yokoyama, H. Direct Observation of Anisotropic Interparticle Forces in Nematic Colloids with Optical Tweezers. *Phys. Rev. Lett.* **2004**, *92*, 185501.

CHAPTER 6

RECONFIGURABLE SWARMS OF COLLOIDAL PARTICLES CONTROLLED BY PHOTOACTIVATED SURFACE PATTERNS

6.1 Introduction

In the previous chapter, I presented the unidirectional controlled transport of inclusions of different nature driven by LCEEP. The propelled inclusions followed the fixed NLC director field orientation, which was determined by the planar directional boundary conditions on the cell plates. That system was only able to transport the inclusions in straight trajectories, thus being less effective compared to other microfluidics systems.[1,2] While strategies to steer fluids are well established through the use of photolithographic networks, further versatility of integrated lab-on-a-chip devices demands the ability to transport femtosized volumes of solid[3] or liquid[4] chemical cargo using approaches that allow to externally command their collective dynamics and assembly without relying on permanent geometrical constraints. Different strategies, such as holographic tweezers or the formation of localized chemical gradients, are used in the literature to drive individual colloids dispersed in a liquid,[5–12] and to command their assembly,[13–15] although the control and large-scale addressability of collections of motile inclusions has proven challenging to realize.

In this chapter, I present an electro-optical technique that permits to remotely address the reversible assembly and collective transport of micrometer-sized colloidal inclusions of arbitrary shape and composition, either solid or liquid, dispersed in a thin NLC film. Liquid Crystal-Enabled Electrophoresis (LCEEP)[16] is used to propel the colloidal inclusions embedded in a NLC cell, and a photosensitive anchoring layer is used to modify the local director field, which, in turn, sets the direction of colloidal motion. With this technique, one can assemble or disassemble swarms, and control their placement and motion over arbitrary paths on a surface. In addition, as a demonstration of the huge potentiality this technique exhibits, several interesting applications are presented in the last part of this chapter, such as particle segregation or the formation of particle jets.

6.2 Experimental Procedures

The NLC cells for the electrophoretic experiments consist of two functionalized ITO-coated glass plates glued together separated a few microns (13-46μm) by polyethylene terephthalate (Mylar, Goodfellow) spacers. One of the two plates is chemically functionalized with an azosilane monolayer, as described in chapter 2 section 2.1.4, and the counterplate is spin-coated with a polyimide film to obtain strong homeotropic (perpendicular) alignment of the liquid crystal molecules (figure 6.1a). Commercial polystyrene anisometric particles (pear-shaped, Magsphere, typically 3x4μm^2, although 8.3x10.2μm^2 are used in some tests), are dispersed in the nematic liquid crystal MLC-7029 as explained in chapter 2 section 2.2.3. NLC cells are then filled by capillary action with freshly prepared dispersions.

For the particle jet formation, directional planar alignment counterplates are used instead. Homeotropic silica spheres (see chapter 2 section 2.2.2) are used in these cells to minimize particle sticking on the surfaces.

AC sinusoidal electric fields are applied to NLC cell plates via electric contacts using a function generator (ISO-TECH IFA 730) coupled to a voltage amplifier (TREK model PZD700). Amplitudes range from 0 to 50 Volt peak to peak, while frequencies range from 3 to 50Hz. Bright field and polarized optical images are captured with an AVT Marlin F-131B CMOS camera controlled with the software AVT SmartView 1.10.2. Digitized images are subsequently processed and analyzed using software packages ImageJ, IgorPro, and Matlab.

Irradiation of the samples at wavelengths of 455nm and 365nm is performed by means of a custom-built LED epi-illumination setup integrated into an optical microscope (see chapter 2 section 2.3.3). Typical irradiated light power densities is 1W/cm^2 and 0.1W/cm^2 for blue and UV light respectively, measured using an optical power meter (S120A Optical Power Meter System, Thorlabs Inc.). The irradiated spot has a size below 1mm, and the irradiation decreases as the distance from the center of the spot increases.

6.3 Results and Discussion

6.3.1 Reconfigurable Swarm Formation: Aster and Mill

As explained in the previous section, one of the plates is functionalized with a photosensitive self-assembled azosilane monolayer in order to induce, upon illumination, an alternation between homeotropic (perpendicular) or planar (tangential) boundary conditions (anchoring).

Without external influences, the NLC features uniform homeotropic anchoring. By irradiation with UV light (365 nm), the azosilane monolayer is forced to adopt the *cis* (planar) configuration, which can be easily reverted to a *trans* (homeotropic) configuration when using blue light (455 nm) illumination. For this study, a NLC with negative dielectric anisotropy (that is, it aligns perpendicular to an applied electric field) is employed. This leads to degenerate planar alignment conditions upon application of an electric field perpendicular to the glass plates, since all in-plane orientations for the director field are energetically equivalent (in the same way as explained in chapter 4, section 4.3.1). This feature enables to address locally the orientation of the NLC director field. Taking advantage of this degenerate planar alignment, one can generate centers of attraction to accumulate particles by previous irradiation with UV light.

The basic protocol to form particle swarms is as follows: when a UV light spot is shined onto the LC cells, the irradiated azosilane molecules isomerize from a *trans* initial state to a *cis* configuration. They develop a radial pattern due to the intensity profile. As a result, a hybrid NLC anchoring is obtained: homeotropic on the top plate, and radially planar on the bottom plate (figure 6.1a,b). Application of an AC field amplitude above 2.2V, which corresponds to the Fredericks transition, forces the NLC molecules to adopt a planar orientation, extending the previously imprinted radial pattern up to a few millimeters (figure 6.1c). By further increasing the amplitude of the AC field, the dispersed particles, which have also tumbled to planar orientation

following the NLC, move due to LCEEP in the direction determined by the local LC director (figure 6.1c,d).

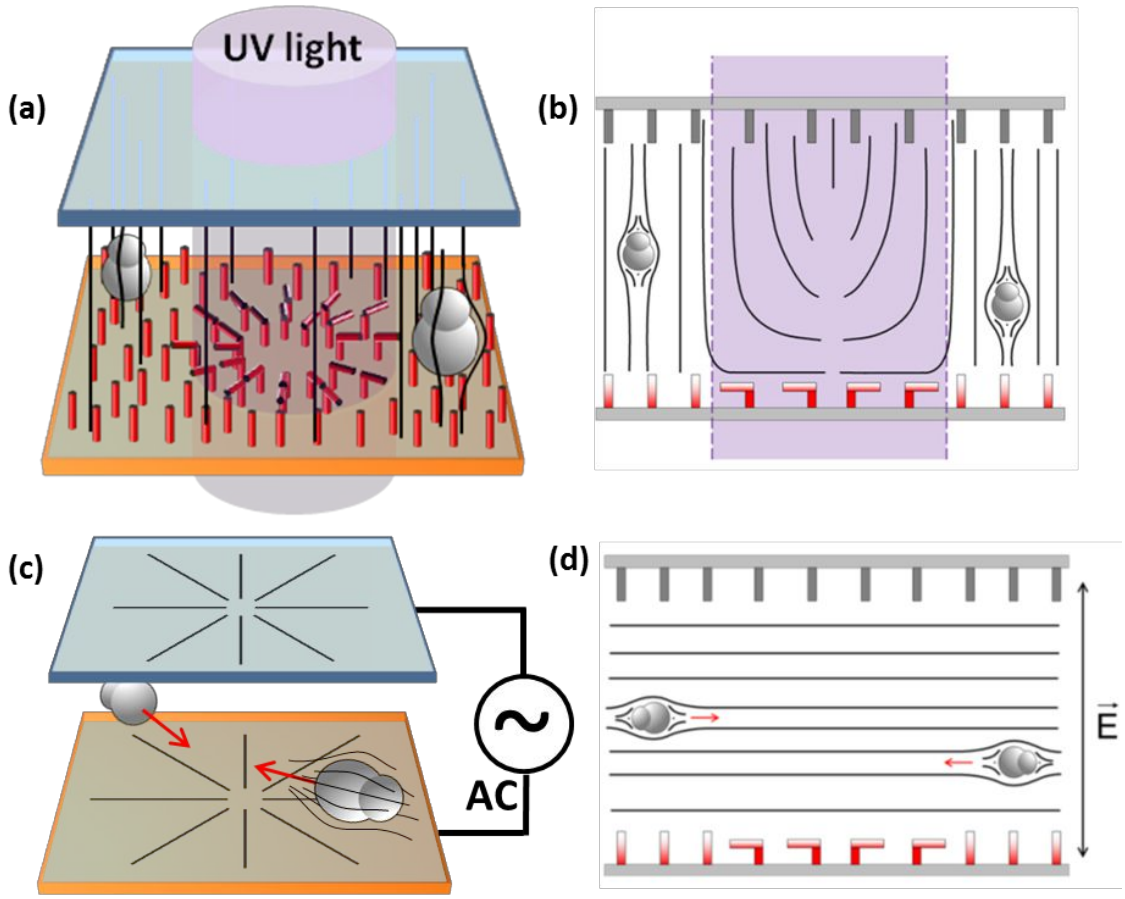

Figure 6.1: (a) Scheme of the experimental cell when a radial pattern is imprinted using UV light (365nm). Colloids are dispersed in a nematic liquid crystal (NLC) confined between a photosensitive (bottom) and a non-photosensitive (top) plate. Patterns of in-plane alignment can be reversibly inscribed with light (here, a circular spot characterized by a radial pattern). The embedded anisometric particles are aligned following the local nematic director (black lines). (b) Scheme of a transversal cut of the experimental cell upon UV irradiation. (c) Scheme of the experimental cell and (d) transversal cut, upon application of an AC electric field. Red arrows indicate the direction of motion of the anisometric particles.

Pear-shaped microparticles made of polystyrene, a material that promotes planar orientation of the NLC on the particle surface, are used as colloidal inclusions. The chosen particle shape guarantees a dipolar component

in the configuration of the local director field, a requirement for LCEEP to be an efficient propulsion mechanism. Earlier studies of this mechanism have employed spherical solid[17] or liquid[18] inclusions (see chapter 5, section 5.3.1), relying on surface functionalization to achieve a homeotropic anchoring on the particle surface, which leads to a dipolar arrangement of the NLC director around the inclusion. However, homeotropic anchoring has the disadvantage that it can degenerate into a director configuration with quadrupolar symmetry

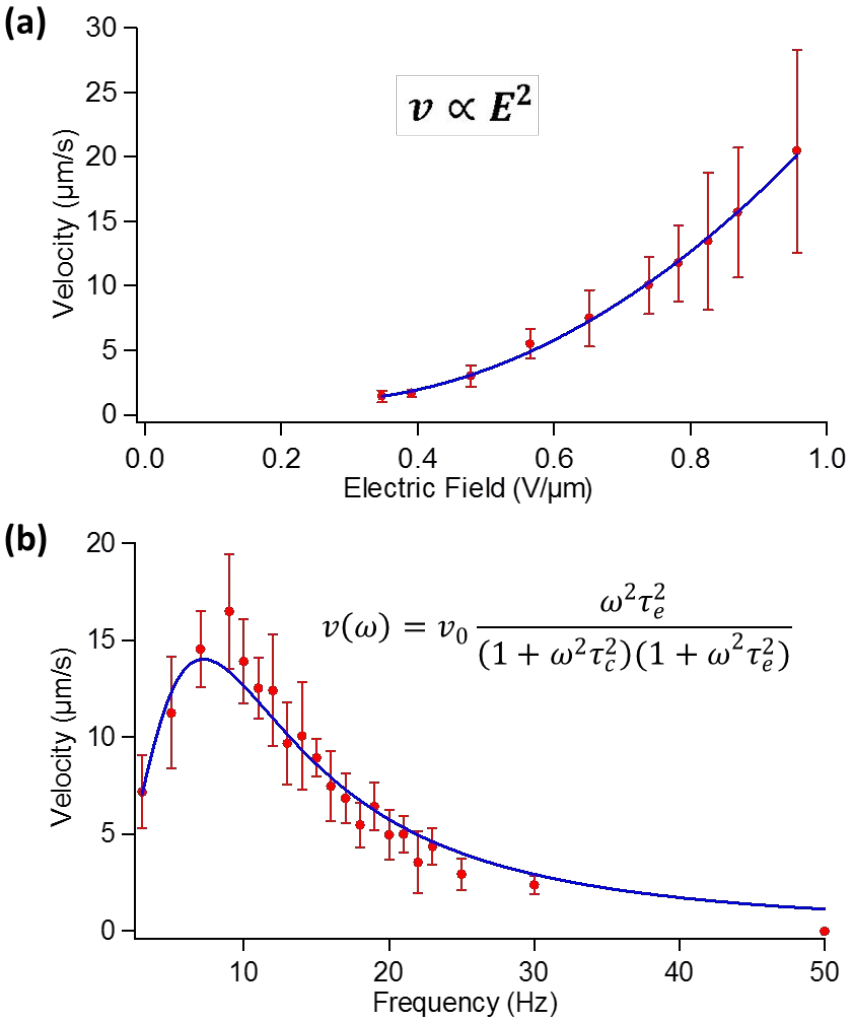

Figure 6.2: (a) Experimental measurements of the dependence of the velocity of anisometric particles on the electric field (at frequency f = 10Hz). Blue line is a polynomial fit showing the quadratic dependence of the velocity on the electric field, as predicted by LCEEP. (b) Velocity dependence versus frequency (at field strength E = 0.73V/µm). Blue line is a fit to the LCEEP equation shown in the inset.

for which LCEEP propulsion is not effective (the Saturn ring defect). In contrast, all pear-shaped particles feature planar anchoring, ensuring that all particles in a large ensemble are similarly propelled, as explained in chapter 1, section 1.4.2.

First I will describe the behavior of an individual particle. According to the mechanism of LCEEP, I observe that the velocity of anisometric particles presents a quadratic dependence on electric field strength, as it is confirmed by the measurements shown in figure 6.2a. It can also be seen in figure 6.2b that the trend exhibited by this experimental data is captured by the model proposed by Lavrentovich et al.[17] and similar to what is reported in the previous chapter with the propelled microdroplets.[18] Here the fitted parameters are the scaling factor v_0, related to the quadratic dependence on the amplitude of the applied electric field, the charging time of the electrode $\tau_e \sim 0.03s$ and the charging time of the pear-shaped particles $\tau_c \sim 0.02s$. The two charging times are of the same order of magnitude as the values calculated for the microdroplets. Nevertheless, a quantitative analysis is not possible with pear-shaped particles because of their non-spherical shape and their dielectric nature.

Next, I will explore the collective behavior of anisometric colloids driven by LCEEP. In the absence of irradiation or an electric field, particles will be oriented perpendicularly to the cell plates, following the uniform NLC director with homeotropic anchoring conditions. Irradiation of the cell with a UV light spot for a few seconds forces the NLC in contact with the azosilane-treated surface to adopt a planar configuration. As shown in figure 6.3a and figure 6.1a, this configuration conforms to the applied irradiation by locally adopting a splay (radially-spread) texture organized around a central defect.[19] Application of an external AC field extends the splay configuration for several millimeters, well beyond the size of the irradiated spot, owing to the anchoring degeneracy. The induced configuration is stable for days in an AC field, which well exceeds the half-life for the relaxation of the azosilane film, of about 30 minutes (see chapter 2 section 2.1.4).

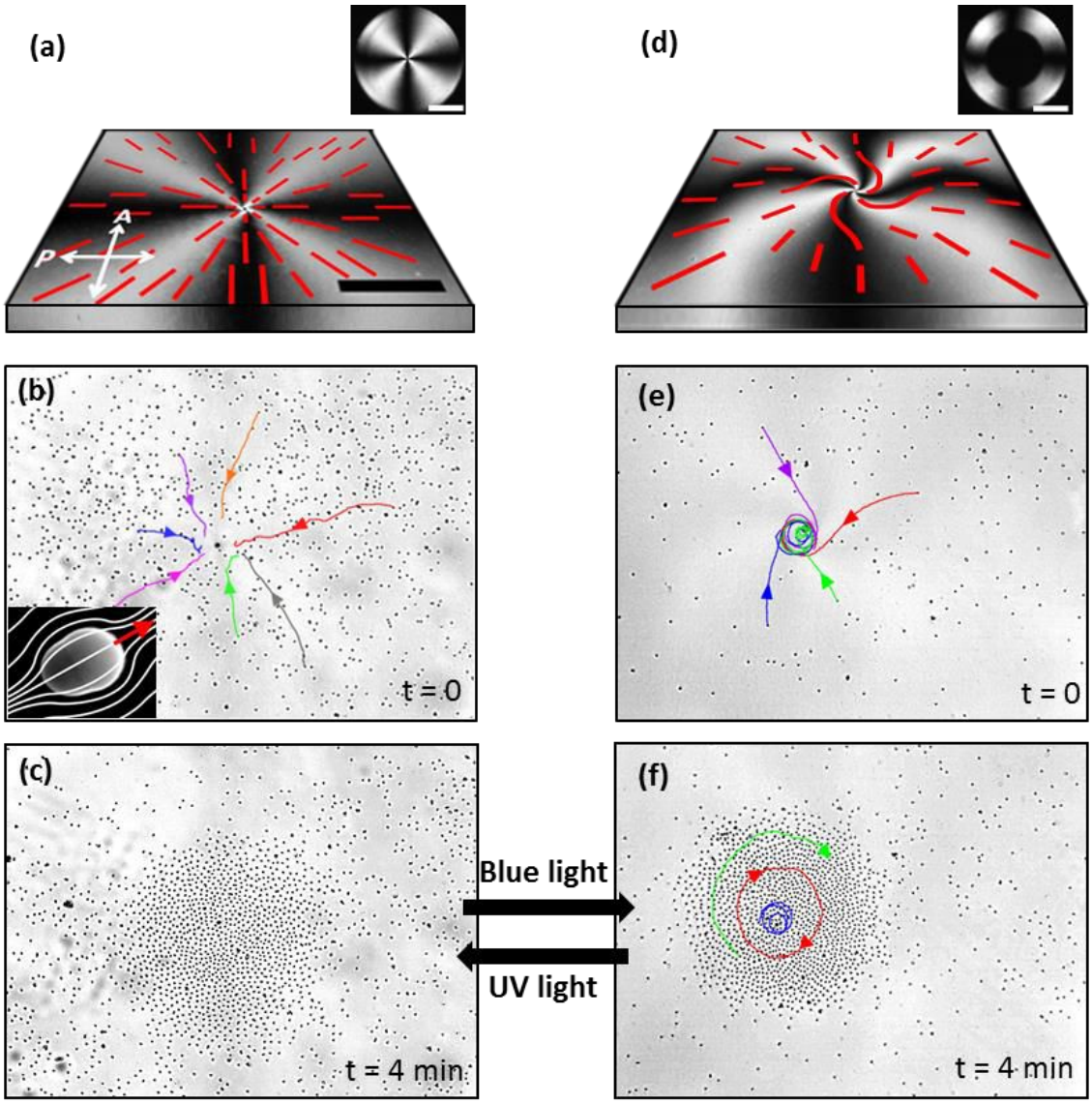

Figure 6.3: Formation of particle swarms. Images (a–c) and (d–f) illustrate the formation of a colloidal aster and mill, respectively. (a,d) Polarized light micrographs, obtained with orthogonal polarizer (P) and analyzer (A), of the imprinted NLC texture leading to a cross-like (a) or a spiral (d) attraction pattern. Dashed red lines represent the orientation of the NLC director. Insets: Planar, photoaligned circle (a) and corona (d) prior to application of the electric field. Formation of an aster (b,c) and a mill (e,f) after application of an electric field with a frequency of 10Hz and an amplitude of 0.87 V/μm. The trajectories of several particles are superimposed on the images to illustrate the swarm formation mechanism. The inset in (b) shows the SEM image of a single pear-shaped particle ($3x4\mu m^2$), with the NLC field lines and the direction of motion. The colloidal aster in (c) and the mill in (f) can be interconverted by suitable irradiation procedures, as explained in the text. Scale bar marks 200μm, except for the two insets which are 500μm.

The region with radial alignment will be the basin of attraction for dispersed particles, which tumble instantaneously following the NLC director so that their long axis lays, on average, parallel to the cell plates (figure 6.1). Simultaneously, LCEEP sets the particle into motion at a constant speed. In this way NLC realignment and particle propulsion can be decoupled, as particle speed is negligible for field frequencies above 50Hz (figure 6.2b), while NLC realignment can be achieved even with frequencies in the kHz range and above.[19]

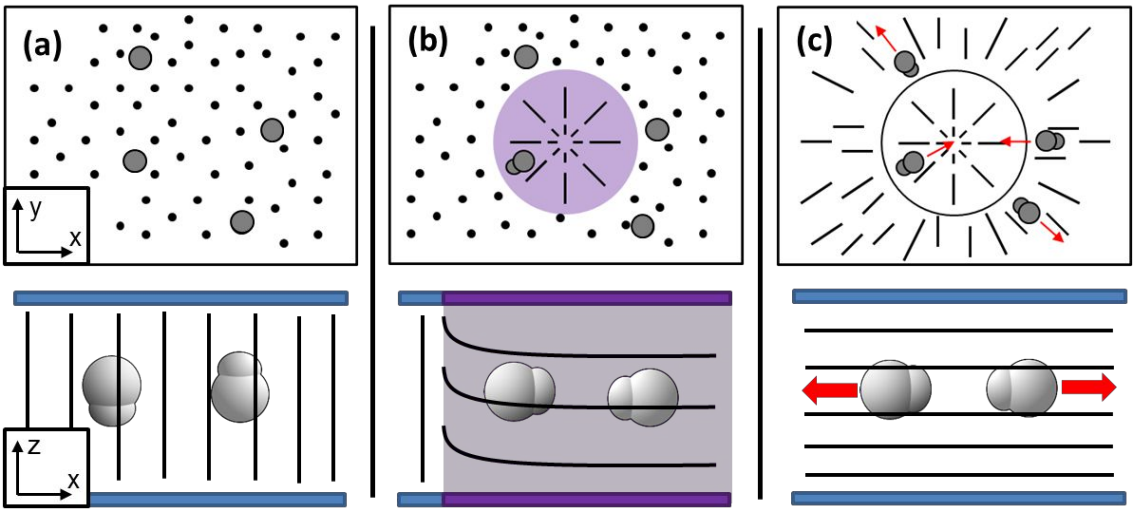

Figure 6.4: Schematics of the top (x,y) and lateral (x,z) view of a LC cell during the irradiation process, explaining the hypothesis of the random 90º tumbling of particles. (a) Initial state, electric field is OFF, light is OFF. NLC molecules and particles are oriented perpendicular to the cell (either upwards or downwards). (b) Attracting pattern imprinted by irradiation with UV light, electric field is OFF. The NLC and particles in the irradiated zone (highlighted in purple) become planar and radially aligned. (c) When the electric field is switched ON, NLC and particles change to a planar alignment throughout the sample, and particles start to move in the direction marked by its larger lobule, either attracted or repelled by the radial pattern.

All particles move along the local NLC director, with roughly half of them being attracted by the photoinduced radial defect and half of them being repelled by it. The main hypothesis proposed to explain this random direction of movement is that this behavior is a consequence of the random 90º tumbling

of particles upon application of the AC field. That is, when the pear-shaped particles are in their initial orientation, which is perpendicular to the cell plates, they can be oriented either with their large lobule upwards or downwards. Then, when the AC field induces the planar alignment, particles tumble 90º from perpendicular to planar orientation following the NLC. However, depending on their initial configuration (upwards or downwards), they may orient either towards or against the center of attraction. This hypothesis is schematized in figure 6.4.

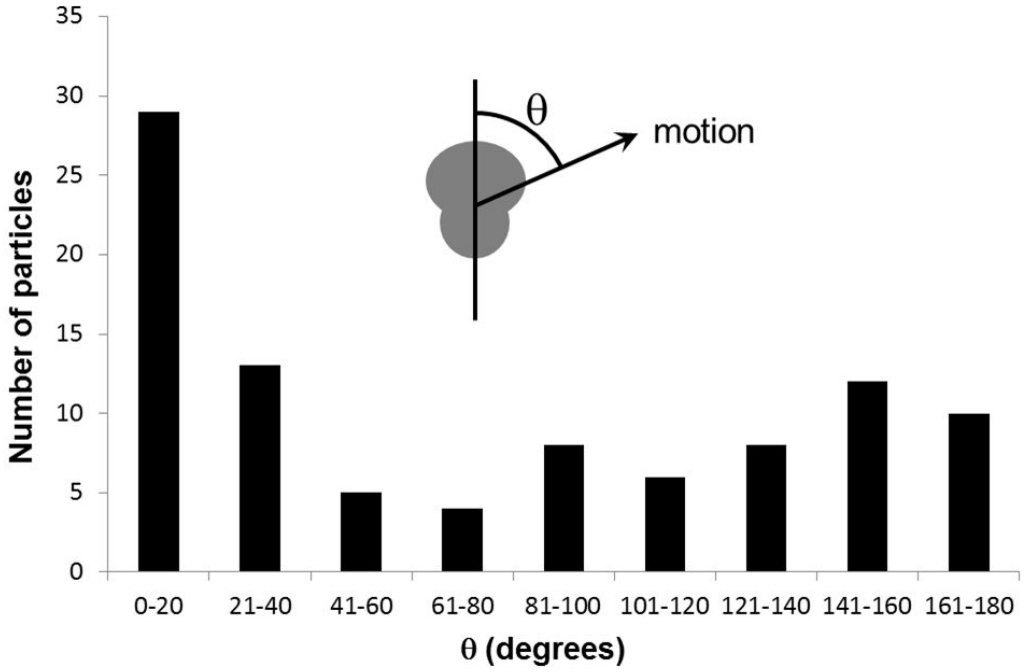

Figure 6.5: Histogram of the orientation of anisometric particles with respect to their moving direction. Experimental data were collected from larger pear-shaped particles (8.3x10.2μm²), in order to properly resolve their orientation.

As shown in figure 6.3b,c and 6.4 (see also video 6.1 in Additional Multimedia Content), particles follow the NLC field lines and assemble into a growing aster (star-like) configuration. After certain time, the particles jam and come to rest. Although the highest fraction of inclusions moves with their large lobule in front, their symmetry axis is somewhat uncorrelated with the direction of motion (figure 6.5). The latter is set by the position of the two non-

equivalent surface defects (double Boojum) that the planar anchoring on the particle surface induces on the surrounding NLC.[20] These defects form when the particles dispersed in the NLC are introduced in the experimental cell by capillary action. That is when the position of the double Boojum defects on each particle is determined, and this position is extremely sensitive to local flow effects that appear during the cell filling. The robustness and generality of the phenomenon described in this chapter is exemplified by the fact that it is insensitive on these fine details of the NLC-particle coupling.

One can easily switch the assembly mode between a confined aster and a rotating mill swarm by taking advantage of the elastic properties of the dispersing NLC, and the fact that the particles follow the NLC director field. This is achieved by erasing the central region of an imprinted UV area with a smaller spot of blue light, which enforces the *cis* to *trans* isomerization leading to homeotropic NLC alignment. As shown in Figure 6.3d and the inset, upon application of the AC field, the planar alignment in the resulting circular corona is extended both outwards and inwards. The region surrounding the inner defect now features degenerate planar anchoring conditions; therefore, it relaxes from the pure splay texture to the less energy-demanding bend (rotational) texture (for this NLC, the bend elastic constant is smaller than the splay elastic constant, therefore, in the absence of strong boundary conditions, bend distortions will be favored). As a consequence, particles follow spiral trajectories and assemble into a rotating mill, spinning around the central defect with a constant linear velocity (each particle is individually propelled, and the tangential velocity is maintained throughout the whole mill, except in the region near the central defect). This can be seen in figure 6.3e,f and also in video 6.1 in Additional Multimedia Content. The mill swarm can be transformed back into a confined aster by irradiating the region with a UV light spot. Both assembly modes can thus be reversibly interconverted in real time by photoelastic control, as shown in the last part of video 6.1 in Additional Multimedia Content.

6.3.2 Theoretical Model

The reported dynamic cluster assembly is driven by the NLC coupled with the underlying photoactivated surface patterns. Particle interactions in our system are assumed negligible if compared with the interaction with the NLC matrix, and thermal noise can be also neglected due to the high viscosity, η, of the medium. As a result, a simple model of driven particles that includes the topology of the director field is able to reproduce the formation of the observed colloidal swarms. The model can be formulated as a minimal simulation scheme of an ensemble of driven particles interacting via a Lennard-Jones repulsive potential and moving on a patterned landscape.

In particular, one can describe the motion of a particle in the ensemble with speed $\boldsymbol{v} \equiv (v_x, v_y)$, and orientation θ using the set of equations:

$$\frac{dv_x}{dt} = -\eta v_x + K_{elp} \cos\theta,$$

$$\frac{dv_y}{dt} = -\eta v_y + K_{elp} \sin\theta,$$

$$\frac{d\theta}{dt} = \tau \sin[\theta - \theta_0(x, y)],$$

where K_{elp} introduces the electrophoretic drive, and τ is related to the elastic torque that orients the particles following the underlying NLC director pattern, represented by the field $\theta_0(x, y)$. For the sake of simplicity, by using the one constant approximation of the Frank-Oseen elastic energy for a liquid crystal, the director field around a central +1 defect can be described by $\theta_0(x, y) = arctan(y/x) + \delta$ for an aster ($\delta = 0$) or a spiral ($\delta \neq 0$) pattern centered at $(x, y) = (0,0)$. A snapshot for a simulated ensemble of particles being attracted into an aster or a mill are shown in figure 6.6a,b respectively. Starting from a random particle distribution, the electrophoretic mechanism is activated with either a radial or spiral arrangement of the underlying director field, as shown by the field lines, which are traced by the particle trajectories (see video 6.2 in Additional Multimedia Content).

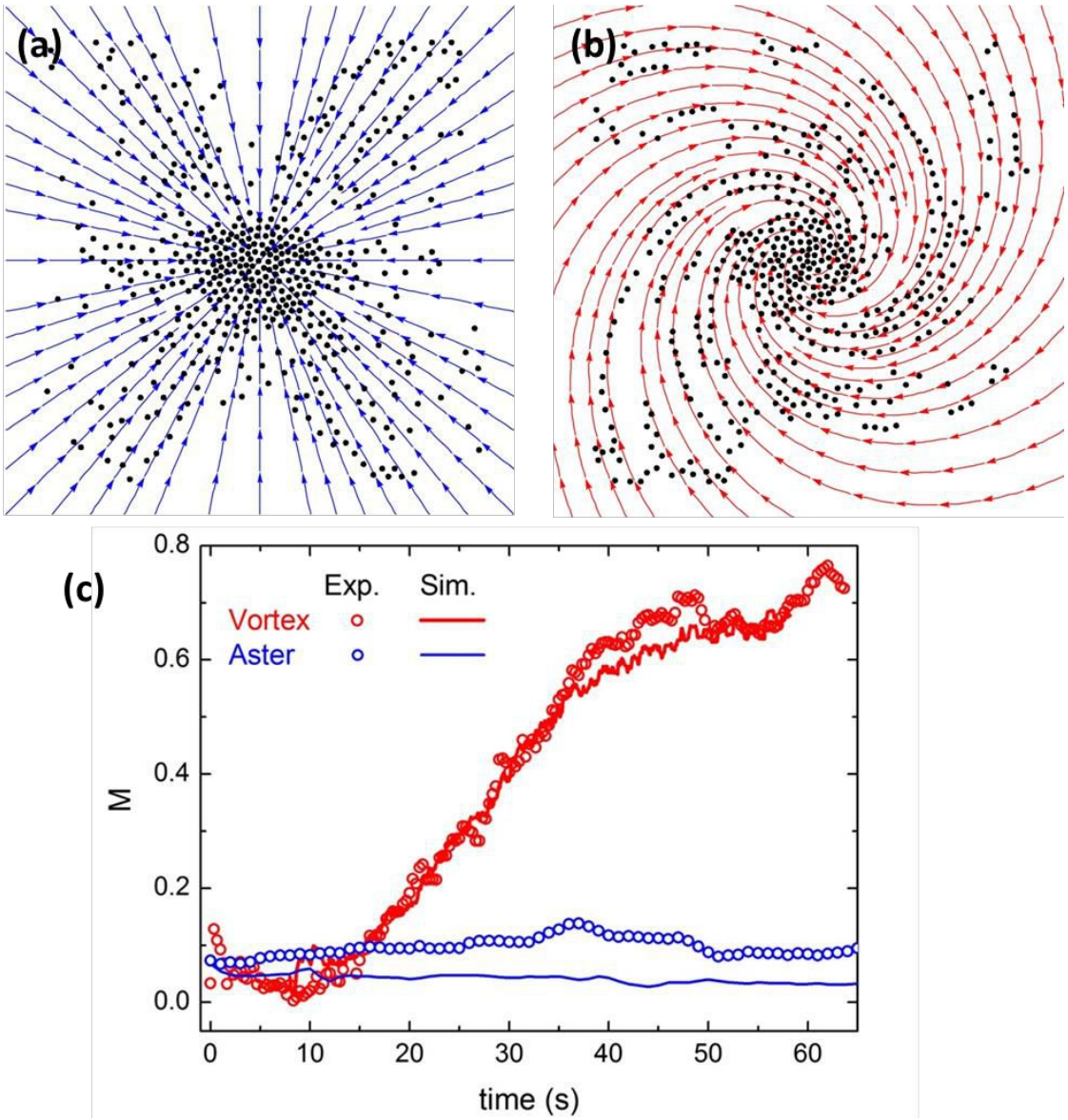

Figure 6.6: Simulated dynamics according to the minimal model described for particles being assembled into an aster (a) or into a mill (b). The field lines of the underlying director field are included in the background. (c) Normalized angular momentum calculated from the experimental (circles) and numerical (continuous lines) data. Blue (red) color refers to an aster (mill) colloidal swarm.

To characterize the formation of aster and mill structures, the normalized angular momentum (M) of the particle ensemble is used as order parameter, defined as:

$$M = \left| \frac{\sum_i \boldsymbol{r}_i \times \boldsymbol{v}_i}{\sum_i |\boldsymbol{r}_i| \, |\boldsymbol{v}_i|} \right|$$

where $\boldsymbol{r_i}$ corresponds to the position of particle *i* from the center of mass of the ensemble and $\boldsymbol{v_i}$ corresponds to its velocity. The summation is performed over all particles of the ensemble. In figure 6.6c it is shown the combination of experimental results and numerical simulations to compare the evolution of *M* for the two assembly modes. The experimental data is obtained from particle tracking of large datasets. The colloidal mill is a pattern of polarized particles that organize in concentric trajectories, thus displaying a growing angular momentum that saturates around $M \sim 0.7$. In contrast, particles forming an aster show no rotational motion, with an almost zero value of *M*. The good qualitative agreement between the simple phenomenological model and the numerical experimental data stresses that few ingredients are required to reproduce the observed collective phenomena.

6.3.3 Relocation of Swarms and Related Phenomena

The reversibility and quick response of the photoalignment layer enables straightforward swarm addressability. A preformed aggregate of arbitrary size, either aster- or mill-like, can be relocated to a preselected place anywhere within the experimental cell with minimum dismantlement of the swarm structure by changing the location of the UV spot (figure 6.7a,b). An example of this process is shown in figure 6.7c (see also video 6.3 in Additional Multimedia Content). After blocking the LCEEP mechanism by increasing the field frequency to above 50Hz, the center of attraction is translated 600μm to the right. Once LCEEP is reactivated, the swarm of particles moves towards the

new position developing a leading edge around which the particles assemble. Alternatively, according to the same principle, predesigned arbitrary paths that connect distant locations inside the cell can be imprinted, or circuits with complex topologies can be drawn as a simple way to accumulate colloidal swarms in the irradiated area and to further entrain them collectively, as shown in Figure 6.7d (second part of video 6.3 in Additional Multimedia Content).

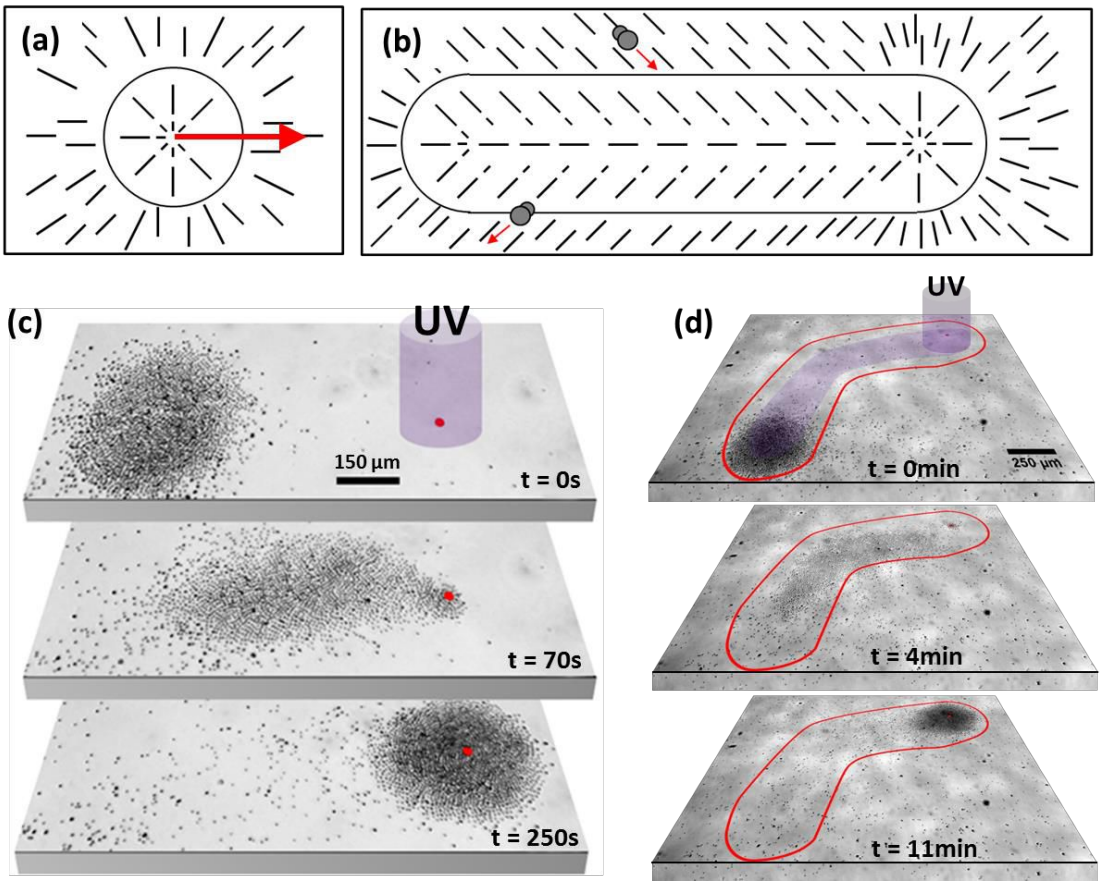

Figure 6.7: Swarm addressability. (a,b) Scheme of the image sequence shown in (c): the formation of a linear attracting path, prepared by moving the UV spot while applying electric field at f=50Hz. When the frequency is switched back to 10Hz, particles start to move following the path and accumulate at its end. (c,d) Image sequences for particle swarms traveling across the LC cell due to the in situ reconfiguration of the NLC field. (c) The photoaligned spot, initially centered in the swarm, is moved 600µm to the right in a straight line, as indicated by the red spot. Scale bar marks 150µm. (d) A longer track combining curved and straight segments. The contour of the track, only visible between crossed polarizers, is outlined in red. Scale bar marks 250µm. The applied sinusoidal electric field for both sequences has an amplitude of 0.74 V/µm and a frequency of 10Hz.

This strategy to control colloidal aggregation can be readily implemented for the direct or indirect transport of chemical cargo in a channel-free microfluidic environment. For instance, photoactivated lattices of swarms with arbitrary symmetry can be built on an extended surface by imprinting the corresponding distribution of irradiation spots. As an example, a triangular lattice of UV spots is imprinted on the photosensitive surface (figure 6.8a, and video 6.4 in Additional Multimedia Content). Upon application of the electric field, these spots compete as attractors for the particles that are dispersed in the NLC, thus generating a triangular lattice of particle swarms.

Rearrangement of the entire lattice is readily achieved by conveniently reshaping the pattern of projected light spots. This addressability is demonstrated in figure 6.8b (second part of video 6.4 in Additional Multimedia Content), where the initially triangular lattice is transformed into a square one. Particle swarms redistribute in the NLC cell according to the new director landscape. Once the electric field is switched off, the generated swarm pattern is preserved for an extended amount of time. For the used NLC, which has a dynamic viscosity of $\eta \approx 0.1 \mathrm{Pa \cdot s}$, the estimated self-diffusion coefficient (calculated using the Stokes-Einstein equation) for pear-shaped particles is $D \approx 10^{-3}\,\mu m^2/s$. Therefore, it would take several hours for particles of the size used herein to diffuse a few micrometers, and the spontaneous disaggregation of a swarm could take months.

One can also take advantage of the ability to remotely control the dynamic state of an individual swarms to achieve complex mixing patterns in a confined chemical system. As demonstrated for a single aggregate, the state of any site in a lattice can be reversibly switched between a confined aster or a rotating mill of particles. As an example, in figure 6.8c (last part of video 6.4 in Additional Multimedia Content) it is shown the remote control of just one of the swarms in a square lattice. The dynamics of this swarm are arrested irradiating with a UV light spot, while neighboring swarms remain unaffected.

This highlights the singular ability to selectively address a single swarm and thus to arbitrarily implement complex local mixing patterns.

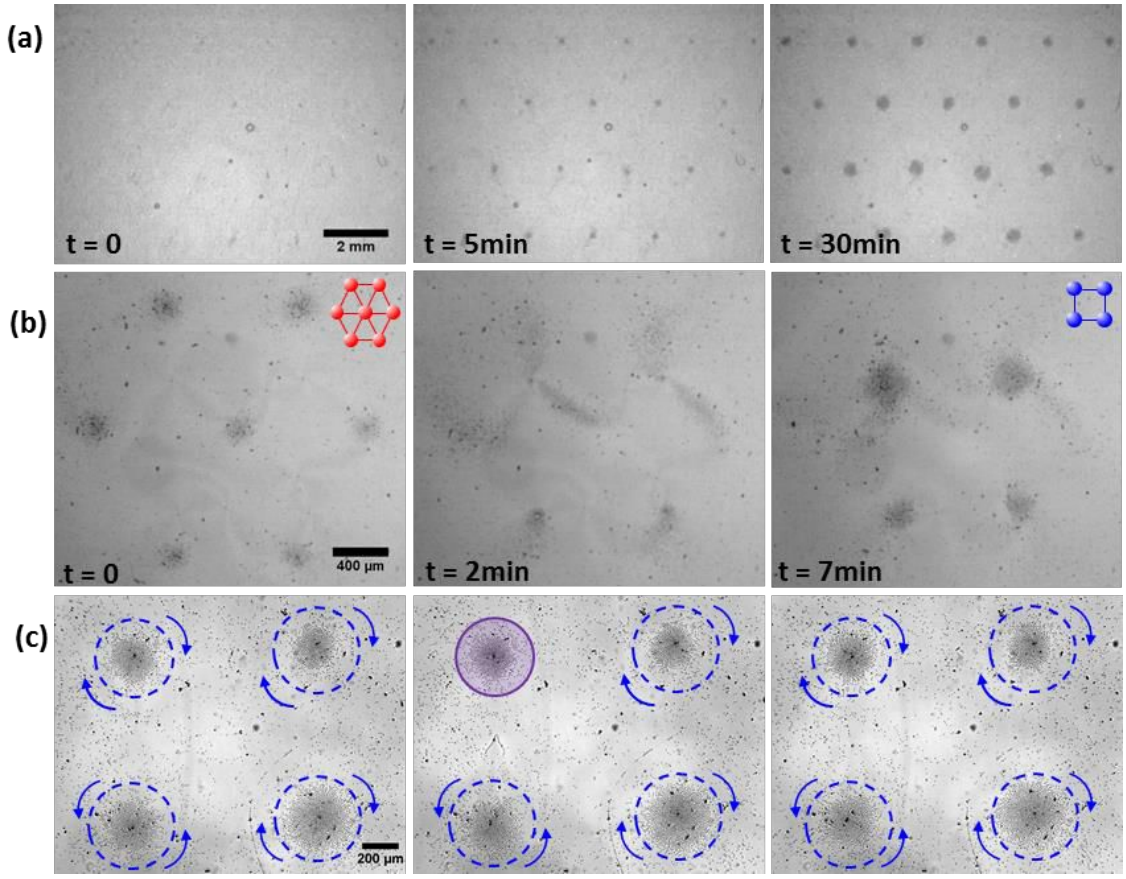

Figure 6.8: Reconfigurable lattices of swarms. (a) Image sequence for the formation of a triangular lattice of particle swarms. A sinusoidal electric field of 0.74 V/µm and 10Hz is used to drive the particles. Scale bar is 2mm. (b) Image sequence for the transformation from a triangular to a square lattice. The original distribution of attractor spots is erased with blue light (455nm), and a square lattice is subsequently imprinted using UV light (365nm). The swarm rearrangement occurs when a sinusoidal electric field of 0.78 V/µm and 10Hz is applied. Particle swarms are subsequently redistributed into the reconfigured lattice. Scale bar is 400µm. (c) The dynamic state of the swarms on a lattice can be individually addressed. While all of the swarms are rotating, the dynamics of the top left swarm are first arrested and then restarted again. Scale bar is 200µm.

The reported swarming behavior can be employed to actuate on larger embedded objects for which electrophoretic propulsion is not effective. For

example, as shown in figure 6.9a (video 6.5 in Additional Multimedia Content), a large glass cylinder is set into rotational motion by the collective interaction with the particles in a mill, which has been previously nucleated on the cylindrical inclusion. The angular speed of the embedded object can be tuned by varying the speed of the driven particles, which is controlled by the applied AC field.

Inclusions of any nature are susceptible to being transported using the strategies described here, with the sole requirement being that the NLC director has dipolar symmetry around the colloids. In the case of liquid inclusions, which will spontaneously adopt a spherical shape, the presence of an adsorbed surfactant can be employed to adjust NLC anchoring to obtain the necessary dipolar configuration (see chapter 5, section 5.3.1). In figure 6.9b (second part of video 6.5 in Additional Multimedia Content), it is shown the controlled aggregation of femtosized volumes of glycerol (stabilized with sodium dodecylsulphate) into an arbitrary spot. Droplets within a designed basin of attraction can be temporarily stored in a defined location for further processing.

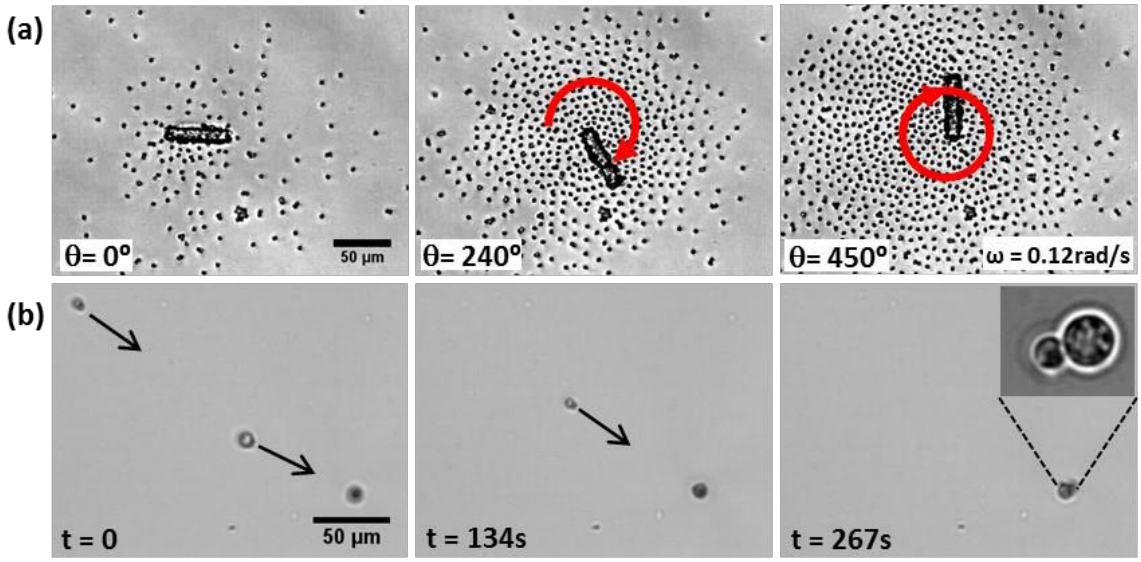

Figure 6.9: (a) A micrometer-sized glass rod (50μm long, 10μm in diameter) embedded in a microparticle swarm is set into rotation by the action of the surrounding inclusions. (b) Glycerol droplets are accumulated on a spot. Two droplets aggregated in this way are shown in the inset.

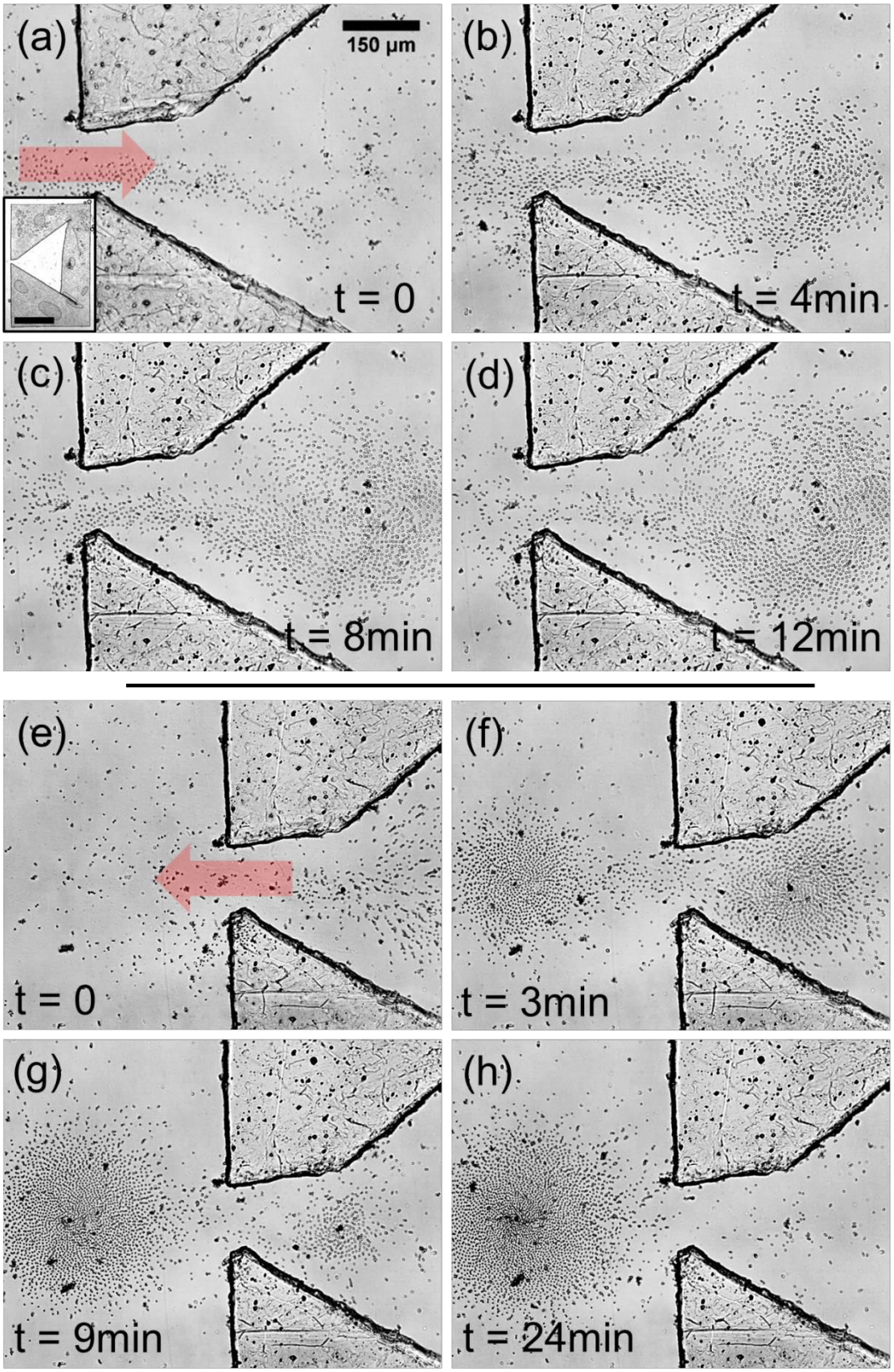

Figure 6.10: Image sequence of a colloidal swarm driven inside (a-d) and outside (e-h) a triangular confinement. AC electric field applied in both parts is 0.9V/µm and 10Hz. Inset in (a) shows an enlargement of the rectangular structure with a triangular opening, its scale bar marks 1.5mm.

With this system, one can also combine the generation and transport of swarms with microfluidics, by the insertion of physical constrains in the NLC cell. As an example, a rectangular structure of 3x4.5mm^2 having a triangular orifice with an aperture of ~100μm wide is embedded inside a NLC cell (figure 6.10a inset). This "corral" can be used to store particle swarms, which would be later released when required. In figure 6.10a-d, a center of attraction is imprinted inside the corral, and after application of AC field, particles from outside enter the corral and get accumulated forming a mill swarm. If the field is switched off, movement stops, and particles remain inside the corral due to their very slow diffusivity. After that, as presented in figure 6.10e-h, a new center of attraction can be imprinted just outside the entrance and, upon application of AC field, particles are driven away from the corral towards their new accumulation point, ready to be transported to another part of the LC cell. The whole process is also shown in video 6.6 in Additional Multimedia Content.

I have also explored the effect of particles having different sizes on the formation of colloidal swarms, and observe a segregation phenomenon. In particular, I use pear-shaped particles of sizes 3x4μm^2 and 8.3x10.2μm^2 mixed together to form an aster swarm. During application of the AC field, the smaller particles outrun the larger ones when they are accumulated in the center of attraction, as shown in figure 6.11. As the swarm grows, the larger particles are expelled by the smaller ones and remain at the external part of the swarm, while the smaller particles occupy the central region, as shown in video 6.7 in Additional Multimedia Content.

Finally, additional phenomena are observed by substituting the homeotropic counterplate of the NLC cell (see section 6.2) for one with a directional planar alignment, when the particles are driven by the AC field to form a swarm. As shown in figure 6.12a, if one irradiates the sample with UV light in a circular pattern, there is significant difference with the circular pattern shown in figure 6.3. If an AC electric field having intensity above the Frederiks

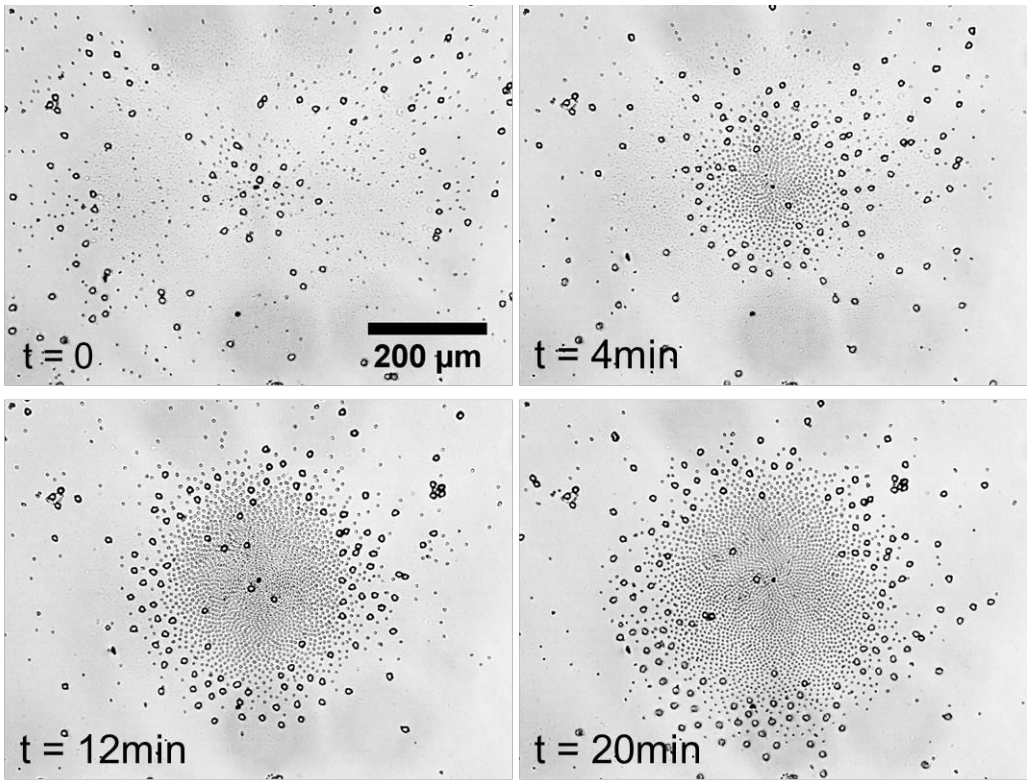

Figure 6.11: Image sequence of a colloidal swarm composed by a binary mixture of small (3x4µm²) and large (8.3x10.2µm²) anisometric particles as they organize in an aster.

transition is applied, the NLC transits to a planar directional alignment, since the planar counterplate breaks the orientation degeneracy that is otherwise present in the usual NLC cells studied above. Therefore, in the irradiated spot there is a competition between the planar directional alignment from the counterplate, and the induced radial alignment from the photosensitive plate. Due to this competition, a hybrid anchoring forms, resulting in a circular pattern characterized by a twist-escaped disclination (defect line) along one of its radii.[21] This results in a "funnel-like" effect, as can be seen in figure 6.12c by observing the trajectories followed by the particles. In this case, particles on the right side of the cell arrive following horizontal trajectories due to planar directional alignment. As soon as they enter the area of influence of the photo-induced pattern, the particles are steered toward the defect line and subsequently leave the funnel-like pattern by its left side. As time proceeds, more particles arrive at the irradiated spot and a particle jet is obtained, formed

at the "exit" of the funnel-like pattern, as shown in figure 6.12d and video 6.8 in Additional Multimedia Content. In this way, the particles are collected on the right-side of the pattern (the "funnel entrance" of 1.6mm wide), and are expelled from the left-side of the pattern (the "funnel exit") in the form of a particle jet of ~100μm width. It is worth mentioning that particles moving in the opposite direction (i.e. from left to right) deviate from their horizontal trajectories and move along the edge of the irradiated spot, without entering the funnel-like pattern.

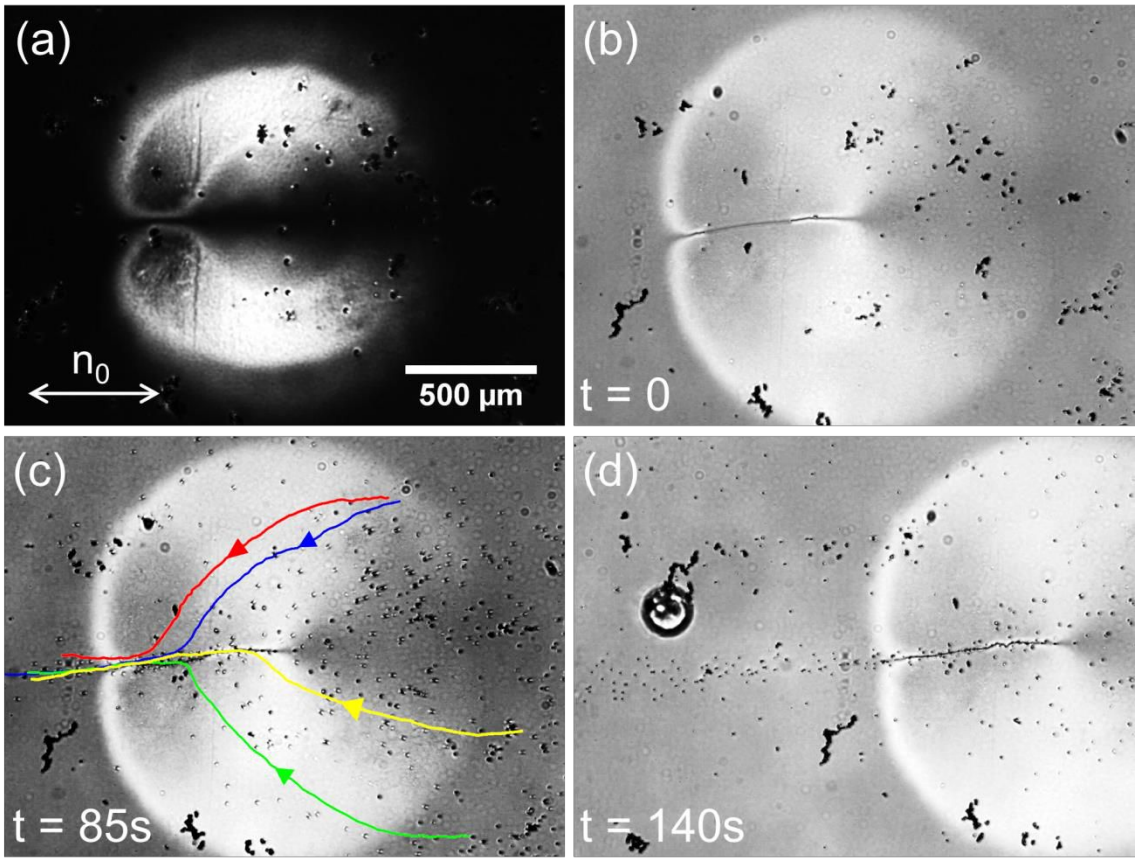

Figure 6.12: Images between crossed polarizers of the formation of a particle jet. (a) Image of the imprinted circular pattern before application of the AC field. (b-d) Upon application of the electric field (E = 1.1V/μm, f = 5Hz), particles move towards the funnel-like pattern and are expelled forming a particle jet. In (b), the defect line on the left side of the pattern appears when the AC field is applied. In this case the cell is composed of a photosensitive plate and a planar directional counterplate (in (a) n_0 marks the rubbing direction), and the dispersed particles used are homeotropic silica spheres, instead of planar pear-shaped particles.

I found that this funnel-like pattern is always oriented in the same direction along which the cell was filled by capillary action. The reason why funnel-like patterns in the opposite direction are not obtained is because the anchoring angle at the planar counteplate is actually never zero, i.e. there is always some tilt in the NLC molecules in contact with the directional planar counterplate. This tilt angle, negligible in other circumstances, is enough to define the location of the defect line with respect to the flow-filling direction, and thus the orientation of the induced funnel-like pattern.

6.4 Conclusions

- Pear-shaped particles with planar anchoring can be effectively transported by means of LCEEP in a negative dielectric anisotropy NLC medium. Their shape anisotropy breaks the otherwise quadrupolar symmetry of the NLC director field around them, thus enabling propulsion under AC electric fields.

- It is possible to separate particle driving, induced by LCEEP, from particle steering, controlled by UV-visible light reconfiguration of a photosensitive boundary layer. Using photo-induced patterns, ensembles of colloidal inclusions can be reconfigured into different modes of dynamic self-assembly as they are individually driven in an extended nematic liquid crystal layer.

- The presented experiments can be considered a proof of concept for a new strategy that enables the control of ensembles of driven colloidal inclusions of different nature, since the involved materials have to meet only generic requirements for the reported driving and steering mechanism to be effective.

- One can envisage further extension of the reported strategy. For example it could be used with living systems by employing biocompatible lyotropic liquid crystals, or it could also be used to obtain model systems to study swarming behavior and the dynamics of soft active matter.

6.5 Additional Multimedia Content

Four video files can be found in the following web page:

http://tinyurl.com/phd-shn-chapter6

- Video 6.1 shows the formation of an aster and a mill of anisometric particles, and their reversible transformation. Particles are accumulated in a radial (spiral) pattern, eventually forming an aster (mill). In the second part of the video transformations between mill and aster swarms are presented. Sinusoidal electric field of 0.87V/μm (0.74V/μm) and 10Hz was applied in the first (second) part of the video. Cell gap is 23μm. Scale bars mark 100μm.

- Video 6.2 shows a simulation for the formation of an aster and a mill swarm computed from the theoretical model described in the text.

- Video 6.3 shows relocations of particle swarms. Explanation on the used procedure is in experimental procedures section and in figure 6.7. On the second part, the contour of the irradiated path is highlighted. For the first (second) part a sinusoidal electric field of 0.74V/μm (0.85V/μm) and 10Hz was applied, and the cell gap was 23μm (13μm).

- Video 6.4 shows lattices of particle swarms. First part corresponds to the formation of a triangular lattice of particle swarms. Second part shows the transformation from a triangular lattice to a square lattice. Last part shows individual mill-aster transformations inside a lattice. In all parts a sinusoidal electric field of 0.78V/μm and 10Hz was applied, and the cell gap was 46μm (23μm) in the first and second parts (third part) of the video.

- Video 6.5 shows two microfluidic applications. First part of the video shows the rotation of a glass microrod caused by its interaction with the

rotating inclusions of a mill. Second part shows the accumulation of two glycerol droplets. For the first (second) part a sinusoidal electric field of 0.74V/μm (0.48V/μm) and 10Hz was applied, and the cell gap was 23μm for both parts.

- Video 6.6 (speed x30) shows first the storage and then the release of a particle swarm inside a triangular corral, corresponding to figure 6.10. A sinusoidal electric field of 0.74V/μm and 10Hz is applied, and the cell gap is 23μm.

- Video 6.7 (speed x30) shows the accumulation and segregation of pear-shaped particles of two different sizes (3x4μm^2 and 8.3x10.2μm^2) in a swarm, corresponding to figure 6.11. A sinusoidal electric field of 0.78V/μm and 10Hz is applied, and the cell gap is 23μm.

- Video 6.8 (speed x10) shows (between crossed polarizers) the formation of a particle jet upon application of a sinusoidal electric field of 1.1V/μm and 5Hz. As remarked in the text, in this case the cell has a planar directional counterplate, and the dispersed particles are homeotropic silica spheres. Cell gap is 46μm. This video corresponds to figure 6.12.

6.6 References

(1) Kim, E.; Xia, Y. N.; Whitesides, G. M. Polymer Microstructures Formed by Molding in Capillaries. *Nature* **1995**, *376*, 581–584.

(2) Squires, T. M.; Quake, S. R. Microfluidics: Fluid Physics at the Nanoliter Scale. *Rev. Mod. Phys.* **2005**, *77*, 977–1026.

(3) Baraban, L.; Makarov, D.; Streubel, R.; Monch, I.; Grimm, D.; Sanchez, S.; Schmidt, O. G. Catalytic Janus Motors on Microfluidic Chip: Deterministic Motion for Targeted Cargo Delivery. *ACS Nano* **2012**, *6*, 3383–3389.

(4) Song, H.; Tice, J. D.; Ismagilov, R. F. A Microfluidic System for Controlling Reaction Networks in Time. *Angew. Chemie-International Ed.* **2003**, *42*, 768–772.

(5) Grier, D. G. A Revolution in Optical Manipulation. *Nature* **2003**, *424*, 810–816.

(6) Paxton, W. F.; Kistler, K. C.; Olmeda, C. C.; Sen, A.; St. Angelo, S. K.; Cao, Y.; Mallouk, T. E.; Lammert, P. E.; Crespi, V. H. Catalytic Nanomotors: Autonomous Movement of Striped Nanorods. *J. Am. Chem. Soc.* **2004**, *126*, 13424–13431.

(7) Paxton, W. F.; Baker, P. T.; Kline, T. R.; Wang, Y.; Mallouk, T. E.; Sen, A. Catalytically Induced Electrokinetics for Motors and Micropumps. *J. Am. Chem. Soc.* **2006**, *128*, 14881–14888.

(8) Howse, J. R.; Jones, R. A. L.; Ryan, A. J.; Gough, T.; Vafabakhsh, R.; Golestanian, R. Self-Motile Colloidal Particles: From Directed Propulsion to Random Walk. *Phys. Rev. Lett.* **2007**, *99*, 48102.

(9) Wang, J. Can Man-Made Nanomachines Compete with Nature Biomotors? *ACS Nano* **2009**, *3*, 4–9.

(10) Buttinoni, I.; Bialké, J.; Kümmel, F.; Löwen, H.; Bechinger, C.; Speck, T. Dynamical Clustering and Phase Separation in Suspensions of Self-Propelled Colloidal Particles. *Phys. Rev. Lett.* **2013**, *110*, 238301.

(11) Wang, W.; Chiang, T. Y.; Velegol, D.; Mallouk, T. E. Understanding the Efficiency of Autonomous Nano- and Microscale Motors. *J. Am. Chem. Soc.* **2013**, *135*, 10557–10565.

(12) Gao, W.; Pei, A.; Dong, R.; Wang, J. Catalytic Iridium-Based Janus Micromotors Powered by Ultralow Levels of Chemical Fuels. *J. Am. Chem. Soc.* **2014**, *136*, 2276–2279.

(13) Duan, W. T.; Liu, R.; Sen, A. Transition between Collective Behaviors of Micromotors in Response to Different Stimuli. *J. Am. Chem. Soc.* **2013**, *135*, 1280–1283.

(14) Ibele, M.; Mallouk, T. E.; Sen, A. Schooling Behavior of Light-Powered Autonomous Micromotors in Water. *Angew. Chemie-International Ed.* **2009**, *48*, 3308–3312.

(15) Kagan, D.; Balasubramanian, S.; Wang, J. Chemically Triggered Swarming of Gold Microparticles. *Angew. Chemie-International Ed.* **2011**, *50*, 503–506.

(16) Lavrentovich, O. D. Transport of Particles in Liquid Crystals. *Soft Matter* **2014**, *10*, 1264–1283.

(17) Lavrentovich, O. D.; Lazo, I.; Pishnyak, O. P. Nonlinear Electrophoresis of Dielectric and Metal Spheres in a Nematic Liquid Crystal. *Nature* **2010**, *467*, 947–950.

(18) Hernàndez-Navarro, S.; Tierno, P.; Ignés-Mullol, J.; Sagués, F. AC Electrophoresis of Microdroplets in Anisotropic Liquids: Transport, Assembling and Reaction. *Soft Matter* **2013**, *9*, 7999–8004.

(19) Oswald, P.; Pieranski, P. *Nematic and Cholesteric Liquid Crystals: Concepts and Physical Properties Illustrated by Experiments*; Taylor& Francis: Boca Raton, 2005.

(20) Whitesides, G. M.; Grzybowski, B. Self-Assembly at All Scales. *Science* **2002**, *295*, 2418–2421.

(21) Petit-Garrido, N.; Trivedi, R. P.; Ignés-Mullol, J.; Claret, J.; Lapointe, C. P.; Sagués, F.; Smalyukh, I. I. Healing of Defects at the Interface of Nematic Liquid Crystals and Structured Langmuir-Blodgett Monolayers. *Phys. Rev. Lett.* **2011**, *107*, 177801.

CONCLUSIONS

CONCLUSIONS

1. Anisometric pear-shape particles dispersed in water and confined in thin cells, when subjected to AC fields, exhibit the same behavior as the spherical particles: they form aggregates at lower frequencies and repulsive states at higher frequencies. However, the anisometric particles present richer morphologies compared to spherical particles. Pear-shaped particles tend to form smaller, more elongated and less ordered clusters. In the repulsive phases, the pear-shaped particles feature three different orientations: all planar, all vertical or mixed orientation), which are not present for the spherical particles. Anisometric particles also have faster aggregation kinetics than spherical ones. Finally I developed novel strategies based on the use of magnetic beads to test the cohesion force of the clusters assembled by the AC fields. Nevertheless, these strategies are only capable to provide qualitative results. Further experimental tests will be required in order to obtain quantitative data.

2. Non-spherical paramagnetic colloidal inclusions can be used to control the local orientation of the NLC director field in an induced planar degenerated NLC cell. An external weak magnetic field applies a torque to anisotropic aggregates or ellipsoidal paramagnetic inclusions, which in turn reorient the surrounding NLC molecules, provided there are suitable boundary conditions. Upon increasing the local applied torque, interesting winding target patterns are generated, which relax upon switching off the magnetic field. These target structures are described by a simple model based on the Frank-Oseen elastic free energy for a liquid crystal. When a target pattern is formed, its chirality can be revealed by oscillating the amplitude of the AC field used to generate the induced planar degenerated alignment.

3. Liquid Crystal-Enabled Electrophoresis (LCEEP) allows the transport of aqueous microdroplets dispersed in a negative dielectric anisotropy NLC medium subjected to an external AC field. I have demonstrated that the model presented in the literature developed for solid particles, is also valid for microdroplets propelled by LCEEP. These microdroplets are used to transport and encapsulate small polystyrene particles, as well as chemical reactants. The transported cargoes can be released inside other microdroplets, or used to perform a localized chemical reaction, by coalescing two microdroplets containing separate reactants. These phenomena unveil a novel perspective for controlled transport of water miscible chemicals or drugs. Moreover, I have demonstrated the control of the activation or deactivation of LCEEP by using photosensitive particles.

4. I have developed a novel technique to separately control particle driving and steering under LCEEP. Using photo-induced patterns and LCEEP, I assemble, transport and dynamically control swarms of particles in a negative dielectric anisotropy NLC medium. With this technique I have demonstrated different potential applications: from the formation and reconfiguration of lattices composed of particle swarms, to segregation of particles with different sizes, as well as the storage and subsequent release of a swarm inside a microfluidic compartment, or the formation of particle jets. All these phenomena unveil novel possibilities in the field of collective transport of driven inclusions.

PUBLICATIONS

PUBLICATIONS

"Breaking the Degeneracy of Nematic Liquid Crystals by Means of Actuated Anisometric Paramagnetic Colloids" Hernàndez-Navarro, S.; Tierno, P.; Ignés-Mullol, J.; Sagués, F. *Soft Matter* **2011**, *7*, 5109-5112.

"Role of Anisotropy in Electrodynamically Induced Colloidal Aggregates" Hernández-Navarro, S.; Ignés-Mullol, J.; Sagués, F.; Tierno, P. *Langmuir* **2012**, *28*, 5981-5986.

"AC Electrophoresis of Microdroplets in Anisotropic Liquids: Transport, Assembling and Reaction" Hernàndez-Navarro, S.; Tierno, P.; Ignés-Mullol, J.; Sagués, F. *Soft Matter* **2013**, *9*, 7999-8004.

VIP "Reconfigurable Swarms of Nematic Colloids Controlled by Photoactivated Surface Patterns" Hernàndez-Navarro, S.; Tierno, P.; Farrera J.A.; Ignés-Mullol, J.; Sagués, F. *Angewandte Chemie* **2014**, *53*, 10696-10700.

"Nematic Colloidal Swarms Assembled and Transported on Photosensitive Surfaces" Hernàndez-Navarro, S.; Tierno, P.; Ignés-Mullol, J.; Sagués, F. *IEEE Transactions on NanoBioscience,* accepted for publication, **2015**.

"Reconfigurable Colloidal Swarms in Nematic Liquid Crystals" Hernàndez-Navarro, S.; Tierno, P.; Ignés-Mullol, J.; Sagués, F. *Molecular Crystals and Liquid Crystals,* accepted for publication, **2015**.

"Liquid Crystal - Enabled Electrophoresis: Scenarios for driving and reconfigurable assembly of colloids" Hernàndez-Navarro, S.; Tierno, P.; Ignés-Mullol, J.; Sagués, F. *The European Physical Journal Special Topics*, Submitted.

APPENDIX

A.1 Mean Square Displacement

In order to quantitatively characterize the random motion in a fluid medium (Brownian motion) of microscopic particles which are visible under an optical microscope, one can calculate their diffusion coefficient. The diffusion coefficient *D*, with units of $[\mu m^2/s]$, describes the area a particle can explore in the unit of time during its random excursion. For a particle in the bulk of a fluid medium like water, the diffusion coefficient is given by the Stokes-Einstein relationship:[1]

$$D = \frac{k_B T}{6\,\pi\,\eta\,a} \qquad \text{eqn (A. 1)}$$

being k_B the Boltzmann constant, T the absolute temperature, η the dynamic viscosity of water and a the particle radius. The diffusion coefficient is related to the particle position $\vec{r}_i \equiv (x_i, y_i)$ via the mean square displacement (MSD).[2] In particular, the MSD is given by:

$$MSD(\tau) = \langle \Delta\vec{r}(t)^2 \rangle = \langle [\vec{r}(t+\tau) - \vec{r}(t)]^2 \rangle \qquad \text{eqn (A. 2)}$$

and

$$MSD(t) = 2\,d\,D\,t \qquad \text{eqn (A. 3)}$$

where d is the dimensionality of the system. By measuring the particle position at different instants of time, it is possible to extract the diffusion coefficient *D* using eqn (A.3).

A.2 Radius of Gyration

The radius of gyration R_g is an average length often used in soft matter systems to characterize the spatial extension of clusters composed by aggregates of polymers, macromolecules, or colloids.[3] and it can be calculated by measuring the moment of inertia I of these clusters. If we assume that the clusters may be subdivided into a number of elements each having a mass m_i, then I about the axis of rotation is given by:

$$I = \sum_i m_i \vec{r}_i^{\,2} \qquad \text{eqn (A. 4)}$$

where $\vec{r}_i$ is the distance of the ith element of mass from the axis of rotation. The radius of gyration R_g is related to the moment of inertia via the following relation:

$$R_g^2 \sum_i m_i = I = \sum_i m_i \vec{r}_i^{\,2} \qquad \text{eqn (A. 5)}$$

By isolating R_g one obtains:

$$R_g = \sqrt{\frac{\sum_i m_i \vec{r}_i^{\,2}}{\sum_i m_i}} \qquad \text{eqn (A. 6)}$$

The radius of gyration can be calculated directly from particle positions in the x-y plane. In particular, eqn. A.4 can be rewritten in terms of the position of individual particles $\vec{r}_i \equiv (x_i, y_i)$, and the total number of particles N composing an aggregate, as:[4]

$$R_g = \sqrt{\frac{\sum_i^N \left(\vec{r}_i - \vec{R}_{CM}\right)^2}{N}} \qquad \text{eqn (A. 5)}$$

being $\vec{R}_{CM}$ the center of mass of the cluster.

The scaling of the radius of gyration with the number of particles N is directly connected to the local fractal dimension d_f as $R_g \sim N^{1/d_f}$.[5] The fractal dimension quantifies the compactness of a cluster aggregate. For example, for

fully compact structures, the fractal dimension is $d_f = 3$ in the case of 3D aggregates, and $d_f = 2$ in the case of two dimensional clusters.

A.3 Pair Correlation Function

The pair correlation function *g(r)* allows distinguishing the positional order of a crystalline solid from the disorder of a liquid or gas. It is a measure of the probability of finding a particle at a distance *r* away from a given reference particle. For example, if the studied system has a crystalline order, its pair correlation function features narrow peaks at determined distances *r*. These narrow peaks broaden as the crystalline order decreases, as shown in figure A.1.[6] It is possible to calculate *g(r)* in dispersions of micron-sized particles by directly extracting the particle positions from optical microscopy.[7] This enables the study of morphology and dynamics of local structures in colloidal crystals[8], glasses,[9] or gels.[10] In this thesis, *g(r)* is used in chapter 3 section 3.3.1 to study two-dimensional colloidal ordering in confined dispersions of spherical and non-spherical particles.

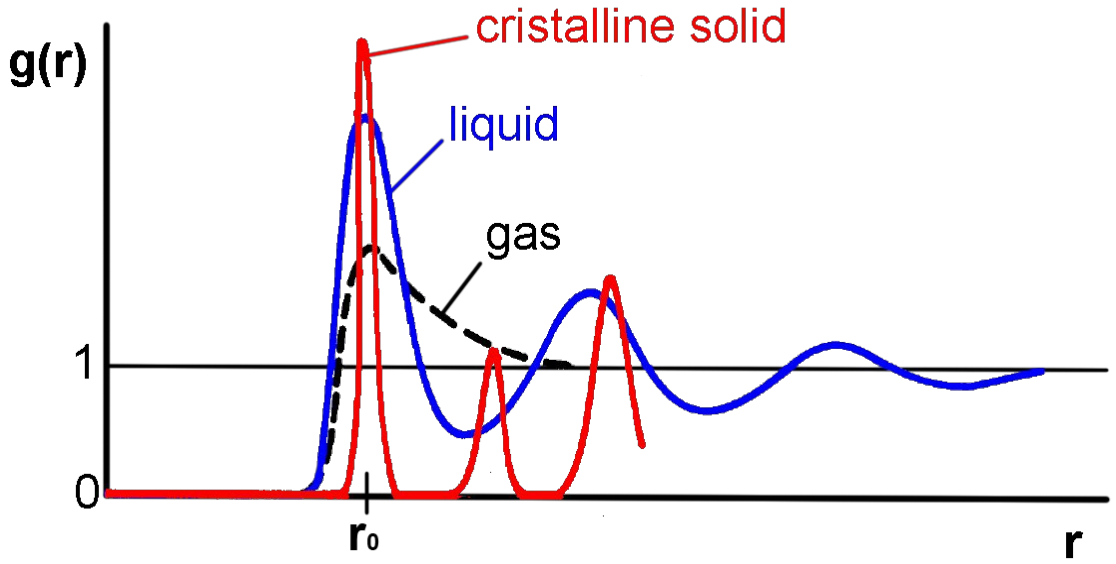

Figure A.1: Three types of *g(r)*, as a function of the distance *r* from a reference particle, for crystalline solid (red), liquid (blue) and gas (dotted black) phases. Each peak indicates, from left to right, the position of the first, second, third, etc. nearest neighbors. The diameter of the particles is marked as r_0, which coincides with the position of the first peak.

For a 2D system of particles characterized by positions $\vec{r}_i \equiv (x_i, y_i)$, the pair correlation function $g(r)$ can be calculated using the expression:[11]

$$g(r) = \frac{1}{(2\pi r\rho)}\left\langle \sum_{ij} \delta(r - r_{ij}) \right\rangle \qquad \text{eqn (1.9)}$$

with ρ being the 2D particle density, $\delta(r)$ is the δ function, $r_{ij} = r_i - r_j$ the distance between pairs of particles i and j, and $\langle ... \rangle$ denotes an average over all particles.

A.4 References

(1) Hunter, R. J. *Foundations of Colloid Science*; Oxford University Press: New York, 2001.

(2) McQuarrie, D. A. *Statistical Mechanics*; Harper & Row: New York, 1976.

(3) Hiemenz, P. C.; Rajagopalan, R. *Principles of Colloid and Surface Chemistry*; Marcel Dekker: New York, 1997.

(4) Grosberg, A. Y.; Khokhlov, A. R. *Statistical Physics of Macromolecules*; AIP Press: Woodbury, NY, 1994.

(5) Dewey, T. G. *Fractals in Molecular Biophysics*; Oxford University Press: New York, 1997.

(6) Chandler, D. *Introduction to Modern Statistical Mechanics*; Oxford University Press: New York, 1987.

(7) Crocker, J. C.; Grier, D. G. Methods of Digital Video Microscopy for Colloidal Studies. *J. Colloid Interface Sci.* **1996**, *179*, 298–310.

(8) Gasser, U.; Weeks, E. R.; Schofield, A. B.; Pusey, P. N.; Weitz, D. A. Real-Space Imaging of Nucleation and Growth in Colloidal Crystallization. *Science* **2001**, *292*, 258–262.

(9) Weeks, E. R.; Crocker, J. C.; Levitt, A. C.; Schofield, A. B.; Weitz, D. A. Three-Dimensional Direct Imaging of Structural Relaxation Near the Colloidal Glass Transition. *Science* **2000**, *287*, 627–631.

(10) Varadan, P.; Solomon, M. J. Direct Visualization of Long-Range Heterogeneous Structure in Dense Colloidal Gels. *Langmuir* **2003**, *19*, 509–512.

(11) Tierno, P.; Thonke, K.; Goedel, W. A. Using Paramagnetic Particles as Repulsive Templates for the Preparation of Membranes of Controlled Porosity. **2005**, 9476–9481.

RESUM (EN CATALÀ)

1. Introducció

1.1 Motivacions

La humanitat ha observat i fet ús de sistemes col·loïdals des dels primers dies de la civilització: des de pintures prehistòriques o ungüents medicinals, als cosmètics, salses o preparats farmacèutics moderns. No obstant això, la caracterització i preparació de noves suspensions col·loïdals és encara un camp àmpliament explorat de la investigació, amb potencial aplicació en nano i micro-tecnologia,[1,2] i biologia[3] o ciència mèdica.[4]

Potser un dels mitjans més comuns per dispersar partícules col·loïdals i estudiar les seves propietats és l'aigua. De tota manera, l'interès de combinar col·loides i fluids complexos ha augmentat enormement durant les últimes dècades. Un bon exemple són les dispersions de col·loides en cristalls líquids, que constitueixen avui dia sistemes que poden ser utilitzats per donar a conèixer nous conceptes fonamentals o per descobrir innovadores aplicacions originals.[5–8]

En aquesta tesi, he estudiat dispersions col·loïdals compostes de partícules de mida micromètrica de diferent naturalesa, disperses en aigua, així com també en un cristall líquid nemàtic (NLC).

1.2 Dispersions col·loidals

Una dispersió col·loïdal està composta d'una fase dispersa de matèria en forma de partícules micro o nano-mètriques, i una fase contínua, que és el mitjà de suspensió. Les dispersions col·loïdals són importants per a aplicacions industrials, i una gran varietat d'exemples es poden trobar en la vida quotidiana: des de llet, melmelada, crema de mans o tintes, fins a fum o boira.[9] A causa de la seva gran superfície respecte al volum, les dispersions col·loïdals són termodinàmicament inestables i tendeixen a agregar-se espontàniament

amb el temps. Per a moltes aplicacions industrials, l'estabilitat d'una dispersió col·loïdal és una qüestió vital. Aquesta tendència a l'agregació es pot superar mitjançant un ajust fi de les interaccions atractives i repulsives entre les partícules col·loïdals.

Les interaccions atractives es deuen principalment a forces de Van der Waals entre partícules. Aquestes forces sorgeixen de la interacció dels conjunts de molècules que constitueixen les partícules, interactuant a través dels seus corresponents dipols elèctrics moleculars. Encara que el potencial d'atracció de Van der Waals a nivell molecular decau ràpidament amb la distància ($vdw \sim 1/r^6$), no és menyspreable quan ho extrapolem a distàncies microscòpiques.

Les interaccions repulsives entre les partícules col·loïdals poden ser induïdes principalment de dues maneres: ja sigui aprofitant la repulsió entre la *doble capa elèctrica* de dues partícules carregades, o a través de la interacció estèrica per un recobriment de polímer.

1.3 Cristalls Líquids

Els cristalls líquids són fluids anisotròpics (ja siguin substàncies pures, mescles o solucions) que tenen propietats de líquid i de sòlid cristal·lí al mateix temps.[10,11] Les unitats que formen un cristall líquid (molècules, agregats o clústers) es poden moure fàcilment unes respecte les altres, igual que en un líquid ordinari. No obstant això, aquestes unitats tendeixen a tenir el mateix ordre d'orientació o fins i tot un cert grau d'ordre de translació, de manera similar a les fases cristal·lines sòlides. En aquesta tesi, he fet servir un cristall líquid *nemàtic*, on les molècules que el composen no tenen una posició determinada en l'espai (sense ordre de translació), però estan orientades en la mateixa direcció (ordre d'orientació de llarg abast), tal com il·lustra la figura 1.1.

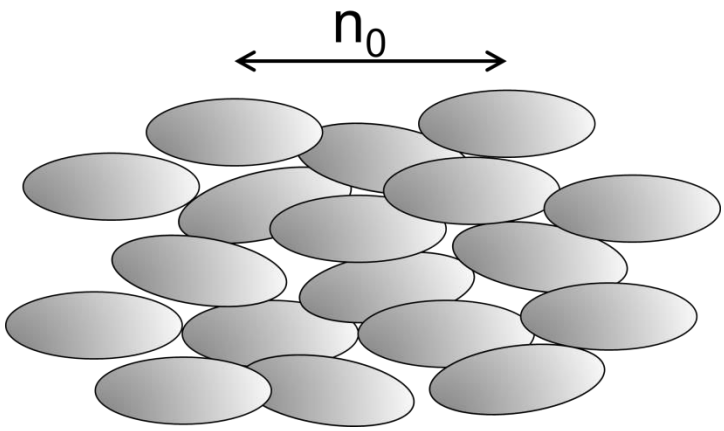

Figura 1.1: Representació esquemàtica d'un cristall líquid nemàtic (NLC). L'orientació mitjana de les molècules (el·lipses grises) ve indicada pel *camp director* $\boldsymbol{n_0}$.

L'ordre d'orientació de llarg abast es descriu mitjançant el vector unitari $\vec{n}$ (també indicat per $\boldsymbol{n_0}$) el qual s'anomena el *camp director*, tal i com s'indica a la figura 1.1. L'orientació del camp director es pot establir mitjançant les condicions de contorn on s'ubica el cristall líquid nemàtic. Aquestes condicions es poden controlar mitjançant la funcionalització apropiada de les plaques limitants de la cel·la experimental (més detalls sobre els processos de funcionalització i condicions d'ancoratge corresponents es troben en el capítol 2 secció 2.1). Com a alternativa, també es poden fer servir camps externs per orientar el director d'un NLC. Quan una mostra de cristall líquid nemàtic se sotmet a un camp elèctric o magnètic extern, les molècules de NLC tendeixen a reorientar-se paral·lel o perpendicularment al camp, depenent de la seva estructura molecular i propietats.[11] Aquesta desviació del director degut a un camp extern se'n diu *transició de Frederiks*.

En absència de restriccions externes un NLC tendeix a tenir una alineació homogènia del camp director $\vec{n}$. No obstant això, en molts escenaris aquest cas ideal no es satisfà, com per exemple a prop de les plaques de la cel·la, al voltant d'inclusions disperses o en presència de camps externs. Les deformacions bàsiques que poden patir els NLC són *splay*, *bend* o *twist*. El *splay* i el *bend* són deformacions 2D del camp director, i estan representats en la figura 1.2a i 1.2c, respectivament. La distorsió de *twist* és una deformació 3D, com es veu en la figura 1.2b.

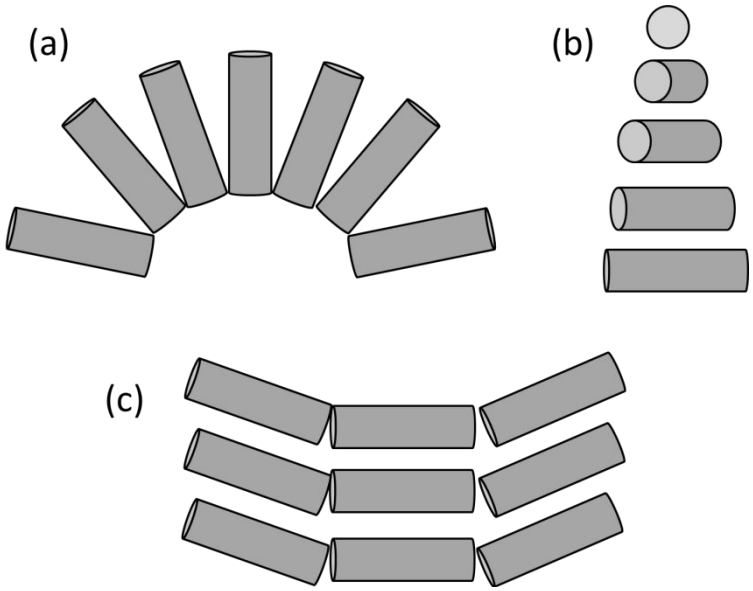

Figura 1.2: Representació esquemàtica de les distorsions de splay (a), twist (b), I bend (c). La orientació local del director està representada per cilindres grisos.

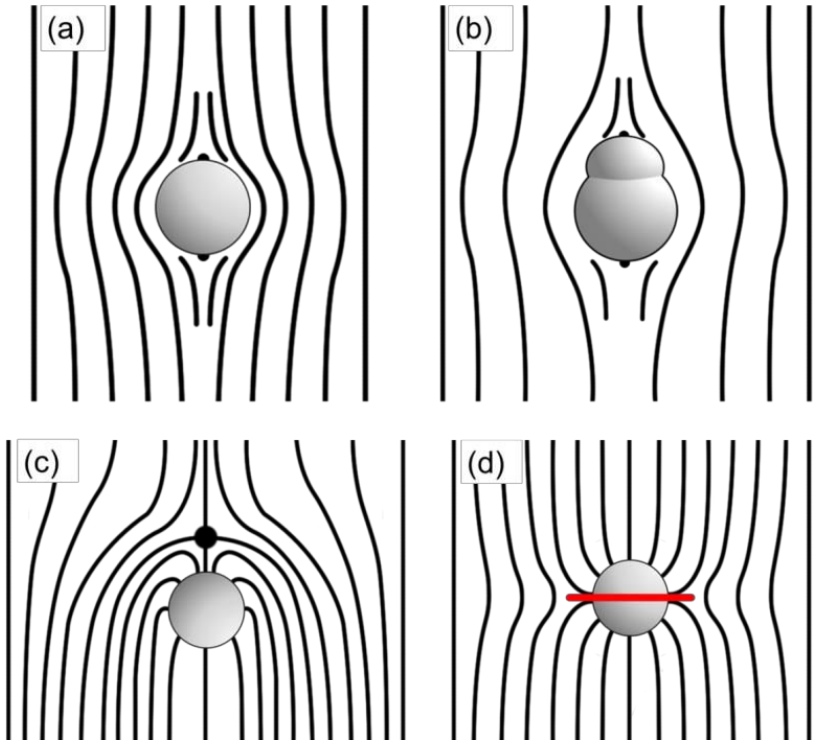

Figura 1.3: Representació esquemàtica de les distorsions generades per partícules de diferent forma i condicions d'ancoratge, suspeses en un NLC amb alineació vertical uniforme. Les partícules esfèriques (a) i *pear-shaped* (b) planars (ancoratge tangencial) presenten dos defectes als pols anomenats *double Boojum*. Les partícules esfèriques homeotròpiques (ancoratge perpendicular) poden presentar un defecte puntual Hedgehog en un dels pols (c), o bé una línia de defecte al voltant de l'equador anomenada *Saturn Ring* (d). Tots els panells tenen simetria axial.

Quan una micropartícula es dispersa en un medi de NLC, la distorsió del camp director causada per la partícula condueix a la formació de defectes als voltants de la inclusió, que dependran principalment de les condicions d'ancoratge a la superfície de la partícula, l'elasticitat del cristall líquid i el radi de la partícula.[12,13] L'orientació del NLC a prop d'una superfície pot ser *homeotròpica* o *planar*. En el primer cas, les molècules s'orienten perpendicularment a la superfície, mentre que en l'altre cas s'orienten en paral·lel a la mateixa. Exemples dels defectes que es formen quan aquestes partícules es submergeixen en NLC es poden veure a la figura 1.3.

1.4 Electroforesi no Lineal

Si tenim una inclusió polaritzable esfèrica submergida en un electròlit líquid sotmès a un camp elèctric extern, es forma un flux electro-osmòtic quadrupolar al voltant de la inclusió, des dels seus pols a l'equador, com es mostra a la figura 1.4. Aquest fenomen no lineal s'anomena *electro-osmosi per càrrega induïda* (ICEO).[14] El camp elèctric indueix primer una separació de càrregues en la partícula, que al seu torn atrau ions de signe oposat del dissolvent, generant així el corresponent núvol d'apantallament en el dissolvent. Després d'induir la separació de càrregues, el camp impulsa el flux electro-osmòtic resultant de la mateixa manera que en l'electroforesi lineal clàssica, però aquest cop amb una dependència quadràtica del camp aplicat, cosa que fa possible que camps alterns generin també aquest flux.

En fluids isotròpics com l'aigua, ja sigui per camps elèctrics continus o alterns, aquest flux electro-osmòtic quadrupolar voltant de les inclusions esfèriques no carregades és simètric, i per tant no produeix propulsió efectiva, com es pot veure a la figura 1.4. Per generar propulsió en les partícules, la simetria quadrupolar del flux s'ha de trencar,[15] i això es pot aconseguir mitjançant l'ús de, per exemple, partícules *Janus* (micropartícules amb una

semiesfera dielèctrica i una semiesfera recoberta de metall),[16] inclusions no esfèriques,[17] o fent servir com a medi de dispersió un fluid anisotròpic com ara un NLC.

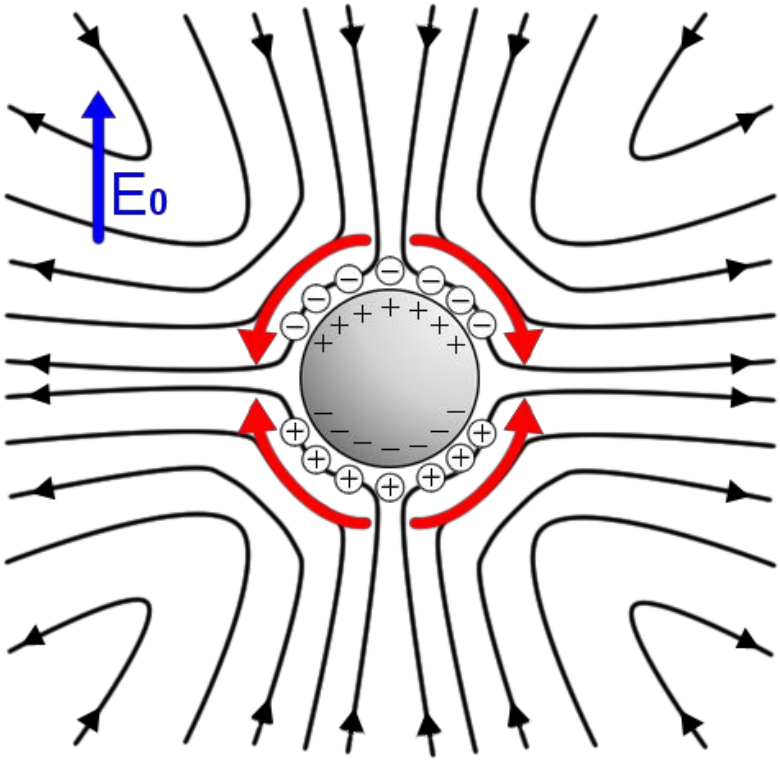

Figura 1.4: Representació del flux electro-osmòtic de càrrega induïda al voltant d'una partícula no carregada. Les línies negres indiquen la direcció del flux quadrupolar, mentre que les línies vermelles gruixudes remarquen el flux just a tocar de la partícula, des dels pols fins a l'equador. Cal fixar-se en que si el sentit del camp elèctric s'inverteix, el flux no canvia.

En el cas de fer servir un cristall líquid nemàtic com a medi de dispersió per generar la ICEO, el fenomen s'anomena Electroforesi Possibilitada per Cristall Líquid (LCEEP) descoberta per Lavrentovich i col·laboradors.[7,18–20] Aquesta LCEEP es basa en el fet que les distorsions del cristalls líquid al voltant de la partícula poden trencar la simetria quadrupolar del flux electro-osmòtic. Això genera una descompensació en els fluxos, cosa que deriva en una propulsió efectiva de les partícules. En la figura 1.5 es poden veure les configuracions del NLC que fan possible (a,c) o no (b) la propulsió.

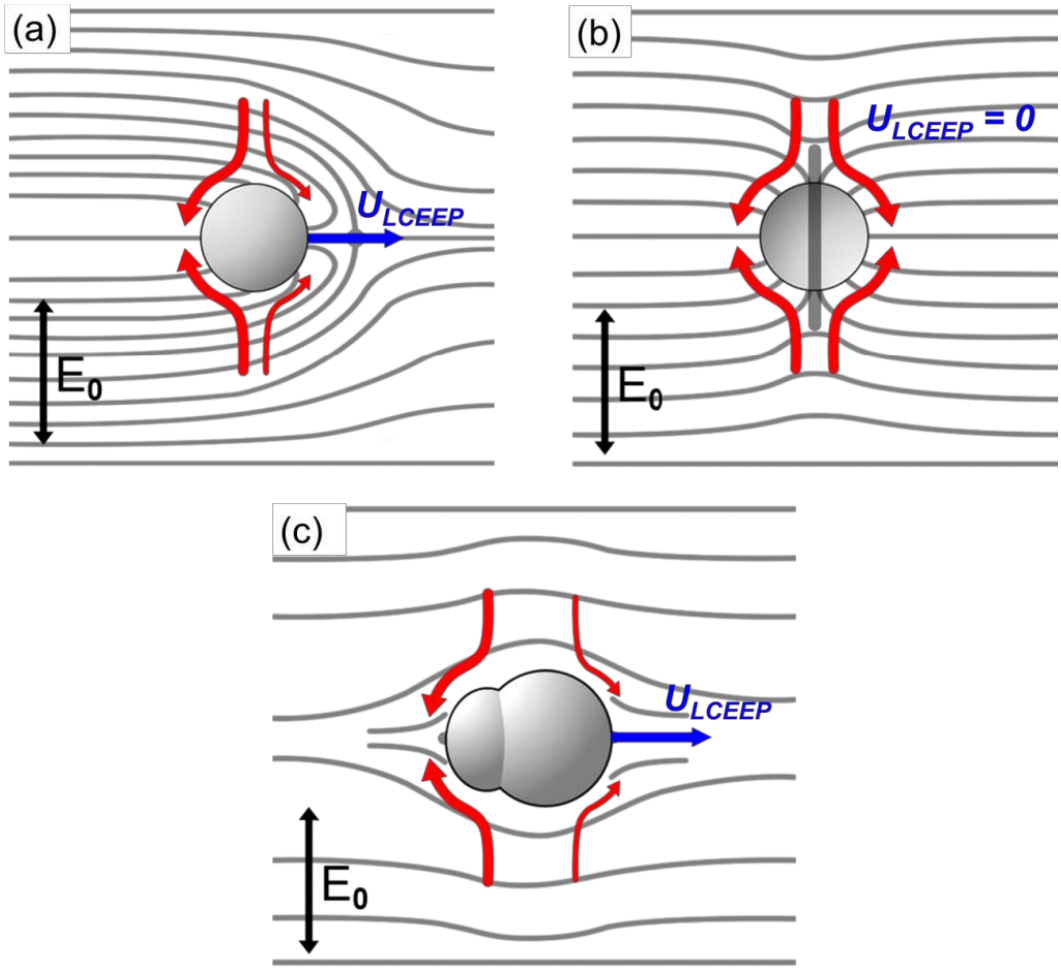

Figura 1.5: Representació del mecanisme de LCEEP al voltant de una partícula Hedgehog (a), una partícula Saturn ring (b) i una partícula planar *pear-shaped* (c). Les fletxes vermelles indiquen el flux electro-osmòtic, mentre que el camp director del NLC estan marcades al fons en negre. Només hi ha propulsió en els casos (a) i (c), on el flux electro-osmòtic queda distorsionat pel NLC al voltant de les partícules.

1.5 Objectius

1. Estudiar l'agregació i les propietats estructurals de partícules col·loïdals sota camps elèctric alterns. Comparar el comportament i la dinàmica de partícules esfèriques i no esfèriques. Utilitzar partícules magnètiques externament dirigides per testejar les propietats estructurals del agregats col·loïdals.

2. Controlar la orientació d'un cristall líquid nemàtic utilitzant inclusions paramagnètiques anisomètriques externament controlades amb un camp magnètic feble.

3. Validar l'ús de l'Electroforesi Possibilitada per Cristall Líquid (LCEEP) per microgotes aquoses o partícules fotosensibles. Utilitzar aquestes gotes per desenvolupar noves estratègies pel transport de diferents càrregues microscòpiques, com partícules sòlides o reactius químics. Controlar l'activació o desactivació de la LCEEP mitjançant partícules fotosensibles.

4. Controlar la direcció de moviment de partícules anisomètriques propulsades per LCEEP, utilitzant cel·les amb superfícies fotosensibles. Estudiar el moviment col·lectiu de partícules i explorar les possibilitats del sistema de cara a aplicacions en laboratoris-en-un-chip.

2. Capítol 2: Protocols i Muntatges Experimentals

2.1 Cel·les Experimentals

Les cel·les experimentals, utilitzades en aquesta tesi per estudiar dispersions col·loïdals, es componen bàsicament de dues plaques de vidre-ITO (vidre amb una fina capa conductora transparent) separades per espaiadors prims i enganxades entre si. Les plaques de vidre es poden funcionalitzar amb diferents molècules o materials, depenent del tipus d'experiments realitzats. Pels estudis d'aquesta tesi s'han fet servir separacions de placa que van des les 13µm fins a 70µm, que corresponen al gruix dels espaiadors de Mylar col·locats entre les plaques de vidre. En la figura 2.1 es pot veure un esquema bàsic de les cel·les experimentals.

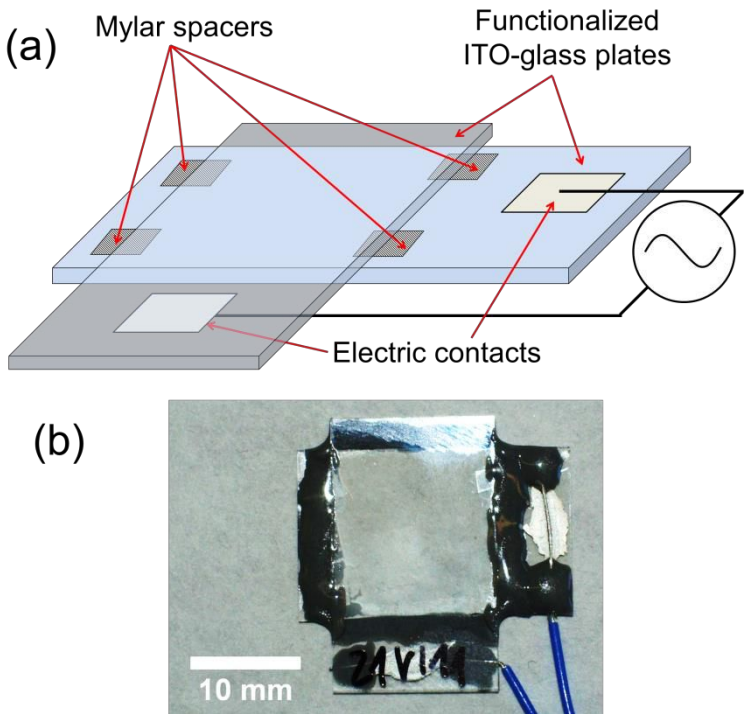

Figura 2.1: (a) Esquema de les parts bàsiques de les cel·les experimentals utilitades en aquesta tesi. (b) fotografia d'una cel·la experimental.

Potser la forma més senzilla per funcionalitzar les plaques de vidre de les cel·les experimentals, àmpliament utilitzat en aplicacions que impliquen

dispersions col·loïdals en aigua, així com en cristalls líquids, és dipositar una monocapa auto-ensamblada (SAM) en la superfície de les plaques. Les SAMs són agregacions ordenades de molècules formades per la unió de molècules d'un tensioactiu actiu sobre un substrat sòlid.[21,22] El procediment consisteix bàsicament en la immersió del substrat sòlid en una solució que conté la molècula designada durant una certa quantitat de temps, de segons a hores depenent de les molècules i el substrat utilitzat.

Una altra alternativa és el procediment de *Spin-coating*, que s'utilitza per dipositar pel·lícules fines i uniformes de resines o polímers en substrats plans. El procediment bàsic consisteix en dipositar primer la solució de recobriment damunt del substrat, per seguidament fer-lo girar a alta velocitat per tal d'estendre la solució de manera homogènia gràcies a la força centrífuga, mentre a l'hora s'expulsa l'excés de líquid.

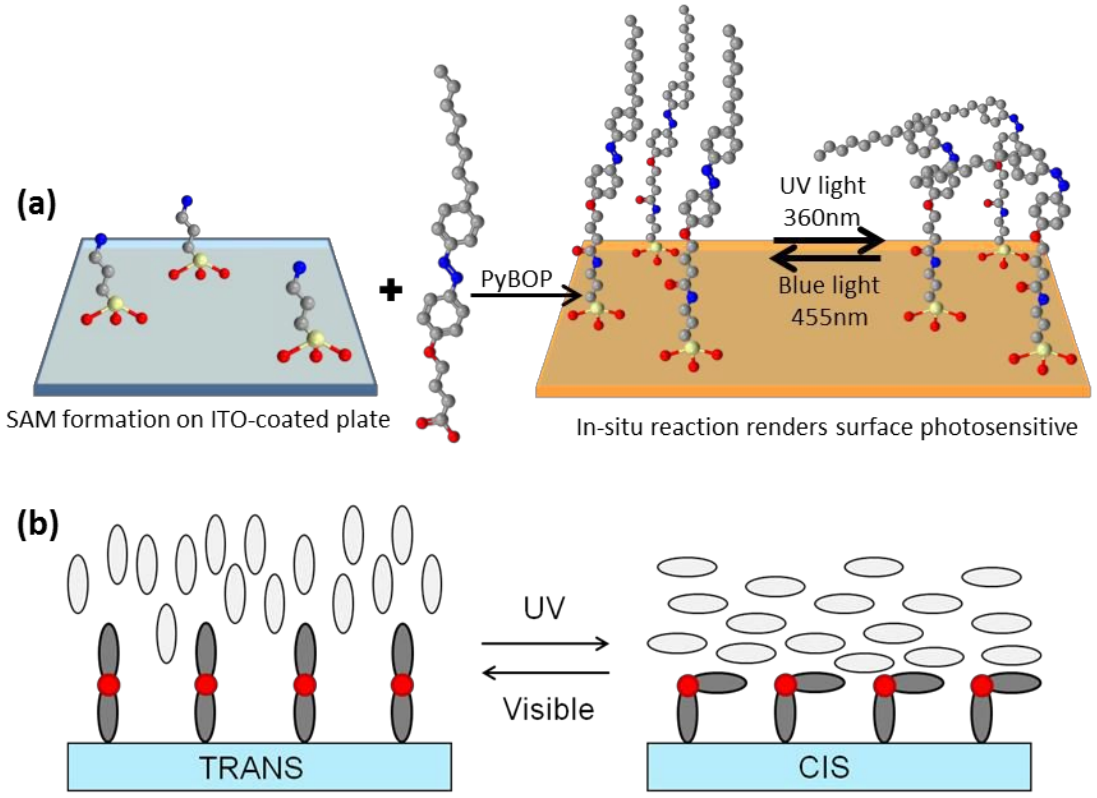

Figura 2.2: (a) Mètode de funcionalització en dos passos per preparar substrats de vidre fotosensibles utilitzant APTES i 8Az3COOH. (b) la isomerització *trans-cis* induïda a través de la irradiació UV-visible fa canviar l'ancoratge del cristall líquid nemàtic (representat per el·lipses blanques).

Amb aquests tractaments es poden canviar les propietats de les plaques de les cel·les, ja sigui fer-les més hidrofíliques o hidrofòbiques, així com induir ancoratges homeotròpics com planars en les cel·les de cristall líquid.

Per preparar les plaques fotosensibles es fa servir una reacció en dos passos, esquematitzada en la figura 2.2. El primer pas és recobrir les plaques de vidre-ITO amb una monocapa auto-ensamblada de (3-aminopropil)trietoxisilà (APTES, Sigma-Aldrich).[23] El segon pas consisteix en la formació d'un enllaç amida entre el grup amino terminal del APTES, i el grup àcid del compost azobenzènic 4-octil-4'-(carboxi-3-propiloxi)azobenzè (8Az3COOH).[24,25]

2.2 Dispersions de Partícules

En la majoria dels experiments presentats en aquesta tesi, les partícules col·loïdals comercials es netegen prèviament per redispersió en diferents dissolvents. El procés de neteja assegura l'eliminació de tensioactius o altres productes químics presents a la solució comercial, així com la suspensió de les partícules en els diferents medis necessaris per a ulteriors tractaments.

Les partícules fotosensibles del capítol 5 s'obtenen a partir de partícules comercials de sílica funcionalitzades amb grups amino, d'una forma similar a l'explicada pels vidres-ITO, aplicant només el segon pas de la reacció. Pel que fa als el·lipsoides paramagnètics utilitzats al capítol 4, es preparen estirant mecànicament un film ple de les partícules comercials de poliestirè esfèriques i paramagnètiques.[26]

Pel que fa a les dispersions en cristall líquid, en els experiments presentats en aquesta tesi el cristall líquid utilitat és el MLC-7029 (Merk). Una forma de crear les dispersions partícules en NLC és redispersar les partícules en metanol, afegir uns microlitres de la dispersió damunt d'uns microlitres de NLC, deixar que s'evapori el metanol i agitar a l'ultrasons. Com a alternativa, es

pot afegir uns pocs microlitres del cristall líquid damunt de partícules seques (en forma de pols), i agitar la dispersió resultant.

2.3 Muntatges Experimentals

En aquesta tesi, les cel·les experimentals s'observen a través del microscopi òptic de polarització Nikon Eclipse 50iPol, al qual s'hi afegeixen diferents mòduls en funció dels experiments realitzats.

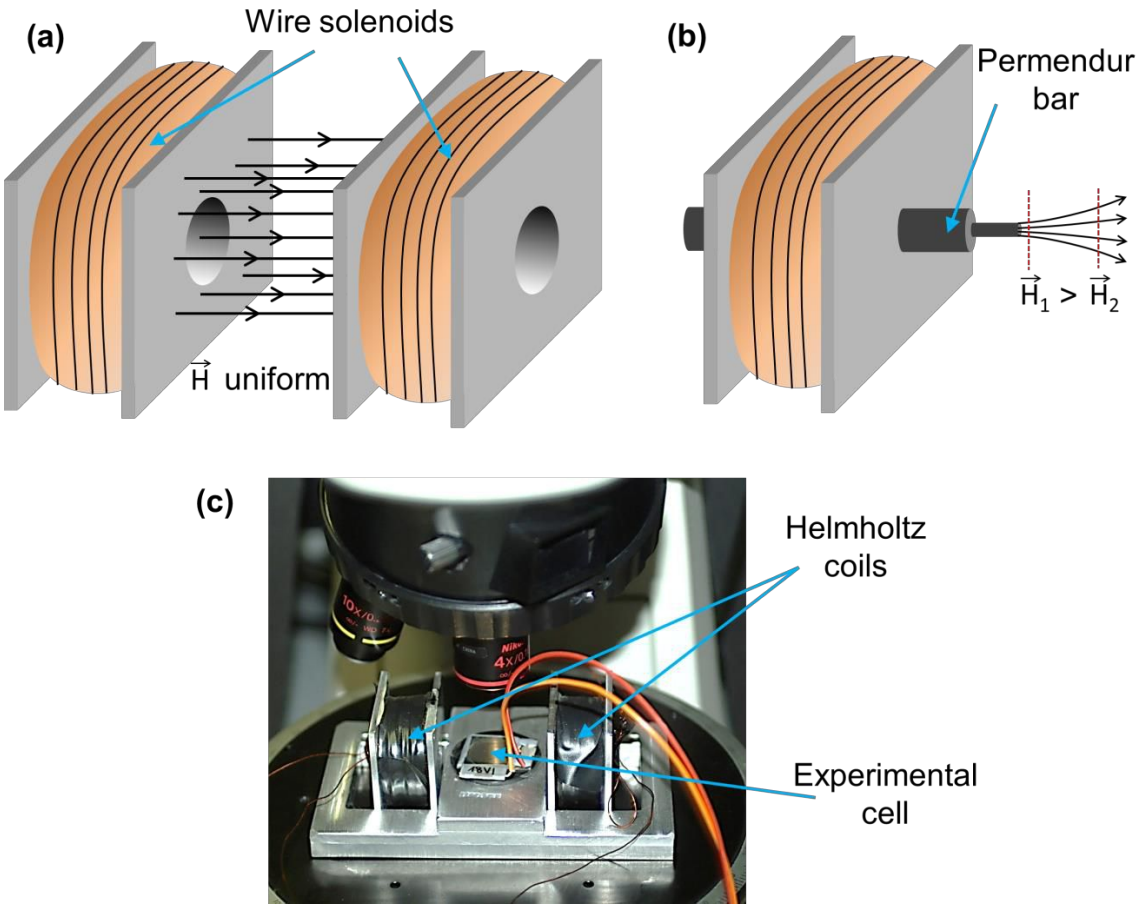

Figura 2.3: (a) Esquema de les bobines de Helmholtz, on un camp magnètic uniforme, representat per fletxes negres, es genera entre les bobines. (b) Esquema d'una sola bobina amb la barra de Permendur inserida al llarg del seu eix principal. Les línies de camp magnètic es concentren en la punta de la barra de Permendur. (c) Fotografia del muntatge de les bobines de Helmholtz en el microscopi òptic de polarització.

Per poder aplicar camps magnètics uniformes sobre les cel·les experimentals, s'ha preparat sobre la platina del microscopi un muntatge tipus bobines de Helmholtz, tal i com es mostra a la figura 2.3. En aquesta configuració la separació de les dues bobines és més gran que el seu radi interior, a causa de restriccions geomètriques. Aquesta disposició permet la rotació del suport d'alumini, on estan subjectes les bobines, que al seu torn fa girar l'orientació del camp magnètic en el pla respecte a la cel·la, que es manté fixa. El camp magnètic generat es calibra en termes de la intensitat del corrent aplicat a les bobines, i la separació entre elles. Per focalitzar el camp magnètic generat per les bobines, se'ls pot inserir una barra de Permendur (un aliatge de cobalt i ferro) tal i com mostra la figura 2.3b.

La irradiació de les mostres amb llum de longituds d'ona de 365nm o 455nm es fa a través d'un muntatge d'epi-il·luminació LED (Thorlabs, Inc.) integrat en el microscopi òptic de polarització. L'esquema de la seva disposició es pot trobar a la figura 2.4.

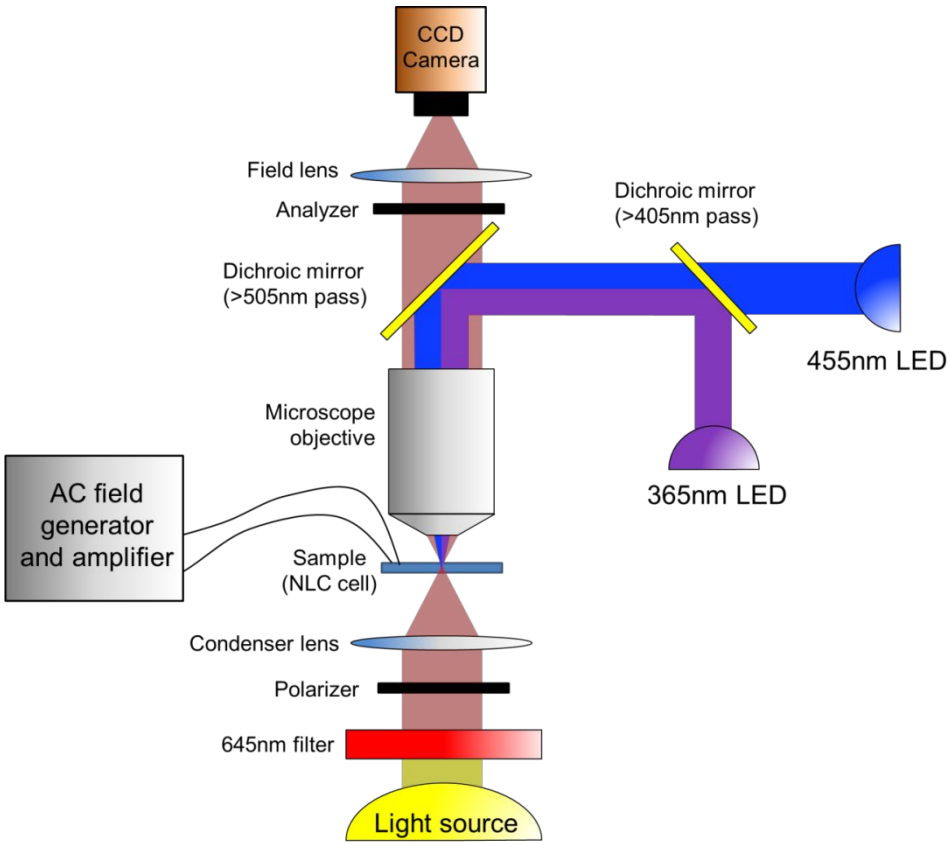

Figura 2.4: Esquema del muntatge d'epi-il·luminació LED en el microscopi de polarització.

3. Capítol 3: Estudi d'Agregats Col·loïdals Induïts per Electrodinàmica

3.1 Introducció

Com a primer estudi d'aquesta tesi, s'ha investigat la influència dels camps elèctrics en dispersions col·loïdals de partícules sòlides en medi aquós. Se sap que si es confinen adequadament aquestes dispersions, és possible ordenar les partícules que les componen en diferents estructures.9-11 Aquestes estructures poden tenir diferents graus d'ordenació, forma i paràmetres de cel·la, i això obre tot un ventall de possibles aplicacions en diferents camps com la creació de dispositius òptics i electroòptics,[27,28] biosensors[29] o reactors a escala micromètrica.[30]

Està reportat en la literatura que quan es treballa amb partícules esfèriques confinades bidimensionalment entre dues plaques conductores, i s'aplica un camp elèctric altern a través d'elles, apareixen dos efectes contraposats: un és la interacció dels dipols elèctrics de les partícules creats pel camp elèctric (que tendeix a separar les partícules en el pla), i l'altre és un efecte d'atracció a causa del flux electrohidrodinàmic.[14] Aquest flux electrohidrodinàmic apareix per la distorsió que generen les partícules en la densitat de càrregues (ions) acumulades prop de els elèctrodes. En funció del camp altern aplicat es pot afavorir un o altre efecte, donant així lloc als diferents tipus d'ordenació esmentats anteriorment.

En el nostre cas estudiem l'agregació de partícules col·loïdals isòtropes (esfèriques) i partícules anisomètriques de forma allargada (*pear-shaped*) en medi aquós confinades en dues dimensions quan estan subjectes a camps elèctrics alternats externs. Amb això volíem desvetllar el paper de l'anisotropia en el procés d'agregació col·loïdal.

Per altra banda, a la segona part d'aquest capítol he estudiat la interacció d'agregats de partícules isotròpiques amb inclusions magnètiques, per tal de mesurar la força de cohesió entre les partícules que formen els cúmuls.

3.2 Agregació de Col·loides No Magnètics

A diferència d'altres estudis anteriors amb partícules anisomètriques descrits en la literatura, nosaltres apliquem el camp elèctric altern perpendicular al pla de confinament de les partícules. En el rang d'amplituds utilitzat, a freqüències baixes (f <2.5kHz) el camp extern genera un flux electrohidrodinàmic que tendeix a agrupar les partícules, donant lloc a una interacció atractiva que promou la nucleació d'agregats compactes. Per contra, si es fan servir freqüències més altes, dominen les interaccions repulsives de tipus dipolar, i les partícules es queden disperses en el medi.

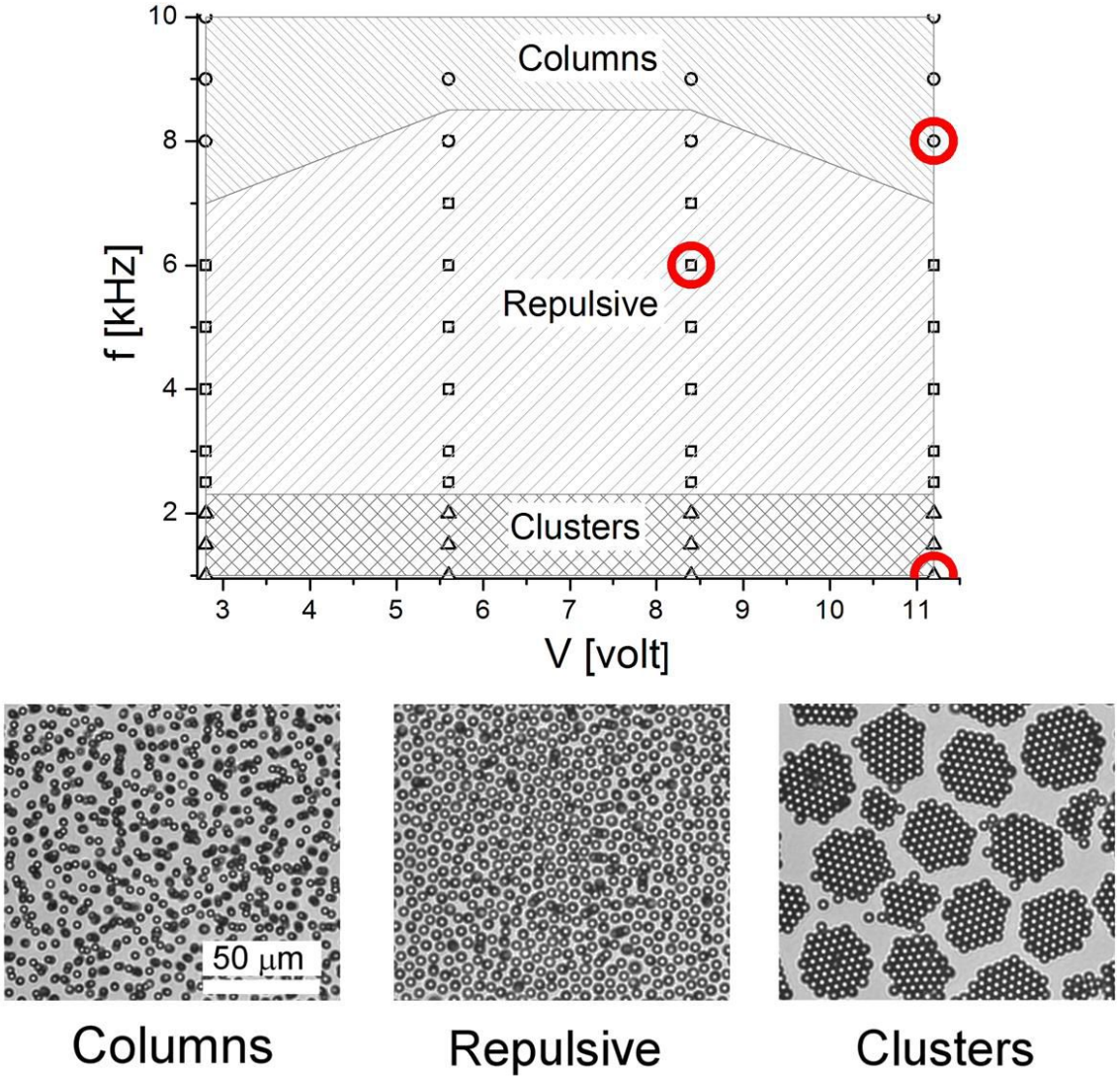

Figura 3.1: Diagrama de fases en el pla de freqüència/voltatge, on es veuen les diferents ordenacions que presenten les partícules esfèriques.

Tot i que en ambdós tipus de partícules s'han observat comportaments similars, les *pear-shaped* presenten un diagrama de fases més ric és a dir, amb major nombre de fases- que el de les partícules esfèriques, tal i com es pot observar en les figures 3.1 i 3.2. També s'ha trobat que les *pear-shaped* tendeixen a formar agregats més petits i allargats, i amb una cinètica d'agregació més ràpida.

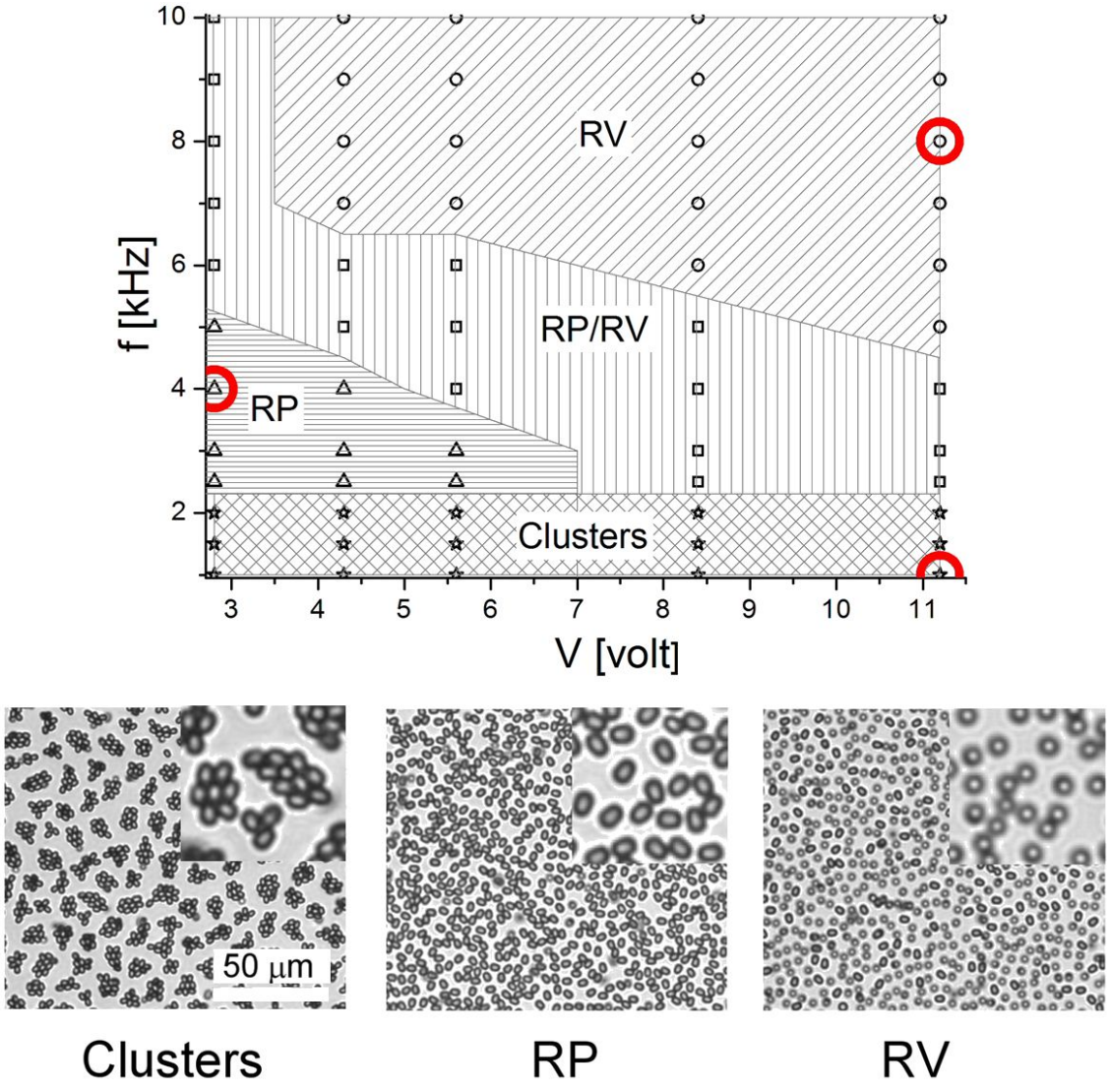

Figura 3.2: Diagrama de fases en el pla de freqüència/voltatge, on es veuen les diferents ordenacions que presenten les partícules *pear-shaped*.

Per quantificar l'efecte de l'anisotropia de les *pear-shaped* en les estructures observades, mesurem la funció de parell de correlació (pair correlation function) g (r), que quantifica l'ordre translacional dels agregats, és a dir, el grau d'ordenació del sistema. En les fases repulsives es veia clarament un ordre translacional molt pobre, tant per a les esfèriques com per a les anisomètriques, indicant una fase de tipus "líquid" (les partícules estaven desordenades). En la fase d'agregats en canvi es va observar que les partícules esfèriques presentaven un millor ordre posicional (tenien una forma més ordenada, com els àtoms d'un cristall), absent en les anisomètriques, pel fet que les segones formaven agregats de menys partícules, més fragmentats i anisòtrops. Aquesta tendència es devia bàsicament a la forma anisomètrica de les *pear-shaped*, que frustrava el creixement d'agregats majors durant la nucleació.

La compactació dels agregats mesura calculant el *radius of Gyration* R_g dels agregats en funció del nombre de partícules que componien aquests agregats. Amb això es podia calcular la dimensió fractal dels agregats, que per a les partícules esfèriques era 2.0, indicant el màxim grau de compactació en dues dimensions, i per a les *pear-shaped* era lleugerament inferior (1.7).

Per estudiar la dinàmica de formació dels agregats de partícules mesurem la grandària mitjana dels agregats (mida mitjana de clúster) en funció del temps per als dos tipus de partícules. Els resultats que vam obtenir van ser que la velocitat d'agregació de les partícules *pear-shaped* era superior a les esfèriques, tot i que la difusió (que tendeix a entorpir el procés d'agregació) de les *pear-shaped* era més gran que les esfèriques. L'explicació que trobem a aquests resultats inesperats és que les partícules anisomètriques, en estar orientades paral·leles a les plaques, tenien una major superfície de contacte amb l'elèctrode i això generava una major distorsió en la densitat de càrrega prop d'aquest, amb la qual cosa la força d'atracció de tipus electrohidrodinàmic entre les partícules *pear-shaped* era superior (i per tant s'agregaven més ràpid).

3.3 Inclusions Magnètiques en Clústers No Magnètics

Per mesurar la força de cohesió dels clústers creats pels fluxos electrohidrodinàmics (EHD), primer intento estudiar el desmantellament d'un grup de partícules esfèriques controlant la interacció de repulsió-atracció entre parells de partícules paramagnètiques inserides en els clústers. Aquesta interacció entre partícules magnètiques es controla a través de camp magnètics aplicats a la cel·la, tal i com es veu en la figura 3.3.

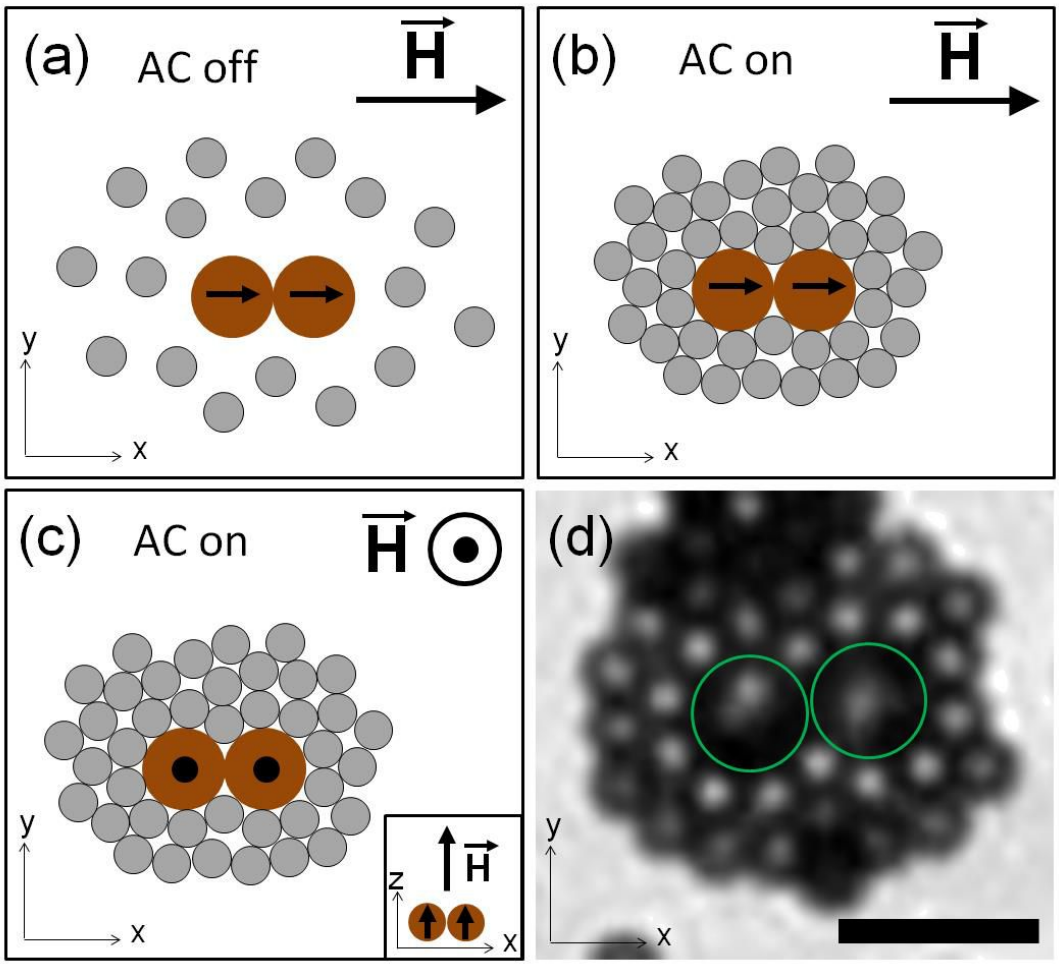

Figura 3.3: (a-c) Esquema del procediment proposat per mesurar la força d'un clúster 2D mitjançant l'ús de dues partícules paramagnètiques (cercles marrons) envoltades per partícules de poliestirè (cercles grisos). Les fletxes negres en les partícules paramagnètiques indiquen els seus dipols induïts magnèticament (en l'eix x en (a, b) i en l'eix z en (c)). El requadre a la cantonada inferior dreta del panell (c) mostra els dipols magnètics induïts en l'eix z. (D) mostra una imatge experimental de dues partícules paramagnètiques (5.8μm de diàmetre, marcats per cercles verds) al mig d'un grup de partícules de poliestirè petites (2.8μm de diàmetre). La barra d'escala marca 10μm.

Malauradament, el sistema experimental en aquesta configuració només és capaç d'aplicar camps magnètics perpendicular fins a deu mil·liTesles, que no són prou forts com per superar la força cohesiva electrohidrodinàmica.

Com a estratègia alternativa per mesurar la força de cohesió dels clústers, he estudiat també les col·lisions de partícules magnètiques contra clústers 2D. Mitjançant l'aplicació d'un gradient de camp magnètic controlat mitjançant l'ús de bobines de Helmholtz (vegeu el capítol 2), es pot fer que les partícules individuals, així com cadenes o agregats de partícules paramagnètiques, es moguin a una velocitat determinada, degut al gradient magnètic $\nabla\vec{H}$ (velocitat $\sim \nabla\vec{H}$). Un de les primers resultats obtinguts és que les partícules individuals no tenen prou força per trencar els clústers, es necessiten cadenes de partícules paramagnètiques llargues propulsades per gradients magnètics per poder travessar els clústers. Un exemple d'aquest comportament es pot veure en la figura 3.4.

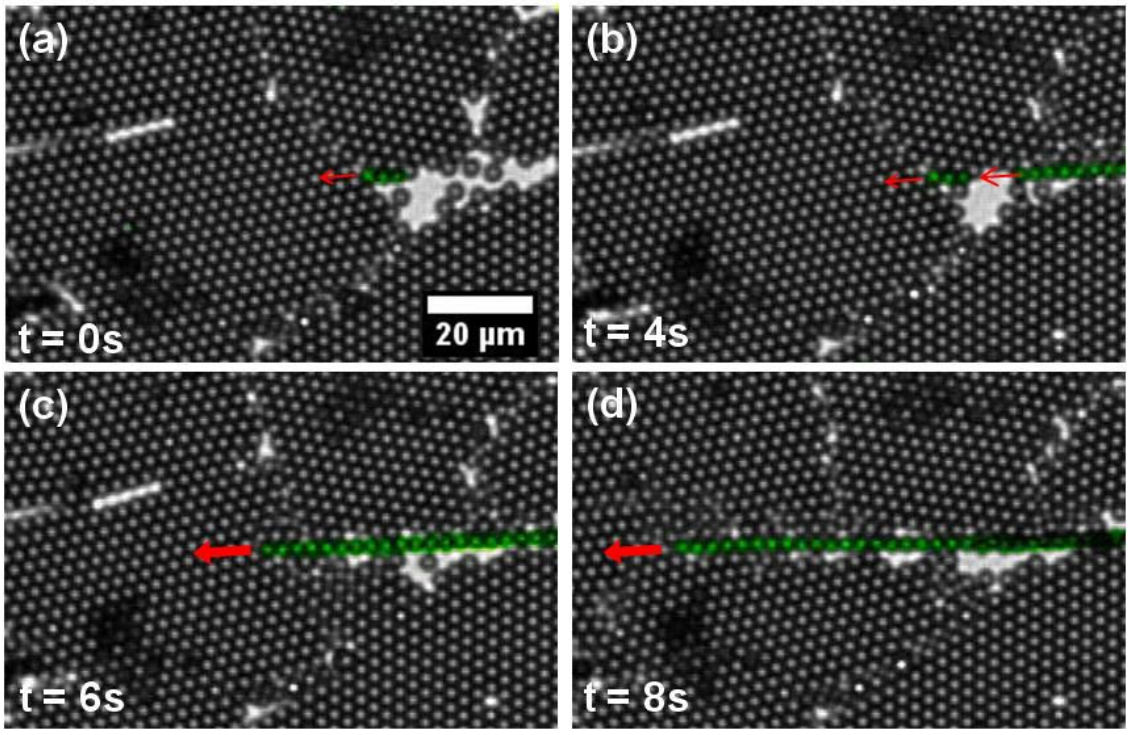

Figura 3.4: Seqüència d'imatges d'una cadena paramagnètica (acolorida artificialment per a major claredat) que passa a través d'un grup de partícules no magnètiques esfèriques. La tracció magnètica s'indica per les fletxes vermelles. La cadena de 3 partícules inicial en (a) no és capaç d'anar a través del clúster, però quan una cadena més llarga s'adjunta amb aquesta, la cadena (ara composta per més de 30 partícules en una fila) pot anar a través del clúster.

3.4 Conclusions

- Les partícules anisomètriques *pear-shaped*, quan se sotmeten a camps elèctrics de CA perpendiculars als elèctrodes, presenten morfologies més riques en comparació amb les partícules esfèriques isotròpiques.

- La forma anisomètrica altera el procés d'agregació per fer-lo més ràpid, encara que menys ordenat, en comparació amb els col·loides esfèrics. No obstant això, el mecanisme d'agregació sembla ser de la mateixa naturalesa per a ambdós tipus de partícules.

- S'han provat diferents estratègies per mesurar la cohesió dels clústers de partícules esfèriques. Si bé se'n poden extreure resultats qualitatius fàcilment, es necessitaran més proves experimentals per tal d'obtenir dades quantitatives.

4. Capítol 4: Trencant la Degeneració d'un Cristall Líquid Nemàtic Mitjançant Col·loides Anisomètrics Paramagnètics

4.1 Introducció

En contrast amb les investigacions sobre les dispersions de cristall líquid de partícules submicró- o nanomètriques,[31,32] l'estudi presentat en aquest capítol se centra en les inclusions en l'escala micromètrica, que permeten un control local del medi. Tot i l'extensa investigació reportada en la literatura, encara hi ha una perspectiva no explorada, que consisteix en l'ús d'inclusions paramagnètiques no esfèriques per controlar l'orientació d'un cristall líquid. Aquest enfocament és contrari al normalment adoptat, ja que en aquest cas les partícules controlades externament modifiquen el medi de dispersió enlloc d'adaptar-s'hi passivament.

4.2 Alineament Magnètic mitjançant Inclusions Paramagnètiques

En aquest capítol demostro que els agregats anisomètrics de partícules esfèriques paramagnètiques o micro-el·lipsoides paramagnètics aïllats, orientats pels camps magnètics febles, poden trencar la degeneració d'orientació d'un cristall líquid nemàtic que es fa transitar a una configuració plana des d'una alineació homeotròpica uniforme. En particular, una combinació d'un camp elèctric (actuant sobre el medi de cristall líquid) i un camp magnètic (que actua sobre les inclusions) s'utilitza per orientar el cristall líquid nemàtic en àrees localitzades al voltant dels col·loides dispersos. En aquest sistema, la força del camp magnètic d'orientació (uns pocs mil·liTesles) és molt inferior (uns dos ordres de magnitud) al llindar de la Transició de Frederiks magnètica, ja que la transició inicial des de l'alineació homeotròpica a la planar està completament reservada a l'acció del camp elèctric altern. En la figura 4.1 es pot veure el

comportament d'una cel·la sense partícules i una amb agregats partícules paramagnètiques en resposta als camps aplicats.

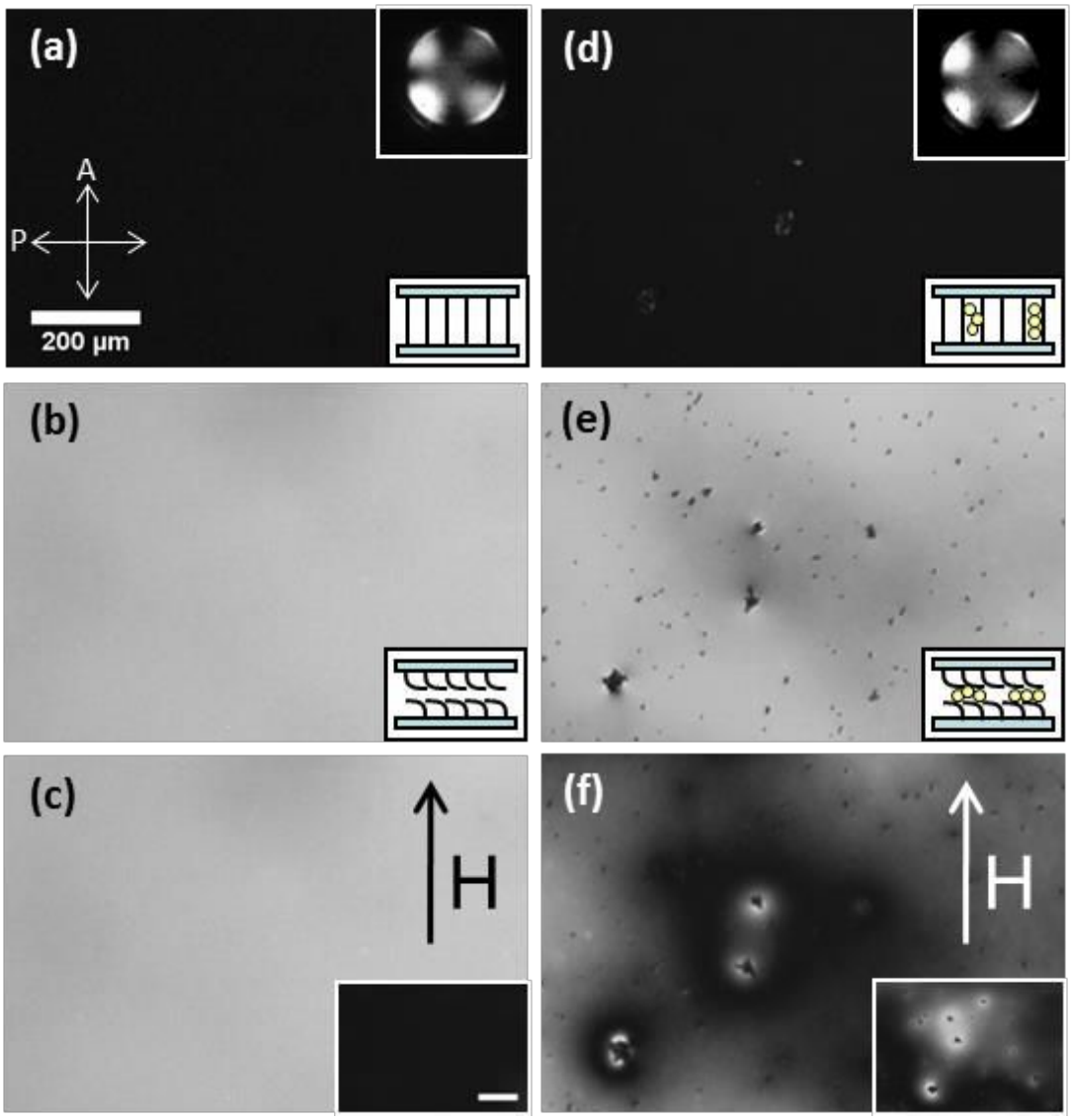

Figura 4.1: Imatges del microscopi de polarització que mostren l'efecte de les inclusions paramagnètiques en l'orientació del NLC. (a-c) són imatges d'una cel·la NLC sense partícules, i (d-f) són imatges d'una cel·la NLC dopada amb les partícules esfèriques. En absència de camps externs, (a) i (d), les cel·les són homeotròpiques (en la imatge conoscòpica inserida, el patró de creu de Malta indica ancoratge homeotròpic). Un camp elèctric perpendicular a les plaques de la cel·la s'aplica en (b), i (e), i un camp addicional en el pla magnètic (6mT) s'aplica a (c) i (f). Les imatges inserides en els últims quadres corresponen a les mostres girades 30° en sentit antihorari (CCW) per veure el canvi de reflectivitat. Els esquemes dibuixats a la part inferior dreta de les imatges (a), (b), (d) i (e) són representacions d'una secció transversal de les cel·les.

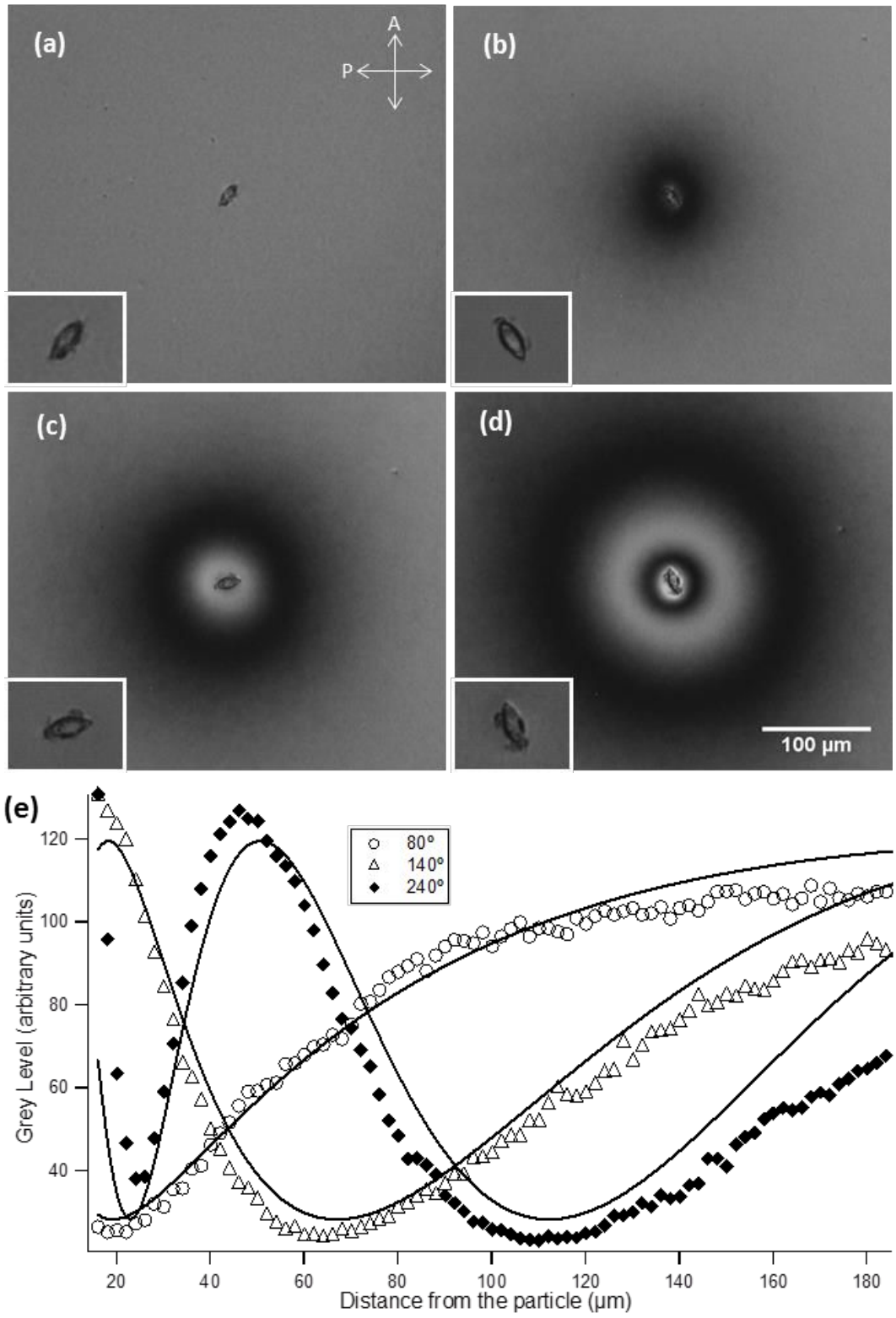

Figura 4.2: La distorsió generada per un el·lipsoide de 25µm de llarg i 10µm d'ample girat antihoràriament. Les quatre imatges inserides són ampliacions (factor 1,8) de l'el·lipsoide central. L'orientació inicial (sense camp magnètic aplicat) es pren com a 0° (a). El camp magnètic (3 mT) s'aplica a (a), i després la partícula gira seguint el camp magnètic, en un angle de 80 ° (b), 140 ° (c), i 240 ° (d). Nivell de gris enfront de la distància de la partícula per a diferents angles de rotació es mostren en (i). Línies contínues són ajustos a l'equació presentada en el text.

A més a més, s'ha descobert que amb aquest mètode és possible generar i controlar textures de diferents simetries, com per exemple patrons de diana (així com també formes espirals), que es poden obtenir i manipular fàcilment a través dels el·lipsoides paramagnètics controlats pel camp magnètic. Tal i com es pot veure en la figura 4.2. Aquest patró de diana es pot explicar mitjançant un senzill model basat en l'energia de distorsió elàstica del cristall líquid, donant com a resultat que la orientació del cristall líquid al voltant dels el·lipsoides segueix l'expressió

$$\phi(r) = \frac{\phi_p \ln\left(\frac{r}{R}\right)}{\ln\left(\frac{r_0}{R}\right)}$$

On ϕ_p és la orientació de l'eix llarg de l'el·lipsoide, r és la distància des de l'el·lipsoide, i els paràmetres ajustables r_0 i R ens indiquen el radi efectiu de l'el·lipsoide, i la distància a la que s'estén la diana.

4.3 Conclusions

- Inclusions paramagnètiques col·loïdals disperses en un cristall líquid nemàtic poden tenir un paper actiu en el control de la orientació del NLC.

- L'ús d'agregats anisomètrics o partícules paramagnètiques anisomètriques fa possible aplicar un parell local de forces per mitjà de camps magnètics febles, sempre i quan el director del nemàtic no estigui fixat per unes fortes condicions d'ancoratge a les plaques de les cel·les.

- Utilitzant les tècniques descrites és possible crear patrons complexos estables, com per exemple textures en forma de diana.

- El fenomen aquí exposat es pot descriure bastant acuradament mitjançant un model simple basat en l'energia de distorsió elàstica d'un cristall líquid.

5. Capítol 5: Electroforesi No Lineal de Microgotes i Partícules Fotosensibles

5.1 Introducció

El transport controlat d'aquestes microgotes és de crucial importància per a moltes aplicacions relacionades amb *lab-on-a-chip*,[33–36] aplicació localitzada de fàrmacs, [37] 5 o la realització de micromotors controlats remotament.[38–42]

En una tercera etapa d'aquest projecte s'ha investigat el moviment controlat de microgotes de solució aquosa disperses en cristall líquid nemàtic, propulsades per un camp elèctric altern mitjançant l'Electroforesi Possibilitada per Cristall Líquid (LCEEP). També s'ha investigat sobre la possibilitat d'activar i desactivar la LCEEP de partícules individuals mitjançant irradiació a diferents longituds d'ona, fent servir partícules fotosensibles preparades especialment.

5.2 LCEEP de microgotes

Recentment s'ha reportat en la literatura que partícules micromètriques sòlides amb un defecte tipus hedgehog es poden transportar en un NLC usant un camp elèctric altern .[7] Aquest desplaçament electroforètic de les partícules es deu a la naturalesa dipolar del defecte puntual que, a diferència del defecte Saturn Ring, trenca la simetria de la partícula. Aquesta asimetria desbalanceja el flux d'ions creat pel camp altern al voltant de la partícula, generant així un desplaçament net (veure capítol 1). El principal avantatge d'aquesta tècnica pel que fa a l'electroforesi tradicional és que fer servir camps elèctrics alterns evita problemes com ara la migració d'ions, l'electròlisi i les reaccions electroquímiques no desitjades, fent-la adequada per transportar no només partícules sòlides, sinó també inclusions líquides.

En el nostre cas hem aconseguit demostrar que la LCEEP es pot fer servir per transportar microgotes en cristall líquid nemàtic. Els defectes puntuals generats en el NLC per les microgotes trenquen la simetria davant-darrere i permeten el desplaçament controlat de les gotes en la direcció del defecte, tot i que aquest és perpendicular al camp AC aplicat, tal com es pot veure en la figura 5.1.

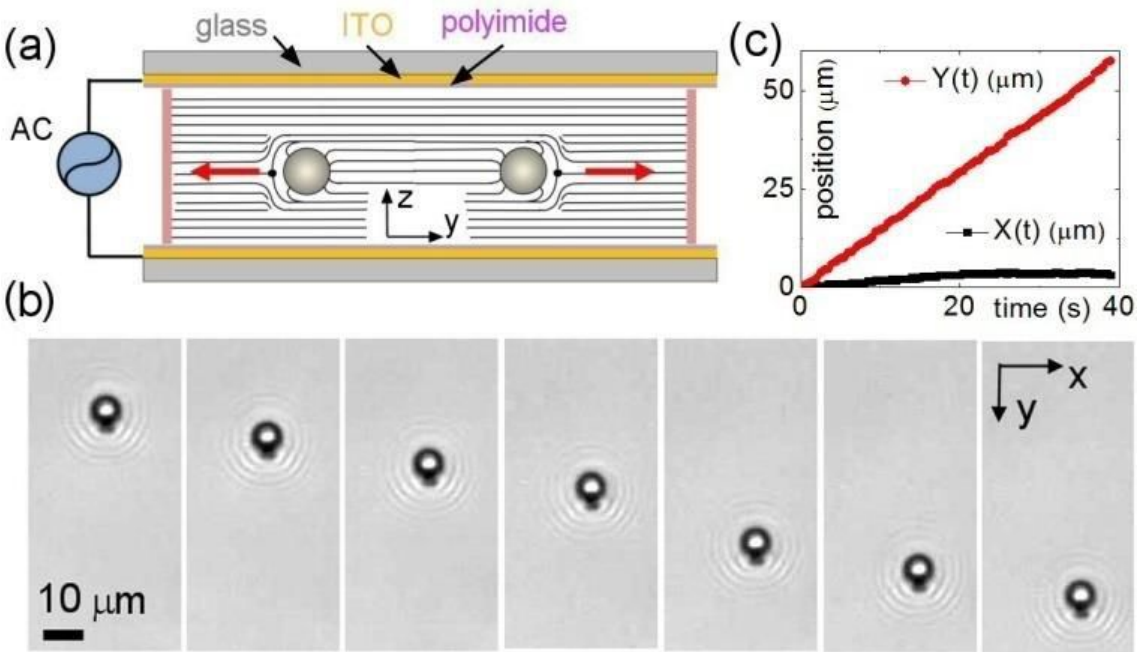

Figura 5.1: (a) Esquema de la cel·la experimental composta de microgotes d'aigua dispersades en un cristall líquid nemàtic. Les gotes d'aigua s'impulsen amb l'aplicació d'un camp elèctric altern entre les plaques de la cel·la. (b) imatges preses cada 4.5s d'una gota d'aigua de 6.5μm de diàmetre propulsada a una velocitat de 1.7μm / s per un camp altern amb amplitud E = 0,7 V / m i freqüència f = 10 Hz. (c) mostra les posicions (x, y) enfront del temps per la gota que es mostra en el panell (b).

Mitjançant aquest sistema hem pogut caracteritzar la velocitat de les gotes en funció de la seva mida, de la freqüència, i de l'amplitud del camp aplicat, que coincideixen amb les indicades per la teoria. També hem demostrat que aquestes gotes es poden emprar com a transportadors de càrregues microscòpiques sòlides (figura 5.2a). A més a més, s'ha pogut demostrar també que les gotes es poden fer servir com a microreactors per transportar i barrejar

volums molt petits de reactius (10^{-14} - 10^{-16}L). Com a exemple (figura 5.2b)s'han fet reaccionar dues gotes, una de les quals contenia una solució de Clorur de Ferro (III) i l'altra una solució de hexacianoferrat (II) de Potassi, donant lloc a una gota més gran que contenia un precipitat blau intens, hexacianoferrat (II) de Ferro (III) (reacció del Blau de Prússia).

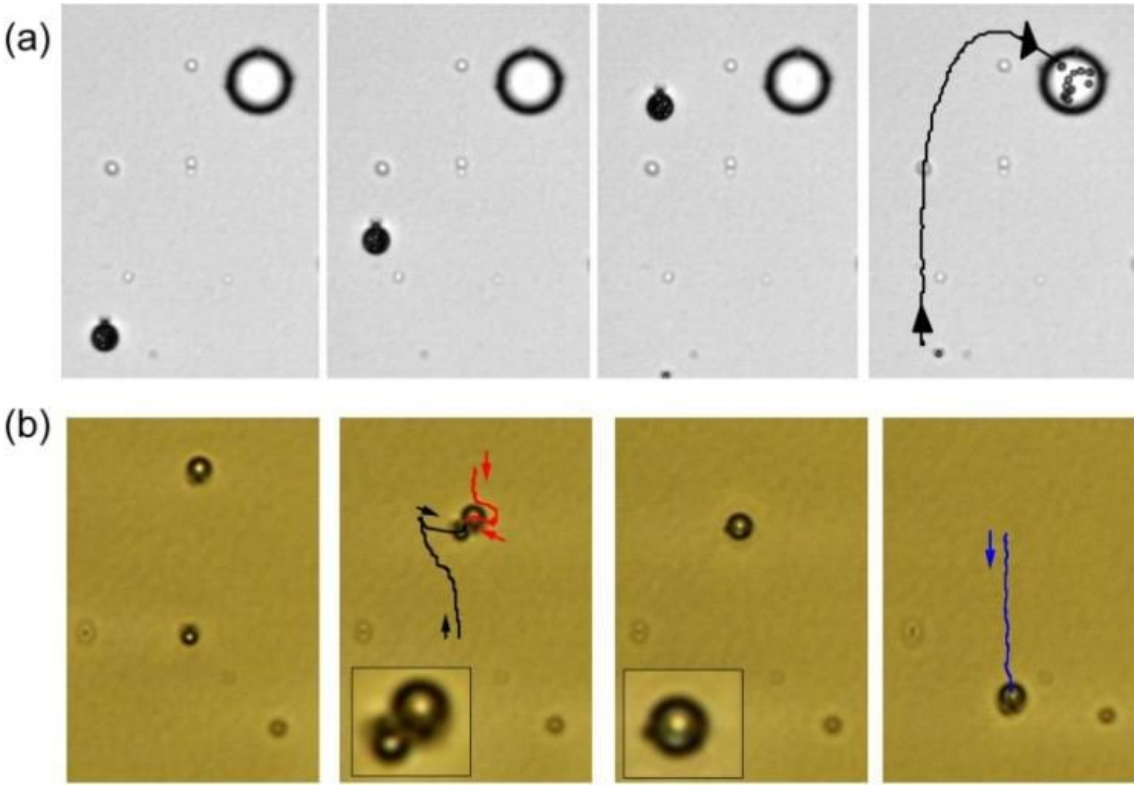

Figura 5.2: (a) Seqüència d'imatges que mostren l'absorció d'una microgota ($\phi = 7.3\mu m$) transportant 11 partícules de poliestirè (1.7μm de diàmetre), per part d'una gota més gran ($\phi = 18\mu m$) immòbil, amb un defecte *Saturn ring* (E = 0,7 V / m, f = 10 Hz). L'interval de temps entre imatges és 17.2s. (b) Seqüència d'imatges que mostra dos microgotes d'aigua ($\phi = 2.7\mu m$ and $3.7\mu m$) impulsades en direccions oposades per un camp altern (E = 0,7 V / m, f = 10 Hz) i que contenen reactius separats: hexacianoferrat de potassi (II) (0,2 M) i clorur de ferro (III) (0,3 M). Les gotes s'aproximen i s'uneixen en una de més gran ($\phi = 4.3\mu m$), formant el Blau de Prússia [ferro (III) hexacianoferrat (II)] com a precipitat. El camp altern fa moure llavors la gota resultant allunyant-se de la zona de reacció. El temps total transcorregut és 46s.

5.3 LCEEP de Partícules Fotosensibles

L'eficiència de la LCEEP està condicionada principalment per la naturalesa dels defectes del NLC que envolta les inclusions. En ajustar les condicions d'ancoratge a la superfície de la partícula, es poden controlar els defectes generats, que al seu torn indueixen la LCEEP sobre les partícules. En aquesta secció explico com les condicions d'ancoratge es poden controlar mitjançant llum gràcies a un azoderivat unit químicament a la superfície de les partícules de sílica disperses en el medi.

Inicialment, en absència d'irradiació, les partícules presenten ancoratge homeotròpic amb un defecte hedgehog (dipolar, defecte asimètric), com es mostra en les figures 5.3a,b. Quan aquestes partícules s'irradien amb llum UV (365 nm) durant 1-3 segons, la configuració del seu defecte canvia a una doble Boojum (quadrupolar, defecte simètric), una configuració típicament trobada en partícules amb un ancoratge planar (figura 5.3c,d).

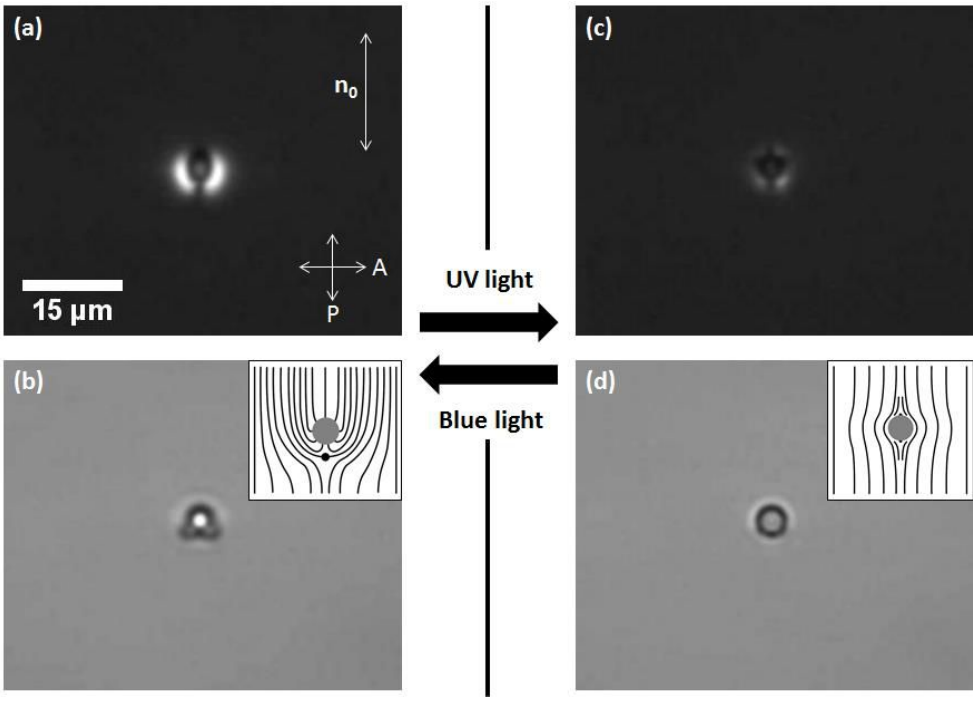

Figura 5.3: Imatges entre polaritzadors creuats (a, c) i sense polaritzadors (b, d) dels dos tipus de defectes diferents al voltant de les partícules fotosensibles. El defecte Hedgehog (a, b) es forma sota irradiació de llum blava (455nm) o en condicions de llum ambiental, mentre que el defecte doble Boojum (c, d) es forma sota llum UV (365 nm). Al panell (a) s'indica l'orientació dels polaritzadors P,A, i l'orientació del NLC($\mathbf{n}_0$). Les insercions en els panells (b, d) mostren esquemes dels defectes de Hedgehog i de doble Boojum, respectivament.

Sent capaços de canviar la configuració dels defectes en les partícules fotosensibles disperses en el NLC, el següent pas és intentar la LCEEP en aquestes partícules. De fet, quan un camp de corrent alterna s'aplica a la cel·la, aquestes partícules comencen a moure's, sempre que presentin una configuració de Hedgehog dipolar (és a dir, en condicions de llum blava). Quan la cel·la NLC electroforètica s'irradia localment uns segons amb llum UV, les partícules il·luminades canvien la naturalesa del seu defecte de dipolar a quadrupolar, i paren de moure's sota el camp altern. Si llavors irradiem les partícules amb llum blava, aquestes recuperen el defecte Hedgehog dipolar i es comencen a impulsar de nou. Un exemple d'aquest fenomen es pot trobar a la figura 5.4.

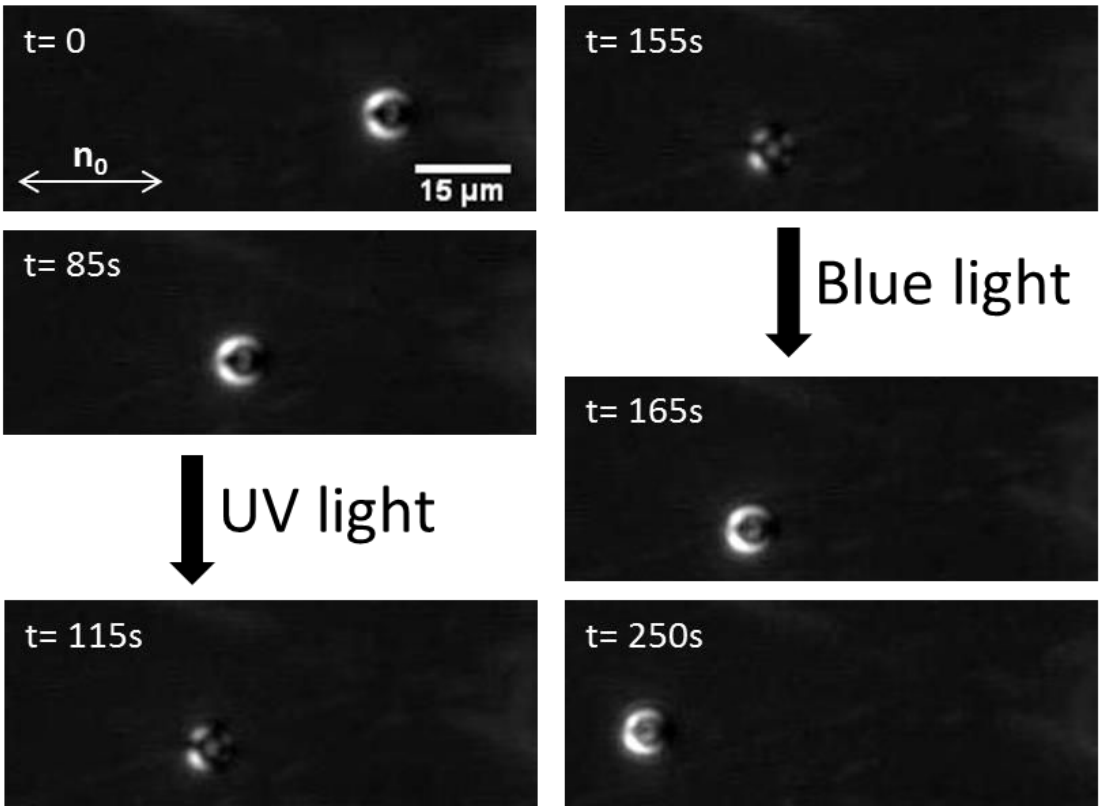

Figura 5.8: Seqüència d'imatges entre polaritzadors creuats del moviment de partícules fotosensible en una cel·la NLC electroforètica. Un camp altern E = 0,7 V / m i f = 25 Hz s'aplica entre les plaques de cel·la durant tot l'experiment. La partícula, que inicialment té una configuració Hedgehog dipolar, comença a moure's. A t = 115s s'irradia amb llum UV (365 nm) i el seu defecte canvia a un doble Boojum quadrupolar, i la partícula deixa de moure's fins que a t = 165s s'irradia amb llum blava (455 nm) i el seu defecte es transforma de nou en un Hedgehog dipolar, i el moviment es restaura.

5.4 Conclusions

- He pogut demostrat diverses estratègies per al transport, reacció i agrupació de microgotes de solucions aquoses impulsats per camps elèctrics alterns en un medi de cristall líquid nemàtic, obrint noves perspectives per al transport controlat de substàncies químiques o medicaments miscibles en aigua.

- Aquest procés es pot descriure mitjançant el model d'Electroforesi Possibilitada per Cristall Líquid, malgrat que el mecanisme real que impulsa les inclusions líquides té encara algunes qüestions pendents, com ara la forma en què la naturalesa del NLC determina la direcció del moviment de les gotes respecte a la posició del defecte Hedgehog.

- És possible controlar localment el camp director del NLC al voltant de partícules fotosensibles mitjançant irradiació amb llum blava o ultraviolada. Aquest control de la configuració dels defectes mitjançant llum permet l'activació o desactivació de la LCEEP en aquestes partícules a través de canvis reversibles entre la configuració de defecte dipolar (hi ha propulsió) i la quadrupolar (no hi ha moviment) al voltant de les inclusions.

6. Capítol 6: Eixams Reconfigurables de Partícules Col·loïdals Controlades per Superfícies Photosensibles

6.1 Introducció

En el capítol anterior he presentat el transport unidireccional controlat d'inclusions de diferent naturalesa impulsades per LCEEP. Les inclusions propulsades seguien el NLC, que tenia una orientació del camp director fixa, determinada per les condicions de contorn planar direccional sobre les plaques de les cel·les. Aquest sistema només és capaç de transportar les inclusions en trajectòries rectes, i per tant és menys eficaç en comparació amb altres sistemes microfluïdics.[34,43]

En aquest capítol presento una tècnica electro-òptica que permet controlar de forma remota l'agrupament reversible i el transport col·lectiu d'inclusions col·loïdals de mida micromètrica, amb diferents formes i composicions, disperses en una cel·la de NLC.

6.2 Formació d'Eixams Reconfigurables: Aster i Mill

En les cel·les NLC utilitzades, una de les plaques es funcionalitza amb una monocapa d'azosil·là fotosensible amb la finalitat d'induir, quan s'irradiï amb llum adequada, una alternança entre condicions de contorn (ancoratge) homeotròpiques (perpendiculars) o planars (tangencials).

El protocol bàsic per formar eixams de partícules és el següent: quan s'irradien les cel·les NLC amb un punt de llum UV, les molècules d'azosil·là irradiades isomeritzen des d'un estat inicial *trans* a una configuració *cis*, i apareix un patró radial a causa del perfil d'intensitat (decau des del centre). Com a resultat, s'obté un ancoratge del NLC híbrid: homeotròpic a la placa superior no fotosensible, i radialment planar sobre la placa inferior (figura 6.1a,

b). L'aplicació d'un de camp altern per sobre de 2.2V, que correspon a la transició Fredericks, obliga les molècules NLC a adoptar una orientació planar, i llavors el patró radial prèviament imprès s'estén fins a uns pocs mil·límetres (figura 6.1c). En augmentar encara més l'amplitud del camp altern, les partícules disperses, que també han adoptat orientació planar junt amb el NLC, es comencen a moure degut a la LCEEP en la direcció determinada localment pel director del NLC (figura 6.1c, d).

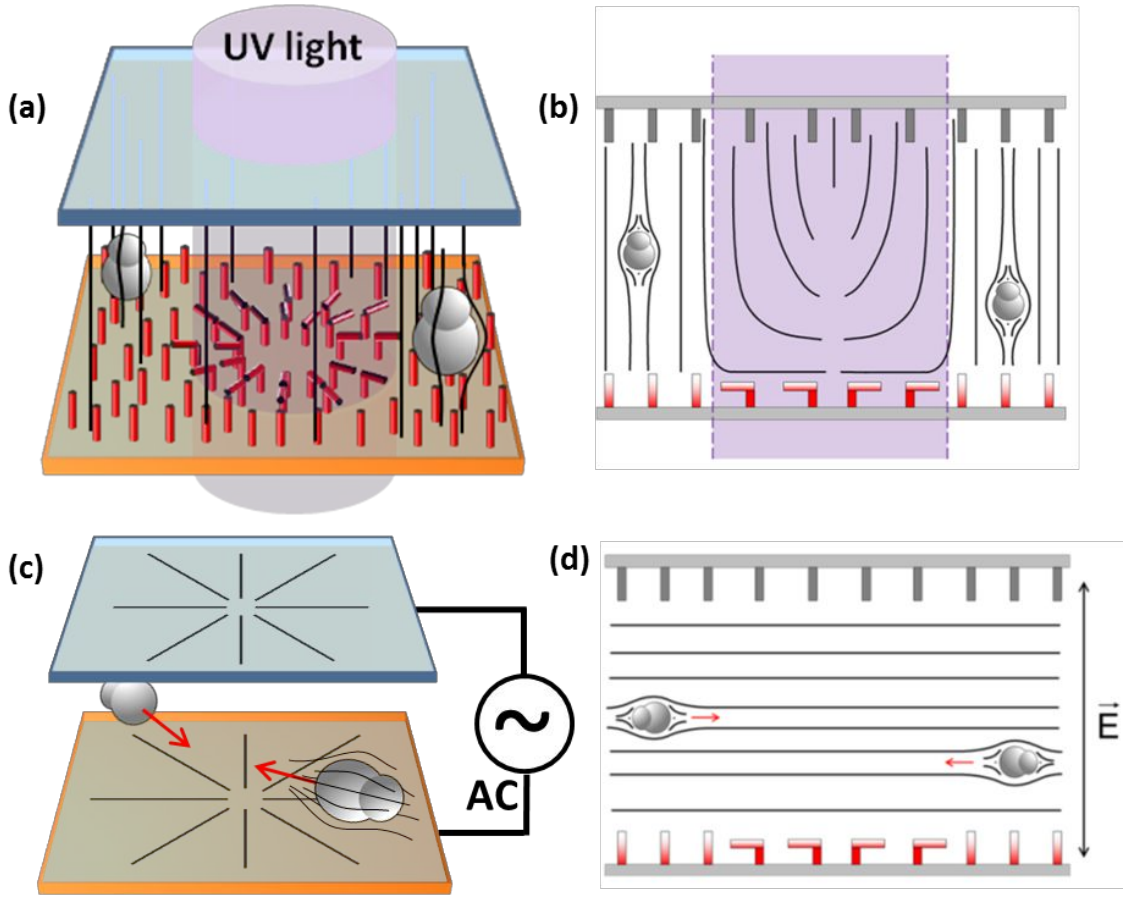

Figura 6.1: (a) Esquema de la cel·la experimental quan un patró radial s'imprimeix utilitzant llum UV (365 nm). Els col·loides es dispersen en el cristall líquid nemàtic (NLC) confinat entre una placa fotosensible (part inferior) i una altra no fotosensible (a dalt). Els patrons d'alineació en el pla impresos amb llum són reversibles. Les partícules anisomètriques disperses estan alineades seguint el director local del NLC (línies negres). (b) Esquema d'un tall transversal de la cel·la experimental després de la irradiació amb UV. (c) Esquema de la cel·la experimental i (d) del tall transversal, quan s'aplica un camp elèctric altern. Les fletxes vermelles indiquen la direcció de moviment de les partícules anisomètriques.

Amb aquest sistema es poden crear dos tipus d'eixams: Tipus *aster*, on les partícules s'acumulen i queden quietes, o tipus *mill*, on s'acumulen girant al voltant del centre d'atracció. A la figura 6.2 es mostra un exemple d'ambos tipus d'eixams.

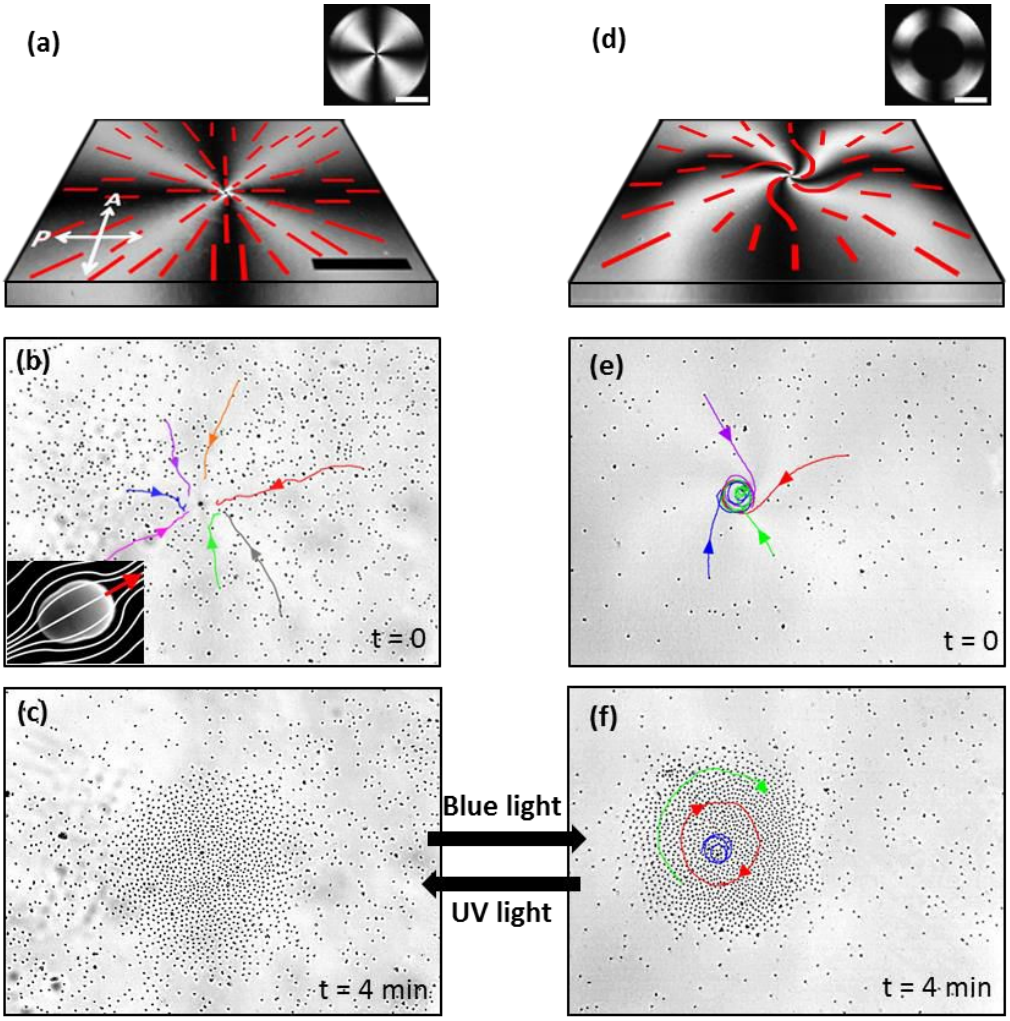

Figura 6.2: Formació d'eixams de partícules. Imatges (a-c) i (d-f) il·lustren la formació d'un *aster* col·loïdal i un *mill*, respectivament. (a, d) Imatges entre polaritzadors creuats dels patrons d'atracció impresos en el NLC amb forma de creu (a) o d'espiral (d). Les línies vermelles discontínues representen l'orientació del director del NLC. Requadres inserits: cercle planar foto-alineat (a) i corona circular (d) abans de l'aplicació del camp elèctric. Formació d'un *aster* (b, c) i un *mill* (i, f) després de l'aplicació d'un camp elèctric amb una freqüència de 10 Hz i una amplitud de 0,87 V/micres. Les trajectòries de diverses partícules es superposen a les imatges per il·lustrar el mecanisme de formació d'eixam. El requadre en (b) mostra la imatge SEM d'una partícula *pear-shaped* (3x4μm^2), amb les línies de camp NLC i la direcció de moviment. El *aster* col·loïdal (c) i el *mill* (f) es poden interconvertir mitjançant una irradiació adequada. La barra d'escala representa 200 micròmetres, excepte per a les dues insercions que són 500μm.

6.3 Transport dels Eixams i Fenòmens Relacionats

La reversibilitat i la resposta ràpida de la capa fotosensible permet un control directe dels eixams. Una acumulació de mida arbitraria, ja sigui *aster* o *mill*, es pot reubicar a qualsevol lloc preseleccionat dins de la cel·la experimental amb un desmantellament mínim de l'estructura de l'eixam, simplement canviant la ubicació de la taca UV (figura 6.3a, b). Un exemple d'aquest procés es mostra en la figura 6,3c.

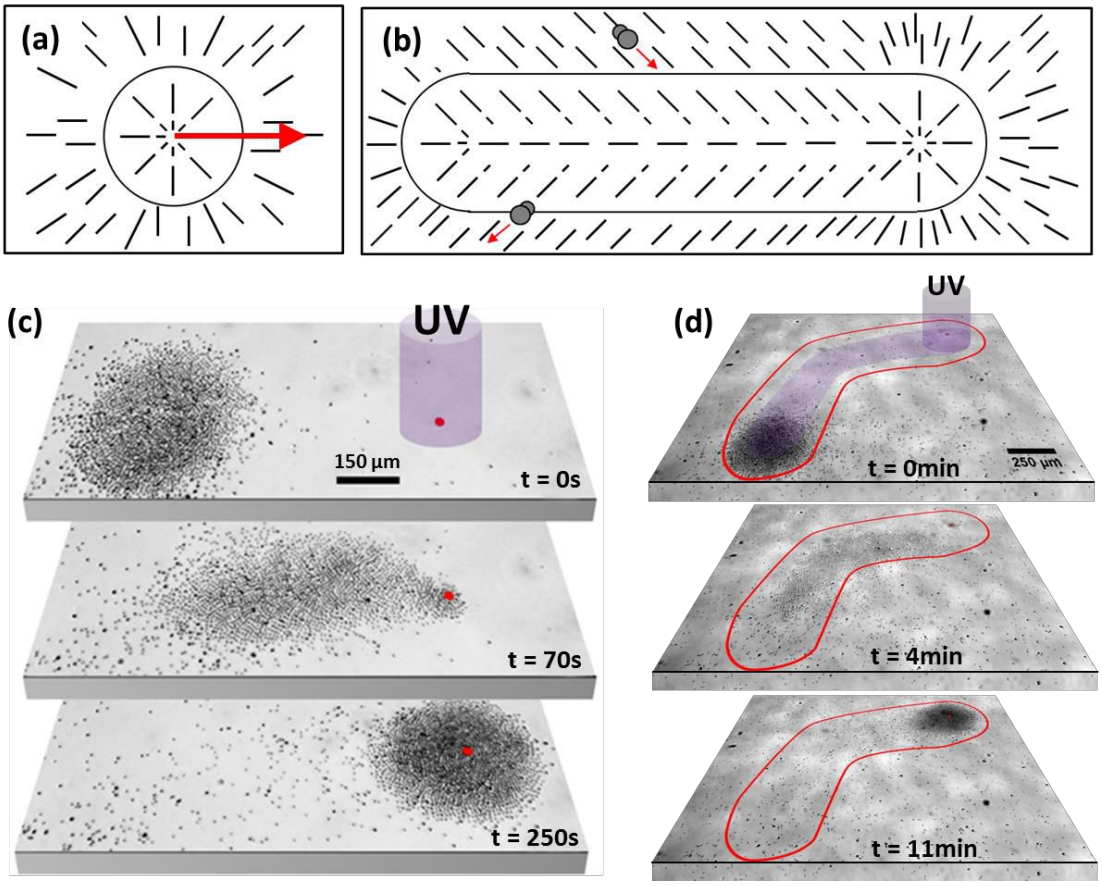

Figura 6.3: Control d'eixams. (a, b) Esquema de la seqüència d'imatges es mostra en (c): la formació d'una trajectòria lineal d'atracció, preparada movent el punt d'irradiació UV mentre la LCEEP està inhibida degut a la alta freqüència del camp elèctric (f > 50Hz). Quan la freqüència es canvia de nou a 10 Hz, les partícules comencen a moure's seguint el camí i s'acumulen en el seu extrem. (c, d) Seqüències d'imatges d'eixams de partícules que viatgen a través de la cel·la NLC causa de la reconfiguració in situ del camp NLC. (c) El punt fotoalineat, inicialment centrat en l'eixam, es mou 600µm a la dreta en una línia recta, com indica el punt vermell. La barra d'escala marca 150µm. (d) Una pista més llarga combinant segments corbs i rectes. El contorn de la pista, només visible entre polaritzadors creuats, es descriu en vermell. La barra d'escala representa 250 micres.

Altres fenòmens derivats de la translació dels eixams són la creació de xarxes d'eixams (figura 6.4a), el canvi de simetria d'aquestes xarxes d'eixams (figura 6.4b) o el control localitzat del tipus d'eixam (*aster* o *mill*) que formen aquestes xarxes (figura 6.4c)

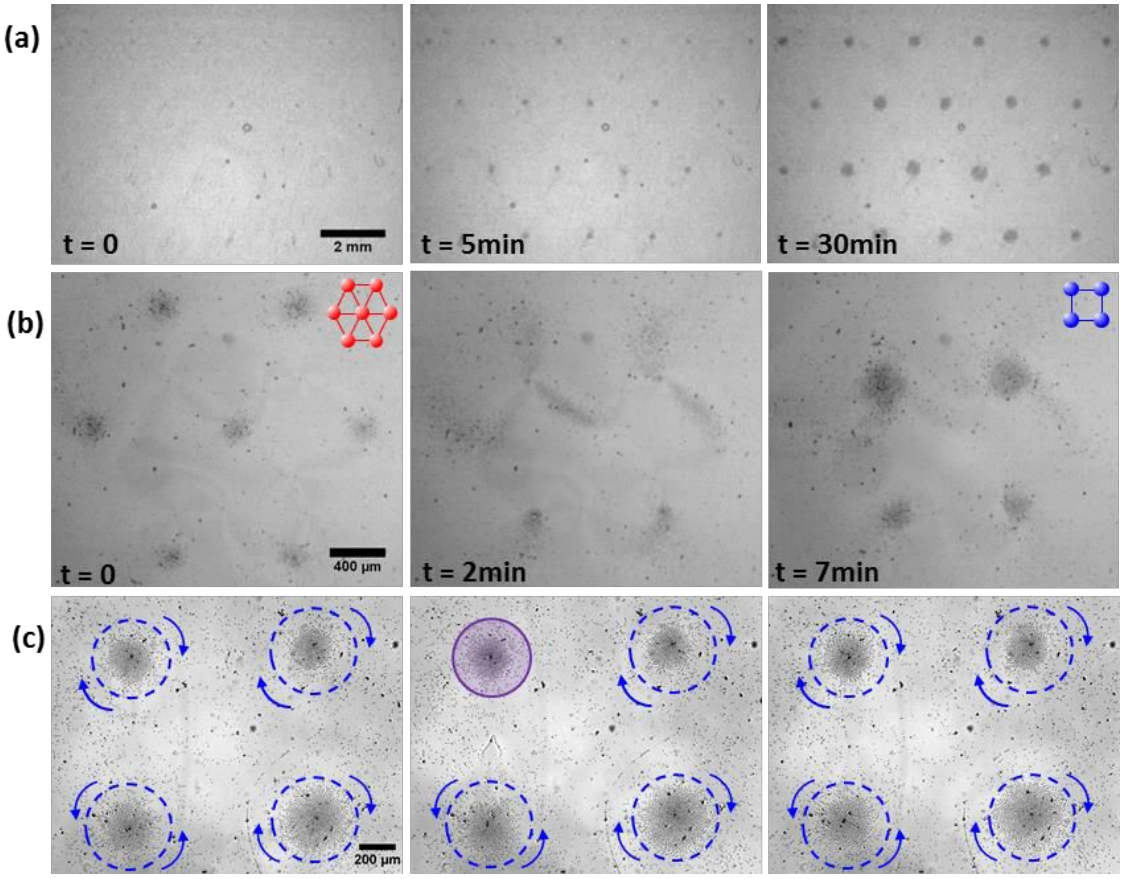

Figura 6.4: Xarxes reconfigurables d'eixams. (a) Seqüència d'imatges per a la formació d'una xarxa triangular d'eixams. La barra d'escala és de 2 mm. (c) Seqüència d'imatges per a la transformació d'una xarxa triangular en una quadrada. La distribució original dels punts atractors s'esborra amb llum blava (455 nm), i una xarxa quadrada s'imprimeix posteriorment usant llum UV (365 nm). El reordenament dels eixams es produeix quan s'aplica un camp elèctric altern 10 Hz i 0,78 V/µm. La barra d'escala és 400µm. (c) L'estat dinàmic dels eixams en una xarxa es pot controlar de forma individual. Mentre tots els eixams estan girant, la dinàmica de l'eixam de la part superior esquerra s'atura primer (passa de *mill* a *aster*) per després tornar a moure's de nou (torna a *mill*). La barra d'escala és 200µm.

Amb aquest sistema també és possible actuar sobre inclusions de diferent naturalesa, per exemple cilindres micromètric o gotes (figura 6.5). A més a més s'ha vist la organització espontània de partícules de diferents mides dins d'un mateix eixam (figura 6.6), així com també s'ha aconseguit emmagatzemar un

eixam dins d'un confinament físic (figura 6.7 corral). Finalment s'ha pogut crear un feix de partícules propulsades mitjançant la combinació d'una placa fotosensible i una planar en una cel·la NLC (figura 6.8).

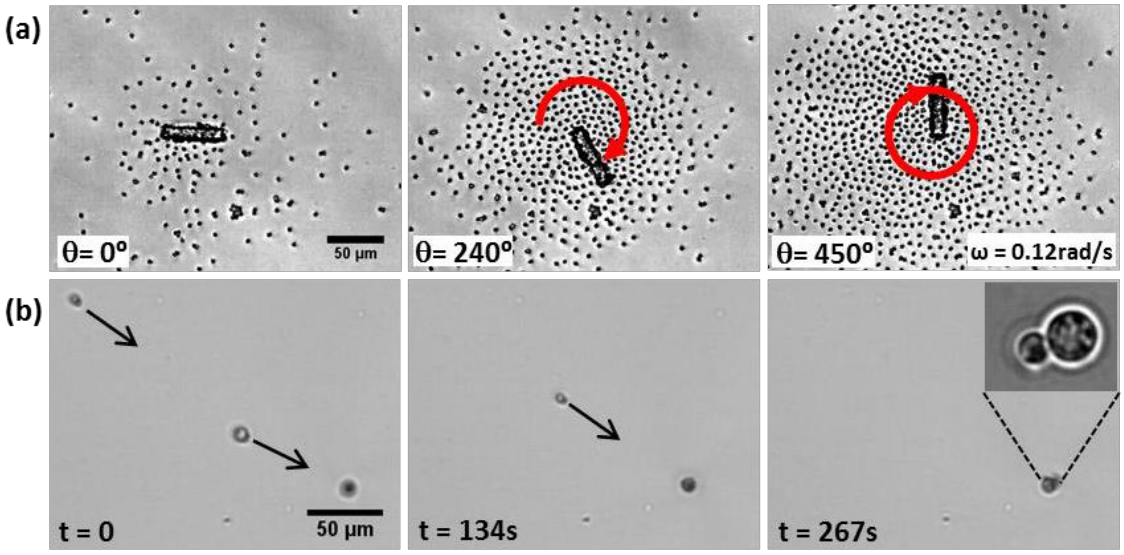

Figura 6.5: (a) una vareta de vidre micromètrica de 50µm de longitud i 10µm de diàmetre gira per l'acció de les micropartícules de l'eixam. (b) Gotes de glicerol s'acumulen en un punt. en el requadre es mostren dues gotes agregades d'aquesta manera.

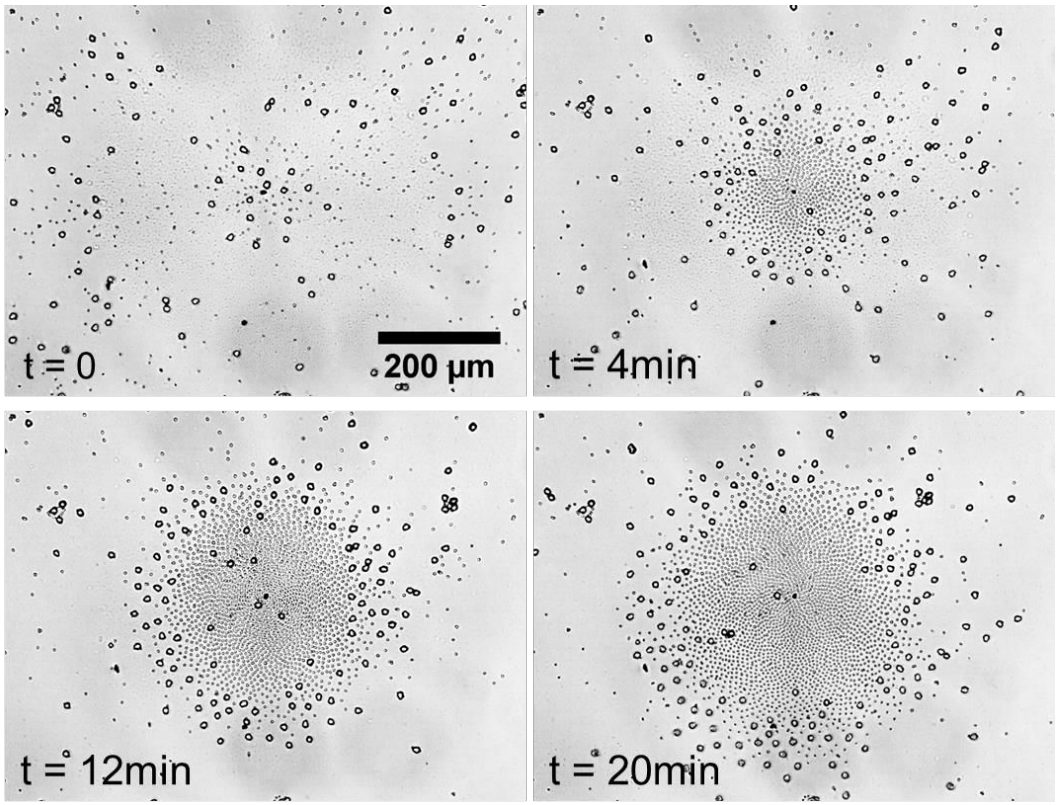

Figura 6.6: Seqüència d'imatges d'un eixam col·loïdal format per una barreja de partícules anisomètriques petites (3x4µm^2) i grans (8.3x10.2µm^2) que s'organitzen en un aster.

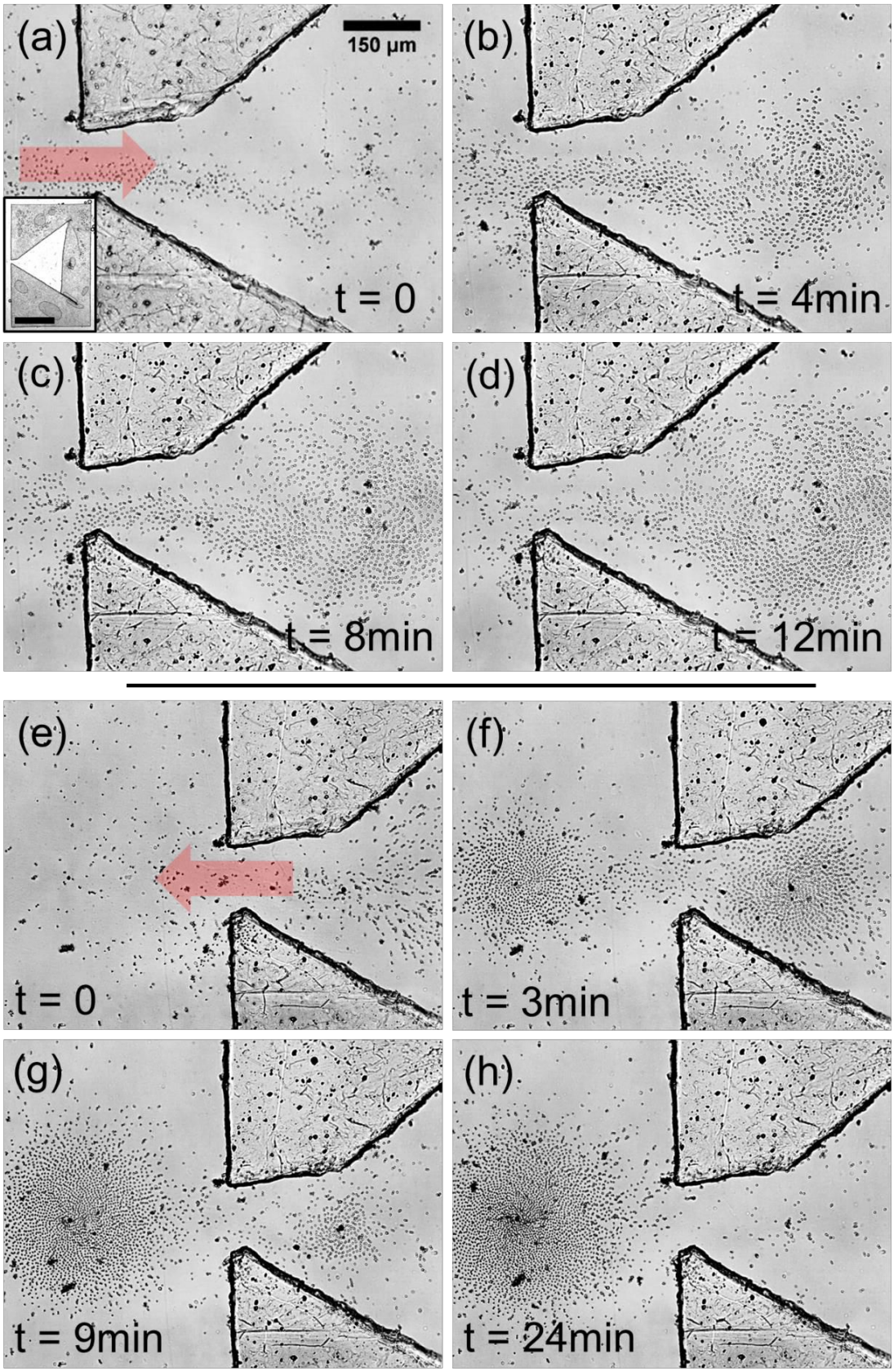

Figura 6.7: Seqüència d'imatges d'un eixam col·loïdal impulsat a dins (a-d) i a fora (e-h) d'un confinament triangular. El camp elèctric altern aplicat en les dues parts és 0.9V/µm i 10 Hz. El requadre en (a) mostra una ampliació de l'estructura rectangular amb una obertura triangular, el seu marques de barra d'escala de 1,5 mm.

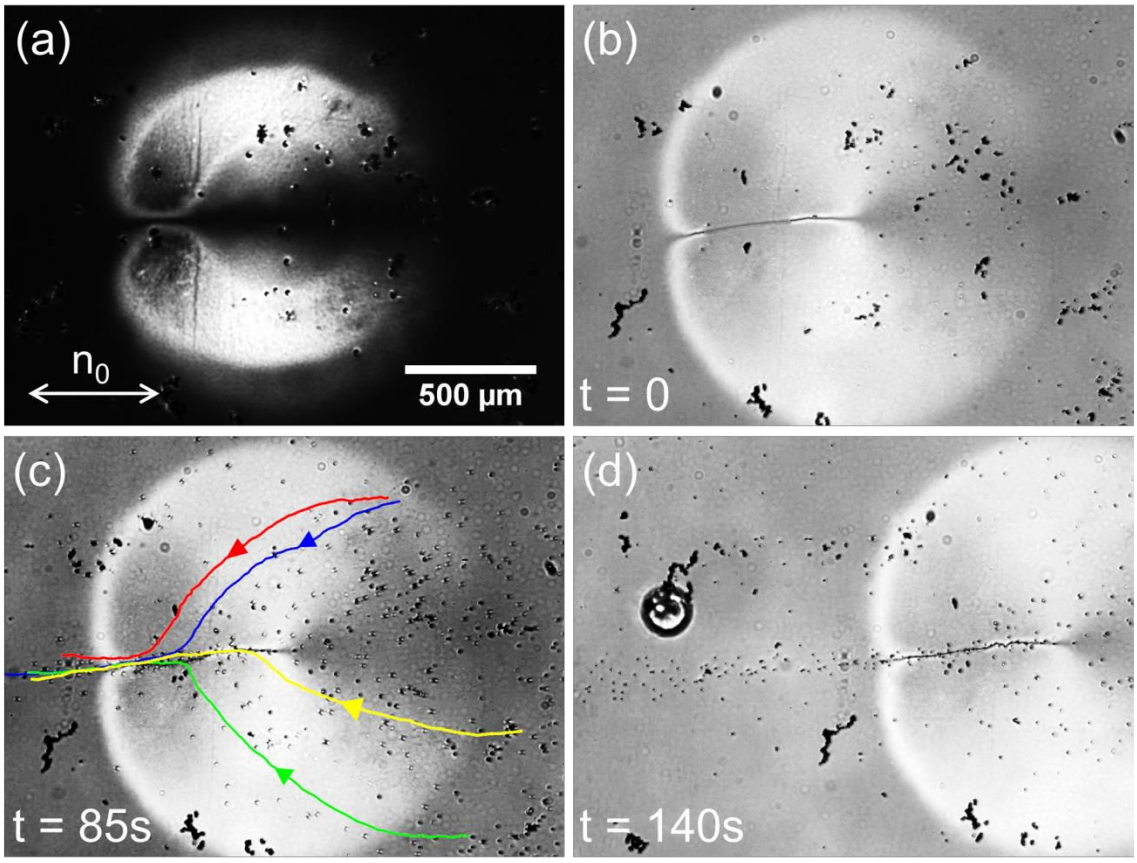

Figura 6.8: Imatges entre polaritzadors creuats de la formació d'un feix de partícules. (a) Imatge del patró circular imprès abans de l'aplicació del camp altern. (b-d) Després de l'aplicació del camp elèctric (E = 1.1V/µm, f = 5Hz), les partícules es mouen cap al patró en forma d'embut i són expulsades formant un feix de partícules. En (b), el defecte de línia a la banda esquerra del patró apareix quan s'aplica el camp altern. En aquest cas la cel·la es compon d'una placa fotosensible i una contraplaca planar direccional (en (a) n0 marca la direcció inicial del NLC), i les partícules disperses utilitzades són esferes de sílica homeotròpiques, en lloc de partícules *pear-shaped* planars.

6.4 Conclusions

- Les partícules *pear-shaped* amb ancoratge planar es poden transportar de manera efectiva per mitjà d'LCEEP. La seva forma anisomètrica trenca la simetria del camp director NLC al seu voltant, cosa que en permet la propulsió sota camps elèctrics de corrent altern.

- És possible separar la propulsió de les partícules, induïda per LCEEP, del control de la direcció de moviment, determinada per la reconfiguració d'una capa fotosensible mitjançant la irradiació de llum UV-visible. D'aquesta manera, fent servir patrons foto-induïts, conjunts d'inclusions col·loïdals es poden reconfigurar dinàmicament en diferents formes d'agregació, ja que les partícules es propulsen individualment en el cristall líquid.

- Els experiments presentats poden considerar-se com una prova de concepte per a una nova estratègia que permet el control dels conjunts d'inclusions col·loïdals propulsades de diferent naturalesa, ja que els materials involucrats han de complir només uns requisits genèrics perquè els mecanismes de propulsió i de control de direcció siguin eficaços.

- Es pot preveure una major extensió de l'estratègia reportada en aquest capítol. Per exemple, es podria utilitzar en sistemes vius mitjançant l'ús de cristalls líquids liotròpics biocompatibles, o també es podria emprar per obtenir sistemes model per estudiar el comportament d'eixams o la dinàmica de la matèria tova (*soft matter*) activa.

7. Referències

(1) Bumb, A.; Sarkar, S. K.; Billington, N.; Brechbiel, M. W.; Neuman, K. C. Silica Encapsulation of Fluorescent Nanodiamonds for Colloidal Stability and Facile Surface Functionalization. *J. Am. Chem. Soc.* **2013**, *135*, 7815–7818.

(2) Sacanna, S.; Irvine, W. T. M.; Chaikin, P. M.; Pine, D. J. Lock and Key Colloids. *Nature* **2010**, *464*, 575–578.

(3) Park, S. Y.; Lytton-Jean, A. K. R.; Lee, B.; Weigand, S.; Schatz, G. C.; Mirkin, C. A. DNA-Programmable Nanoparticle Crystallization. *Nature* **2008**, *451*, 553–556.

(4) Monti, D. M.; Guarnieri, D.; Napolitano, G.; Piccoli, R.; Netti, P.; Fusco, S.; Arciello, A. Biocompatibility, Uptake and Endocytosis Pathways of Polystyrene Nanoparticles in Primary Human Renal Epithelial Cells. *J. Biotechnol.* **2015**, *193*, 3–10.

(5) Koenig, G. M.; Lin, I.-H.; Abbott, N. L. Chemoresponsive Assemblies of Microparticles at Liquid Crystalline Interfaces. *Proc. Natl. Acad. Sci.* **2010**, *107*, 3998–4003.

(6) Lintuvuori, J. S.; Stratford, K.; Cates, M. E.; Marenduzzo, D. Colloids in Cholesterics: Size-Dependent Defects and Non-Stokesian Microrheology. *Phys. Rev. Lett.* **2010**, *105*, 178302.

(7) Lavrentovich, O. D.; Lazo, I.; Pishnyak, O. P. Nonlinear Electrophoresis of Dielectric and Metal Spheres in a Nematic Liquid Crystal. *Nature* **2010**, *467*, 947–950.

(8) Pishnyak, O. P.; Tang, S.; Kelly, J. R.; Shiyanovskii, S.; Lavrentovich, O. D. Levitation, Lift, and Bidirectional Motion of Colloidal Particles in an Electrically Driven Nematic Liquid Crystal. *Phys. Rev. Lett.* **2007**, *99*, 127802.

(9) Petrucci, R. H.; Herring, F. G.; Madura, J. D.; Bissonnette, C. *General Chemistry: Principles & Modern Applications*; 10th editi.; Pearson Canada: Toronto, 2011.

(10) Kleman, M.; Lavrentovich, O. D. *Soft Matter Physics - An Introduction*; Springer, 2003.

(11) Oswald, P.; Pieranski, P. *Nematic and Cholesteric Liquid Crystals: Concepts and Physical Properties Illustrated by Experiments*; Taylor& Francis: Boca Raton, 2005.

(12) Burylov, S. V; Raikher, Y. L. Orientation of A Solid Particle Embedded In A Monodomain Nematic Liquid-Crystal. *Phys. Rev. E* **1994**, *50*, 358–367.

(13) Stark, H. Physics of Colloidal Dispersions in Nematic Liquid Crystals. *Phys. Rep.* **2001**, *351*, 387–474.

(14) Squires, T. M.; Bazant, M. Z. Induced-Charge Electro-Osmosis. *J. Fluid Mech.* **2004**, *509*, 217–252.

(15) Squires, T. M.; Bazant, M. Z. Breaking Symmetries in Induced-Charge Electro-Osmosis and Electrophoresis. *J. Fluid Mech.* **2006**, *560*, 65–101.

(16) Gangwal, S.; Cayre, O.; Bazant, M.; Velev, O. D. Induced-Charge Electrophoresis of Metallodielectric Particles. *Phys. Rev. Lett.* **2008**, *100*, 58302.

(17) Yariv, E. Induced-Charge Electrophoresis of Nonspherical Particles. *Phys. Fluids* **2005**, *17*, 051702.

(18) Lavrentovich, O. D. Transport of Particles in Liquid Crystals. *Soft Matter* **2014**, *10*, 1264–1283.

(19) Lazo, I.; Peng, C.; Xiang, J.; Shiyanovskii, S. V; Lavrentovich, O. D. Liquid Crystal-Enabled Electro-Osmosis through Spatial Charge Separation in Distorted Regions as a Novel Mechanism of Electrokinetics. *Nat. Commun.* **2014**, *5*, 5033.

(20) Lazo, I.; Lavrentovich, O. D. Liquid-Crystal-Enabled Electrophoresis of Spheres in a Nematic Medium with Negative Dielectric Anisotropy. *Philos. Trans. R. Soc. A-mathematical Phys. Eng. Sci.* **2013**, *371*, 20120255.

(21) Ulman, A. *An Introduction to Ultrathin Organic Films*; Academic Press: Boston, 1991.

(22) Ulman, A. Formation and Structure of Self-Assembled Monolayers. *Chem. Rev.* **1996**, *96*, 1533–1554.

(23) Howarter, J. A.; Youngblood, J. P. Optimization of Silica Silanization by 3-Aminopropyltriethoxysilane. *Langmuir* **2006**, *22*, 11142–11147.

(24) Crusats, J.; Albalat, R.; Claret, J.; Ignés-Mullol, J.; Sagués, F. Influence of Temperature and Composition on the Mesoscopic Textures of Azobenzene Langmuir Monolayers. *Langmuir* **2004**, *20*, 8668–8674.

(25) Albericio, F.; Bofill, J. M.; El-Faham, A.; Kates, S. A. Use of Onium Salt-Based Coupling Reagents in Peptide Synthesis1. *J. Org. Chem.* **1998**, *63*, 9678–9683.

(26) Tierno, P.; Albalat, R.; Sagués, F. Autonomously Moving Catalytic Microellipsoids Dynamically Guided by External Magnetic Fields. *SMALL* **2010**, *6*, 1749–1752.

(27) Lin, S. Y.; Chow, E.; Hietala, V.; Villeneuve, P. R.; Joannopoulos, J. D. Experimental Demonstration of Guiding and Bending of Electromagnetic Waves in a Photonic Crystal. *Science* **1998**, *282*, 274–276.

(28) Blanco, A.; Chomski, E.; Grabtchak, S.; Ibisate, M.; John, S.; Leonard, S. W.; Lopez, C.; Meseguer, F.; Miguez, H.; Mondia, J. P.; et al. Large-Scale Synthesis of a Silicon Photonic Crystal with a Complete Three-Dimensional Bandgap near 1.5 Micrometres. *Nature* **2000**, *405*, 437–440.

(29) Velev, O. D.; Kaler, E. W. In Situ Assembly of Colloidal Particles into Miniaturized Biosensors. *Langmuir* **1999**, *15*, 3693–3698.

(30) Gau, H.; Herminghaus, S.; Lenz, P.; Lipowsky, R. Liquid Morphologies on Structured Surfaces: From Microchannels to Microchips. *Science* **1999**, *283*, 46–49.

(31) Qi, H.; Kinkead, B.; Hegmann, T. Unprecedented Dual Alignment Mode and Freedericksz Transition in Planar Nematic Liquid Crystal Cells Doped with Gold Nanoclusters. *Adv. Funct. Mater.* **2008**, *18*, 212–221.

(32) Acharya, S.; Kundu, S.; Hill, J. P.; Richards, G. J.; Ariga, K. Nanorod-Driven Orientational Control of Liquid Crystal for Polarization-Tailored Electro-Optic Devices. *Adv. Mater.* **2009**, *21*, 989+.

(33) Stone, H. A.; Stroock, A. D.; Ajdari, A. Engineering Flows in Small Devices: Microfluidics toward a Lab-on-a-Chip. *Annu. Rev. Fluid Mech.* **2004**, *36*, 381–411.

(34) Squires, T. M.; Quake, S. R. Microfluidics: Fluid Physics at the Nanoliter Scale. *Rev. Mod. Phys.* **2005**, *77*, 977–1026.

(35) Song, H.; Chen, D. L.; Ismagilov, R. F. Reactions in Droplets in Microflulidic Channels. *Angew. Chemie-international Ed.* **2006**, *45*, 7336–7356.

(36) Shim, J.; Cristobal, G.; Link, D. R.; Thorsen, T.; Jia, Y.; Piattelli, K.; Fraden, S. Control and Measurement of the Phase Behavior of Aqueous Solutions Using Microfluidics. *J. Am. Chem. Soc.* **2007**, *129*, 8825–8835.

(37) Buhr, D. L.; Acca, F. E.; Holland, E. G.; Johnson, K.; Maksymiuk, G. M.; Vaill, A.; Kay, B. K.; Weitz, D. A.; Weiner, M. P.; Kiss, M. M. Use of Micro-Emulsion Technology for the Directed Evolution of Antibodies. *Methods* **2012**, *58*, 28–33.

(38) Paxton, W. F.; Kistler, K. C.; Olmeda, C. C.; Sen, A.; St. Angelo, S. K.; Cao, Y.; Mallouk, T. E.; Lammert, P. E.; Crespi, V. H. Catalytic Nanomotors: Autonomous Movement of Striped Nanorods. *J. Am. Chem. Soc.* **2004**, *126*, 13424–13431.

(39) Fournier-Bidoz, S.; Arsenault, A. C.; Manners, I.; Ozin, G. A. Synthetic Self-Propelled Nanorotors. *Chem. Commun.* **2005**, 441–443.

(40) Sanchez, S.; Solovev, A. A.; Mei, Y.; Schmidt, O. G. Dynamics of Biocatalytic Microengines Mediated by Variable Friction Control. *J. Am. Chem. Soc.* **2010**, *132*, 13144–13145.

(41) Howse, J. R.; Jones, R. A. L.; Ryan, A. J.; Gough, T.; Vafabakhsh, R.; Golestanian, R. Self-Motile Colloidal Particles: From Directed Propulsion to Random Walk. *Phys. Rev. Lett.* **2007**, *99*, 48102.

(42) Gao, W.; Pei, A.; Wang, J. Water-Driven Micromotors. *ACS Nano* **2012**, *6*, 8432–8438.

(43) Kim, E.; Xia, Y. N.; Whitesides, G. M. Polymer Microstructures Formed by Molding in Capillaries. *Nature* **1995**, *376*, 581–584.